Diffusion MRI in premanifest Huntington's disease and early Parkinson's disease: tensor and tractography analyses



Chris Patrick Pflanz, BSc, MSc, AFHEA

St Catherine's College

University of Oxford

A thesis submitted in partial fulfillment of the requirements for the degree of

Doctor of Philosophy

2019

D.Phil. Supervisors

Professor Gwenaëlle Douaud, PhD

Professor Mark Jenkinson, DPhil

Abstract

Huntington's and Parkinson's disease are neurodegenerative movement disorders that both affect the basal ganglia, a system of interconnected deep cerebral nuclei that receive converging input from various cortical areas through white matter tracts. Here we have used diffusion MRI to investigate changes in the tissue microstructure of the basal ganglia, as well as the white matter in presymptomatic/early Huntington's and early Parkinson's disease. In the presymptomatic Huntington's disease group longitudinal sensitivity of diffusion MRI across presymptomatic stages was investigated. We also have investigated the connectivity of the basal ganglia with the cortex, and derived connectivity-based parcellations of the gobus pallidus, and subthalamic nucleus, two important hubs of the basal ganglia system, into motor, limbic, and associative territories.

In presymptomatic Huntington's disease distinct longitudinal changes in the microstructure of the posterior part of the basal ganglia and the splenium of the corpus callosum, as revealed by diffusion tensor metrics, were detectable at different presymptomatic stages. Both patients with Huntington's and Parkinson's disease showed micro-structural alterations in the internal segment of the globus pallidus, and the posterior limb of the internal capsule, two important neuroanatomical

structures of the basal ganglia system. Huntington's disease patients also showed marked decreases in their structural connectivity in the motor basal ganglia pathway, and the cortico-subthalamic hyperdirect pathway. The volumes of connectivity-based territories of the globus pallidus, pars interna, and subthalamic nucleus undergo disease-specific alterations that capture opposing effects in Huntington's vs. Parkinson's disease. Connectivity-based territories undergo disease-related changes in their coordinates that might be of clinical importance. Neuroimaging outcomes were found to be correlated with clinical questionnaire data.

Acknowledgements

First and foremost, I would like to thank my supervisors, Professor Gwenaelle Douaud and Professor Mark Jenkinson for their valuable guidance and support during the DPhil thesis. I am also grateful for the help from my colleagues form the Welcome Centre for Integrative Neuroimaging/Oxford Center for functional MRI of the brain (FMRIB), especially Marina Charquero-Ballester, Sirius Boessenkool, and Dr. Matteo Bastiani.

I am also most grateful to Dr. Stefania Evangelisti from the Department of Biomedical and Neuromotor Sciences, Università degli Studi di Bologna, who has manually edited the masks of the globus pallidus and subthalamic nucleus that were used for probabilistic tractography in chapters 6 and 7.

I would like to acknowledge our collaborators at University of California San Diego (UCSD), especially Dr. Adnan Majid, Professor Adam Aron, who have acquired the data used for the data analysis in chapters 1-3.

This work was supported by funding from the Engineering and Physical Sciences Research Council (EPSRC) and Medical Research Council (MRC) [grant number EP/L016052/1].

Table of Contents

Part I: Longitudinal diffusion MRI in presymptomatic Huntington's disease.....15

I.0 Introduction.....15

I.0.1 Introducing Huntington's disease.....15

I.0.2 Introducing Diffusion MRI and diffusion tensor imaging.....21

Chapter I.1: Huntington's disease differentially affects gray matter micro-structure across presymptomatic stages over a one-year period.....34

1.0. Abstract.....34

1.1. Introduction.....37

1.2. Methods.....39

1.2.1. Participants and study design.....39

1.2.2. Data acquisition.....44

1.2.3. Data processing.....45

1.2.4. Statistical analyses.....50

1.3. Results.....51

1.3.1. Comparing the entire presymptomatic Huntington's disease group with the control group.....51

1.3.2. Groups according to estimated years to onset of symptoms vs. control subjects.....52

1.3.2.1. Mean diffusivity.....52

1.3.2.2. Fractional anisotropy.....54

1.4. Discussion.....57

1.5. Conclusions.....63

Chapter I.2: Can longitudinal diffusion MRI of the white matter be used as an early biomarker for neurodegeneration in presymptomatic Huntington's disease?.....64
2.0. Abstract.....64
2.1. Introduction.....67
2.2. Methods.....69
2.2.1. Data processing.....70
2.2.2. Atlas-based Region of Interest Analysis.....71
2.2.3. Cortico-subcortical probabilistic tractography.....73
2.2.4. Whole white matter TBSS.....76
2.2.5. Statistical analyses.....77
2.3. Results.....79
2.3.1 Atlas-based white matter ROIs.....79
2.3.2 Cortico-subcortical tractography ROIs.....82
2.3.3. Whole white matter voxel-wise analysis.....84
2.4. Discussion.....94
Chapter I.3: Longitudinal changes in clinical questionnaire scores and behavioral data in presymptomatic Huntington's disease and their correlations with diffusion metrics.....101
3.0. Abstract.....101
3.1. Introduction.....103
3.2. Methods.....104
3.2.1. Overview of clinical and psychometric assessment tools.....104
3.2.2. Statistical analysis.....105
3.3. Results.....106

3.3.1. Exploratory data analysis on questionnaire scores.....106
3.3.2. Longitudinal changes in questionnaire scores.....110
3.3.3. Group differences in longitudinal changes in questionnaire scores.....111
3.4. Discussion.....115
Part II. Ultra high-field Diffusion MRI in early Huntington's and Parkinson's disease.....120
II.0. Introduction.....120
II.0.1. Introducing Parkinson's disease.....120
II.0.2. Introducing ultra-high-field diffusion MRI at 7T.....123
Chapter II.4: Comparison of the gray matter micro-structure in early Huntington's and Parkinson's disease using ultra high-field diffusion MRI.....126
4.0. Abstract.....126
4.1. Introduction.....128
4.2. Methods.....131
4.2.1. Participants and study design.....132
4.2.2. Data acquisition.....135
4.2.3. Data processing.....136
4.2.3.1 Pre-processing in native space.....136
4.2.3.2. Spatial normalization and preprocessing in standard space.....139
4.2.4. Data analysis.....139
4.2.4.1. Inferential statistical analyses.....140
4.2.4.2. Dimensionality reduction of questionnaire scores using sparse PCA.....142
4.2.4.3. Dimensionality reduction of questionnaire scores using exploratory factor analysis.....143

4.2.4.4. Post-hoc correlation analysis between neuroimaging data and sparse PCA/factor analysis components....144
4.3. Results....145
4.3.1. Voxel-wise comparisons of diffusion metrics....145
4.3.1.1. Linear contrasts comparing multiple patient groups with age-/gender-matched healthy controls....145
4.3.1.2. Comparing single patient groups with their age-/gender matched healthy controls....146
4.3.2. Sparse PCA of UHDRS and UPDRS questionnaire scores....154
4.3.2.1. Decomposition of UHDRS and UPDRS questionnaire scores into sparse main components....154
4.3.2.2. Correlation between imaging outcomes and UHDRS/UPDRS sparse principal components....159
4.3.3. Exploratory factor analysis of UHDRS and UPDRS questionnaire scores....161
4.3.3.1. Decomposition of UHDRS and UPDRS questionnaire scores into latent factors 161
4.3.3.2. Correlation between imaging outcomes and UHDRS/UPDRS latent variables from exploratory factor analysis....166
4.4. Discussion....168
Chapter II.5: Comparison of the white matter micro-structure in early Huntington's and Parkinson's disease using ultra high-field diffusion MRI....176
5.0. Abstract....176
5.1. Introduction....178

5.2. Methods....181
5.2.1. Tract-based spatial statistics....181
5.2.2. Statistical analyses....184
5.2.2.1 Voxel-wise statistical analyses....184
5.2.2.2 Post-hoc correlation analysis between neuroimaging data and sparse PCA/factor analysis components....185
5.3. Results....186
5.3.1. Voxel-wise comparisons of diffusion metrics....186
5.3.1.1. Linear contrasts comparing multiple patient groups with age-/gender-matched healthy controls....186
5.3.1.2. Comparing single patient groups with their age-/gender matched healthy controls....195
5.3.2 Correlations of imaging outcomes with components from sparse PCA....201
5.3.3 Correlations of imaging outcomes with latent variables from exploratory factor analysis....211
5.3.3.1 Correlations of imaging outcomes with latent variables from exploratory factor analysis within the Huntington's disease group....211
5.3.3.2 Correlations of imaging outcomes with latent variables from exploratory factor analysis within the Parkinson's disease group....219
5.4. Discussion....226
Chapter II.6: Probabilistic tractography of the hyper-direct pathway and connectivity-based parcellation of the subthalamic nucleus in early Huntington's and Parkinson's disease using ultra high-field diffusion MRI....234

6.0. Abstract.....234
6.1. Introduction.....236
6.2. Methods.....241
6.2.1. Participants and study design.....241
6.2.2. Data acquisition.....241
6.2.3. Data processing: Probabilistic tractography.....241
6.2.4. Connectivity strength.....245
6.2.5. Connectivity-based parcellation, volumetric analysis, and centre of gravity.....245
6.2.6. Spatial regression of tracts against diffusion metric images.....247
6.2.7 Statistical inference.....247
6.3. Results.....251
6.3.1. Strength of connectivity in motor, limbic, and associative hyperdirect pathways..253
6.3.2. Volumetric measures of motor, associative, and limbic territories within the subthalamic nucleus.....254
6.3.3. Measures of overlap and similarity for the motor and associative territories.....259
6.3.4. Centre of gravity (mass) statistics for the motor, limbic and associative connectivity-based parcellations.....261
6.3.5. Correlation of imaging data with UHDRS/UPDRS sparse components.....266
6.3.5.1. Post-hoc correlation of strength of connectivity and volumetric measures with UHDRS sparse components.....266
6.3.5.2. Post-hoc correlation of centre of gravity statistics with UHDRS sparse components.....270

6.3.5.3. Correlations between latent variable from exploratory factor analysis of UHDRS data and STN connectivity and volumetric metrics.....270
6.3.5.4. Correlations between latent factors from exploratory factor analysis of UHDRS data and centre of gravity statistics from STN tractography.....274
6.3.5.5. Post-hoc correlation of strength of connectivity and volumetric measures with UPDRS sparse components.....276
6.3.5.6. Post-hoc correlation of centre of gravity statistics with UPDRS sparse components.....278
6.3.5.7. Correlations between latent factors from exploratory factor analysis of UPDRS data and STN connectivity and volumetric metrics.....283
6.3.5.8. Correlations between latent variable from UPDRS exploratory factor analysis and centre of gravity statistics from STN tractography.....288
6.4. Discussion.....290
Chapter II.7: Probabilistic tractography of the motor, limbic, and associative basal ganglia loops and connectivity-based parcellation of the globus pallidus pars interna in early Huntington's and Parkinson's disease using 7Tesla diffusion MRI.....303
7.0. Abstract.....303
7.1. Introduction.....306
7.2. Methods.....311
7.2.1. Data processing: Probabilistic tractography.....311
7.2.2. Connectivity strength.....312
7.2.3. Connectivity-based parcellation, volumetric analysis, and centre of gravity.....312
7.2.4. Spatial regression of tracts against diffusion metric images.....315

7.2.5 Statistical inference.....315
7.3. Results.....316
7.3.1. Strength of connectivity in motor, limbic, and associative cumulative basal ganglia pathways.....318
7.3.2. Volumetric measures of motor, associative, and limbic territories within the globus pallidus, pars interna.....320
7.3.3. Measures of overlap and similarity for the motor and associative GPi territories..324
7.3.4. Centre of gravity (mass) statistics for the motor, limbic and associative connectivity-based parcellations.....327
7.3.5. Spatial regression of probabilistic reconstructions of the cumulative corticofugal basal ganglia pathway against diffusion metric images.....333
7.3.6. Correlation of imaging data with UHDRS/UPDRS sparse components.....336
7.3.6.1. Correlations of strength of connectivity and GPi volumetric measures with UHDRS sparse components.....336
7.3.6.2. Correlations between GPi centre of gravity statistics and UHDRS sparse components.....340
7.3.6.3. Correlations between latent factors from exploratory factor analysis of UHDRS data and strength of connectivity and GPi volumetric measures.....341
7.3.6.4. Correlations between latent factors from exploratory factor analysis of UHDRS data and GPi centre of gravity statistics.....347
7.3.6.5. Correlation of strength of connectivity and GPi volumetric measures with UPDRS sparse components.....352

7.3.6.6. Correlation of GPi centre of gravity statistics with UPDRS sparse components 353

7.3.6.7. Correlations between latent factors from exploratory factor analysis of UPDRS data and strength of connectivity and GPi volumetric metrics.....354

7.3.6.8. Correlations between latent factors from UPDRS exploratory factor analysis and GPi centre of gravity statistics.....356

7.4. Discussion.....361

8. Future work and perspectives on diffusion MRI in Huntington's and Parkinson's disease…383

9. Appendix : Results tables of chapter 3.....386

Part I: Longitudinal diffusion MRI in presymptomatic Huntington's disease

I.0 Introduction

I.0.1 Introducing Huntington's disease

Huntington's disease (HD) is an autosomal dominant inherited, neurodegenerative, hyperkinetic-hypotonic movement disorder, caused by a polyglutamine-expansion (a so-called PolyQ disease). From a symptomatic point of view it is characterized by so-called choreiform hyperkinesias, i.e. involuntary jerky movements, decreased muscle tone, and neuropsychiatric symptoms. HD is caused by a polyglutamine-expansion resulting from a mutant cytosine-adenine-guanine (CAG) repeat located on the short arm (p, from French *petit* meaning small) of chromosome 4 (4p16.3) (Ross and Tabrizi, 2011). Huntington's disease is considered to be a model neurodegenerative disorder, in that it is amenable to predictive genetic testing with estimation of years to the onset of symptoms, thereby enabling the entire natural history of neurodegeneration to be studied from a presymptomatic stage at 100% risk of conversion to the disease (Ross and Tabrizi, 2011).

Adult onset HD has an average age of onset of 40 year (Myers, 2004). The symptomatic stage of HD is preceded by a long pre-symptomatic period, during which various neuropathological alterations are also detectable in the absence of any

clinical symptoms (Chandra, Johri and Beal, 2014). This presymptomatic period, the time between genetic and motor diagnosis, spans several decades (Walker, 2007). Clinical diagnosis of HD is not the start but already an advanced stage with respect to pathophysiological changes in the cerebral neural tissue with degeneration of neurons already taking place. Indeed, at the time of motor diagnosis, large parts of neuronal tissue are already irreversibly lost. Metabolic, neuroinflammatory, and structural changes were detectable up to 10 years before the onset of symptoms (Chandra, Johri and Beal, 2014). Neuroprotective, disease-modifying agents are currently investigated in preclinical, and clinical research, but without a prognostic state biomarker the optimal time-frame for disease modifying therapy is being missed. Hence, there is a clear need for an early, prognostic state biomarker to monitor progression of the disease and proximity to the onset of the disease above and beyond genetic information, and to ensure that the optimal time-frame for disease modifying, neuroprotective therapy is not missed (Weir *et al.*, 2011).

The Biomarker Definitions Working Group defines biomarker as a "characteristic that is objectively measured and evaluated as an indicator of normal biological processes, pathogenic processes, or pharmacological responses to therapeutic intervention" (Biomarkers Definitions Working Group, 2001). To be useful as a state

biomarker for preHD, neuroimaging measures need to be sensitive enough to (1) monitor proximity to the onset of the disease (prognostic marker), (2) detect microstructural changes over time, thereby elucidating underlying pathophysiological mechanisms (mechanistic marker), and (3) indicate effectiveness of potential treatment options in clinical trials (surrogate marker). More specifically, a prognostic marker should provide useful information to stratify individuals with presymptomatic Huntington's disease (preHD) into presymptomatic stages according to their proximity to the manifest stage of the disease, and be useful to monitor factors that delay the onset of the disease. A mechanistic marker needs to distinguish neuroinflammatory and neurodegenerative stages of the presymptomatic phase of the disease. A surrogate marker should be useful for monitoring the clinical benefits of potential treatment options, and identifying their window of opportunity.

Diffusion MRI might be a promising candidate for such a biomarker. Indeed, MRI sequences can be rendered sensitive to the diffusion of water molecules through the application of diffusion gradients that are oriented parallel to that direction. In the brain parenchyma diffusion is restricted by microstructural barriers. The magnitude and direction of water diffusion can therefore be used as a probe of the underlying tissue microstructure. The diffusion of water in neural tissues occurs inside, outside,

and across its cellular components (Alexander *et al.*, 2007). In the brain, diffusion is restricted by its characteristic microstructure, i.e. the hydrophobic lipid bilayer of the neuronal cell membrane hinders diffusion in the gray and white matter, and the dielectric myelin sheath, covering the axon, further restricts diffusion in the white matter (Beaulieu, 2002). Diffusion across the neural cell membrane occurs through various mechanisms, including pinocytosis, co-transport with ions, and aquaporins; but at a slower rate, when compared with bulk diffusion parallel to the cell membrane (Beaulieu, 2010). These diffusion restrictions lead to signal attenuation in diffusion MRI, if the direction of the diffusion gradient is perpendicular to the diffusion restrictions. As a result, diffusion MRI is sensitive to subtle abnormalities to the gray matter microstructure, which serves as a proxy marker of tissue integrity. As such, it has the potential to detect early brain tissue alterations in the presymptomatic stage preceding the volume loss detected at a macro-scale with structural MRI (Douaud, Behrens, *et al.*, 2009; Rosas *et al.*, 2010; Douaud *et al.*, 2011).

It has been hypothesized that diffusion MRI has the potential to distinguish whether atrophy of both the gray and white matter is general or the result of selective degeneration of neuronal cell ensembles, whose connections have a certain

orientation, whereas other cell ensembles are relatively spared (Douaud, Behrens, *et al.*, 2009). Fractional anisotropy (FA) is found to be lower in neurodegenerative diseases in tissue with a particular directional organization, such as white matter tracts, due to less diffusion restrictions (Pierpaoli and Basser, 1996; Beaulieu, 2002). By contrast, higher FA in neurodegenerative diseases, including HD (Ciccarelli *et al.*, 2001; Douaud, Mackay, *et al.*, 2009) might result from the selective loss of neurons, whose axons have a certain directional orientation, compared with other spared projections. More specifically, in the white matter higher FA might result from selective loss of tracts that cross each other, whereas other tracts are spared (Ciccarelli *et al.*, 2001); and in the gray matter of deep cerebral nuclei higher FA might result from selective degeneration of neurons with a certain polarity, i.e. the asymmetry in the distribution of cellular components, (especially the axon, and dendrites), whereas neurons with a different polarity are spared (Douaud, Behrens, *et al.*, 2009). Mean diffusivity (MD) is often increased in both the gray and white matter in response to neurodegenerative processes, which reflects a decrease in diffusion restrictions irrespective of fiber orientation (Alexander *et al.*, 2007).

However, evidence for longitudinal microstructural changes in presymptomatic Huntington's disease is lacking so far. Previous longitudinal research did not reveal

any microstructural changes in presymptomatic Huntington's disease over a period of 18 months (Domínguez *et al.*, 2013; Poudel *et al.*, 2015), or 2y (Odish, Leemans, *et al.*, 2015). Effects were only detected using cross-sectional analyses (Domínguez *et al.*, 2013; Odish, Leemans, *et al.*, 2015; Poudel *et al.*, 2015), or longitudinally once Huntington's disease was symptomatic (Domínguez *et al.*, 2013; Poudel *et al.*, 2015). The only diffusion MRI study in preHD reporting significant longitudinal effects used graph theoretical analyses, and found longitudinal changes in nodal network organization in a group near the predicted onset of symptoms when compared with a group far from onset, and controls; as well as reduced inter-nodal information processing in the connectome in the entire preHD group (Odish, Caeyenberghs, *et al.*, 2015). However, graph theory offers limited information on underlying microstructure and pathophysiology, and its clinical usefulness remains elusive. By contrast, previous cross-sectional research has been promising in finding differences between participants with presymptomatic Huntington's disease compared with healthy controls (Rosas *et al.*, 2010; Stoffers *et al.*, 2010; Di Paola *et al.*, 2012).

I.0.2 Introducing Diffusion MRI and diffusion tensor imaging

" 'True,' said the Sphere, 'it appears to you a Plane, because you are not accustomed to light and shade and perspective; just as in Flatland a Hexagon would appear a Straight Line to one who has not the Art of Sight Recognition. But in reality it is a Solid, as you shall learn by the sense of Feeling.'' He then introduced me to the Cube, and I found that this marvelous Being was indeed no Plane, but a Solid; and that he was endowed with six plane sides and eight terminal points called solid angles; and I remembered the saying of the Sphere that just such a Creature as this would be formed by a Square moving, in Space, parallel to himself."

Edwin A Abbott: Flatland a romance of many dimensions

Diffusion can be defined as the random Brownian movement of molecules in a fluid (i.e. a liquid or a gas) that is due to the thermal energy of these molecules. In a completely homogeneous fluid the magnitude of diffusion is equal in all directions, i.e. diffusion is isotropic. By contrast, in living cells, tissues and organs the diffusion of fluids, especially of water molecules, is restricted by its characteristic micro-structure, and the diffusion is therefore not equal in all directions, i.e. diffusion is anisotropic. In the central nervous system diffusion is restricted by the characteristic microstructure of neurons, and myelinated axons that form white matter tracts (Beaulieu, 2010, 2014).

To further explain the properties of anisotropic diffusion, we will consider the following thought experiment, and imagine that diffusion occurs only along one axis

in a one-dimensional coordinate system (Hagmann *et al.*, 2006). For each displacement distance **r** along this one-dimensional coordinate system a corresponding probability **p** can be defined as **n/N**, the proportion of molecules within a volumetric element (also know as voxel) that moved the given distance **r** within a given time **t** (Hagmann *et al.*, 2006). In an isotropic medium, this probability will be high at the origin of the coordinate system that corresponds to no net displacement, and will decrease for higher distances **r**. Thus the Brownian movement for all distances can be described as a displacement distribution that can be modeled as a Gaussian normal distribution, or random variable with its moments as the characteristic properties:

1. First moment or distribution mean: the magnitude of diffusion along the dimension
2. Second moment or variance: the deviation from the mean, or spread around the mean
3. Third moment or skewness: the asymmetry of the distribution around the mean.

This 1-dimensional model of diffusion can now be easily generalized into 3D-space. Geometrically, isotropic diffusion can be model as a sphere with the radius as the

magnitude of diffusion (1st moment), and anisotropic diffusion can be modeled as a spheroid with 2nd, and 3rd moments describing its derivation from the sphere. Mathematically, anisotropic diffusion can be described as a multivariate Gaussian probability density function using the following equation introduced by Basser et al (Basser, Mattiello and LeBihan, 1994a, 1994b; Basser, 1995):

$$P(\Delta\vec{r}, \Delta t) = \frac{1}{\sqrt{(4\pi\Delta t)^3 \mid \mathbf{D}\mid}} exp\left\{\frac{-\Delta\vec{r}^{\,T}\mathbf{D}^{-1}\Delta\vec{r}}{4\Delta t}\right\}$$

$$\mathbf{D} = \begin{bmatrix} D_{xx} & D_{xy} & D_{xz} \\ D_{yx} & D_{yy} & D_{yz} \\ D_{zx} & D_{zy} & D_{zz} \end{bmatrix}$$

where P(Δr,Δt) represents the probability of moving Δr within the time Δt, and D is the diffusion tensor, a 3×3 symmetrical covariance matrix of displacements **r** in a given time **t**.

Since the diffusion tensor D is symmetrical, it can be brought into its diagonal form (with off diagonal elements equal to zero) by transformation of the principal axes of the 3D-coordinate system using an orthogonal transformation matrix E (Bronshtein *et al.*, 2007). The diagonal elements of the diagonal form of the diffusion tensor are

called singular values or eigenvalues λ_1, λ_2, and λ_3. The column vectors of the transformation matrix that is used for the rotation of the principal axes of the coordinate system are called the singular vectors or eigenvectors ε_1, ε_2 , ε_3 . The directions of these eigenvectors correspond to the direction of the transformed principal axes.

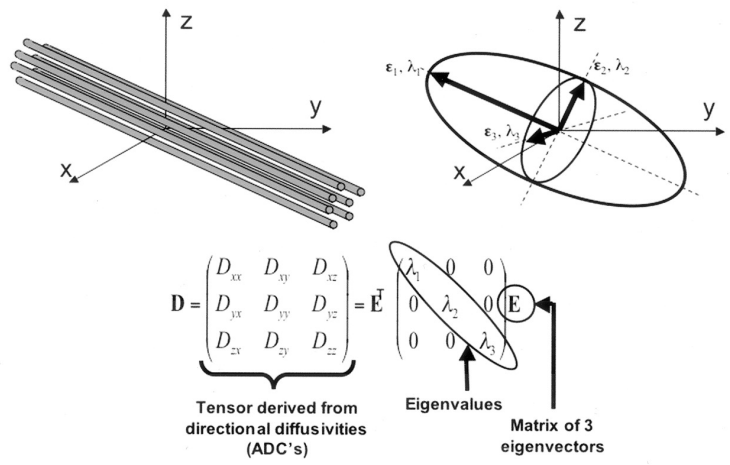

Figure 0.1. Geometrical interpretation and mathematical decomposition of the diffusion tensor into its eigenvalues and the eigenvectors by rotation of the principal axes (Jellison *et al.*, 2004) .

Geometrically the diffusion tensor can be described as an ellipsoid, i.e. a three dimensional body derived from the rotation of an ellipse along its main axis, using the following equation (Kingsley, 2006):

$$\frac{x'^2}{2\lambda_{x'}t} + \frac{y'^2}{2\lambda_{y'}t} + \frac{z'^2}{2\lambda_{z'}t} = 1$$

where x', y', and z' correspond to the transformed principal axis of the coordinate system, $\lambda_{x'}$, $\lambda_{y'}$, and $\lambda_{z'}$ are the eigenvalues of the diffusion tensor, and t corresponds to the time. From the equation it is immediately clear that if $\lambda_{x'} = \lambda_{y'} = \lambda_{z'}$, the ellipsoid becomes a sphere, and the resulting equation is that of a sphere.

In order to get a meaningful description of diffusion in 3D space, it is necessary to base any inference about diffusion on tensor invariants, i.e. on properties of the diffusion tensor that are invariant to any transformation of the coordinate system. In analogy to our initial thought experiment about diffusion in one-dimensional space, the following tensor invariants can be derived from the moments of the multivariate Gaussian probability density function:

1. Fist moment: the mean apparent diffusion coefficient or mean diffusivity, the overall magnitude of diffusion irrespective of any direction (Pierpaoli and Basser, 1996)

$$MD = \frac{\text{Trace (D)}}{3} = \frac{\lambda_1+\lambda_2+\lambda_3}{3}$$

2. Second moment: various measures of anisotropy that describe the deviation of the diffusion ellipsoid from the sphere have been defined (Pierpaoli and Basser,

1996; Curran, Emsell and Leemans, 2016). The most widely used is the fractional anisotropy:

$$\mathrm{FA} = \sqrt{\frac{1}{2}}\frac{\sqrt{(\lambda_1-\lambda_2)^2+(\lambda_2-\lambda_3)^2+(\lambda_3-\lambda_1)^2}}{\sqrt{\lambda_1^2+\lambda_2^2+\lambda_3^2}},$$

3. Third moment: The mode of anisotropy geometrically describes how much the diffusion tensor spheroid deviates from an ellipsoid. It has been mathematically derived by (Ennis and Kindlmann, 2006). A negative mode means that the ellipse has been rotated along its minor axis, and the resulting spheroid is planar anisotropic, or disk-like (oblate), i.e. $\lambda 1 \sim \lambda 2 > \lambda 3$, which corresponds to regions of crossing fibers in the brain. A mode equal to zero means that the spheroid is orthotropic, and has three mutual planes of symmetry defined by the eigenvectors. A positive mode means that the ellipse has been rotated along its major axis, and the resulting spheroid is linear anisotropic, or cigar-like (prolate), i.e. , $\lambda 1 > \lambda 2 \sim \lambda 3$, which corresponds to regions with one predominate fiber direction in the brain.

$$Mode = \frac{\lambda_1\lambda_2\lambda_3}{\left(\sqrt{(\lambda_1-\langle D\rangle)^2+(\lambda_2-\langle D\rangle)^2+(\lambda_3-\langle D\rangle)^2}\right)^3}$$

4. Fourth moment or kurtosis: is the deviation of the multidimensional displacement probability density function from a Gaussian. This is described

as the apparent kurtosis coefficient. Kurtosis is a measure of peakedness or sharpness of an arbitrary distribution (Veraart and Sijbers, 2016). A positive kurtosis indicates that distribution is more peaked than a Gaussian, i.e. small displacements are more likely. A kurtosis of zero corresponds to the normal distribution. A negative kurtosis means that the probability density function is less peaked than a Gaussian distribution. i.e. small displacements are less likely.

These tensor invariants describe the shape of the diffusion tensor, i.e. its geometrical properties that remain the same regardless of the orientation. Besides magnitude, degree of anisotropy, skewness, and kurtosis, diffusion can also be described by the direction of diffusion. From the mathematical properties of the diffusion tensor it follows that only the main direction of diffusion ε1 can be estimated accurately, because ε2 and ε3 are constraint to lie in the plane orthogonal to ε1 (Hagmann *et al.*, 2006). Thus the second and third eigenvector ε2 and ε3 are unable to provide useful information about the orientation of additional fibre populations, and so alternative modeling techniques, not based on the tensor are used to model multiple fibres (Hagmann *et al.*, 2006).

Using specialized pulse sequences with diffusion gradients, magnetic resonance imaging (MRI) can be rendered sensitive to the diffusion of water molecules (H_2O) in the human body, and especially in the brain where this method provides a valuable tool for inference about its characteristic micro-structure. These diffusion gradients cause a signal attenuation in MRI images that is proportional to the amount of diffusion along the direction of the applied diffusion gradient (Dhollander, 2016).

The attenuation of the diffusion signal follows an exponential decay and can be quantified using the following equation:

$$\mathbf{S = S_o e^{-bD}}$$

where S is the diffusion-weighted signal, S0 is the attenuated signal, b is the amount of diffusion-weighting, and D is the apparent diffusion coefficient or as explained in more detail above the diffusion tensor. By acquiring diffusion signals S and signals without diffusion S_0 at each voxel of the brain, and solving this equation for $D = b^{-1} * \ln(S/S_0)$, a spatial map can be obtained that is clinically called diffusion-weighted imaging (DWI) and scientifically corresponds to the apparent diffusion coefficient

map. The b-values (unit: s/mm²) describe the degree of sensitivity of a given diffusion-weighted sequence as determined by the gradient characteristics.

To get from the diffusion-weighted imaging (DWI) map to the diffusion tensor map and maps based on the tensor invariants, it is necessary to acquire several S images with varying directions of the applied diffusion gradient. Since it is well known that to find n unknown variables in linear algebra at least n simultaneous equations needs to be solved, and the diffusion tensor is symmetric and therefore has 6 unique values, it is theoretically necessary to acquire at least 6 diffusion-encoding images with varying diffusion directions alongside with the S_0 image to estimate the diffusion tensor. In practice, more diffusion directions are usually acquired to improve the accuracy of the tensor estimates.

Various analysis methods are available for diffusion tensor imaging and diffusion MRI data. Here I will only mention the ones relevant for this thesis: voxel-based diffusivity (VBD) analysis, tract-based spatial statistics, region of interest (ROI) analysis and probabilistic tractography.

Inspired by the successful use for structural MRI data similar methods as the ones used in vowel-based morphometry can be applied to spatial maps of various tensor invariants. In brief, this approach involves transforming the maps of the diffusion

metrics from native space into standard space using non-linear transformations with high degrees of freedom (spatial normalization), spatial smoothing using a Gaussian kernel, and carrying out inferential statistics using permutational tests using specific cluster thresholding algorithms. VBD analyses have various limitations including, the following: (1) residual misalignment after non-linear registration into standard space, (2) correspondence problem at voxel-level (i.e. does a given voxel in subject A correspond to the same voxel in subject B), (3) partial volume effects at the tissue boundaries (GM/WM), (4) loss of topology following non-linear registration with high degrees of freedom, and (5) arbitrary choice of smoothing extent (Van Hecke, Emsell and Sunaert, 2015). I have used voxel-wise analysis of mean diffusivity and fractional anisotropy maps in chapter 4 using a basal ganglia mask for small volume correction. In brief, the following steps have been taken to overcome the problems of the VBD analyses: (1) transformation warps were derived from voxel-based morphometry pipeline, i.e. high-res , high contrast structural data to minimize residual misalignment, (3) partial volume effects are minimal because the SVC mask focused on sub-cortical nuclei, (4) loss of topology is minimal due to the spheroidal shape of the subcortical nuclei.

When looking at the white matter and not the gray matter however, these limitations of VBD analysis are more severe, and another analysis approach was used

that overcomes these problems, i.e. tract-based spatial statistics (TBSS). TBSS uses an additional projection step that accounts for residual misalignments between subjects, and ensures that the fine alignment across subjects is done in the direction perpendicular to the tract, not parallel to the tract, thereby preserving the topology of white matter tracts. In brief, TBSS involves the following analysis steps (Smith *et al.*, 2006) (1) The fractional anisotropy images of all subjects are aligned to a common target using linear (FLIRT) and non-linear (FNIRT) registrations. Perfect alignment not required at this stage due to the projection step. (2) The mean of all aligned fractional anisotropy images is created and thinned to yield a skeletonized mean FA image, from which regions of high cross-subject variability are removed by thresholding. (3) Each subjects' aligned fractional anisotropy image is projected onto the skeleton by filling the skeleton with FA values from the nearest relevant tract centre. (4) Voxel-wise statistical inference is then carried out across subjects on the data in skeleton space. I have used TBSS analysis of 3T diffusion data in presymptomatic Huntington's disease in chapter 2, and of 7T diffusion data in early Huntington's and Parkinson's disease in chapter 5.

In region of interest (ROI) analysis the average of a diffusion metric is calculated across a spatial map that is often defined a priori based on neuroanatomical knowledge, for example the basal ganglia mask in chapter 1, when investigating

preclinical Huntington's disease. The main advantage of ROI analysis is its higher sensitivity to small effects compared to other methods, particularly if the effect is only seen in small brain structures, such as deep cerebral/cerebellar nuclei (Jones, 2010; Froeling, Pullens and Leemans, 2016). By averaging over several voxels measuring a similar signal in the ideal case the overall signal seen in ROI analysis is "enhanced", and the noise averages out. However, if diffusion metrics do not show a homogeneous effect in an ROI that is too large, it is possible that a potential signal is canceled out by averaging over too many voxels. Another advantage is that ROI-based analyses do not rely on the accuracy of the spatial normalization into standard space, because they can be directly carried out in native space. However, ROI analyses introduce a bias by selection of specific ROIs.

In probabilistic tractography the directional information of diffusion MRI data is used to reconstruct fiber connections and tracts by fitting streamlines to diffusion data. A streamline through a vector field, for example the vector field defined by the image of the first eigenvector of the diffusion tensors, is any curve whose tangent is always parallel to the vector field.

Due to the limitations of the diffusion tensor in estimating secondary, and tertiary fiber directions, the tensor model is now rarely used for tractography but a more flexible fiber orientation distribution is estimated at each voxel using various

algorithms including Bayesian estimation (Behrens, H. Johansen Berg, *et al.*, 2007) and constrained spherical deconvolution (Tournier *et al.*, 2004).

Various heuristics are used to avoid tracking improbable streamlines, including a fiber threshold (>0.01), i.e. the volume fraction before subsidiary fiber orientations are considered, and a curvature threshold to avoid neuroanatomically unlikely bends in the streamline addition, user-specified masks for excluding tracts (exclusion masks) or forcing tracts to pass through particular regions (waypoint masks), can be specified to enforce extra neuroanatomical constraints.

The reconstructed fibre pathways from probabilistic tractography can be used to carry out various group inferential statistics, including using the tracts as unbiased ROIs for spatial regression (as conducted in chapter 2), using the number of streamline counts, the so called waytotal as an indicator of the strength of connectivity, as well as deriving a connectivity based parcellation of subcortical nuclei. In chapter 6 and 7, I have carried out such a connectivity-based parcellation for the subthalamic nucleus and globus pallidus.

Chapter I.1: Huntington's disease differentially affects gray matter micro-structure across presymptomatic stages over a one-year period

1.0. Abstract

Rationale. Huntington's disease is a progressive, neurodegenerative movement disorder, for which no curative treatment is currently available. Since the symptomatic disease is preceded by a long presymptomatic stage, there is a clear need for a reliable state biomarker sensitive enough to monitor disease progression, shed light on underlying pathophysiological mechanisms, and stratify participants into presymptomatic disease stages. Diffusion MRI is a promising candidate as it can detect subtle abnormalities in the brain microstructure, but so far longitudinal research has failed to demonstrate its sensitivity to the progression of Huntington's disease at a presymptomatic stage.

Objective. To determine whether diffusion magnetic resonance imaging (MRI) can detect the effect of disease progression in the gray matter microstructure at presymptomatic stages.

Methods. Participants with presymptomatic Huntington's disease (N = 35, > 38 mutant CAG repeats), and age- and gender-matched healthy controls (N =19) were followed over a one-year period on two visits using diffusion MRI. Data were analyzed using various distinct diffusion metrics, including mean diffusivity and fractional anisotropy, with the basal ganglia as a-priori region of interest. Analyses compared participants with presymptomatic Huntington's disease and healthy controls, as well as subgroups defined by their predicted age at the onset of symptoms.

Results. Whereas there was no significant effect when directly comparing the entire presymptomatic Huntington's disease group with the control group, we consistently found significant overall effects when further stratifying participants with presymptomatic Huntington's disease into three subgroups according to their estimated onset of symptoms. There was a significant difference over the four groups (one control, three presymptomatic) in change of mean diffusivity in the posterior basal ganglia. This overall effect was mainly driven by significant differences between the groups far-from-onset of symptoms on the one hand, and near-the-onset of symptoms on the other hand. This seemingly counter-intuitive but consistent decrease of mean diffusivity in the far-from-onset group compared with a subsequent

increase in the near-the-onset group might be a very early indicator of neuroinflammatory processes preceding the neurodegenerative phase.

Conclusions. Based on these findings, diffusion MRI emerges as a promising state marker in presymptomatic Huntington's disease, with not only a high sensitivity to longitudinal changes in the microstructure of the basal ganglia, but also a differential response across groups that were stratified based on the genetic and hereditary information. Diffusion MRI might thus play an important role in monitoring treatment response in clinical trials of individuals with presymptomatic Huntington's disease, and in identifying the optimal therapeutic window of opportunity for potential neuroprotective therapy.

1.1. Introduction

"Corpus striatum seu medullae oblongatae apices,
sunt duo prominentiae lentiformes,
quae intra piores cerebri ventriculos"
Sir Thomas Willis – Cerebri anatome (1664)

The neuropathological hallmark feature of Huntington's disease is the degeneration of GABA-ergic, medium-size spiny neurons in the neostriatum (Graveland, Williams and DiFiglia, 1985), resulting in enlargement of the ventricles seen post-mortem. Besides these neuropathological findings, atrophy of the neostriatum – and more generally alterations in gray matter (GM) macrostructure – can be detected as much as 15 years before the predicted onset of the disease using non-invasive neuroimaging techniques (Paulsen *et al.*, 2006; Aylward *et al.*, 2011).

Using magnetic resonance imaging (MRI), reduced striatal volumes have been found long before the onset of symptoms, and proposed as a biomarker to track disease progression (Rees, Scahill and Hobbs, 2013; Aylward, 2014). Striatal volume loss, as quantified using structural MRI, is a reliable but rather un-specific biomarker of disease stage and progression, in that it is not sensitive to microstructural changes, and therefore offers limited information about the underlying pathophysiology. In addition, structural MRI has been shown to detect longitudinal changes in the basal

ganglia volume in presymptomatic Huntington's disease (Aylward *et al.*, 2011; Majid, Aron, *et al.*, 2011; Majid, Stoffers, *et al.*, 2011), but these changes are monotonic over the course of the disease – with a progressive decrease in volume – making it difficult to capture differential effects across various presymptomatic stages of the disease. This caveat might be overcome using diffusion MRI, a technique sensitive to microstructural changes.

Here, we used diffusion MRI to investigate whether diffusion metrics such as mean diffusivity or fractional anisotropy could detect longitudinal changes over a one-year period in presymptomatic Huntington's disease, and discriminate across the different presymptomatic stages of the disease.

1.2. Methods

The present study was aimed at investigating longitudinal changes in the diffusion metrics, mean diffusivity (MD) and fractional anisotropy (FA) (Pierpaoli and Basser, 1996), in the basal ganglia in participants with presymptomatic Huntington's disease (preHD, N = 35) with age- and gender-matched healthy controls (N = 19). The basal ganglia were selected as a-priori region of interest (ROI) in this study because several strands of evidence have shown that these subcortical structures, especially the caudate nucleus and putamen, are the neuroanatomical substrates of neuropathological changes characteristic of HD (Vonsattel *et al.*, 1985). At the histological level, several post-mortem studies found neuronal loss in the basal ganglia in HD, especially the striatum (Vonsattel et al., 1985; Vonsattel, Keller and Cortes Ramirez, 2011), which correlated with clinical symptoms of motor impairment (Guo *et al.*, 2012). Using structural MRI, it has been found that patients with clinical HD have significantly lower striatal volume compared with controls (Rosas *et al.*, 2001).

1.2.1. Participants and study design

Participants were recruited from the Huntington's disease Centre of Excellence at the University of California, San Diego (Majid, Aron, *et al.*, 2011; Majid, Stoffers, *et al.*,

2011). They provided written informed consent in accordance with an institutional review board protocol of the University of California, San Diego. Briefly, 38 participants with preHD (> 38 mutant CAG repeats) and 22 control subjects (CON) were scanned on two visits, with a one-year interval between visits. Of these participants, three were excluded from the present data analysis due to missing or corrupted data, and three further subjects were excluded, because the imaging protocol was not consistent with the one used for the other participants (different b-value, see section 1.2.2).

In total, 35 preHD (20 females; mean age at first visit ± standard deviation = 41.8 ± 9.9; years of education = 15.6 ± 2.5, mutant CAG repeat length = 41.9 ± 2.5, mutant CAG range = 36 – 48), and 19 age- and gender-matched control subjects (CON, 12 females; mean age at first visit = 38.8 ± 12.1; years of education = 15.8 ± 1.3) were included in the final diffusion data analysis (**Table 1.1**). The genetic expansion length of the mutant CAG repeat in Huntington's disease is predictive for age at the onset of symptoms (Langbehn *et al.*, 2010; Rosenblatt *et al.*, 2012). To account for this variability in age at the onset of symptoms, we further subdivided participants with preHD into 3 different subgroups according to the estimated onset of their disease using the following prediction formula (Aylward et al., 1996):

Age at onset = [- 0.81 × repeat length] + [0.51 × parental onset age] + 54.87)

Years to onset were then calculated by subtracting age at time of the first visit from estimated age at the onset of symptoms, which resulted in the following groups: far from the onset of symptoms (FAR, N = 11, years-to-onset mean ± standard deviation = 14.77 ± 3.56, range = 9.73 – 20.96), halfway (midway) to the onset (MID, N = 11, mean years-to-onset = 5.26 ± 2.66, range = 1.17 – 9.29), and near the onset (NEAR, N = 13 , mean years-to-onset = -3.5 ± 2.3, range = -9.54 – -0.56). Two of the participants in the NEAR subgroup progressed from presymptomatic to manifest stage of the disease between baseline and follow-up visits (See **Figure 1.1** for an overview of the study design, and participants chart). Demographical data are summarized in **Table 1.1.**

	Controls	PreHD	FAR	MID	NEAR
N	19	35	11	11	13
Sex	12♀ / 7♂	20♀ / 15♂	4♀ / 7♂	7♀ / 4♂	9♀ / 4♂
Age at baseline (y)	38.8 ± 12.1	41.8 ± 9.9	35.6 ± 6.1	38.8 ± 9.7	49.6 ± 7.8
Mutant CAG length	NA	41.9 ± 2.6 36 – 48	41.5 ± 3.2 36 – 47	43.1 ± 2.4 40 – 48	41.3 ± 1.8 39 – 45
Nonmutant CAG length	NA	18.3 ± 3.5 12 – 29	18.6 ± 2.3 16 – 24	18.6 ± 4.2 12 – 28	17.8 ± 3.9 12 – 29
Years of education	15.8 ± 2.5	15.6 ± 2.5	15.6 ± 2.6	15.5 ± 1.9	15.7 ± 2.9
UHDRS motor score at baseline	0.05 ± 0.2	1.7 ± 1.7	1.5 ± 1.6	1.5 ± 1.8	2.2 ± 1.9

Table 1.1. Demographic data for healthy controls and all subjects with presymptomatic Huntington's disease (preHD), as well as for subgroups according to the onset of symptoms (FAR, MID, NEAR) (mean ± standard deviation). UHDRS: Unified Huntington's disease rating scale

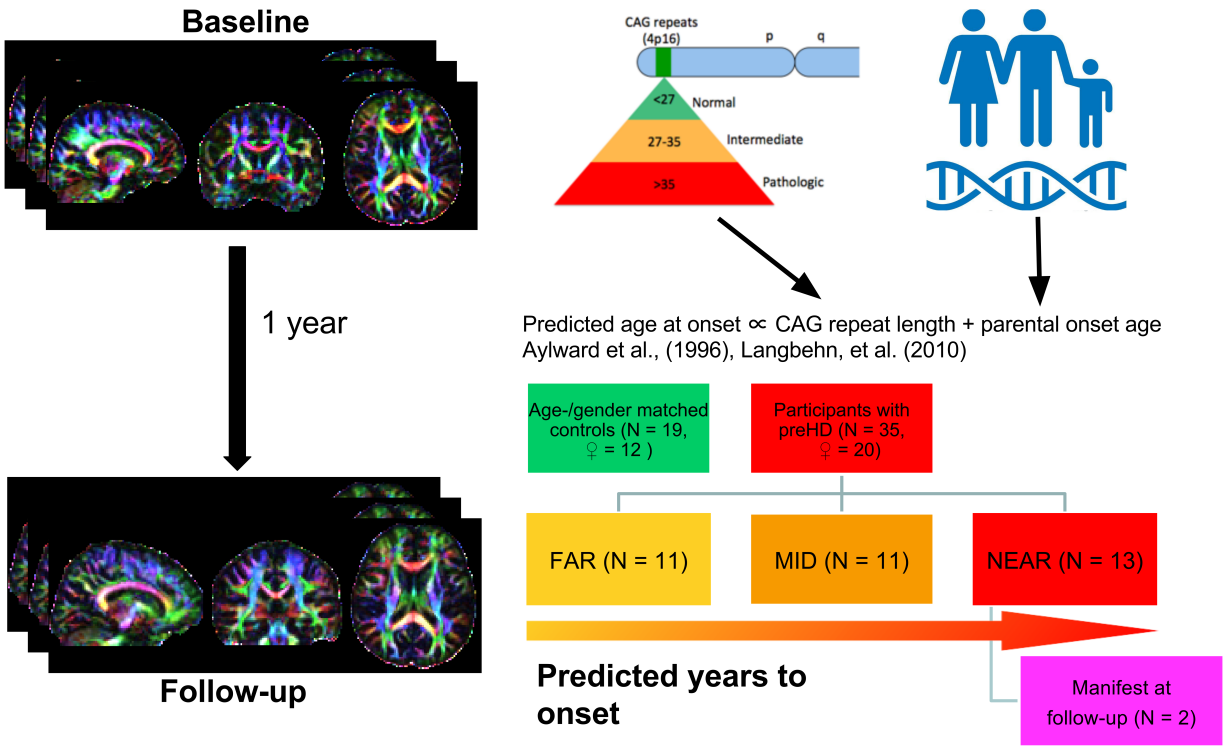

Figure 1.1. Study design and participants flow chart.

1.2.2. Data acquisition

Data were acquired with a General Electric (Milwaukee, WI, USA) 1.5T EXCITE HDx scanner (Software Version 14x) with an 8-channel phased-array head coil. Image acquisition included a General Electric ‘‘PURE’’ calibration sequence and a high-resolution 3-dimensional T1-weighted inversion recovery spoiled gradient recalled (IRSPGR) sequence (echo time TE = 2.8 ms, repetition time TR = 6.5 ms, inversion time TI = 600 ms, flip angle = 12°, band width = 244 Hz/pixel, field of view = 24 cm, matrix size = 256 × 192, slice thickness =1.2 mm). Diffusion-weighted data were acquired on a General Electric 1.5T EXCITE HDx scanner using single-shot echo-planar imaging sequence with isotropic 2.5 mm voxels, b-value = 1000 s/mm^2 and 51 diffusion directions (TE = 80.4 ms, TR = 13,200 ms, field of view = 24 cm, matrix size = 96 × 96, 47 axial slices, slice thickness = 2.5 mm).

1.2.3. Data processing

MRI data were processed using FMRIB software library (FSL version 5.0.4, FMRIB Analysis group, Oxford University, UK) (Smith *et al.*, 2004; Jenkinson *et al.*, 2012).

Diffusion-weighted and T1-weighted structural images were brain extracted using the BET FSL tool (Smith, 2002) with a fractional intensity threshold of 0.3 for the diffusion-weighted images, and a fractional intensity threshold of 0.6 and robust brain centre estimation for the T1-weighted images. A diffusion tensor model was fitted at each voxel of the brain-extracted data using FMRIB's DTIfit tool, and mean diffusivity and fractional anisotropy maps were estimated for each subject (Behrens, Woolrich, *et al.*, 2003) (Behrens et al., 2003).

Pre-processing and image registration have been optimized for the longitudinal study design to avoid any bias between time-points (Thomas *et al.*, 2009; Douaud *et al.*, 2011), as follows: The baseline and follow-up fractional anisotropy images were registered into their halfway space for each subject (with 6 degrees of freedom). The resulting halfway transformation matrices were then used to initialize the nonlinear registration from each fractional anisotropy baseline and follow-up image to their average after affine transformation. The average fractional anisotropy image between baseline and follow-up in halfway-space was then non-linearly registered onto the

FMRIB fractional anisotropy template (FMRIB58). Both warps were concatenated and applied to create a study-specific template using an equal number of participants with presymptomatic Huntington's disease and control subjects (by averaging over 19+19 subjects and over time-points). Finally, baseline and follow-up fractional anisotropy images for each subject were non-linearly registered to this study-specific template. This study-specific registration algorithm was used to avoid any bias between time-points, and to avoid any bias introduced by using standard templates in clinical populations.

The basal ganglia were chosen as a-priori ROI for the GM analysis in this study, as these subcortical structures, and particularly the caudate nucleus and putamen, are the neuroanatomical substrates of neuropathological changes characteristic of Huntington's disease (Furtado *et al.*, 1996; Rosas *et al.*, 2001; Vonsattel, Keller and Cortes Ramirez, 2011; Guo *et al.*, 2012). An automatic segmentation tool, FIRST, was used on the T1-weighted images in their native space to delineate the caudate nucleus, putamen, globus pallidus, and nucleus accumbens (Patenaude *et al.*, 2011). Registration into a common space was necessary to make additional subdivisions using MNI coordinates consistently across subjects. The masks were non-linearly

registered from native space into MNI standard space using the warp field from the registration of the T1-weighted images onto the MNI standard brain. The masks in standard space where then averaged over all subjects, and thresholded at 20%. For convenience, we will call "basal ganglia" the combination of caudate, putamen, "nucleus accumbens", and pallidum in the following. Masks were created in MNI space, to ensure that they had the same size for all subjects, and make an additional subdivision using MNI coordinates feasible. The basal ganglia mask was then subdivided along a coronal plane (MNI space y = 63) into an anterior and posterior subdivision rather than into caudate/putamen divisions, as the more anterior part of the striatum is predominantly connected to prefrontal areas and associated with cognitive and limbic processing, whereas the more posterior part is predominantly connected with sensorimotor regions of the brain (Lehericy *et al.*, 2004; Draganski *et al.*, 2008; Douaud, Behrens, *et al.*, 2009). The newly subdivided masks in MNI space were then registered back into each native space (by inverting the warpfield from T1-weighted to MNI space). The masks in native space were thresholded at 0.7 and binarized. The binarized ROI masks were eroded using a kernel with a sphere of radius 2 mm to ensure that the spatial extent of the seed masks was confined to the GM. These ROI masks were used to extract the average MD, and FA values across

all voxels included in the mask from the pre-processed images in the native diffusion space. The non-eroded regions of interest are displayed in **Figure 1.2.**

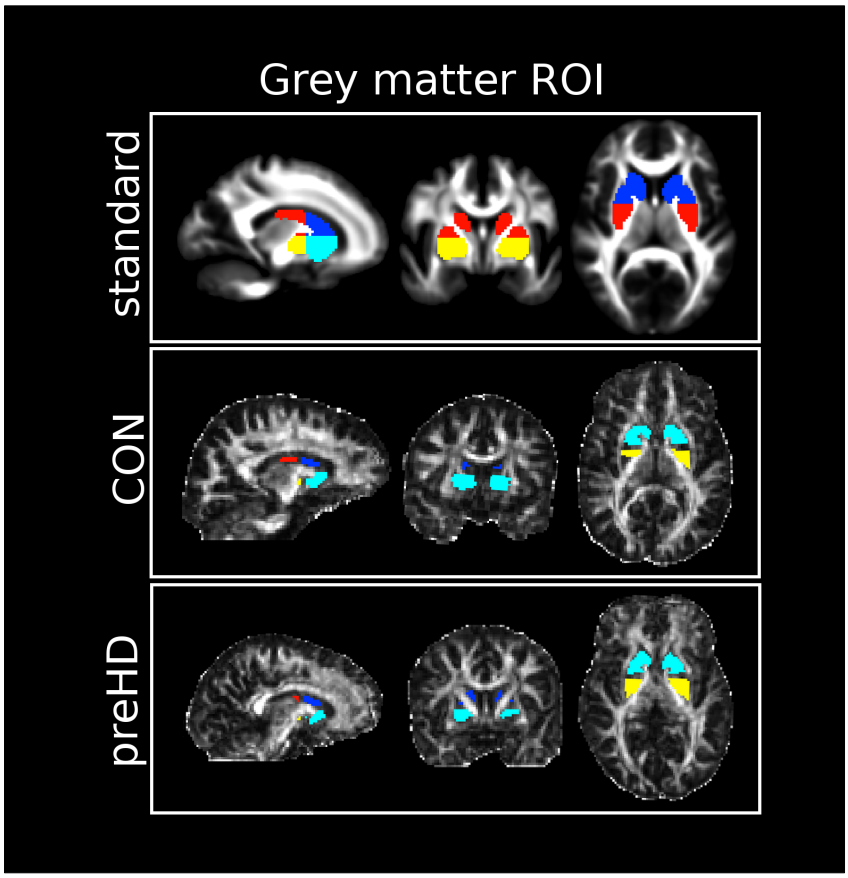

Figure 1.2. Masks of the regions of interest used for the ROI analysis overlaid on the study-specific template (upper panel), on the FA native space of a control subject (middle panel), and on the FA native space of a subject with preHD (lower panel).

1.2.4. Statistical analyses

Statistical analyses of ROI-extracted imaging data were carried out using Statistical Software Package for the Social Sciences (SPSS 20) (IBM Corporation, Armonk, NY USA), Microsoft Excel 2010 (Microsoft Corporation, Redmond, Washington, USA), and R (version 3.2.3, The R Foundation for Statistical Computing (2015)).

Independent samples t-test was performed using SPSS to test for statistically significant group differences in mean diffusivity and fractional anisotropy change between controls and patients with presymptomatic Huntington's disease. ANOVA was performed using SPSS for the presymptomatic Huntington's disease subgroups (according to estimated years to onset of symptoms) and healthy controls. Post-hoc tests, based on Tukey's honestly significant difference (HSD) method, were used to test for significant pairwise group differences between FAR, MID, NEAR and controls. One-sample t-test was performed using SPSS to investigate the mean diffusivity and fractional anisotropy change within each of the 4 groups (FAR, MID, NEAR and controls).

Shapiro-Wilk test was used to test if the data, and the residuals from the ANOVA were normally distributed. If the data were not normally distributed, non-parametric equivalent tests were used: Mann-Whitney U-test, Kruskal-Wallis ANOVA, and

Dunn-Bonferroni test. All inferential statistical analyses were corrected for multiple comparisons using Bonferroni correction across ROIs.

1.3. Results

1.3.1. Comparing the entire presymptomatic Huntington's disease group with the control group

There were no significant group differences between preHD participants and the control group in mean diffusivity or fractional anisotropy change between baseline and follow-up looking at both anterior and posterior subdivisions (lowest corrected p-value for mean diffusivity = 0.463, owest corrected p-value for fractional anisotropy p = 0.623).

When looking at the longitudinal change in the preHD group, we noticed a large amount of variability across subjects, with both increases, and decreases in diffusion metrics. This prompted the decision to stratify preHD participants into subgroups according to their estimated number of years to onset of symptoms, to investigate whether such variability in the longitudinal changes could be explained by distinct diffusion patterns at different presymptomatic stages.

1.3.2. Groups according to estimated years to onset of symptoms vs. control subjects

1.3.2.1. Mean diffusivity

Group comparisons using ANOVA revealed a statistically significant longitudinal change in MD overall between the 4 sub-groups (CON, FAR, MID, NEAR) in the posterior basal ganglia ($F(3,50) = 4.512$, corrected p-value = .014, **Figure 1.3**). Post-hoc pairwise group comparisons revealed a significant group difference in mean diffusivity change in the posterior basal ganglia between FAR and NEAR (p-value = 0.007). This effect was driven by a relative decrease in mean diffusivity in FAR, compared with a relative increase in mean diffusivity in NEAR. There was also a trend in the pairwise comparisons between FAR and MID (p-value = 0.094 before correction).

One-sample t-test revealed that the change in MD between follow-up and baseline was significantly different from zero in the NEAR group in the posterior basal ganglia ($t(12) = 3.344$, corrected $p = 0.012$) (**Figure 1.3, Table 1.2**). One sample t-test for the other subgroups did not reveal any significant change in MD (all corrected $p > .05$).

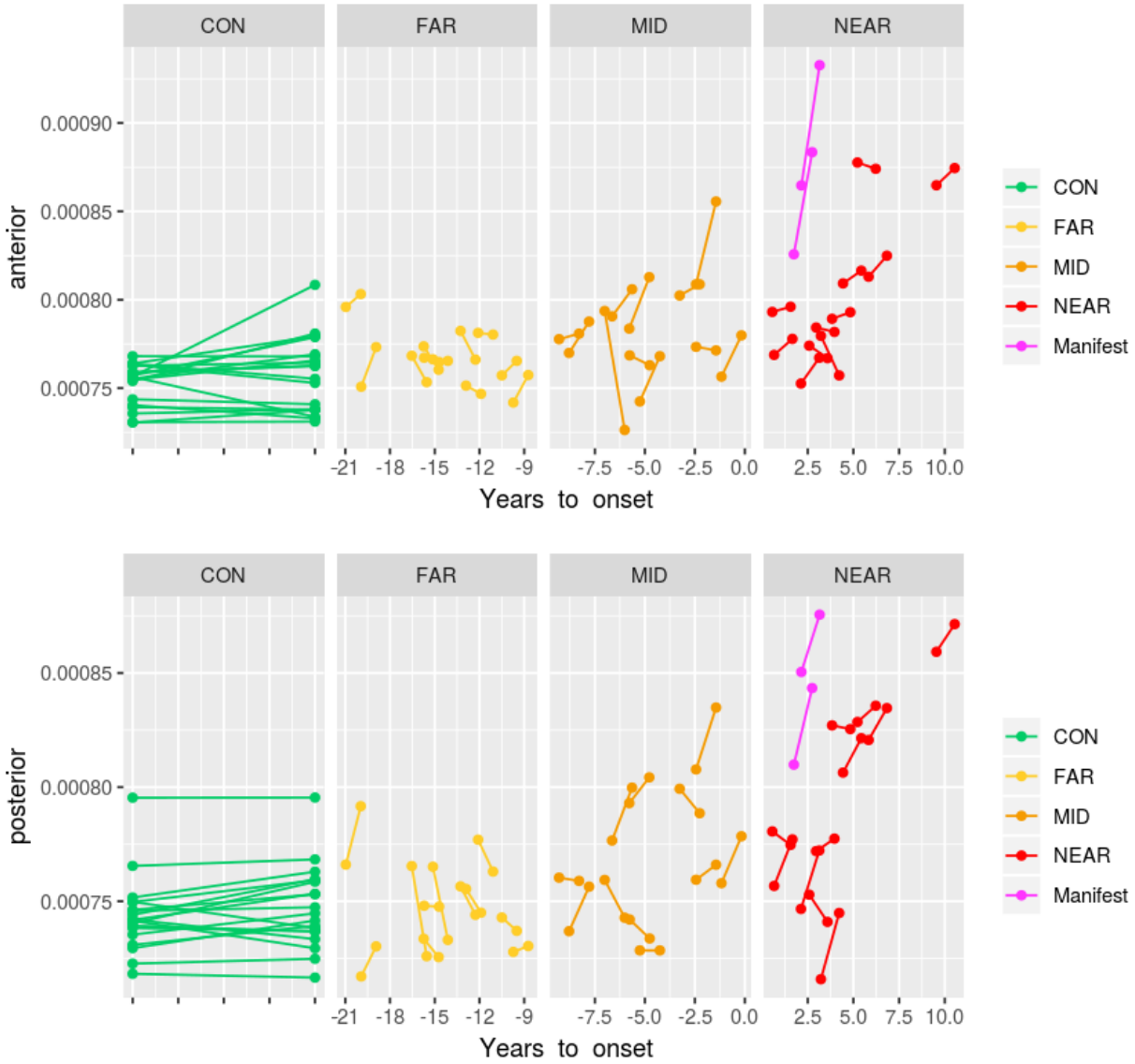

Figure 1.3. Longitudinal change in mean diffusivity in the anterior and posterior basal ganglia comparing subgroups according to their estimated years to onset of symptoms, "far from onset" (FAR), "halfway to onset" (MID), "near the onset" (NEAR), and control subjects (CON). Stars indicate significant longitudinal differences between groups after adjusting for multiple comparisons using Bonferroni correction at $p = 0.05$.

1.3.2.2. Fractional anisotropy

There was no statistically significant overall effect across the 4 groups (CON, FAR, MID, NEAR) on the fractional anisotropy change in the anterior or posterior basal ganglia ROI (lowest p-value = .400, **Figure 1.4, Table 1.2**). Exploratory uncorrected post-hoc tests between each pair out of the 4 groups did not reveal any significant longitudinal differences (lowest uncorrected p-value = .097, **Figure 1.4, Table 1.2**).

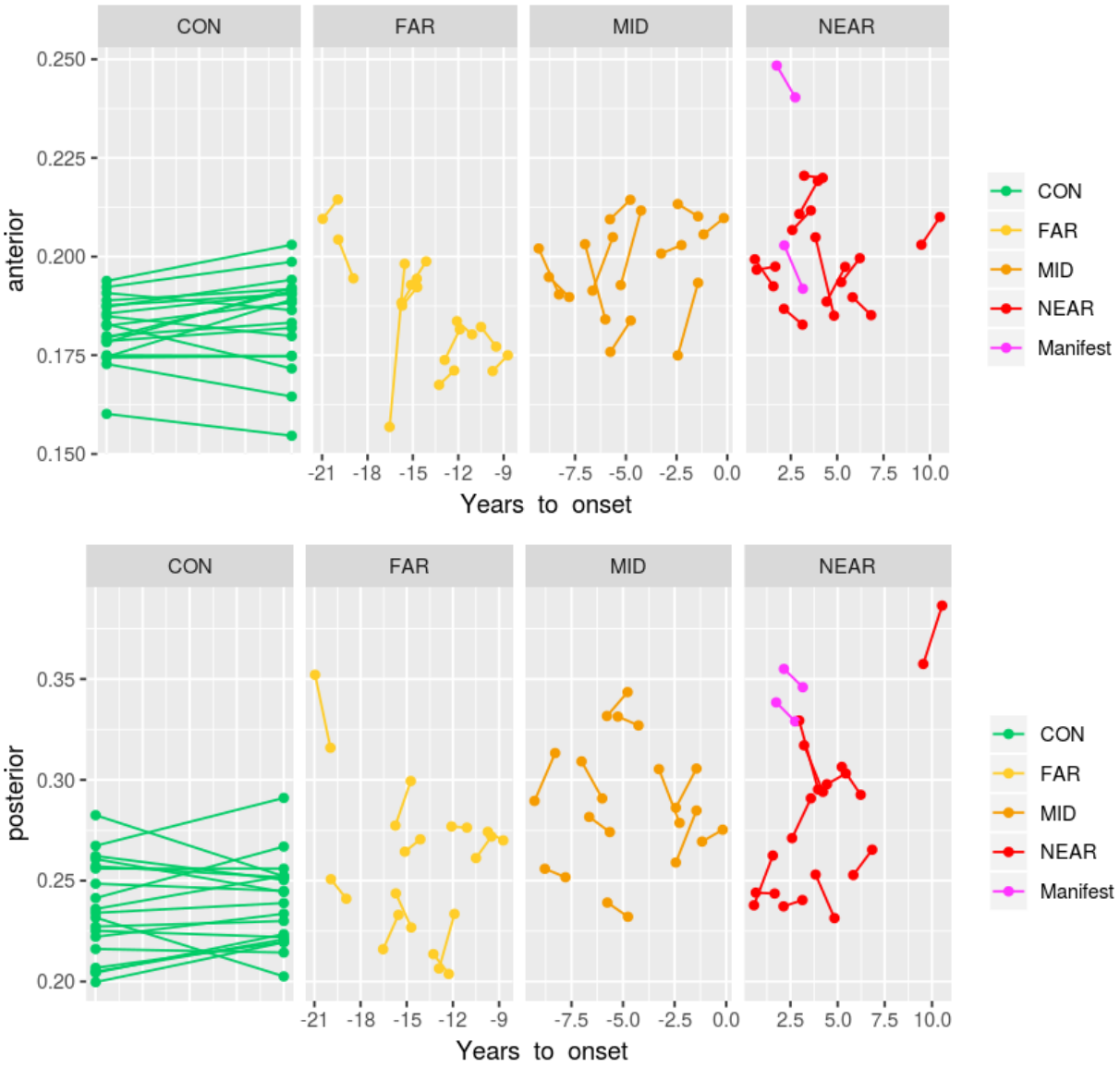

Figure 1.4. Longitudinal change in fractional anisotropy in the anterior and posterior basal ganglia comparing subgroups according to years to onset of symptoms, "far from onset" (FAR), "halfway to onset" (MID), "near onset" (NEAR), and control subjects (CON).

Metric	ROI	Control				all preHD				FAR			
		Mean	SD	t(18)	P	Mean	SD	t(34)	P	Mean	SD	t(10)	P
MD	ant	5.603E-06	1.613E-05	1.514	0.147	6.918E-06	2.328E-05	1.758	0.088	1.305E-08	1.248E-05	0.003	0.997
	pos	3.773E-06	8.754E-06	1.879	0.077	4.506E-06	1.754E-05	1.520	0.138	-7.391E-06	1.837E-05	-1.334	0.212
FA	ant	2.736E-03	7.232E-03	1.649	0.116	2.069E-03	1.130E-02	1.083	0.287	5.467E-03	1.311E-02	1.383	0.197
	pos	2.658E-03	1.654E-02	0.700	0.493	1.945E-04	1.798E-02	0.064	0.949	4.975E-04	1.861E-02	0.089	0.931
Metric	ROI	MID				NEAR							
		Mean	SD	t(10)	P	Mean	SD	t(12)	P				
MD	ant	8.415E-06	2.938E-05	0.950	0.365	1.149E-05	2.487E-05	1.666	0.122				
	pos	6.471E-06	1.498E-05	1.433	0.182	1.291E-05	1.392E-05	3.344	**0.006**				
FA	ant	2.826E-03	1.198E-02	0.782	0.452	-1.448E-03	8.637E-03	-0.604	0.557				
	pos	1.682E-03	1.714E-02	0.326	0.752	-1.321E-03	1.944E-02	-0.245	0.811				
Metric	ROI	all preHD vs CON				ANOVA							
		Statistic		Z	P	Statistic		P		Post-hoc			
MD	ant	U(52) =	308.000	-0.444	0.657	$\chi^2(3)$ =	3.339	0.342					
	pos	t(51.771) =	-.205		.839	F(3,50) =	4.512	0.007		#, ¶			
FA	ant	U(52) =	316.000	-0.299	0.765	F(3,50) =	1.000	0.400					
	pos	t(52) =	0.494		0.623	F(3,50) =	0.137	0.938					

Table 1.2. Longitudinal results from the gray matter analysis with basal ganglia as region of interest. P-values are uncorrected, P-values in bold are significant after Bonferroni-correction for multiple ROIs. (MD: mean diffusivity, FA: fractional anisotropy, ROI: region of interest, ant: anterior basal ganglia, pos: posterior basal ganglia, CON: control, preHD: presymptomatic Huntington's disease, FAR: far from the onset of symptoms, MID: mid-way from the onset of symptoms, NEAR: near the onset of symptoms, #: significant difference between FAR and MID, ¶: significant difference between FAR and NEAR).

1.4. Discussion

Here we have investigated longitudinal changes in diffusion metrics in the basal ganglia in participants with presymptomatic Huntington's disease compared with healthy controls. The major longitudinal finding of this study was a significant difference in MD change when looking across sub-groups of preHD following their estimated years to the onset of symptoms and CON. No significant difference was found when comparing directly CON with all preHD. This is likely because the behavior of the DTI metric changes appears very different between these pathologically meaningful sub-groups of preHD. Indeed, further post-hoc t-tests revealed decreased MD in the posterior part of the basal ganglia in FAR compared with NEAR.

To the best of our knowledge, this is the first study that has demonstrated longitudinal changes in diffusion metrics in the basal ganglia within the presymptomatic stages of Huntington's disease. Previous longitudinal diffusion MRI studies in presymptomatic Huntington's disease either did not detect any significant effects, or found significant effects only cross-sectionally (Domínguez *et al.*, 2013; Odish, Leemans, *et al.*, 2015; Poudel *et al.*, 2015), or solely when comparing patients with clinical Huntington's disease to the presymptomatic Huntington's disease group

(Domínguez *et al.*, 2013; Poudel *et al.*, 2015). In addition, previous diffusion MRI studies in clinical Huntington's disease have also failed to detect any longitudinal effects (Vandenberghe *et al.*, 2009; Sritharan *et al.*, 2010). This lack of significant longitudinal effect in diffusion imaging is most likely due to the need for stratifying participants with Huntington's disease into meaningful subgroups to ensure that increases and decreases in diffusion metrics are not averaged out across the various presymptomatic and clinical stages.

A previous study found a longitudinal reduction in MD in the putamen when comparing presymptomatic patients with Huntington's disease compared with patients with manifest HD, which is in line with our findings (Domínguez *et al.*, 2013). This seems to be in line with our results showing a decrease of mean diffusivity at earlier stages of the disease, when compared with later stages (although our findings were obtained within the presymptomatic stages of the disease). In the present study, however, the longitudinal decrease in MD was only found when investigating differences across CON and the sub-groups of preHD, not when comparing directly CON with all preHD. Post-hoc, we could determine that the main effect was seen between FAR and NEAR, but not when comparing preHD subgroups with CON.

The significant difference between groups, with a longitudinal decrease in MD in the posterior part of the basal ganglia in FAR compared with NEAR is prima facie counter-intuitive in a neurodegenerative disorder, because increased MD is traditionally seen as a hallmark feature of neurodegeneration. However, recent evidence in presymptomatic Alzheimer's disease point at significantly decreased MD in multiple white matter regions in preclinical stage 1, which pseudo-normalizes at stage 2 (Wang, Yong Wang, *et al.*, 2015). This pattern is to a certain extent similar to our finding of opposing longitudinal changes in MD in FAR vs. NEAR. Thus, the initial decrease in MD seen in the posterior putamen in FAR might represent an early microstructural sign of future neurodegeneration (see **Figure 1.5**), which is then revealed in the MID and NEAR groups by an increase in MD. In line with such a hypothesis, a study on patients with presymptomatic familial Alzheimer's disease, found decreased MD in the right hippocampus and in the right cingulum, whereas symptomatic mutation carriers showed increased MD with reduced FA in all of the white matter tracts of interest (Ryan *et al.*, 2013).

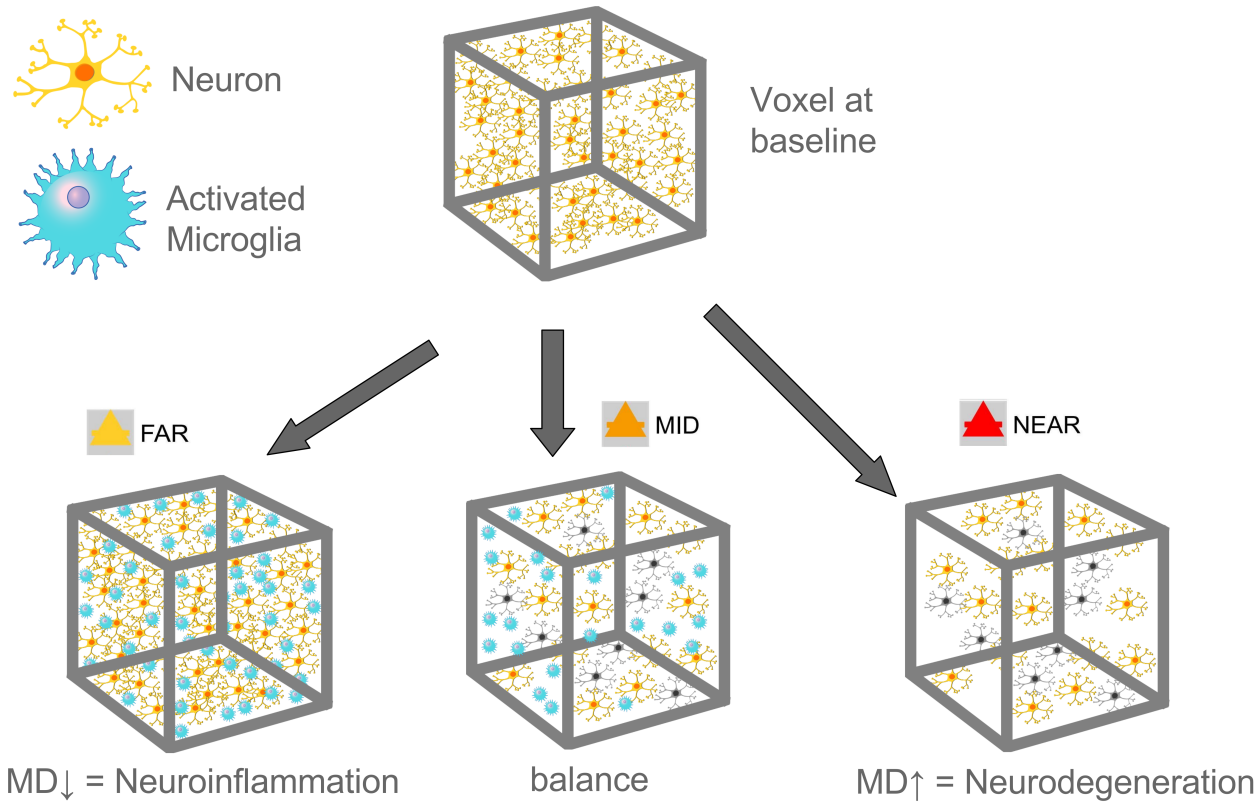

Figure 1.5. Distinct patterns of mean diffusivity change from baseline to follow-up, can be explained by considering the underlying tissue geometry, and might correspond to distinct pathophysiological changes in the posterior basal ganglia.

More specifically, one might speculate that the activation and migration of microglia are especially important during the early neuro-inflammatory phase and might underlay this initial decrease in MD, for several reasons: First, microglial activation precedes neurodegenerative reactions of other brain cells, and is therefore a highly sensitive marker of neuronal insult (Kreutzberg, 1996). Second, using positron emission tomography, increased striatal binding of 11C-(R)-PK11195, a marker of microglial activation, has been found in participants with preHD (Tai *et al.*, 2007a, 2007b). Third, microgliosis has been shown to be an early sign of clinical HD, which pseudo-normalizes in later stages. Indeed, an up-regulation of the Iba1-positive microglia in striatal tissue has been found at grade 1 HD but not grade 3, compared to neurologically normal controls (Dowie *et al.*, 2014). Finally, in Alzheimer's disease, a simulation of white matter geometry confirmed that an increase in microglia cell activation is sufficient to cause a decrease in MD and other diffusivity metrics at an early preclinical stage, and that the combination of axon damage, cell infiltration and oedema might cause pseudo-normalization of MD at a later stage (Wang, Yong Wang, *et al.*, 2015). Certainly, further research is needed to validate this hypothesis. However, since the initial decrease of MD was found consistently at the earliest stage in our preHD cohort, it might correspond to neuroinflammatory processes, and thus represent a very early microstructural sign of neurodegeneration.

A one-year, longitudinal diffusion MRI study in patients with manifest HD found significantly higher MD in the caudate and putamen for patients compared with healthy controls at both time-points separately, but did not find any significant longitudinal change in patients (Sritharan *et al.*, 2010), which is similar to the finding of our study in the presymptomatic population.

A particular strength of the present study was that preHD were split into subgroups according to their predicted age-of-onset, which made it possible to account for differences in disease severity. From our results, it seems clear that MD is the most sensitive diffusion measure. Unfortunately, however, it does not show any significant difference between CON and preHD, which is a large limitation for the use of diffusion MRI as a biomarker, as compared to structural MRI measures of subcortical volume changes (Majid, Aron, *et al.*, 2011; Majid, Stoffers, *et al.*, 2011). This is probably due to the fact that diffusion MRI has a high sensitivity to microstructural changes of a different nature as the disease progress, which thus makes it an interesting complement to atrophy measures (less sensitive in some contexts but more specific to the underlying pathological process).

1.5. Conclusions

In conclusion, diffusion MRI is able to detect significant and interpretable changes over a one-year period in presymptomatic Huntington's disease. Such short period of follow-up is crucial to establish whether a state biomarker has the potential to detect the effect of treatment. However, it is necessary to divide subjects into subgroups according to their predicted age at onset to detect meaningful effects. Without such a subdivision, longitudinal changes are averaged out due to distinctly different patterns in participants NEAR vs. FAR. The longitudinal increase in MD in the posterior part of the basal ganglia in NEAR compared with FAR might hint at an initial early stage of neuroinflammation followed by neurodegenerative processes.

Chapter I.2: Can longitudinal diffusion MRI of the white matter be used as an early biomarker for neurodegeneration in presymptomatic Huntington's disease?

2.0. Abstract

Rationale. Huntington's disease is a progressive, neurodegenerative movement disorder of monogenic origin, for which no curative treatment is currently available. Since the manifest disease is preceded by a long presymptomatic stage, there is a clear need for a surrogate marker sensitive enough to monitor disease progression, elucidate underlying pathophysiological mechanisms, and stratify participants into presymptomatic disease stages. Diffusion MRI is a promising candidate as it can detect subtle abnormalities in the brain microstructure, but so far longitudinal research has failed to demonstrate its sensitivity to the progression of Huntington's disease at a presymptomatic stage.

Objective. The aim of the present study was to investigate longitudinal changes in the diffusion metrics, fractional anisotropy (FA) and mean diffusivity (MD), in participants with preHD (N = 35) compared with age-/gender-matched healthy controls (CON, N = 19) over a one-year period at two timepoints.

Methods. A longitudinal design was used acquiring diffusion MRI data at two time-point over a one year period. Patients were stratified into groups according to the predicted age at the onset of symptoms. Region of interest analysis, tract-based spatial statistics, and probabilistic tractography were used to investigate the white matter.

Results. Using both ROI and tract-based spatial statistics analysis, a significant difference over the four groups (one control, three presymptomatic) was found in change of mean diffusivity in the splenium of the corpus callosum. This overall effect was mainly driven by significant differences between the groups far-from-onset of symptoms on the one hand, and halfway-to-onset of symptoms on the other hand. We also found longitudinal differences in fractional anisotropy change mainly in the splenium of the corpus callosum between healthy controls and the halfway-to-onset group, and between far-from-onset and halfway-to-onset groups. A seemingly counter-intuitive but consistent decrease of mean diffusivity in the far-from-onset group compared with a subsequent increase in groups closer to onset of symptoms might be a very early indicator of neuroinflammatory processes preceding the neurodegenerative phase. Probabilistic tractography with basal ganglia as seed

regions did not detect any significant longitudinal change in FA or MD, when looking at the overall effect of subgroup.

Conclusions. Based on these results, diffusion MRI appears to be an auspicious biomarker in presymptomatic Huntington's disease, with not only a high sensitivity to longitudinal changes in the microstructure of the basal ganglia and cerebral white matter across presymptomatic stages, but also a differential response to distinct pathophysiological mechanisms of the disease. Diffusion MRI might thus play a pivotal role in evaluating treatment response in clinical trials of individuals with presymptomatic Huntington's disease, and in identifying the optimal therapeutic window of opportunity for potential neuroprotective treatments.

2.1. Introduction

"In utroque Cerebri Hemisphaerio, circa partes anteriores hoc corpus callosum, sive substantia medullaris, supra quam in alio quovis loco longe crassior et spissior evadit."

Sir Thomas Willis – De cerebri anatome (1664)

Neuropathological research has shown that atrophy in Huntington's disease is by no means limited to the basal ganglia, but that white matter atrophy can clearly be detected post-mortem (de la Monte, Vonsattel and Richardson, 1988; Aylward *et al.*, 1998). Based on post-mortem and in-vivo research it has been hypothesized that premature myelin breakdown might be a major pathopysiological factor driving Huntington's disease progression (Bartzokis *et al.*, 2007; Bourbon-Teles *et al.*, 2017). Longitudinal decreases in the white matter volume have been detectable ten years before the onset of symptoms (Tabrizi *et al.*, 2013). As mentioned in chapter 1, these macro-structural changes are unfortunately by there very nature monotonic, and cannot shed light on more subtle changes in the brain's micro-structure. Here, diffusion MRI might be once more value as already shown for the gray matter in the previous chapter. Indeed, using cross-sectional diffusion MRI, micro-structural alterations in the white matter (WM) were already detectable in the presymptomatic stage of the disease (Reading *et al.*, 2005; Rosas *et al.*, 2006a, 2010). It has also been shown that these cross-sectional alterations involved, among other brain regions, the

corpus callosum (Rosas *et al.*, 2006a, 2010). Based on these findings, it has been hypothesized that Huntington's disease can be best described as a cortical disconnection disease that involves loss of inter-hemispheric connections (Rosas *et al.*, 2010). However, so far evidence is lacking for longitudinal micro-structural changes in the white matter in general, and more specifically in the corpus callosum, and previous studies could not detect any effect (Domínguez *et al.*, 2013; Odish, Leemans, *et al.*, 2015; Poudel *et al.*, 2015).

In this chapter, we have used diffusion MRI to investigate longitudinal changes in WM micro-structure and connectivity in patients with presymptomatic Huntington's disease compared with healthy controls. Unlike volumetric imaging techniques, diffusion imaging is highly sensitive to micro-structural changes, thereby offering the unique opportunity to study early changes in WM micro-structure in the presymptomatic population that occur before the onset of clinical symptoms. Indeed, a previous cross-sectional diffusion MRI study found micro-structural tissue alterations in participants with preHD in the absence of any detectable WM volume loss (Rosas *et al.*, 2006a).

2.2. Methods

Here we investigated longitudinal changes in diffusion metrics in the white matter (WM), and changes in structural connectivity of the basal ganglia comparing participants with presymptomatic Huntington's disease (N=35) with age- and gender-matched healthy controls (N=19). We used region-of-interest (ROI) analysis to investigate longitudinal changes in mean diffusivity and fractional anisotropy in the corpus callosum, the posterior limb of the internal capsule, and the cerebral peduncles. In addition, probabilistic tractography was used to identify cortico-subcortical tracts and to investigate longitudinal changes in diffusion metrics in these tracts. Finally, tract-based spatial statistics (TBSS) was carried out as an unbiased, whole WM analysis approach to investigate changes in the entire WM skeleton of the participants.

Participants were recruited from the Huntington's disease Centre of Excellence at the University of California, San Diego (Majid, Aron, *et al.*, 2011; Majid, Stoffers, *et al.*, 2011) Details about the demographic data of the participants, study design, and data acquisition can be found in sections 2.1.1 and 2.1.2.

2.2.1. Data processing

We used the FMRIB software library (FSL, version 5.0.4) (Smith *et al.*, 2004; Jenkinson *et al.*, 2012) (Smith *et al.*, 2004; Jenkinson *et al.*, 2012) to pre-process the MRI data.

Diffusion-weighted and T1-weighted structural images were brain extracted (Smith, 2002). A diffusion tensor model was fit at each and every voxel in native space to compute maps of the mean diffusivity and fractional anisotropy that were used for the WM ROI analysis and TBSS analysis (see below). A probabilistic diffusion model with modeling of crossing fibres was fit within each voxel (Behrens, H. Johansen Berg, *et al.*, 2007) and probabilistic tractography was run in native space with default settings (see **section 2.3.3**).

We optimized pre-processing and image registration for the longitudinal study design to avoid any bias between time-points (Thomas *et al.*, 2009; Douaud *et al.*, 2011), as follows: The baseline and follow-up fractional anisotropy images were registered into their halfway space for each subject (with 6 degrees of freedom). The resulting halfway transformation matrices were then used to initialize the nonlinear registration from each fractional anisotropy baseline and follow-up image to their average after affine transformation. The average fractional anisotropy image between baseline and follow-up in halfway-space was then non-linearly registered onto the

FMRIB fractional anisotropy template (FMRIB58). Both warps were concatenated and applied to create a study-specific template using an equal number of participants with presymptomatic Huntington's disease and control subjects (by averaging over 19+19 subjects and over time-points). Finally, baseline and follow-up fractional anisotropy images for each subject were non-linearly registered to this study-specific template.

2.2.2. Atlas-based Region of Interest Analysis

We used the corpus callosum (genu, midbody, splenium), the bilateral posterior limb of the internal capsule, and cerebral peduncles as *a priori* ROIs from the JHU ICBM-DTI-81 WM atlas (Mori *et al.*, 2008; Oishi *et al.*, 2008), and the acoustic radiations from the Jülich histological probabilistic atlas (thresholded at 35) (Burgel *et al.*, 2006; Eickhoff *et al.*, 2007) as a negative control region (**Figure 2.1**). The posterior limb of the internal capsule and cerebral peduncles were chosen as ROIs as WM regions mainly containing fibres of the corticospinal tract, and showing longitudinal changes in diffusion metrics in early clinical Huntington's disease (Della Nave *et al.*, 2010a; Gregory *et al.*, 2015). The corpus callosum on the other hand was shown to play a crucial role in the pathophysiology of presymptomatic Huntington's

disease (Bartzokis et al. 2007; Rosas et al. 2010; Di Paola et al. 2012). All ROI masks were eroded using a kernel with a sphere of radius 2mm to avoid detecting signals from the GM or cerebrospinal fluid. The arithmetic mean of the fractional anisotropy and the mean diffusivity was calculated across all voxels in the eroded ROIs.

2.2.3. Cortico-subcortical probabilistic tractography

Previous cross-sectional research has demonstrated that Huntington's disease is associated with altered connectivity between the basal ganglia and the cortex (Novak *et al.*, 2015). In this study, we were particularly interested in investigating longitudinal changes in the WM microstructure of connections between subregions of basal ganglia as seed regions and the neocortex as identified using probabilistic tractography.

A probabilistic diffusion model was fit on the raw data, and crossing fibres were modeled within each voxel of the brain using the FSL tool, Bayesian Estimation of Diffusion Parameters Obtained using Sampling Techniques (BEDPOSTX, FSL default settings) (Behrens, H Johansen Berg, *et al.*, 2007). The output of BEDPOSTX was used to run probabilistic tractography in native space for each subject and for each time-point separately with seed, target, and exclusion masks (described below) using the FSL tool probtrackx2 (default settings). The basal ganglia masks used for the gray matter ROI analysis (chapter1) were used as seeds for probabilistic tractography. In addition, we used simple, geometric target masks, as well as exclusion masks of the cerebrospinal fluid, brain stem and cerebellum, to focus the analysis on cortico-subcortical pathways. The seed, target, and exclusion masks in native space, and study-specific template space are displayed in **Figure**

2.1. Target masks for the anterior basal ganglia ROI were created in standard space by masking all brain tissue in the axial plane at z = 50 and in the coronal plane at y = 76. Target masks for the posterior basal ganglia ROI were created in standard space by masking all brain tissue in the axial plane at z = 52 and in the coronal planes at y = 74, and y = 35, but excluding brain tissue from the brain stem. Exclusion masks of the brainstem, and cerebellum, were created by drawing a rectangle in the axial plane at z = 33 covering the brainstem and cerebellum. Exclusion masks of the cerebrospinal fluid were created in native space by thresholding and binarizing the S0 image using an 85% threshold. Target masks, and exclusion masks of the brainstem and cerebellum were created in MNI standard space, and then registered onto each subjects' fractional anisotropy image using FLIRT (FMRIB's Linear Image Registration Tool) with 12 degrees of freedom.

We used the density of diffusion streamlines as weights to calculate the weighted mean of the mean diffusivity and a fractional anisotropy cross all voxels belonging to each tract, excluding those voxels in crossing fibre regions. In other words, a greater importance towards the contribution to the mean was assigned to voxels where many streamlines passed through, whereas a lesser weight was assigned to voxels were only few streamlines passed through. We defined voxels belonging to crossing fibre regions by thresholding (at 0.4) and binarizing the average fractional anisotropy image over

the two time-points and all the subjects (in halfway space). The resulting image was registered into each subject's native space using nonlinear transformation warps, and binarized to yield masks of crossing fibre regions.

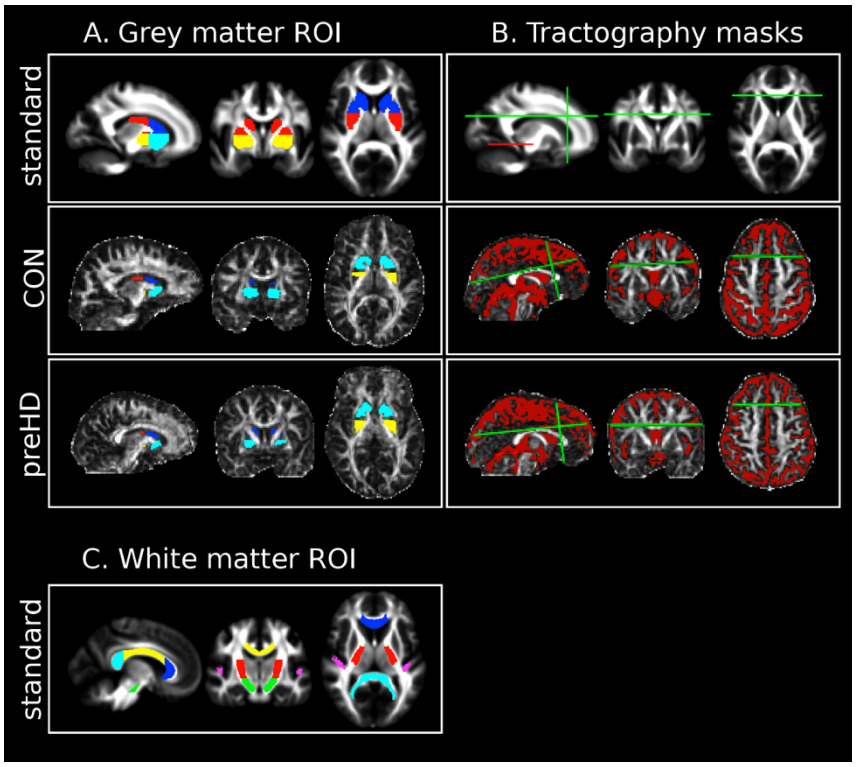

Figure 2.1. White matter ROIs and seed and exclusion masks for probabilistic tractography. A. Seed masks of the basal ganglia, used for probabilistic tractography. **B.** Target (in green) and exclusion (in red) masks for probabilistic tractography. **A and B.** Upper panel: masks in standard space overlaid on the study-specific fractional anisotropy template; middle panel: masks overlaid on native fractional anisotropy image at baseline of a typical control (CON); lower

panel: masks of a typical participant with presymptomatic Huntington's disease (preHD). **C.** White matter ROIs overlaid on the study-specific fractional anisotropy template: corpus callosum (genu in blue, body in yellow, and splenium in turquoise), posterior limb of internal capsule (in red), cerebral peduncle (in green), and auditory radiations as negative control region (in pink).

2.2.4. Whole white matter TBSS

The TBSS analysis was used to investigate whole-brain white matter microstructural abnormalities unconfounded by the choice of ROI, as TBSS is a voxel-wise method (Smith *et al.*, 2006). We developed an optimized registration approach to register baseline and follow-up fractional anisotropy images in a study-specific template space (see **section 2.1.1**). The same spatial transformations were applied to the mean diffusivity images. We then subtracted the baseline from the follow-up images to obtain a difference image of mean diffusivity and fractional anisotropy for each subject. The TBSS skeleton was derived from our study-specific fractional anisotropy template (see chapter 1 for more details). For each subject, the average fractional anisotropy image across the 2 timepoints in template space was used to estimate the distance map necessary to project the corresponding difference fractional anisotropy images onto the TBSS skeleton. The same projection procedure estimated from the

average fractional anisotropy images was used for the projection of the corresponding mean diffusivity difference images onto the TBSS skeleton. Voxel-wise statistics were run using the smoothed (Gaussian kernel with sigma of 1.5 mm) skeletonised mean diffusivity and fractional anisotropy difference images.

2.2.5. Statistical analyses

Statistical analyses of ROI-extracted imaging data were carried out using Statistical Software Package for the Social Sciences (SPSS 20) (IBM Corporation, Armonk, NY USA), MATLAB 2012b (The Math Works, Inc., Natick, Massachusetts, USA), Microsoft Excel 2010 (Microsoft Corporation, Redmond, Washington, USA), and R (version 3.2.3, The R Foundation for Statistical Computing (2015)).

Independent samples t-test was performed using SPSS to test for statistically significant group differences in mean diffusivity and fractional anisotropy between control and presymptomatic Huntington's disease. ANOVA was performed using SPSS for the presymptomatic Huntington's disease subgroups (according to estimated years to onset of symptoms) and healthy controls. Post-hoc tests, based on Tukey's honest significant difference (HSD) method, were used to test for significant pairwise group differences between FAR, MID, NEAR and controls. One-sample t-test was performed using SPSS to investigate the mean diffusivity and fractional

anisotropy difference between follow-up and baseline within each of the 4 groups (FAR, MID, NEAR and controls).

Shapiro-Wilk test was used to test if the data, and the residuals from the ANOVA were normally distributed. If the data were not normally distributed, non-parametric equivalent tests were used: Mann-Whitney U-test, Kruskal-Wallis ANOVA, and Dunn-Bonferroni test. All inferential statistical analyses were corrected for multiple comparisons using Bonferroni correction across the 6 WM ROIs.

For voxel-wise statistics, permutation-based non-parametric inference (5,000 permutations) was used to test for changes in mean diffusivity and fractional anisotropy between all participants with presymptomatic Huntington's disease and healthy controls, and between controls and the 3 subgroups (Nichols and Holmes, 2002). Results were considered to be significant for $P < 0.05$, and corrected for multiple comparisons using threshold-free cluster enhancement with 2D optimization (Smith and Nichols, 2009).

2.3. Results

2.3.1 Atlas-based white matter ROIs

We found a statistically significant overall effect of group (control, FAR, MID, NEAR) on the mean diffusivity change in the splenium of the corpus callosum (**Figure 2.2**). Post-hoc pairwise group comparisons showed that this effect was driven by a significant group difference between FAR and MID, whereby mean diffusivity showed a relative decrease in the FAR group compared with a relative (significant) increase in the MID group. There was also a trend in the pairwise comparisons between control and FAR, and FAR and NEAR ($p = 0.060$ and $p = 0.073$ before correction, respectively). There was no statistically significant overall effect of group on the change in fractional anisotropy (**Table 2.1**).

As expected, there was also no statistically significant overall effect of group in either diffusion metrics in the acoustic radiations (**Table 2.1**).

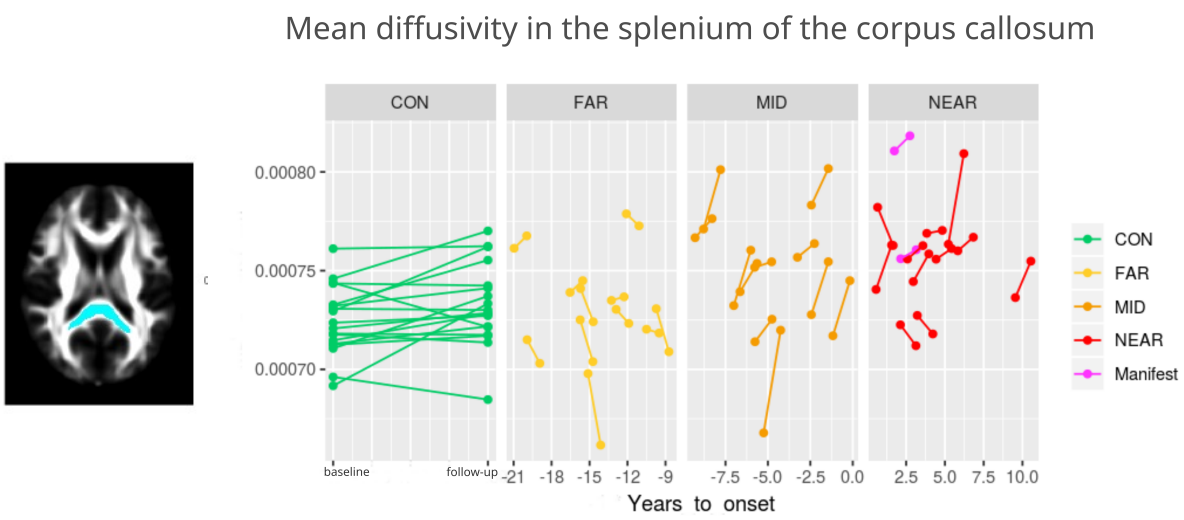

Figure 2.2. Longitudinal change in mean diffusivity in the splenium of the corpus callosum ROI across the 4 groups.

Metric	ROI	Control				all preHD			
		Mean	SD	t(18)	P	Mean	SD	t(34)	P
MD	genu	3.113E-06	3.430E-05	0.396	0.697	-5.140E-08	4.869E-05	-0.006	0.995
	splenium	6.417E-06	1.825E-05	1.533	0.143	6.114E-06	1.892E-05	1.912	0.064
	midbody	7.521E-08	1.429E-05	0.023	0.982	5.468E-06	1.514E-05	2.137	0.040
	posterior limb	2.913E-06	1.109E-05	1.145	0.267	2.781E-06	1.311E-05	1.255	0.218
	cerebral peduncles	1.313E-05	2.098E-05	2.729	0.014	2.705E-06	2.458E-05	0.651	0.519
	acoustic radiation	1.499E-06	1.339E-05	0.488	0.631	4.601E-06	2.354E-05	1.156	0.256
FA	genu	-4.022E-03	2.158E-02	-0.813	0.427	-5.663E-03	2.971E-02	-1.128	0.267
	splenium	-3.383E-03	1.017E-02	-1.450	0.164	-9.408E-03	2.772E-02	-2.008	0.053
	midbody	-5.039E-03	6.192E-03	-3.547	**0.002**	-7.191E-03	1.990E-02	-2.137	0.040
	posterior limb	-7.890E-04	6.395E-03	-0.538	0.597	-4.831E-03	1.689E-02	-1.692	0.100
	cerebral peduncles	-1.561E-03	1.454E-02	-0.468	0.645	-4.259E-03	2.018E-02	-1.249	0.220
	acoustic radiation	-4.824E-04	6.493E-03	-0.324	0.750	-2.114E-03	1.310E-02	-0.955	0.346

Metric	ROI	FAR				MID			
		Mean	SD	t(10)	P	Mean	SD	t(10)	P
MD	genu	-5.244E-06	3.294E-05	-0.528	0.609	-3.365E-07	7.216E-05	-0.015	0.988
	splenium	-9.905E-06	1.323E-05	-2.484	0.032	2.079E-05	1.405E-05	4.908	**0.001**
	midbody	-2.496E-06	1.450E-05	-0.571	0.581	6.231E-06	1.814E-05	1.139	0.281
	posterior limb	-1.863E-06	1.117E-05	-0.553	0.592	6.082E-06	1.650E-05	1.223	0.249
	cerebral peduncles	-2.568E-06	1.517E-05	-0.562	0.587	1.009E-05	3.549E-05	0.943	0.368
	acoustic radiation	-8.141E-06	1.751E-05	-1.542	0.154	1.388E-05	2.483E-05	1.854	0.093
FA	genu	5.843E-03	1.738E-02	1.115	0.291	-1.914E-02	4.553E-02	-1.394	0.193
	splenium	9.478E-05	1.262E-02	0.025	0.981	-2.370E-02	4.344E-02	-1.809	0.101
	midbody	-7.299E-03	1.803E-02	-1.343	0.209	-1.222E-02	2.926E-02	-1.385	0.196
	posterior limb	-1.138E-03	1.638E-02	-0.230	0.822	-1.225E-02	2.145E-02	-1.894	0.088
	cerebral peduncles	-3.253E-04	1.724E-02	-0.063	0.951	-1.470E-02	2.245E-02	-2.171	0.055
	acoustic radiation	-1.851E-03	8.382E-03	-0.732	0.481	-7.667E-03	1.635E-02	-1.555	0.151

Metric	ROI	NEAR				ANOVA			Post-hoc
		Mean	SD	t(12)	P	Statistic		P	
MD	genu	4.584E-06	3.774E-05	0.438	0.669	$\chi^2(3)$ =	2.456	0.483	
	splenium	7.253E-06	1.643E-05	1.591	0.138	F(3,50) =	6.699	**0.001**	#
	midbody	1.156E-05	1.005E-05	4.149	**0.001**	F(3,50) =	2.505	0.070	
	posterior limb	3.918E-06	1.119E-05	1.263	0.231	F(3,50) =	0.812	0.493	
	cerebral peduncles	9.192E-07	1.979E-05	0.167	0.870	$\chi^2(3)$ =	7.603	0.055	
	acoustic radiation	7.529E-06	2.374E-05	1.144	0.275	F(3,50) =	2.570	0.065	
FA	genu	-3.996E-03	1.519E-02	-0.948	0.362	$\chi^2(3)$ =	2.708	0.439	
	splenium	-5.357E-03	1.356E-02	-1.424	0.180	$\chi^2(3)$ =	5.300	0.151	
	midbody	-2.844E-03	9.708E-03	-1.056	0.312	$\chi^2(3)$ =	0.243	0.970	
	posterior limb	-1.680E-03	1.130E-02	-0.536	0.602	$\chi^2(3)$ =	4.014	0.260	
	cerebral peduncles	1.249E-03	1.840E-02	0.245	0.811	F(3,50) =	1.945	0.134	
	acoustic radiation	2.361E-03	1.244E-02	0.684	0.507	$\chi^2(3)$ =	2.882	0.410	

Table 2.1. Results table for the atlas-based white matter analysis. P-values are uncorrected, P-values in bold are significant after Bonferroni-correction for multiple ROIs. (MD: mean diffusivity, FA: fractional anisotropy, ROI: region of interest, CON: control, preHD: presymptomatic Huntington's disease, FAR: far from the onset of symptoms, MID: mid-way from the onset of symptoms, NEAR: near the onset of symptoms, #: significant difference between FAR and MID).

2.3.2 Cortico-subcortical tractography ROIs

We found no significant overall effect across groups or within groups on the change in mean diffusivity or fractional anisotropy across the tracts connecting cortex and the basal ganglia as identified using probabilistic tractography (lowest $p = 0.137$, **Table 2.2**).

Metric	Seed	CON				all preHD			
		Mean	SD	t(18)	P	Mean	SD	t(34)	P
MD	ant	1.426E-10	1.281E-08	0.049	0.962	-1.806E-09	1.301E-08	-0.821	0.417
	pos	-6.455E-10	1.848E-08	-0.152	0.881	1.571E-09	1.810E-08	0.514	0.611
FA	ant	2.825E-07	5.653E-06	0.218	0.830	-7.144E-07	5.632E-06	-0.750	0.458
	pos	-9.395E-07	9.629E-06	-0.425	0.676	5.045E-07	8.978E-06	0.332	0.742
Metric	Seed	FAR				MID			
		Mean	SD	t(10)	P	Mean	SD	t(10)	P
MD	ant	-7.368E-09	1.731E-08	-1.412	0.188	-3.612E-09	8.241E-09	-1.453	0.177
	pos	5.482E-09	1.933E-08	0.941	0.369	2.191E-09	1.246E-08	0.583	0.573
FA	ant	-2.651E-06	7.711E-06	-1.140	0.281	-1.541E-06	4.256E-06	-1.201	0.258
	pos	2.611E-06	9.463E-06	0.915	0.382	4.939E-07	6.841E-06	0.239	0.816
Metric	Seed	NEAR				ANOVA			
		Mean	SD	t(12)	P	Statistic		P	
MD	ant	4.429E-09	1.001E-08	1.595	0.137	F(3,50) =	1.976	0.130	
	pos	-2.262E-09	2.138E-08	-0.381	0.710	F(3,50) =	0.418	0.741	
FA	ant	1.623E-06	3.903E-06	1.500	0.160	F(3,50) =	1.435	0.244	
	pos	-1.268E-06	1.036E-05	-0.442	0.667	F(3,50) =	0.445	0.722	

Table 2.2. Longitudinal results from the probabilistic tractography analysis with the basal ganglia as seeds. P-values are uncorrected, P-values in bold are significant after Bonferroni-correction for multiple ROIs. (MD: mean diffusivity, FA: fractional anisotropy, ROI: region of interest, ant: anterior basal ganglia, pos: posterior basal ganglia, CON: control, preHD: presymptomatic Huntington's disease, FAR: far from the onset of symptoms, MID: mid-way from the onset of symptoms, NEAR: near the onset of symptoms).

2.3.3. Whole white matter voxel-wise analysis

There was no significant overall effect of group on mean diffusivity change in the WM skeleton ($p = 0.231$). However, pairwise group comparisons showed a significant group difference between FAR and MID mainly bilaterally in the splenium of the corpus callosum, but also in parts of the cingulum (parietal) and right superior longitudinal fasciculus, posterior limb of the internal capsule and superior corona radiata (**Figure 2.3**). This was once more explained by a relative decrease of mean diffusivity in FAR, and a relative increase in MID.

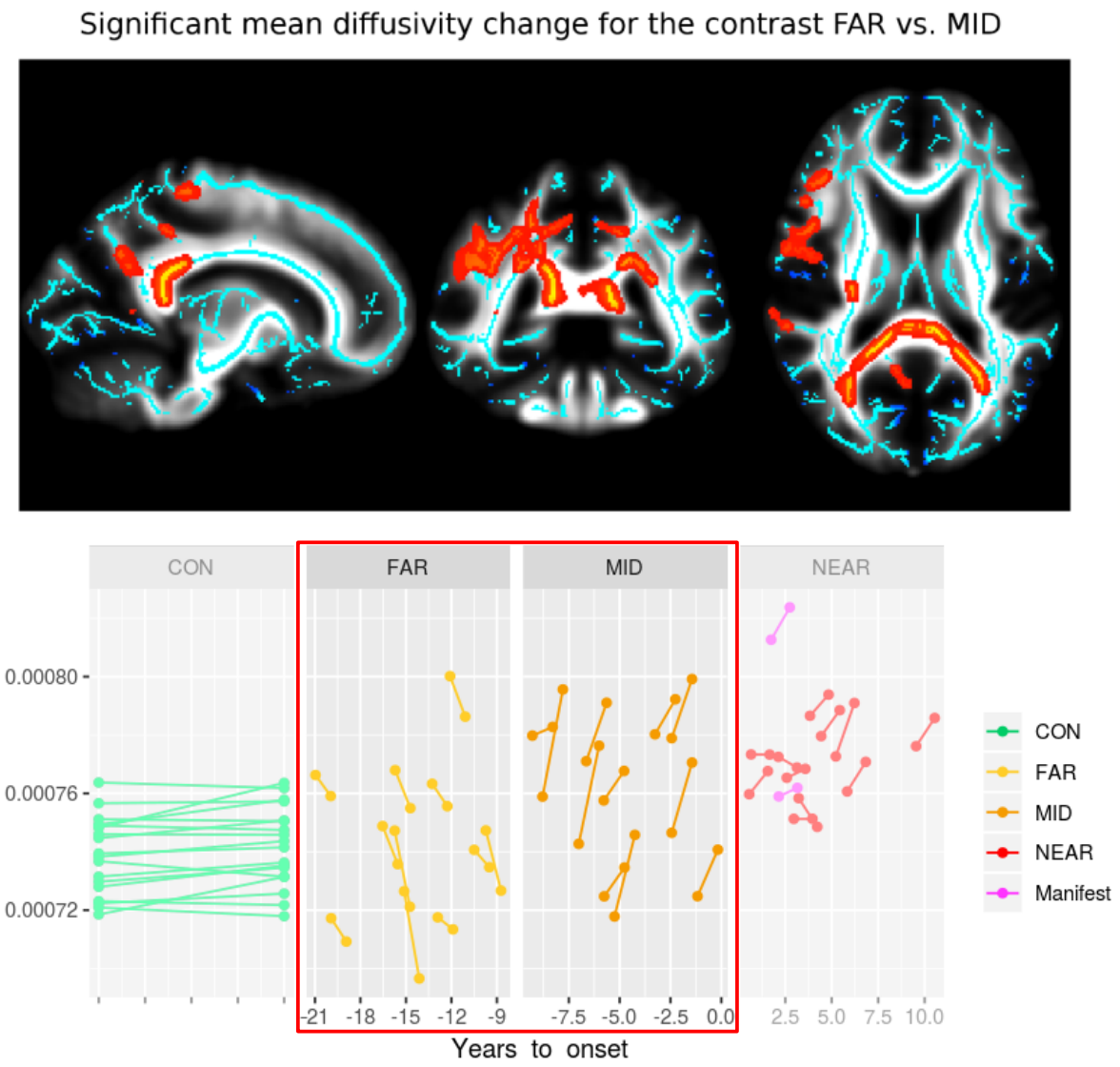

Figure 2.3. Significant TBSS difference between FAR and MID in mean diffusivity change. A. Significant TBSS differences (dilated for visual purposes, red-yellow) in mean diffusivity change between the presymptomatic subgroups FAR and MID overlaid on the TBSS skeleton (light blue) and the fractional anisotropy study specific template. Results are corrected for multiple comparisons across voxels using threshold-free cluster enhancement at $p = 0.05$. **B.** Plots showing, for

illustrative purposes, the longitudinal change of the average mean diffusivity value over all significant voxels of the TBSS map for the contrast FAR vs. MID (as shown in A). The red frame indicates the significant effect found in TBSS.

Similarly, while there was no overall effect of group on fractional anisotropy, there was a significant group difference in fractional anisotropy change between the FAR and MID subgroups in the right splenium of the corpus callosum. This effect seemed mainly driven by a relative decrease in fractional anisotropy in the MID group between the two timepoints, compared with a relative increase in fractional anisotropy in the FAR group between the two timepoints (**Figure 2.4**). There was an additional significant group difference in fractional anisotropy change between the CON and MID groups in the right splenium extending into the posterior part of the body of the corpus callosum, superior longitudinal fasciculus and superior corona radiata (**Figure 2.5**). This difference was mainly driven by a relative decrease in fractional anisotropy in the MID group, compared with a slight increase in the control group.

Voxel-wise within group effect was found in the MID group, whereby mean diffusivity was significantly increased and fractional anisotropy decreased from baseline to follow-up mainly bilaterally in the splenium of the corpus callosum, as well as the right superior longitudinal fasciculus (**Figures 2.6, 2.7**).

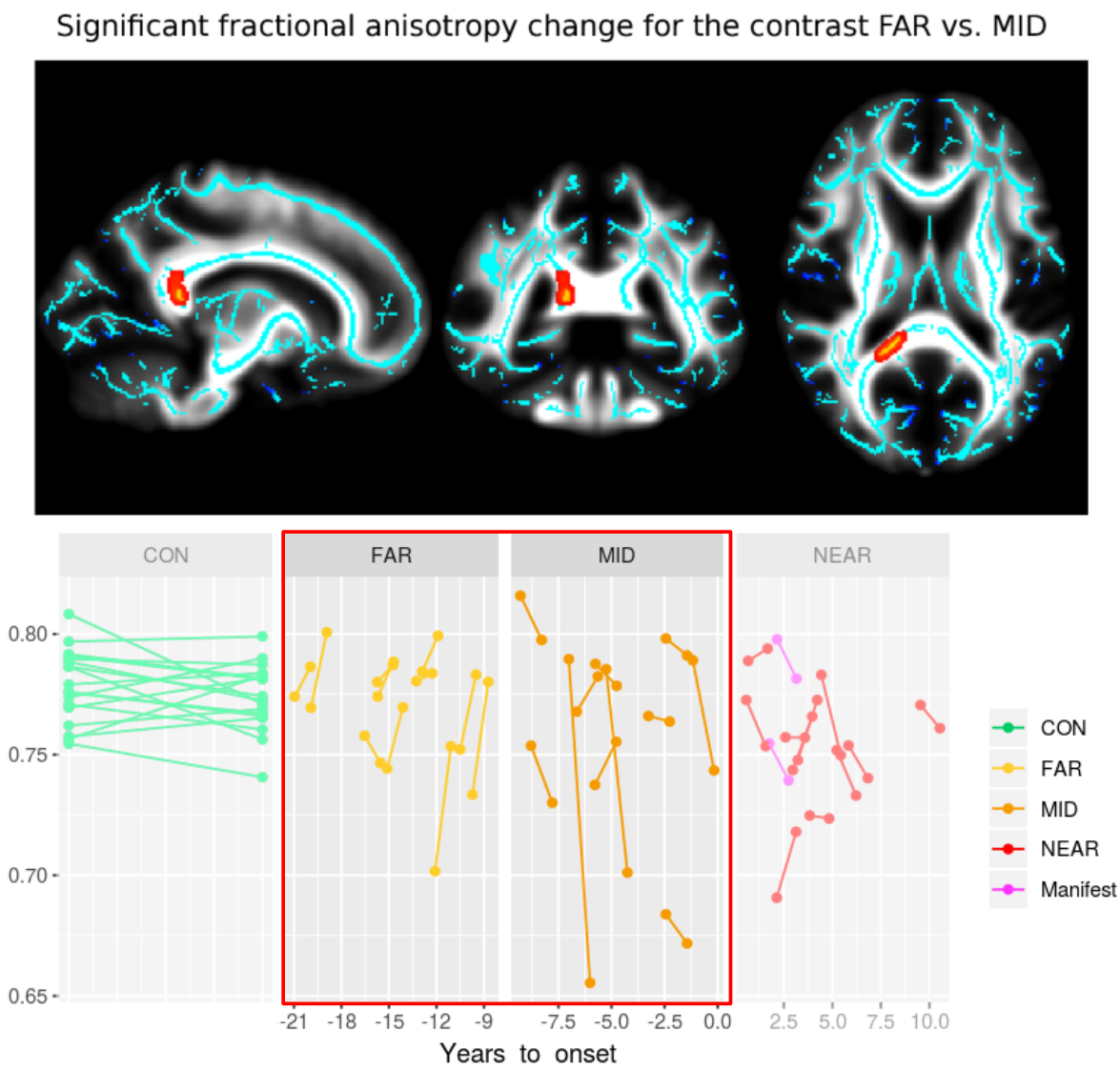

Figure 2.4. Significant TBSS difference between FAR and MID in fractional anisotropy change. **A.** Significant TBSS differences in fractional anisotropy change (red-yellow) between the presymptomatic subgroups FAR and MID overlaid on the TBSS skeleton (blue) and the study specific template. Results are corrected for multiple comparisons across voxels using threshold-free cluster enhancement at $P = 0.05$. **B.** Plots showing the longitudinal change of the average

fractional anisotropy value over all significant voxels of the TBSS map for the contrast FAR vs. MID. The red frame indicates the significant effect found in TBSS.

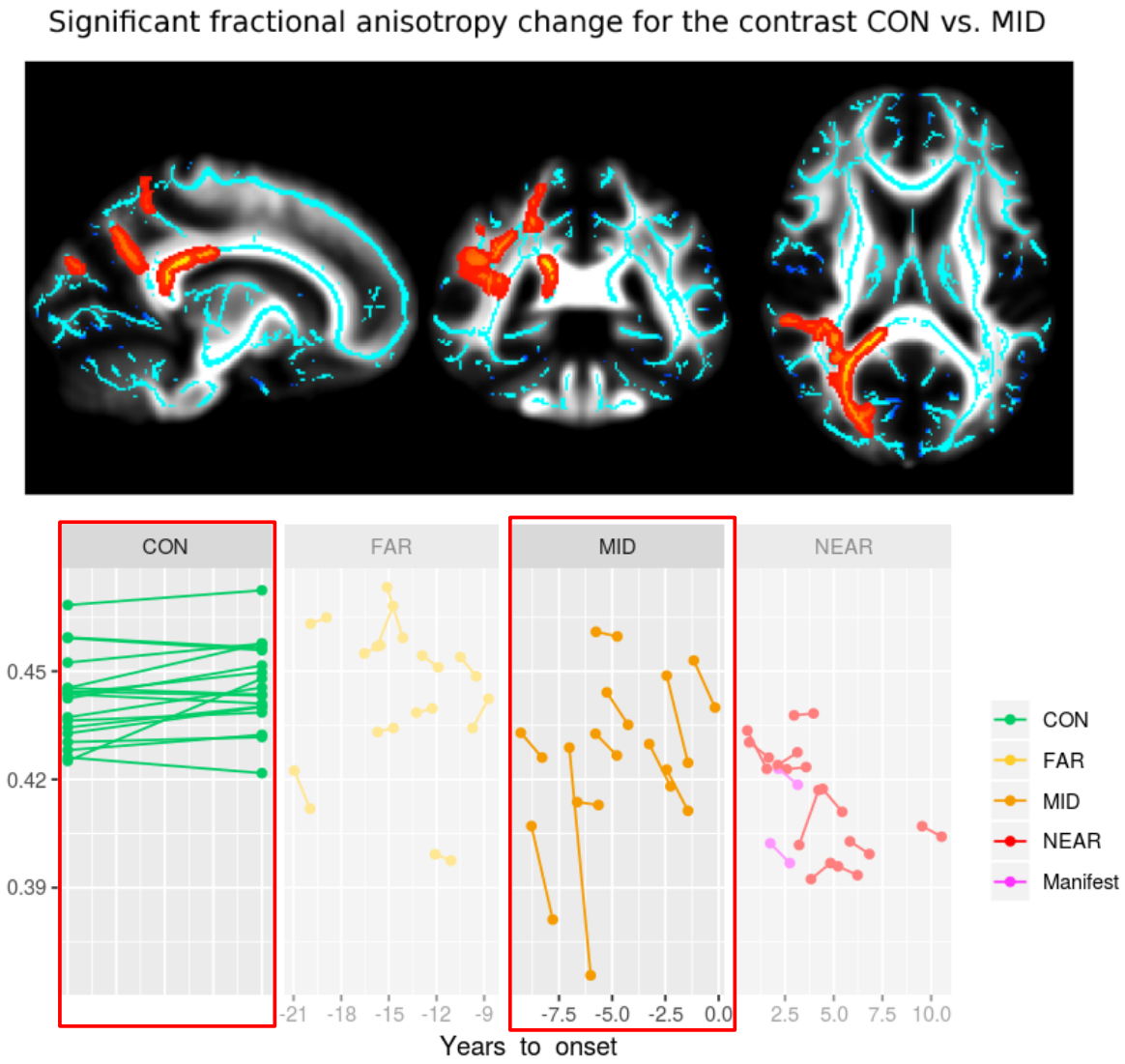

Figure 2.5. Significant TBSS difference between CON and MID in fractional anisotropy change. A. Significant TBSS differences in fractional anisotropy change (red-yellow) between the control group CON and presymptomatic MID group overlaid on the TBSS skeleton (blue) and the study specific template. Results are corrected for multiple comparisons across voxels using threshold-free cluster enhancement at $P = 0.05$. **B.** Plots showing the longitudinal change of the

average fractional anisotropy value over all significant voxels of the TBSS map for the contrast CON vs. MID. The red frames indicate the significant effect found in TBSS.

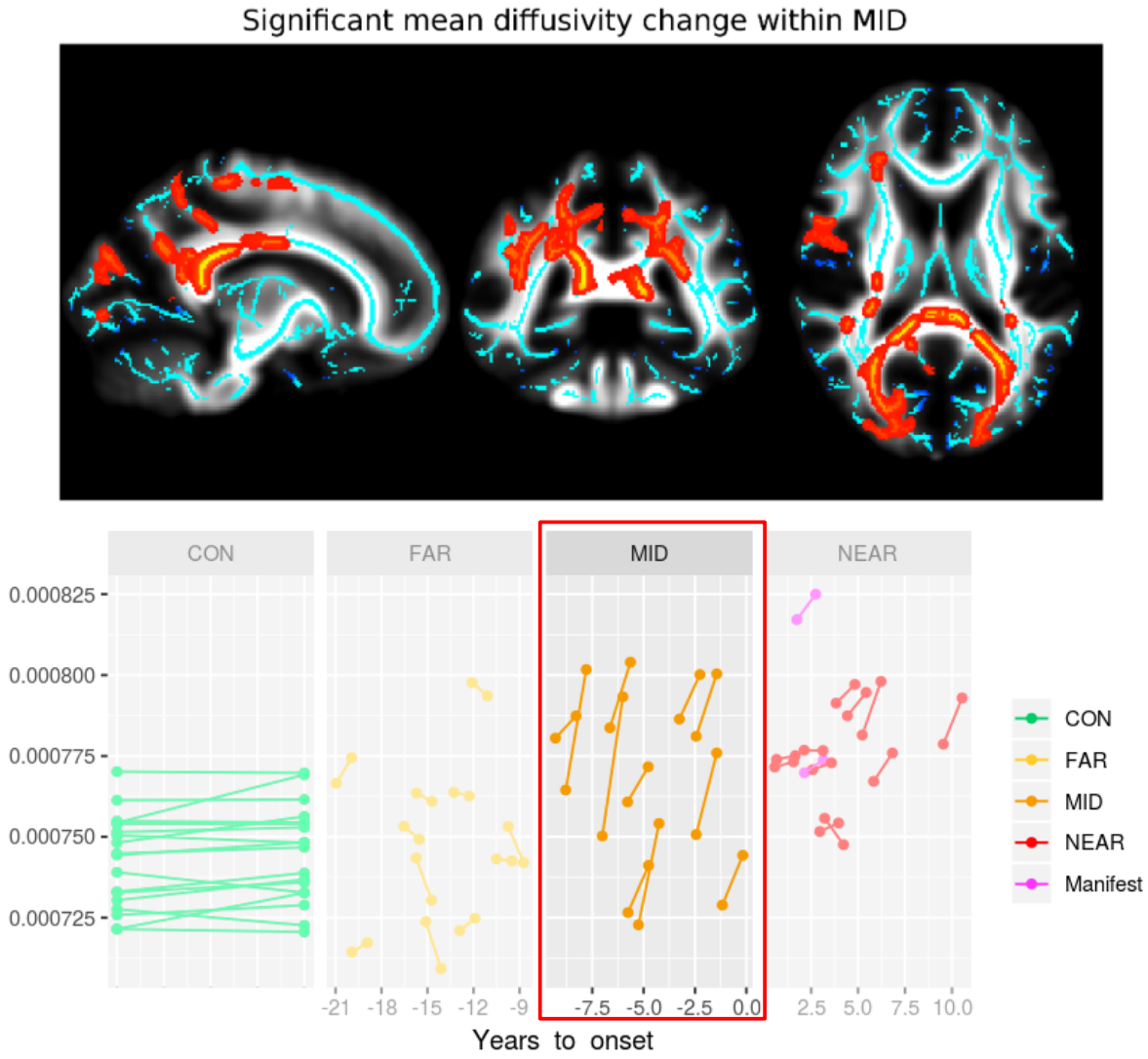

Figure 2.6. Longitudinal increase in mean diffusivity within the group half-way to the onset of symptoms (MID). A. Dilated TBSS map of the significant increase in mean diffusivity (red-yellow) from baseline to follow-up in MID overlaid on the TBSS skeleton (blue) and the study specific template. Results are corrected for multiple comparisons across voxels using threshold-free cluster enhancement at $P = 0.05$. **B.** Profile plots showing the longitudinal change of the average mean diffusivity, over all significant voxels of the TBSS map for longitudinal

increases in MID (as shown in A). The red frame indicates the significant effect found in TBSS. This plot is shown for illustrative purposes only.

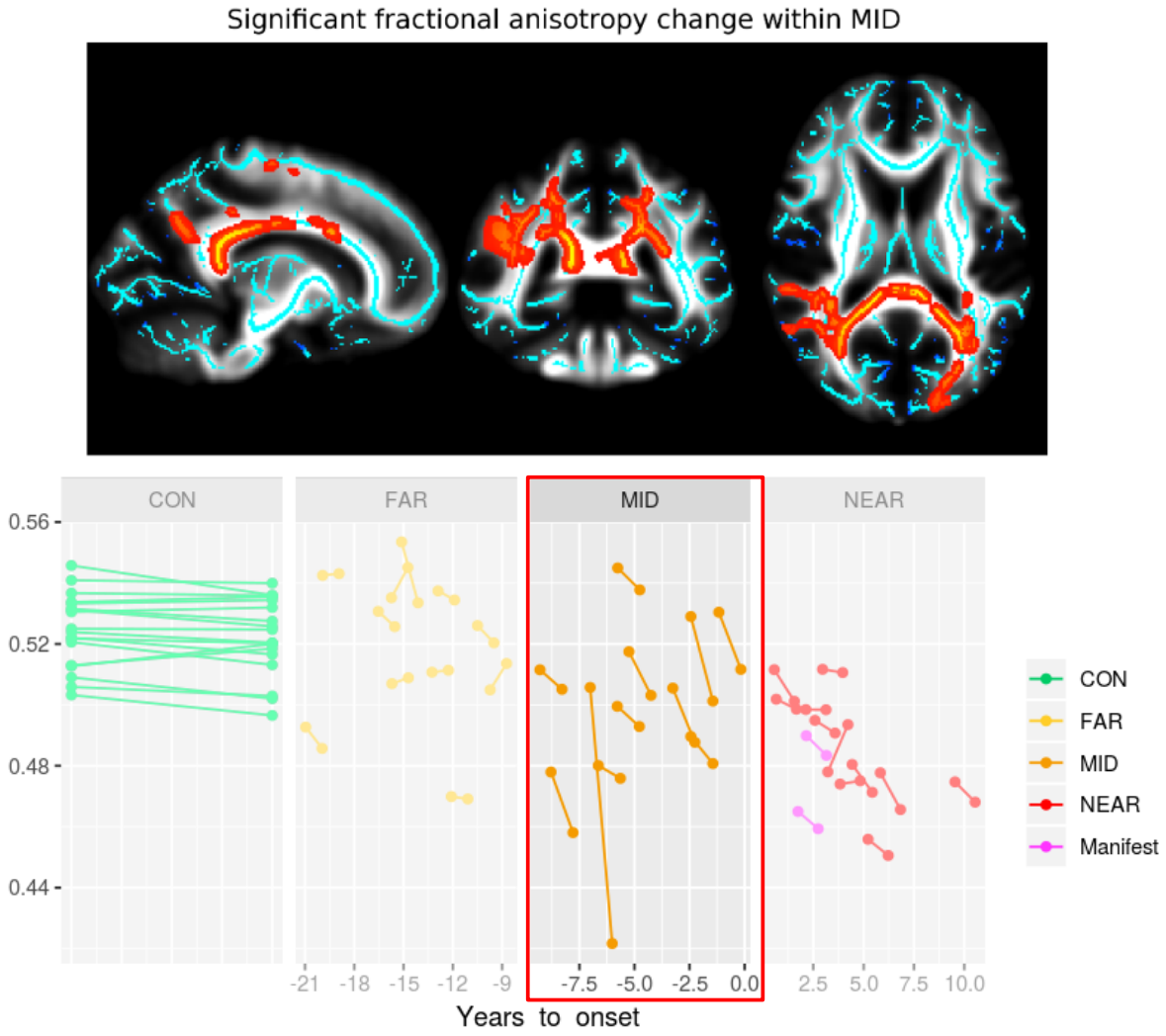

Figure 2.7. Longitudinal decrease in fractional anisotropy within the group half-way to the onset of symptoms (MID). A. Dilated TBSS map of the significant decrease in fractional anisotropy (red-yellow) from baseline to follow-up in the group mid-way to the onset of symptoms (MID) overlaid on the TBSS skeleton (blue) and the study specific template. Results are corrected for multiple comparisons across voxels using threshold-free cluster enhancement at $P = 0.05$. **B.**

Profile plots showing the longitudinal change of the average fractional anisotropy, over all significant voxels of the TBSS map for longitudinal decreases in NEAR (as shown in A).

2.4. Discussion

Here we have investigated longitudinal changes over a one-year period in diffusion metrics in the white matter comparing control subjects and participants with presymptomatic Huntington's disease. Initial results, directly comparing these two groups failed to reveal any significant difference in diffusion metric changes. Conversely, we show here that stratifying participants with presymptomatic Huntington's disease into subgroups according to their estimated years to onset of symptoms yielded results revealing distinct patterns in the diffusion images at different presymptomatic stages. We found significant overall effects on mean diffusivity change in the splenium of the corpus callosum. Using whole WM analysis, we also found a significant longitudinal difference in mean diffusivity and fractional anisotropy change between far- and mid-to-onset groups mainly in the splenium of the corpus callosum, as well as a difference in fractional anisotropy change between control and mid-to-onset groups. These results suggest that diffusion tensor imaging is a promising surrogate marker in presymptomatic Huntington's disease, with a high sensitivity to longitudinal changes in the microstructure of the cerebral WM when combined with genetic and hereditary information.

To the best of our knowledge, this is the first study that has demonstrated longitudinal changes in diffusion metrics within the presymptomatic stages of

Huntington's disease. Previous longitudinal diffusion MRI studies in presymptomatic Huntington's disease either did not detect any significant effects, or found significant effects only cross-sectionally (Domínguez *et al.*, 2013; Odish, Leemans, *et al.*, 2015; Poudel *et al.*, 2015), or solely when comparing the symptomatic HD group with controls. Previous diffusion MRI studies in clinical Huntington's disease have also failed to detect any longitudinal effects (Vandenberghe *et al.*, 2009; Sritharan *et al.*, 2010). This lack of significant longitudinal effect in diffusion imaging is most likely due to the need for stratifying participants with Huntington's disease into meaningful subgroups to ensure that increases and decreases in diffusion metrics are not averaged out across the various presymptomatic and clinical stages.

A previous study found a longitudinal reduction in mean diffusivity in the putamen – but not in the caudate – when comparing presymptomatic with manifest Huntington's disease (Domínguez *et al.*, 2013). This seems to be in line with our results showing a decrease of mean diffusivity at earlier stages of the disease, when compared with later stages (although our findings were obtained within the presymptomatic stages of the disease). Interestingly, in the Dominguez' study, as in ours, the pattern of change in diffusion metrics was also markedly different between posterior basal ganglia/putamen and anterior basal ganglia/caudate. There was a

decrease then increase of mean diffusivity (and the opposite pattern in fractional anisotropy) when transitioning towards later stages of the disease in the posterior basal ganglia/putamen, while there was a constant, progressive increase in mean diffusivity in the anterior basal ganglia/caudate. This might indicate that the tissue of the anterior and posterior basal ganglia is undergoing a pathophysiological process that differs in timing.

Both the ROI and whole WM analyses revealed that changes in mean diffusivity were mainly found in the corpus callosum. This is similar to previous research that found cross-sectional alterations in diffusion metrics in the corpus callosum across years-to-onset groups with presymptomatic Huntington's disease (Rosas *et al.*, 2010). These microstructural alterations preceded macrostructural atrophy, and might reflect altered inter-hemispheric communication that is associated with cognitive deficits seen in Huntington's diseases (Rosas *et al.*, 2010). Notably, we did not find any significant longitudinal effect in the diffusion metrics over the cortico-subcortical tracts, confirming that the corpus callosum is a WM region exquisitely sensitive to very early damage in Huntington's disease. Remarkably, this same region of the cerebral WM also shows pronounced longitudinal changes in the manifest stage of the disease when compared with healthy controls and presymptomatic stage (Poudel *et*

al., 2015). These ROI-based and voxel-based changes in mean diffusivity were mainly found in the splenium, rather than in the genu or body of the corpus callosum, as were the changes in fractional anisotropy. This is in line with topologically selective cross-sectional alterations in diffusion metrics markedly found in the posterior corpus callosum in both presymptomatic and clinical Huntington's disease (Rosas *et al.*, 2010). A previous cross-sectional imaging study also found lower callosal thickness, WM density and fractional anisotropy in the posterior parts of the corpus callosum when comparing presymptomatic Huntington's disease with control group, while comparisons between the symptomatic and control groups showed alterations across the entire corpus callosum (Di Paola *et al.,* 2012). A possible explanation for these gradients of demyelination might be that the corpus callosum contains fibres of different caliber and onset of myelination across its rostro-caudal axis (Aboitiz *et al.*, 1992; Aboitiz and Montiel, 2003), so that callosal fibres might be susceptible to damage at different time-points during the course of the pathology.

Besides being sensitive to longitudinal changes, a state biomarker for presymptomatic Huntington's disease needs to shed light on the underlying pathophysiological mechanism of such changes. Overall significant differences in mean diffusivity change in the posterior basal ganglia were mainly driven by decreases in mean diffusivity in the far-from-onset group compared with a relative increase in the mid-to-onset and

near-to-onset groups. Likewise, an overall significant effect of group observed in the splenium of the corpus callosum was mainly driven by a relative decrease in mean diffusivity in the far-from-onset group, compared with an increase in the mid-to-onset group. Such a decrease in mean diffusivity is prima facie counter-intuitive in a neurodegenerative disorder, because increased mean diffusivity is traditionally seen as a characteristic feature of neurodegeneration. Here however, this initial decrease in mean diffusivity might represent an early microstructural sign of neurodegeneration and corresponds to an early neuro-inflammatory phase. Indeed, in a diffusion study of preclinical Alzheimer's disease, mean diffusivity was found significantly decreased at "stage I" compared with the normal group, while this effect pseudo-normalized at "stage II" (Wang, Yong Wang, *et al.*, 2015). Further simulation of white matter geometry demonstrated that an increase in microglia cell activation was sufficient to cause a decrease in mean diffusivity at an early preclinical stage, and that the combination of axon damage, cell infiltration and oedema might cause the pseudo-normalization of this diffusion metric at a later stage (Wang, Y Wang, *et al.*, 2015). Similarly, in presymptomatic familial Alzheimer's disease mean diffusivity was significantly decreased in the hippocampus and cingulum, whereas symptomatic mutation carriers showed increased mean diffusivity in all white matter tracts of interest (Ryan *et al.*, 2013). As microglial activation is a highly sensitive marker of

neuronal insult (Kreutzberg, 1996), which occurs in presymptomatic Huntington's disease (Tai *et al.*, 2007a, 2007b), and pseudo-normalizes in later stages (Dowie *et al.*, 2014), this altogether strongly suggests that the decrease of mean diffusivity consistently found at an early, preclinical stage of Huntington's disease bears the hallmark of inflammatory processes and might as such represent a sensitive and very early biomarker of neurodegeneration.

Unlike volumetric MRI, changes seen in diffusion metrics are non-monotonic (increases and decreases for the same metric), and can therefore be averaged out when considering the entire presymptomatic group. When compared with structural MRI however, we have seen that these non-monotonic changes in diffusion MRI can be extremely helpful in understanding the underlying disease mechanisms, as well as monitoring progression towards the later stages of the disease and the effects of novel treatment options. Overall, structural and diffusion MRI should therefore be considered to be complimentary research methods, whereby the former might have a higher overall sensitivity (discriminant ability), whereas the latter might have a higher specificity.

In conclusion, diffusion MRI is able to detect significant and interpretable changes over a one-year period in presymptomatic Huntington's disease subgroups. To reveal

these effects, it is necessary to divide subjects into clinically-meaningful subgroups according to their predicted age at onset of symptoms. The longitudinal decrease then increase from earlier to later stages of the presymptomatic disease seen in mean diffusivity of the posterior basal ganglia and splenium of the corpus callosum potentially suggest an initial early stage of neuroinflammation, followed by a neurodegenerative process. Longitudinal changes of the gray and white matter microstructure in these two structures suggest that they play a crucial role in the natural history of presymptomatic Huntington's disease. Diffusion MRI thus offers key complementary information to the monotonic, non-specific changes seen in structural MRI. In particular, we have shown here that diffusion metrics might not only provide crucial mechanistic insights into the putative pathophysiological processes, but also much-needed distinction between presymptomatic stages.

Chapter I.3: Longitudinal changes in clinical questionnaire scores and behavioral data in presymptomatic Huntington's disease and their correlations with diffusion metrics

3.0. Abstract

Rational. Clinical assessment tools (e.g. Unified Huntington's disease rating scale) have wide-spread use in clinical practice and research. Here we have investigated if clinical and behavioral data show longitudinal sensitivity at the presymptomatic stage over a 1-year period, and if changes in clinical and behavioral data were associated with imaging outcomes from diffusion tensor MRI data.

Objective. To investigate longitudinal sensitivity of clinical and behavioral assessment tools in presymptomatic Huntington's disease compared with healthy controls. To identify orthogonal questionnaire data using principal component analysis. To correlate changes in diffusion metrics in the gray and white matter in various presymptomatic groups with longitudinal questionnaire data.

Methods. Several clinical assessment tools, and psychometric instruments were used to investigate various aspects of sensorimotor, neurological, cognitive, and psychiatric functioning in both participants with presymptomatic Huntington's, and healthy controls over a one-year period. Patients with presymptomatic Huntington's disease

were stratified into groups according to their predicted age at the onset of symptoms based on genetic and hereditary information.

Results. Most questionnaire scores were not sensitive to detect longitudinal changes over a one-year period in presymptomatic Huntington's disease. Only the UHDRS motor score showed significant longitudinal group differences, that were driven by longitudinal changes only detectable in the group near-the-onset of symptoms. Longitudinal changes in questionnaire scores across the entire presymptomatic Huntington's disease group only showed weak cross-correlations, whereas they were highly cross-correlated when looking at baseline and follow-up data separately. Longitudinal changes in mean diffusivity in the posterior basal ganglia and in the splenium of the corpus callosum, as revealed in previously described analysis of diffusion tensor data, were highly correlated with changes in motor, psychiatric, and cognitive clinical data.

Conclusions. Clinical questionnaires and behavioral assessment tools were less sensitive to changes over a one-year period in presymptomatic Huntington's disease than diffusion tensor MRI data. Clinical and psychometric questionnaire scores proved to be valuable to provide more information that can help explain longitudinal changes in diffusion metrics.

3.1. Introduction

The focus of this chapter is to investigate longitudinal changes in clinical and behavioral data in presymptomatic Huntington's disease, as well as in stratified groups according to their onset of the disease. We have also investigated if the outcomes of the neuroimaging data from the previous chapters showed any association with longitudinal changes in the clinical and behavioral data.

Previous research investigating longitudinal changes in *early clinical* Huntington's disease revealed promising results in various psychometric and cognitive assessment tools (Ho *et al.*, 2003; Beglinger *et al.*, 2010). In *presymptomatic* Huntington's disease previous cross-sectional research revealed alterations in cognitive and (occulo-)motor tests (Kirkwood *et al.*, 2000; Duff *et al.*, 2010; Harrington *et al.*, 2012), as well as neuropsychiatric assessment tools (Paulsen *et al.*, 2001). Indeed, cognitive impairments were detectable at least 15 years prior to motor diagnosis (Paulsen, 2011). Previous l*ongitudinal* research in presymptomatic Huntington's disease revealed clear changes in psychiatric screening tools, even when a stratification according to age-to-onset was applied (Epping *et al.*, 2016), and changes in various everyday cognitive scores, even after age-to-onset stratification (Williams et al., 2015).

3.2. Methods

3.2.1. Overview of clinical and psychometric assessment tools

Several clinical assessment tools, and psychometric instruments were used to investigate various aspects of sensorimotor, neurological, cognitive, and psychiatric functioning in both participants with presymptomatic Huntington's, and healthy controls. Participants with presymptomatic Huntington's disease were clinically assessed using the Unified Huntington's Disease Rating Scale (UHDRS) at both time-points, healthy controls were also assessed with the UHDRS but only at baseline. Three UHDRS scores were used for the data analysis: the UHDRS motor score that comprises both positive (e.g. chorea), and negative symptoms, the modified motor score that only encompasses negative symptoms (e.g. bradykinesia), and the diagnostic confidence score. The Montreal Cognitive Assessment (MoCA) was used as a screening tool for mild cognitive impairment. Global cognitive ability was also measured using the Mini–Mental State Examination (MMSE) (Folstein, Folstein and McHugh, 2015). Participants were also tested using the Stroop test, a cognitive interference task, the digit span test to assess their working memory, and the vocabulary and matrix sub-tests of the Wechsler Adult Scale of Intelligence (WAIS). Furthermore the Symptom Checklist 90 (SCL-90), a self-report questionnaire assessing psychiatric symptoms, was used as a psychiatric screening instrument. Data

analysis included both the orthogonal sub-scales of the SCL-90, as well as three global indices including Global Severity Index (GSI), Positive Symptom Distress Index (PSDI) and Positive Symptom Total (PST). The Barratt Impulsiveness Scale, was used to assess the personality construct (trait) of impulsiveness (Patton, Stanford and Barratt, 1995).

3.2.2. Statistical analysis

One-sample t-test were used to assess the strongest changes in all questionnaire (motor, cognitive and behavioral) scores, and these changes were cross-correlated for the entire preHD group. We also performed ANOVA and post-hoc tests – in a similar way as described in chapter 1 – across the 4 groups for all changes in cognitive and behavioral questionnaire scores, and 3 preHD sub-groups for the UHDRS motor-related scores.

Since several motor and psychiatric scores, as well as a variety of cognitive test(e.g. Stroop, WAIS, MOCA), were used, we tried to identify latent variables underlying the observed test scores, in order to reduce the dimensionality of the data. A principal component analysis (PCA) was performed on these changes in all questionnaire scores. Finally, we investigated whether any of the significant diffusion changes observed across the four groups in the previous imaging analyses could be

related to changes in motor, cognitive or behavioral changes. The Spearman rank-order correlation coefficient was used to test for post-hoc associations between the significant differences potentially found in diffusion metrics change and change in cognitive and clinical measures. Data were tested for normality, and if found non-normally distributed, equivalent statistical tests (described above) were used. All results were corrected for multiple comparisons across the number of questionnaires.

3.3. Results

3.3.1. Exploratory data analysis on questionnaire scores

To explore the overall data structure of the questionnaire scores cross-correlation matrices were computed for longitudinal changes as well as at baseline and follow-up seperately (**Figure 3.1**), and principal component analysis was used to identify orthogonal components (**Figure 3.2**).

Most of the longitudinal changes in the preHD participants were only weakly to moderately correlated with one another, by contrast scores were highly correlated at each timepoint separately (see **Figure 3.1**). There were a few exceptions where longitudinal changes showed high correlations, notably in the changes in UHDRS motor, modified motor and confidence in motor scores, as well as between the

changes in SCL90 interpersonal sensitivity and a range of other SCL90 scores and the motor scores on the Barratt Impulsiveness Scale (BIS).

A PCA in the preHD group further demonstrated that the main two orthogonal axes consisted of a linear combination of changes in the SCL90 scores, and a linear combination of changes in the UHDRS motor-related scores, respectively (the first 10 axes, explaining more than 80% of the variance of the data, as well as the first 2 axes thresholded, are shown in **Figure 3.2**).

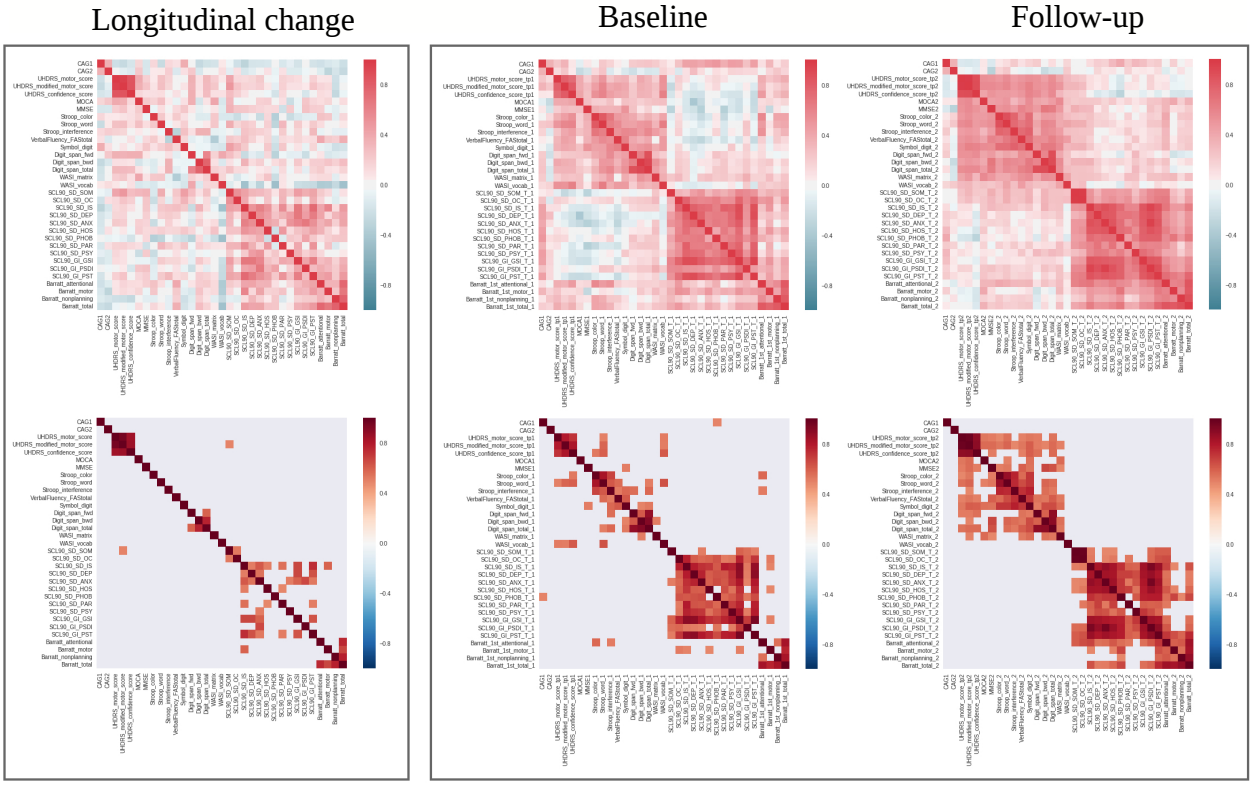

Figure 3.1. Cross-correlation matrices between questionnaire scores and clinical data as longitudinal change over a one-year period in the entire preHD group, as well

as at baseline and at follow-up. Upper correlation matrices are unthresholded, lower correlations matrices are thresholded at p = 0.05 corrected for multiple comparisons (CAG1 = non-mutant length, CAG2 = mutant length). As it can be clearly seen questionnaire scores were highly correlated when looking at them cross-sectionally, i.e. at baseline and follow-up, but not when looking at them longitudinally.

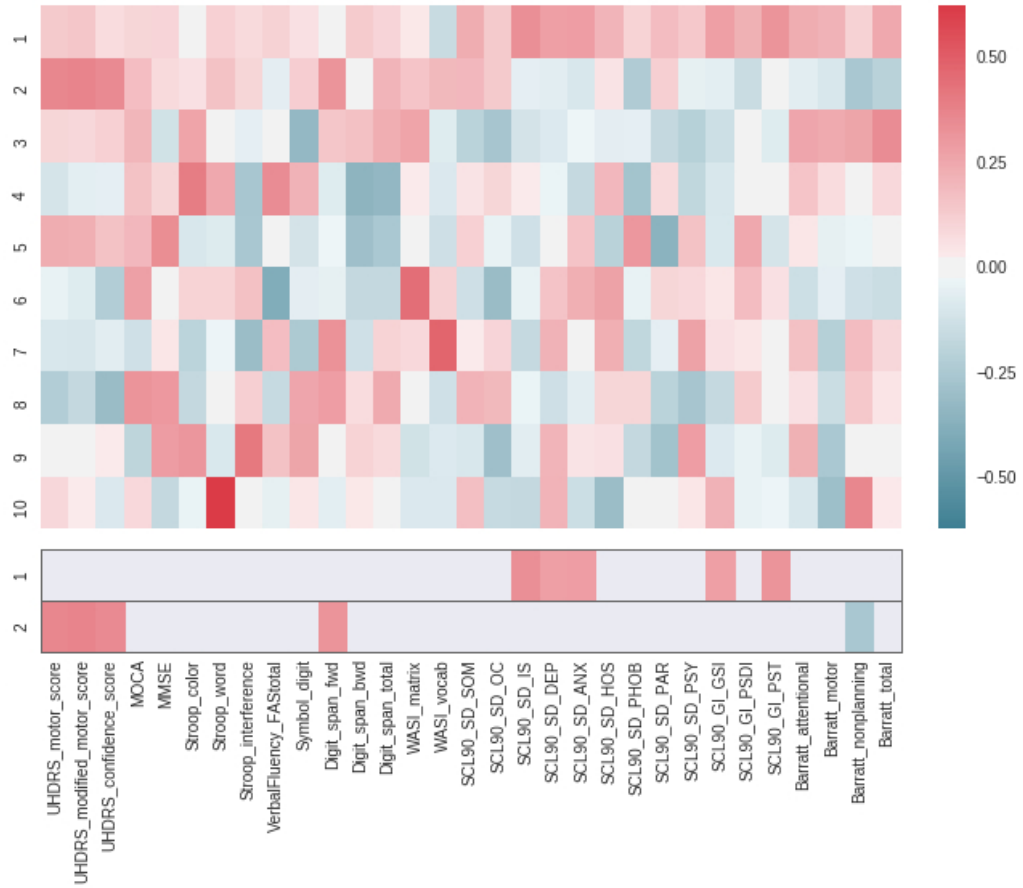

Figure 3.2. Principal component analysis of the longitudinal changes in all questionnaire scores in the preHD group. Top, first ten axes (unthresholded),

which together explain more than 80% of the variance. Bottom, the first two axes, accounting for more than a third of the variance, thresholded at 0.25 for visual purposes. While the first axis consisted of a linear combination of changes in the SCL90 behavioral scores, the second axis was mainly a linear combination of changes in the UHDRS motor-related scores.

3.3.2. Longitudinal changes in questionnaire scores

A significant change in the entire preHD group was found in obsessive-compulsive (OC) symptoms on the Symptom Checklist-90 (SCL90, t (33) = -6.432, p = 3x10-7), but this decrease was mainly due to what appears to be strong test-retest effects (also exhibited in the CON group, and as a result, there was no difference in changes in OC between the two groups). There was also a significant change in UHDRS modified motor score in the entire preHD group (p = 0.0012), and a trend in UHDRS confidence in motor score (p = 0.002 before correction).

Within the NEAR subgroup, the obsessive-compulsive score was significantly decreased from baseline to follow-up (t (12) = - 4.820, p =0.013, **Figure 3.3**). There was also a trend for an increase in the modified motor score within the NEAR subgroup, but it did not survive correction for multiple comparisons (t(12) = 3.579, uncorrected p = 0.004).

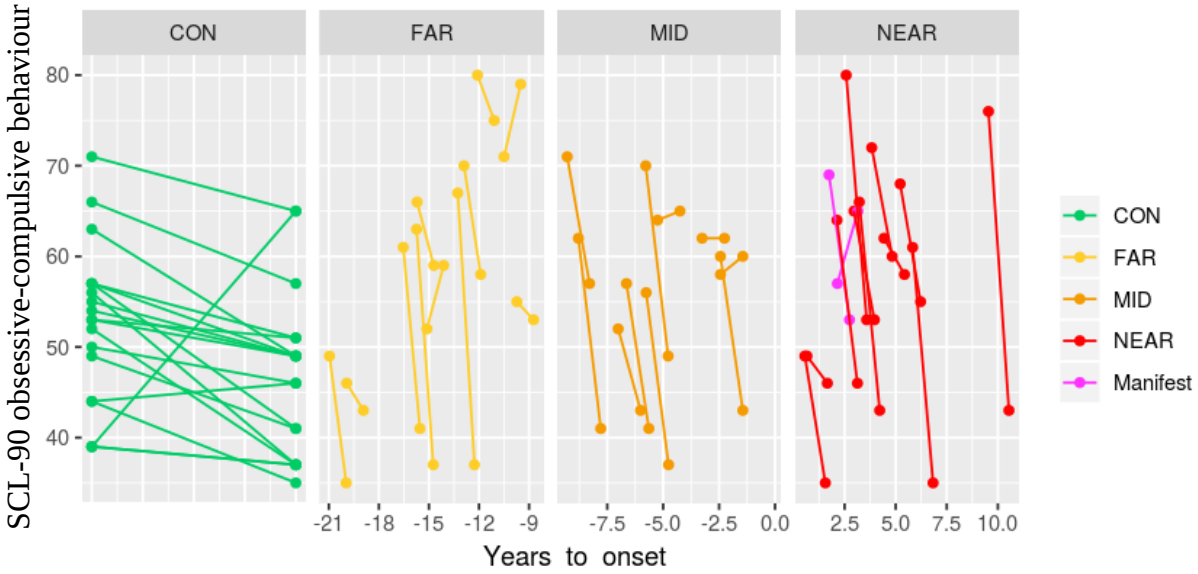

Figure 3.3. Longitudinal change in the obsessive-compulsive behavior scale of the Symptom-Checklist 90.

3.3.3. Group differences in longitudinal changes in questionnaire scores

There was no significant difference across the 4 groups in changes in either cognitive or behavioral scores.

We found a significant effect across the 3 preHD subgroups (FAR, MID, NEAR) on the changes in UHDRS confidence in motor score ($p = 0.0004$), as well as a trend in UHDRS motor and modified motor score ($p = 0.004$ and $p = 0.003$ before correction) (**Figure 3.4**). Post-hoc tests showed that this effect was driven by significant differences between FAR/MID and NEAR, as there was a strong, significant increase

in the UHDRS motor, modified motor, and confidence in motor scores within the NEAR subgroup.

There was no significant difference between all participants with presymptomatic Huntington's disease and healthy controls in the longitudinal change in questionnaire scores between follow-up and baseline (except for the UHDRS score which was only acquired at baseline for the control group).

We found a significant effect across the 3 presymptomatic Huntington's disease subgroups (FAR, MID, NEAR) on the UHDRS motor score ($Chi^2 = 18.493$, $p = 0.010$), UHDRS modified motor score ($Chi^2 = 21.835$, $p = 0.002$), and UHDRS confidence score ($Chi^2 = 27.279$, $p = 1.54E\text{-}04$). Post-hoc tests showed that this effect was mainly driven by significant differences between MID and NEAR groups.

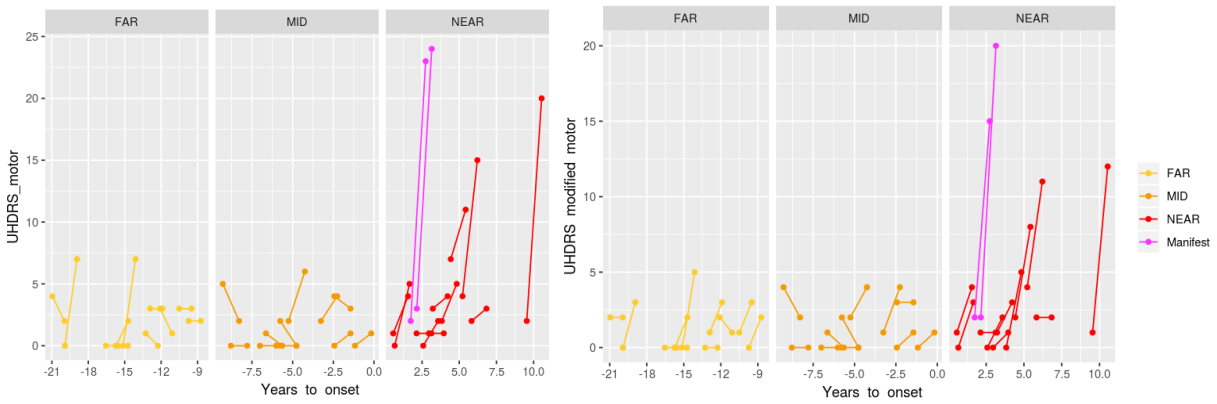

Figure. 3.4. Longitudinal change in the UHDRS motor score and UHDRS modified motor score: from baseline to follow-up, plotted for each subgroup according to their estimated years left to the onset of symptoms.

3.3.4. Correlations between questionnaire scores and diffusion metrics

Finally, we wanted to investigate whether the significant diffusion changes observed across the four groups in the previous analyses (posterior basal ganglia, splenium of the corpus callosum) could be related to changes in motor, cognitive or behavioral scores. Despite the small sample sizes, we found that each group showed meaningful significant correlations ($p < 0.05$, **Figure 3.5**) between changes in questionnaire scores and MD, even though this imaging measure showed both increase and decrease over time depending on the preclinical subgroup. The strongest, significant effects were observed between changes in MD in the splenium of the corpus callosum and changes in phobia and hostility symptoms on the SCL90 for the MID group (Spearman's $\rho = +/-0.86$, $p = 0.001$ for both, **Figure 3.5**).

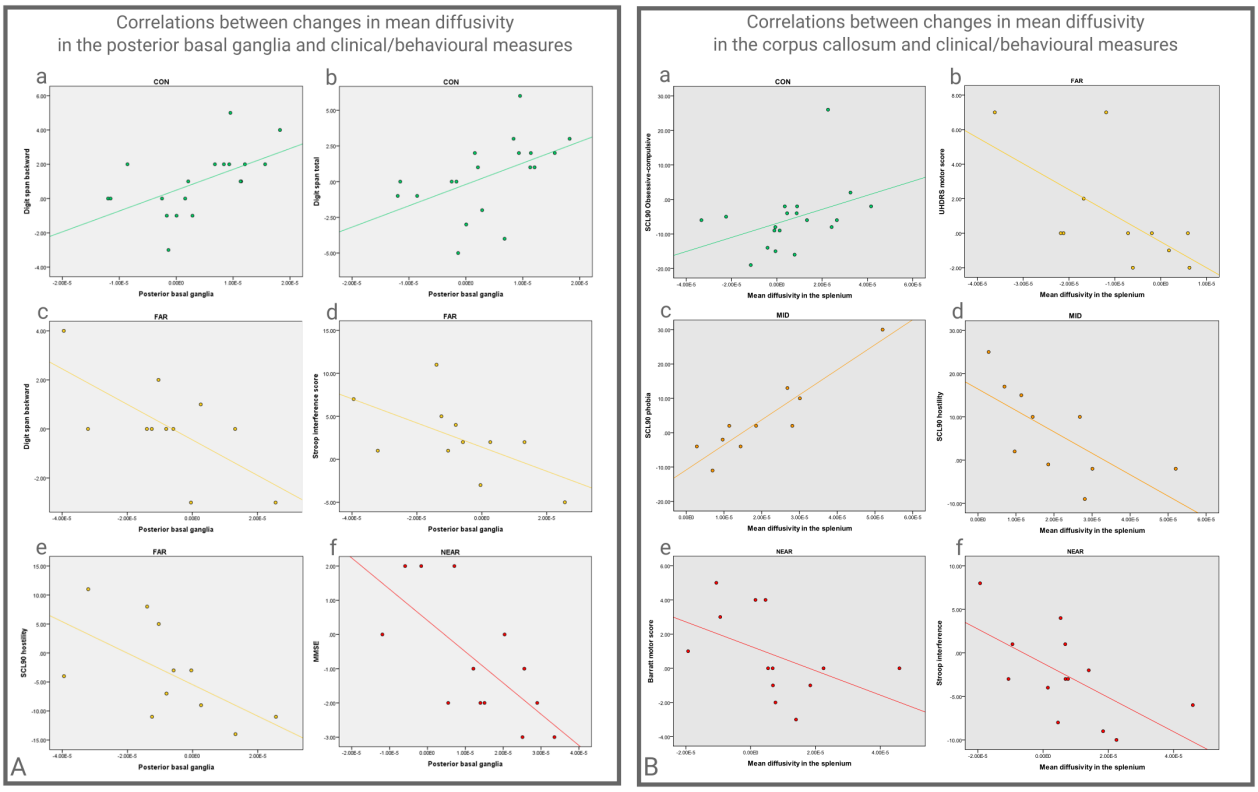

Figure 3.5. Significant correlations (using Spearman's rank correlation coefficient) between changes in cognitive and clinical measures mean diffusivity change in the posterior basal ganglia (A) as well as the splenium of the corpus callosum (B).

3.4. Discussion

In this chapter, we have investigated longitudinal changes in clinical instruments, and questionnaire data, and their association with ROI-based imaging outcomes from the diffusion tensor analyses presented in chapters 1 and 2. A summary of key findings of the present chapter is provided in **Table 3.1**.

Research question	**Analysis approach**	**Key findings**
What is the overall structure of questionnaire scores?	Cross-correlation matrices of questionnaire scores	Longitudinal changes in the preHD group were only weakly correlated with one another, by contrast scores were highly correlated at each timepoint separately
What are the main domains of questionnaire data used in Huntington's disease?	Principal component analysis (PCA) on changes in questionnaire scores	Main two orthogonal axes consisted of psychiatric and motor symptoms respectively
Are clinical and behavioural data sensitive to longitudinal changes at various presymptomatic stages of Huntington's disease?	Group comparisons between years-to-onset groups	Only UHDRS motor scores showed longitudinal sensitiviy and this was mainly driven by an effect seen in the group near the onset of symptoms. Overall questionnaire data are not very sensitive to longitudinal change in preHD.
Are changes in diffusion metrics associated with changes in clinical data?	Spearman correlation analysis	Changes in mean diffusivity in the posterior basal ganglia and splenium of the corpus callosum showed high correlations with changes in clinical scores.

Table 3.1. Key findings of the present chapter.

Whereas we have seen in the previous chapters that diffusion MRI has an exceptional high sensitivity to longitudinal changes, only the UHDRS motor-related measures were able to distinguish clinical stages due to a sharp increase in scores in NEAR (FAR/MID vs NEAR). In contradistinction to the diffusion imaging data, clinical/behavioral scores could not detect any longitudinal changes between FAR, and MID, therefore they are most likely not sensitive enough to detect the optimal time-frame for potential novel treatment options, which most likely corresponds to neuroinflammtory stages of the disease (somewhere in between FAR and MID). It should be noted that such a lack of longitudinal sensitivity in clinical/behavioral data might be due to a floor effect since one year might be a too short time-frame to detect any effect, and clinical instruments might hit the noise floor as latent changes were too small to detect. Indeed, overall group differences in some questionnaire scores were only detectable cross-sectionally at baseline (e.g SCL90-GSI. $p = 0.014$, SCL90-PSD $p = 0.009$, SCL90-PST $p= 0.012$, see appendix). Another factor explaining the lack of longitudinal group differences might be the fact that test-retest effects occurred across all groups (e.g. SCL-90 obsessive-compulsiveness).

In contrast to our longitudinal findings, a previous longitudinal study found significant increases in various SCL-90 scores over a period of 10 years in a much

larger sample (N > 1000), that were more pronounced in a group near the onset of symptoms (Epping *et al.*, 2016). This discrepancy with the findings of the present study might be due to differences in sample size, and differences in the time period that lead to floor effects in the psychiatric assessment tool. Both studies showed that the SCL-90 tool is prone to test-retest effects that were seen in the control group (negative slopes).

The cognitive test instruments might be more useful as clinical tools after diagnosis, and not sensitive to changes in presymptomatic patients. Indeed, previous longitudinal research in early clinical Huntington's disease showed significant longitudinal changes the Stroop test, and digit span test (Ho *et al.*, 2003; Beglinger *et al.*, 2010).

When trying to explain the observed longitudinal changes in the preHD group as a linear combination of test scores, we found that the first two orthogonal axis that explained most of the variance, were corresponding to the motor dimension, and then psychiatric dimension of symptoms. This multivariate approach further shows that motor and psychiatric symptoms are probably the main dimension when investigating presymptomatic Huntington's disease.

When looking at the association between neuroimaging and clinical/cognitive data, both gray and white matter imaging results correlated with changes in distinct clinical and behavioral measures in every single presymptomatic group (even given the small sample size for each group), despite mean diffusivity showing both increase and decrease over time depending on the stage of the disease investigated. The signs of these correlations also seemed to confirm the deleterious nature of both the initial decrease of mean diffusivity at the earliest stage of the disease, and its increase seen at later stages.

In conclusion, we have found that in this particular study diffusion imaging metrics had a higher sensitivity to longitudinal changes, when compared with clinical, and behavioral data. Nonetheless, clinical and cognitive measures proved to be valuable, when used to provide more information that can help explain the changes seen in diffusion metrics.

Part II. Ultra high-field Diffusion MRI in early Huntington's and Parkinson's disease

II.0. Introduction

II.0.1. Introducing Parkinson's disease

Parkinson's disease is the second most common progressive, neurodegenerative disease after Alzheimer's disease (Hague, Klaffke and Bandmann, 2005). In his classic 1817 monograph "Essay on the Shaking Palsy" James Parkinson described the motor symptoms of the disease, for which his name is eponymous today, as follows: "Involuntary tremulous motion, with lessened muscular power, in parts not in action and even when supported; with a propensity to bend the trunk forwards, and to pass from a walking to a running pace" (Parkinson, 2002). Parkinson's disease is a hypokinetic-hypertonic movement disorder of the basal ganglia that is characterized by the classical triad of rest tremor, limb rigidity, and bradykinesia or hypokinesia. The precise etiology of Parkinson's disease is unknown, but both environmental factors and genetic factors have been identified (Poewe *et al.*, 2017).

The neuropathological hallmark feature of Parkinson's disease is a loss of dopaminergic neurons in the substantia nigra, pars compacta, which results in a depletion of dopamine in the striatum, to which these neurons project (Lotharius and

Brundin, 2002). The molecular neuropathological mechanism involves the intracellular accumulation of widespread α-synuclein aggregates, that form characteristic Lewy bodies (Lotharius and Brundin, 2002; Poewe *et al.*, 2017).

There are various pharmacological treatment option available for the treatment of Parkinson's disease, including L-DOPA with augmentation (e.g. carbidopa), novel dopamine receptor agonists, MAO-B and COMT inhibitors (Chen and Swope, 2007). Besides pharmacotherapy, stereo-tactic surgery or deep brain stimulation of the subthalamic nucleus, or the globus pallidus, pars interna, are used as invasive treatment options.

Several diffusion imaging studies showed that FA in the substantia nigra was lower in patients with PD compared with healthy controls (Yoshikawa, 2004; Chan *et al.*, 2007a; Vaillancourt *et al.*, 2009a). It has also been shown that lower FA was associated with higher disease severity (Chan *et al.*, 2007a).

PD and HD represent two opposite aspects of basal ganglia disorders, in that they show the opposite symptomatology, and are characterized by an inverse dysbalance in the inhibitory activity of the basal ganglia circuits. Based on the knowledge about the cortico–striato–thalamo–cortical feedback loops, it was proposed that symptoms in PD and HD could be explained by an imbalance between indirect and direct

pathways: this model suggests that the degeneration of nigrostriatal dopaminergic neurons found in PD leads to an increase in the activity of indirect pathway, and decreases in activity of the direct pathway (Nelson and Kreitzer, 2014). This relative over-activity of the indirect pathway is a putative neuropathological mechanism underlying the hypokinetic-hypertonic symptoms found in PD. By contrast, in HD medium-size spiny neurons of the neostriatum degenerate, resulting in decreased activity of the indirect pathway (Albin *et al.*, 1990; Deng *et al.*, 2004a; Nelson and Kreitzer, 2014). The resulting predominance of the direct pathway was used as an explanation for the hypokinetic-hyertonic symptoms in HD. Most of the evidence for such a dualistic model stems from animal tracing and electro-physiological studies, and further research in humans is needed to investigate the validity of such a model in humans.

II.0.2. Introducing ultra-high-field diffusion MRI at 7T

Magnetic resonance imaging at higher field strengths, such as 7T, can be used to increase the magnetic resonance signal, and thereby increase the resolution and the image contrast. The signal-to-noise ratio (SNR) of MRI images is proportional to the magnetic field strength of the static magnetic field B_0. Even though it is possible to increase the resolution of MR images at lower field strengths, this would result in a drop in the SNR, simply because the number of nuclear spins, i.e resonating hydrogen nuclei (H^+), within each voxel is lower at higher resolutions. At lower field strengths, this drop in SNR can be compensated by averaging over several images, resulting in longer acquisition times. However, using ultra-highfield 7T MRI it is possible to preserve a good SNR even at high resolutions. Indeed, recent research has shown that the SNR of diffusion tensor imaging data is increased at 7T, and that the uncertainty in diffusion tensor image fit, and the principal eigenvector was decreased (Polders *et al.*, 2011).

7T MRI has been successfully applied to study various neurological diseases to investigate them in more detail due to its increased resolution. For example in Parkinson's disease spatial variations in susceptibility with the substantia nigra, pars compacta, revealed a rostrocaudal gradient, as well as significant differences when compared with healthy controls (Lotfipour *et al.*, 2012).

Using 7T MRI is has become feasible to visualize brain structures that could previously only be identified in ex-vivo research of post-mortem specimens, or in non-human primates. The deep cerebral and cerebellar nuclei affected by Huntington's and Parkinson's disease are inherently small. Previous research showed that the subthalamic nucleus could only be successfully identified using 7T structural MRI data, but not at 3T (Forstmann *et al.*, 2010), and the boundary between the STN and SN could only be visualized and identified using 7T susceptibility-weighted data (Abosch *et al.*, 2010). Similarly, the boundary between the globus pallidus, pars externa, and the globus pallidus, pars interna, that is formed by a small a fiber tract, i.e. the internal medullary lamina (lamina pallidi medialis), could only be identified using 7T MRI (Abosch *et al.*, 2010). Using tractographic analysis of diffusion MRI data at 7T it has also become possible for the first time to reconstruct the white matter bundles that are part of the basal ganglia pathways in healthy control subjects (Lenglet *et al.*, 2012).

Despite its potentials in neurological research, 7T diffusion MRI has several limitations. The increased B_0 field-strengths results in shorter transverse relaxation times T2 and effective transverse relaxation times $T2^*$, and in increased B_1^+ inhomogeneities that can increase the bias field (Vu *et al.*, 2015). This results in

signal loss in the cerebellum and in the temporal lobes. The shortening of the T2 relaxation times also result in a decrease in the SNR in diffusion-weighted images (Vu *et al.*, 2015). In addition, increased field strength results in an increase in susceptibility-artefacts, and in geometric distortions.

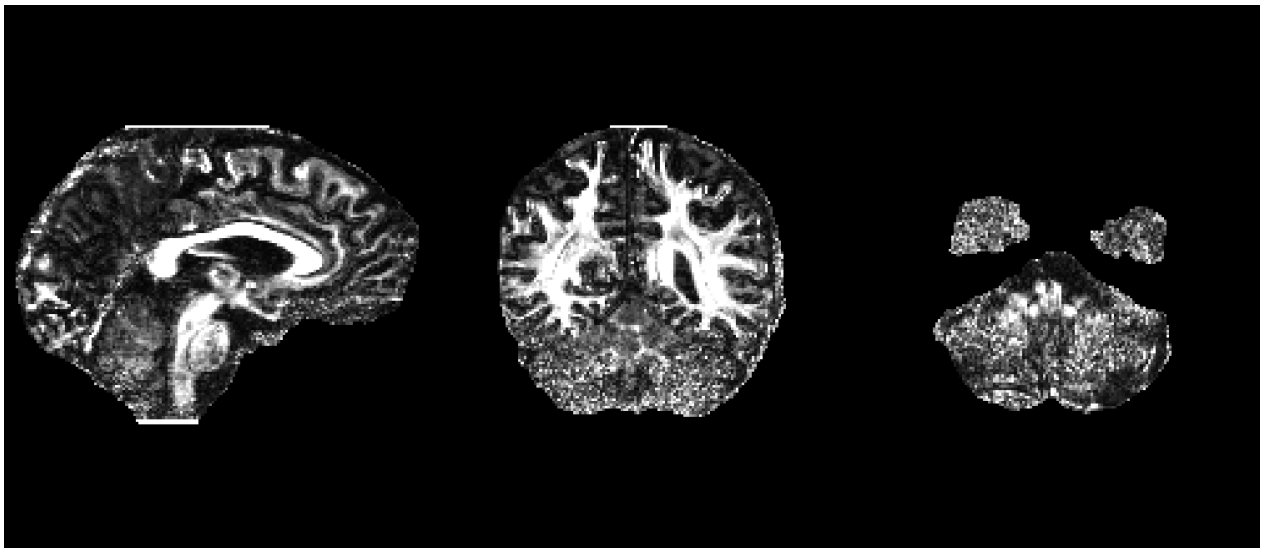

Figure II.1. 7T MRI fractional anisotropy image of a single subject. The cerebellum clearly shows signal dropout.

Chapter II.4: Comparison of the gray matter micro-structure in early Huntington's and Parkinson's disease using ultra high-field diffusion MRI

4.0. Abstract

Rationale. Huntington's and Parkinson's disease are movement disorders with opposing symptom characteristics, i.e. hyperkinetic-hypotonic vs. hypokinetic-hyertonic respectively. In both diseases post-mortem research revealed a clear involvement of the basal ganglia, with a degeneration of medium-size spiny neurons in Huntington's disease, and degeneration of the substantia nigra loss of nigro-striatal input in Parkinson's disease. Using non-invasive high resolution 7Tesla MRI it has now become feasible for the first time to investigate alterations in the tissue microstructure of the basal ganglia and associate nuclei, including very small deep cerebral nuclei, such as the internal segment of the globus pallidus and the dentate nucleus of the cerebellum.

Objectives. To investigate micro-structural alterations in the basal ganglia and associated deep cerebral/cerebellar nuclei including the substantia nigra, the subthalamic nucleus, the thalamus, and the dentate nucleus of the cerebellum in patients with early Huntington's and early Parkinson's disease compared with age-/gender matched controls.

Methods. Gaussian modeling of diffusion data was used to fit a diffusion tensor to the diffusion data at each voxel, and statistical inference was carried out on the resulting mean diffusivity and fractional anisotropy maps using a mask of the deep cerebral nuclei for small volume correction.

Results. A conjunction analysis testing for brain regions that show alterations in both patient groups, i.e. patients with Huntington's and Parkinson's diease, was not significant. Patients with Huntington's disease differed in fractional anisotropy form their control group in the right posterior thalamic nuclei. There as trend towards significance for alterations in mean diffusivity in the dentate nucleus in patients with Parkinson's disease and their matched control group in the dentate nucleus. Diffusion metrics were correlated with dimensionality-reduced UHDRS/UPDRS clinical data.

Conclusions. When investiagting the microstructure of deep cerebal gay nuclei, patients with Huntington's disease and Parkinsons's diease, don't schow similar abnormalities. By contast, distinct nuclei seem to be alterated at early disease stages when comparing them with healthy controls. The dentate nucleus showed alterations in Parkinson's diseases that further hint at its crucial role in the pathophysiology of this disease.

4.1. Introduction

"The disease, respecting which the present inquiry is made, is of a nature highly afflictive. Notwithstanding which, it has not yet obtained a place in the classification of nosologists; some have regarded its characteristic symptoms as distinct and different diseases, and others have given its name to diseases differing essentially from it; whilst the unhappy sufferer has considered it as an evil,from the domination of which he had no prospect of escape."

James Parkinson (1817): An essay on the shaking palsy[1]

Parkinson's disease (PD, synonyms: shaking palsy, paralysis agitans) is a progressive neurodegenerative movement disorder that is clinically characterized by a triad of cardinal motor symptoms, consisting of rigidity (stiff or inflexible muscles), bradykinesia (slowed movements, from greek βραδύς meaning slow, and κίνησις meaning movement), and tremor (shaking) (Samii, Nutt and Ransom, 2004). After Alzheimer's disease, PD is the second most common neurodegenerative disease with a prevalence of 0.5-1% among persons aged 65-69, and 1-3% among persons 80 years of age and older (Schneider and Obeso, 2015a, 2015b). The motor symptoms of PD become progressively worse as the disease advances. The neuropathological hallmark feature of PD is the loss of dopaminergic neurons in the substantia nigra, pars compacta, which results in a depletion of dopamine in the striatum, to which these

1 Parkinson, J. (2002). An Essay on the Shaking Palsy. The Journal of Neuropsychiatry and Clinical Neurosciences, 14(2), 223–236.

neurons project (Lotharius and Brundin, 2002). Several diffusion imaging studies showed that FA in the substantia nigra was lower in patients with PD compared with healthy controls (Chan *et al.*, 2007b; Vaillancourt *et al.*, 2009b). It has also been shown that lower FA was associated with higher disease severity (Chan *et al.*, 2007b). Huntington's and Parkinson's disease are found at the opposite ends of the spectrum of basal ganglia diseases. HD is a hyperkinetic-hypotonic movement disorder, whereas PD is a hypokinetic-hypertonic movement disorder. HD is characterized by excessive movements, whereas in PD movements are reduced, slowed down, and rigid. In PD movements may not be smooth, and patients show resistance towards passive movements of the joints, which is know as cogwheel rigidity. That means a muscle responds with cogwheellike jerks to passive stretching of the muscle as carried out during a physical exam. In the cogwheel phenomen this muscle rigidity is superimposed with the rest tremor. This opposite symptomatology, seen in Parkinson's disease when compared with Huntington's disease, is reflected by antagonistic pathophysiology at the level of the basal ganglia circuits.

More specifically, it was proposed that based on the knowledge about the cortico–striato–thalamo–cortical reentry loops, symptoms in PD and HD could be explained by an imbalance between the indirect and direct pathways of the basal ganglia system that then result in opposite dysfunction of the final common pathway of the

basal ganglia loops, i.e. the internal (medial) segment of the globus pallidus (GPi): this model suggests that the degeneration of nigrostriatal dopaminergic neurons found in PD leads to an increase in the activity of indirect pathway, and decreases in activity of the direct pathway (Nelson and Kreitzer, 2014). This relative over-activity of the indirect pathway results in increased activity of the medial segment of the globus pallidus, and is a putative neuropathological mechanism underlying the hypokinetic-hypertonic symptoms found in PD. By contrast, in HD medium-size spiny neurons of the neostriatum degenerate, resulting in decreased activity of the indirect pathway (Albin *et al.*, 1990; Deng *et al.*, 2004b; Nelson and Kreitzer, 2014), and decreased activity of the final common pathway, the GPi. The resulting predominance of the direct pathway was used as an explanation for the hypokinetic-hyertonic symptoms in HD.

The aim of the present study is to investigate in-vivo micro-structural alterations in the relay nuclei of the basal ganglia re-entry circuits, and associated sub-cortical structures in Huntington's disease (HD), and Parkinson's disease (PD), and compare them with the healthy state using ultra-high-field diffusion MRI at 7T. Due to recent advances in high-field diffusion imaging, such as active shielding, and the improvement of the spatial resolution, it has now become feasible for the first time to distinguish different parts of the basal ganglia system, and investigate their micro-

structure in Huntington's and Parkinson's disease at a previously unprecedented level of detail. Indeed, the small volume of the STN of only 160 mm^3 in humans (Krack *et al.*, 2010), and the small volume of the GPi of 520 mm^3 (male) and 430 mm^3 (female) (Thorner, Lange and Hopf, 1975), require higher resolutions than previously used in clinical research to minimize partial voluming effects and to distinguish them from their neighboring structures, i.e. the substantia nigra, and the lateral segment of the globus pallidus respectively. For example, the subthalamic nucleus (STN) is much easier to distinguish from the substantia nigra (SN) at a resolution of 1.2mm isotropic, compared to at 1.5mm.

4.2. Methods

The present study was aimed at investigating cross-sectional alterations in the diffusion metrics, mean diffusivity (MD), and fractional anisotropy (FA) (Pierpaoli and Basser, 1996) in the basal ganglia and associated deep cerebral nuclei, as well as the dentate nucleus, a deep cerebellar nucleus, in patients with early Parkinson's and Huntington's disease compared with two age- and gender-matched healthy control groups. We have used voxel-wise analysis with small volume correction, because it does not introduce a bias by selection of a specific ROI, and is more suitable to

identify localized effects, that would remain undetected when averaging over many voxels in a large ROI, such as the thalamus.

4.2.1. Participants and study design

Patients were recruited through the Oxford Parkinson's disease centre (OPDC). The study has been approved by the Oxford A Research Ethics Committee (OREC). 12 patients with early HD, and 15 patients with PD took part in the study. Based on the UHDRS criteria 6 participants within the HD group were presymptomatic, 5 were premanifest, and 1 manifest. All PD patients were in stage 1 or stage 2 of the Hoehn and Yahr stages (Hoehn and Yahr, 1967). Since the HD and PD groups differed significantly with respect to their age, we have divided the healthy control group into two groups, which are age- and gender matched for the patients groups (see **Figure 4.1** for a detailed participants chart, and **Table 4.1** for clinical data overview).

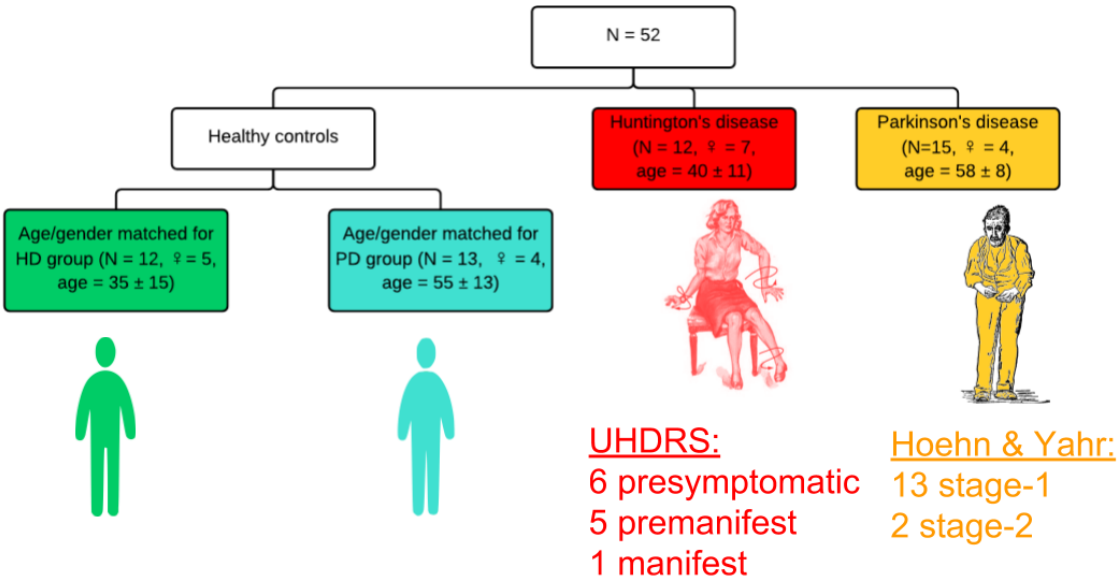

Figure 4.1 Participants chart

	Huntington's disease	Parkinson's disease
Clinical data	6 presymptomatic 5 premanifest 1 manifest	13 medicated 2 unmedicated 14 unilateral 1 bilateral
UHDRS/ UPDRS Total motor score (mean ± SD)	10.3 ± 10.5	20.2 ± 6.4
Total functional capacity	24.7 ± 0.6	NA
Confidence score	1.6 ±1.2	NA

Table 4.1 Clinical data overview.

4.2.2. Data acquisition

MRI data were acquired at the Welcome Centre for Integrative Neuroimaging (formerly: Oxford Centre for functional MRI of the Brain (FMRIB)), John Radcliffe Hospital, University of Oxford using an ultra-highfield (7T) Siemens Magnetom 7T syngo MR B17 MRI scanner. Structural T1-weighted images were acquired using an MPRAGE sequence (TR: 2200 ms, TE: 2.84 ms, TA: 5:25, voxel size: 0.9×0.9×0.9 mm, slice thickness: 0.94 mm, FOV: 240 mm x 240 mm x 166 mm). Proton density images were acquired using an MPRAGE sequence (TR: 1240 ms, TE: 2.84 ms, TA: 3:04 min, voxel size: 0.9×0.9×0.9 mm, slice thickness: 0.94 mm, FOV: 240 mm x 240 mm x 166 mm). Diffusion-weighted images were acquired using a multi-band 2D EPI sequence with GRAPPA acceleration (acceleration factor PE = 2) using 64 diffusion directions (TR: 5382 ms, TE: 68.2 ms, TA: 6:46 min, voxel size: 1.2×1.2×1.2 mm, slice thickness: 1.20 mm, b-value: 1000 s/mm^2, FOV: 192 mm x 192 mm x 125 mm). Diffusion data were collected with reversed phase-encode blips, resulting in pairs of images with geometric distortions going in opposite directions.

4.2.3. Data processing

MRI data were processed using FSL (FMRIB software library, version 5.0.4, FMRIB Analysis group, Oxford University, UK) (Smith *et al.*, 2004; Jenkinson *et al.*, 2012).

4.2.3.1 Pre-processing in native space (Within-subject preprocessing)

Diffusion weighted images were corrected for susceptibility-induced distortions using a method similar to that described in (Andersson, Skare and Ashburner, 2003) as implemented in FSL (Smith *et al.*, 2004). In brief, from pairs of images with reversed phase-encode blips the susceptibility-induced off-resonance field was estimated, and the two images were combined into a single corrected one. Data were simultaneously corrected for eddy-current-induced distortions, and subject movements using the FSL tool eddy (Andersson and Sotiropoulos, 2016). A diffusion-tensor-model was fit at each voxel using the FSL tool dtifit to yield mean diffusivity and fractional anisotropy images.

Proton density images were registered onto each subject's T1 image in native space using FSL tool FLIRT with 6 degrees of freedom. T1 images were then divided by the PD images to yield the final structural image (T1divPD images). This preprocessing step was necessary, because T1-weighted MPRAGE sequences are also

sensitive to proton density contrast, and division by the PD images improved segmentation results. Proton density images were brain extracted using the BET tool with parameters set to f = 0.5 and g = 0, the resulting mask was registered to the T1 image using the matrices from the aforementioned registration, to yield the final brain extraction masks for the T1divPD image. B0 images were registered onto the T1divPD images using linear registrations with 6dof (correlation ratio) (FLIRT), and the resulting transformation matrices were used to register the FA images as well as the mean resting-state EPI images (after linear registration to the B0 images) onto the structural images (T1divPD) for each subject.

The images from several modalities, i.e. T1divPD, mean EPI, FA, and mean B0 images in structural T1divPD space were fed into FSLs Multi-modal Image Segmentation Tool (MIST) (Visser *et al.*, 2016) to automatically segment the basal ganglia nuclei, including the caudate-accumbens, putamen, pallidum, and associated sub-cortical nuclei including the thalamus, subthalamic nucleus, substantia nigra, and dentate nucleus. The resulting segmentations of the dentate nucleus, substantia nigra, and subthalamic nucleus were then manually edited based on the intensity information in the mean functional resting state images, and the pallidum was subdivided into the GPe, and GPi based on the intensity information in the T1 images. The masks were then registered onto the diffusion images, using the inverted

matrices from the linear registrations. In diffusion space, the caudate-accumbens mask, and the thalamus mask were eroded using a spherical Gaussian kernel with a radius of 1.2mm. The putamen was eroded twice using a spherical Gaussian kernel of 1.2mm to reduce partial volume effects at the GM/WM boundary. The caudate-accumbens and putamen were combined to yield the final striatum mask. The GPe and dentate nucleus were thresholded at 0.75, the GPi and SN were thresholded at 0.5, and the STN was thresholded at 0.3. These particular erosion steps and thresholds were used to make sure that these gray matter masks did not extend to much into the white matter, because this would introduce a bias due by partial voluming, and also (as described in more detail in chapters 6 + 7) when using the masks as seeds for probabilistic tractography. These masks were then combined to yield the final mask for the small volume correction for voxelwise statistics. The masks were used to extract MD and FA values from the images in native space during post-hoc exploratory ROI analyses that were carried out if a given effect seen in the voxel-wise statistics needed further explanation.

4.2.3.2. Spatial normalization and preprocessing in standard space

The brain extracted T1divPD images were registered into standard space using the standard VBM preprocessing implemented in FSL. This involved the creation of a GM study template that corresponds to the average GM image across subjects with equal N for all 3 groups (HD, PD, and HC). To avoid misalignment due to signal dropout in the structural images signal dropout masks were created by applying a threshold to the T1divPD images. The warp fields from the VBM registration pipeline were concatenated with the transformation matrices from the B0 registration onto the T1divPD image to yield the final transformation warps used to register the diffusion images from native space to standard space (1x1x1 mm voxel size). Images were smoothed using a Gaussian kernel (sigma = 3).

The masks of sub-cortical nuclei from the multi-modal image registration were transformed into standard space using the VBM warps, and then averaged across subjects and thresholded to yield the small volume correction mask for the voxel-wise analysis of diffusion metrics.

4.2.4. Data analysis

Statistical analyses of extracted imaging data and clinical data were carried out using R (version 3.2.3, The R Foundation for Statistical Computing (2015)), and python's

statistical computing, machine learning packages scipy (Jones *et al.*, no date; McKinney, 2010), and scikit-learn (Pedregosa *et al.*, 2012), as well as python's statistical models package (stats models) (Seabold and Perktold, 2010). Voxel-wise non-parametric permutational statistics were run using the FSL randomise tool (Smith *et al.*, 2004).

4.2.4.1. Inferential statistical analyses

For voxel-wise statistics, permutation-based non-parametric inference (5,000 permutations) was used to test for overall effects of group, differences in mean diffusivity and fractional anisotropy alterations between patients and their age-/gender-matched healthy controls, as well as using one-tailed linear contrast for simultaneous comparisons of multiple patient groups with their age-/gender-matched healthy controls (Nichols and Holmes, 2002). The demeaned age was entered as a covariate of no interest in the model. Results were considered to be significant for $P < 0.05$, and corrected for multiple comparisons using threshold-free cluster enhancement with 3D optimization (Smith and Nichols, 2009). A GLM analysis was carried out to test for differences between single patient groups and healthy control groups, as well as user-defined linear contrasts.

Generalized linear t-contrasts were used to test the null hypotheses that the patient groups, i.e. patients with HD or PD respectively, did not differ when compared with their age-matched controls:

H_0: $\mu(HD) - \mu(HC_{HD}) = 0$

$\mu(PD) - \mu(HC_{PD}) = 0$

We performed a conjunction analysis to test the hypothesis whether any regions of the grey matter mask were affected by both diseases relative to their control groups. This was done by testing for a logical AND on both statistical non-parametric maps for the individual patient group vs. age-matched control groups contrasts, i.e. the correponding null hypothesis is:

H_0: $[\mu(HD) - \mu(HC_{HD}) = 0]$ **AND** $[\mu(PD) - \mu(HC_{PD}) = 0]$.

This is sometimes called the minimum statistic, because inference was performed by calculating the minimum between the correponding 1-P maps for the contrasts HD vs HC_{HD} and PD vs HC_{PD} (Nichols *et al.*, 2005).

Linear contrasts were used to test for interaction effects between the diagnosis and age groups, i.e. if patients with HD differed from patient with PD when compared with their age-/gender matched healthy controls:

H_0: $[\mu(HD) - \mu(HC_{HD})] - [\mu(PD) - \mu(HC_{PD})] = 0$

4.2.4.2. Dimensionality reduction of questionnaire scores using sparse PCA

Sparse Principal Component Analysis (SparsePCA), as implemented in the python machine learning package scikit-learn (Pedregosa *et al.*, 2012) was used to perform dimensionality reduction on the UHDRS, and UPDRS questionnaire scores. Whereas standard PCA decomposes the data into linear combinations of principal components, and thereby tries to explain all the variance in the data, making the factor loadings inherently hard to interpret, sparse PCA increases the interpretability of components by constraining factor loadings to be sparse, i.e. by zeroing relatively low and insignificant factor loadings. This was done by imposing an L1-norm constraint on the factor loadings (Mairal *et al.*, 2009). Sparse PCA was run using the following setting: alpha (amount of sparsity) = 2, maximum number of iterations = 10,000, method to solve the lasso problem: least angle regression method to solve the lasso problem, number of components = 10, ridge alpha = 0.01, tolerance = 1e-08.

4.2.4.3. Dimensionality reduction of questionnaire scores using exploratory factor analysis

Besides sparse PCA, we have also used exploratory factor analysis as implemented in python's scikit-learn package to reduce the dimensionality of the UHDRS and UPDRS questionnaire scores. When compared with sparse PCA, factor analysis has the potential to retain more of the variance in the data, but this is usually at the expense of lower interpretability. In brief, factor analysis assumes that the UHDRS/UPDRS questionnaire scores are caused by linear transformations of lower dimensional latent factors, and random Gaussian noise. The factor analysis algorithm performs a maximum likelihood estimate of the so-called loading matrix (questionnaire scores by components matrix), the transformation of the latent variables to the observed ones, using expectation-maximization. Factor analysis was run with the following settings: number of components = 10, stopping tolerance for EM algorithm = 1e-15, maximum number of iterations = 1,000,000.

4.2.4.4. Post-hoc correlation analysis between neuroimaging data and sparse PCA/factor analysis components

We have run post-hoc correlations between extracted diffusion metrics from the significant/trend voxel-wise clusters, and the sparse PCA/factor analysis components for each patient group separately. The spatial maps of the significant/trend voxel-wise statistics were binarized, and used to calculate the average of the diffusion metric over all voxels within the map. D'Agostoni-Pearson K^2 test was used to test if the data were normally distributed. We have used Pearson's product moment correlation for normally distributed data, and Spearman's rank order correlation for non-normally distributed data.

4.3. Results

4.3.1. Voxel-wise comparisons of diffusion metrics

4.3.1.1. Linear contrasts comparing multiple patient groups with age-/gender-matched healthy controls

Voxel-wise comparisons of mean diffusivity or fractional anisotropy did not reveal any brain regions where both patient groups conjointly differed from their matched control groups., i.e. the patient group with Huntington's disease compared with their matched controls, AND the patient group with Parkinson's disease compared with their matched controls (lowest corrected $p = 0.214$ for mean diffusivity, lowest corrected $p = 0.605$ for fractional anisotropy).

No significant differences in mean diffusivity alterations or fractional anisotropy alterations were found when testing for the main effect of having a motor diagnosis, ie. when comparing both patients with HD and PD with their matched healthy controls ($p = 0.146$ for mean diffusivity, and $p = 0.614$ respectively).

4.3.1.2. Comparing single patient groups with their age-/gender matched healthy controls

There was a trend towards higher mean diffusivity in HD compared with their age-/gender matched controls in the caudo-ventral part of the basal ganglia including the GPi/GPe (corrected p = 0.074, **Figure 4.2**). Significant lower fractional anisotropy was found in the right posterior thalamic nuclei group in patients with HD compared with their matched controls (corrected p = 0.044, **Figure 4.3**). To further explore the neuroanatomical implications of these findings we have used the significant cluster as a seed for probabilistic tractography, and found that this part of the thalamus is predominantly connected with the temporal lobe through the inferior thalamic radiation (**Figure 4.4**).

There was a trend towards higher mean diffusivity in the left dentate nucleus in Parkinson's disease compared with their matched controls (p = 0.053, **Figure 4.5**). To further explore the neuroanatomical implications of this finding we have used the significant cluster as a seed for probabilistic tractography, and found that this part of the dentate nucleus is predominantly connected with the subthalamus, thalamus, and the tegmentum of the mesencephalon through the brachium conjunctiuvum (superior cerebellar peduncles, **Figure 4.5**).

Since the dentate nucleus is a brain region where individual voxels can sometimes be a bit noisy, we have also used a region of interest analysis using the masks of the dentate nucleus from the MIST segmentation that were manually edited on the mean functional images to remove white matter voxels. This additional ROI analysis was carried out, because averaging over several voxels should decrease the noise, and increase the sensitivity to detect any effect. There was a significant difference in mean diffusivity in the dentate nucleus when comparing patients with PD with their age matched controls ($p = 0.0048^{**}$). No significant differences between groups were found for the other contrasts (all $p > 0.05$, see **Figure 4.6**).

Voxel-wise comparisons of fractional anisotropy did not reveal any significant differences between patients with PD and their matched healthy controls ($p = 0.071$).

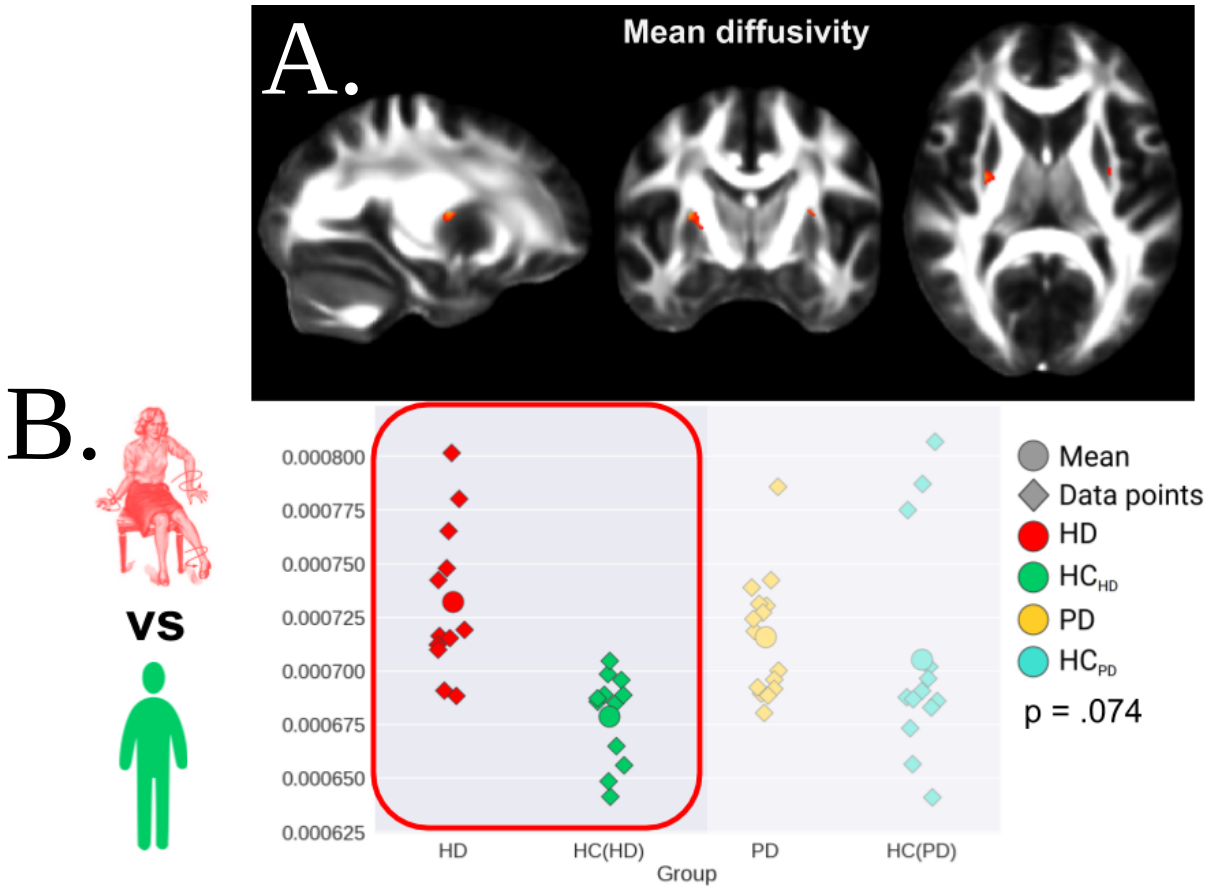

Figure 4.2. Trend towards lower mean diffusivity in patients with Huntington's disease compared with their age-/gender-matched healthy controls in the bilateral GPi/GPe. A. Statistical non-parametric map showing the trend in orange-red overlaid on the average FA image across all subjects in standard space. B. Dispersion plots showing the average mean diffusivity over all trend voxels of the voxel-wise map (shown in A) for the contrast HD vs. age-/gender-matched HC. The red frame indicates the trend effect found in the voxel-wise analysis of diffusion metrics.

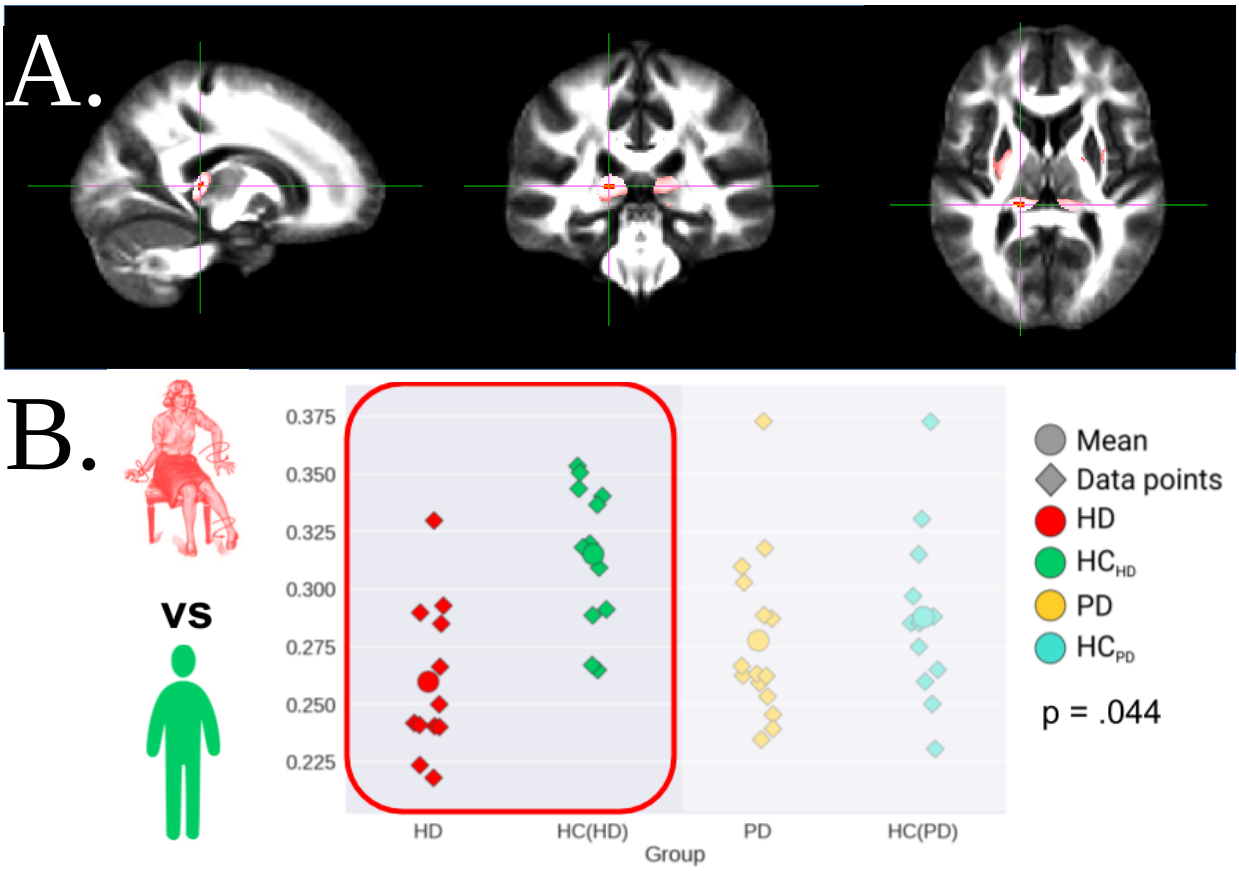

Figure 4.2. Significant lower fractional anisotropy in patients with Huntington's disease compared with their age-/gender-matched healthy controls in the right posterior thalamic nuclei. A. Statistical non-parametric map showing the significant effect in the posterior thalamic nuclei in red and the uncorrected voxel-wise map including the bilateral posterior thalamus, and right globus pallidus in pink, overlaid on the average FA image across all subjects in standard space. B. Dispersion plots showing the average fractional anisotropy over all significant voxels of the voxel-wise

map (shown in A) for the contrast HD vs. age-/gender-matched HC. The red frame indicates the significant effect found in the voxel-wise analysis of diffusion metrics.

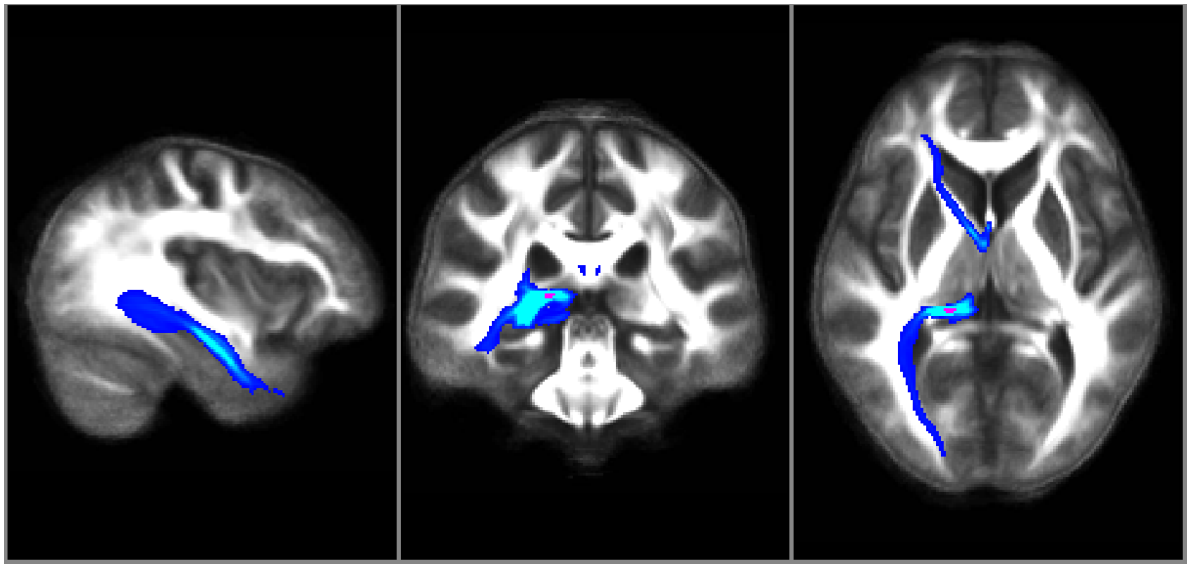

Figure 4.3. Probabilistic tractography using the significant cluster from the comparison between patients with HD and healthy controls as a seed (shown in pink), showing that this region is mainly connected with the superior and middle temporal gyri through the inferior thalamic radiation (reconstructed in blue). (Note that a minor rostral part of this reconstruction, only visible on the axial slice is neuroantomically part of the limbic system and goes through the fornix. This is most likely neuroanatomically a false positive tract).

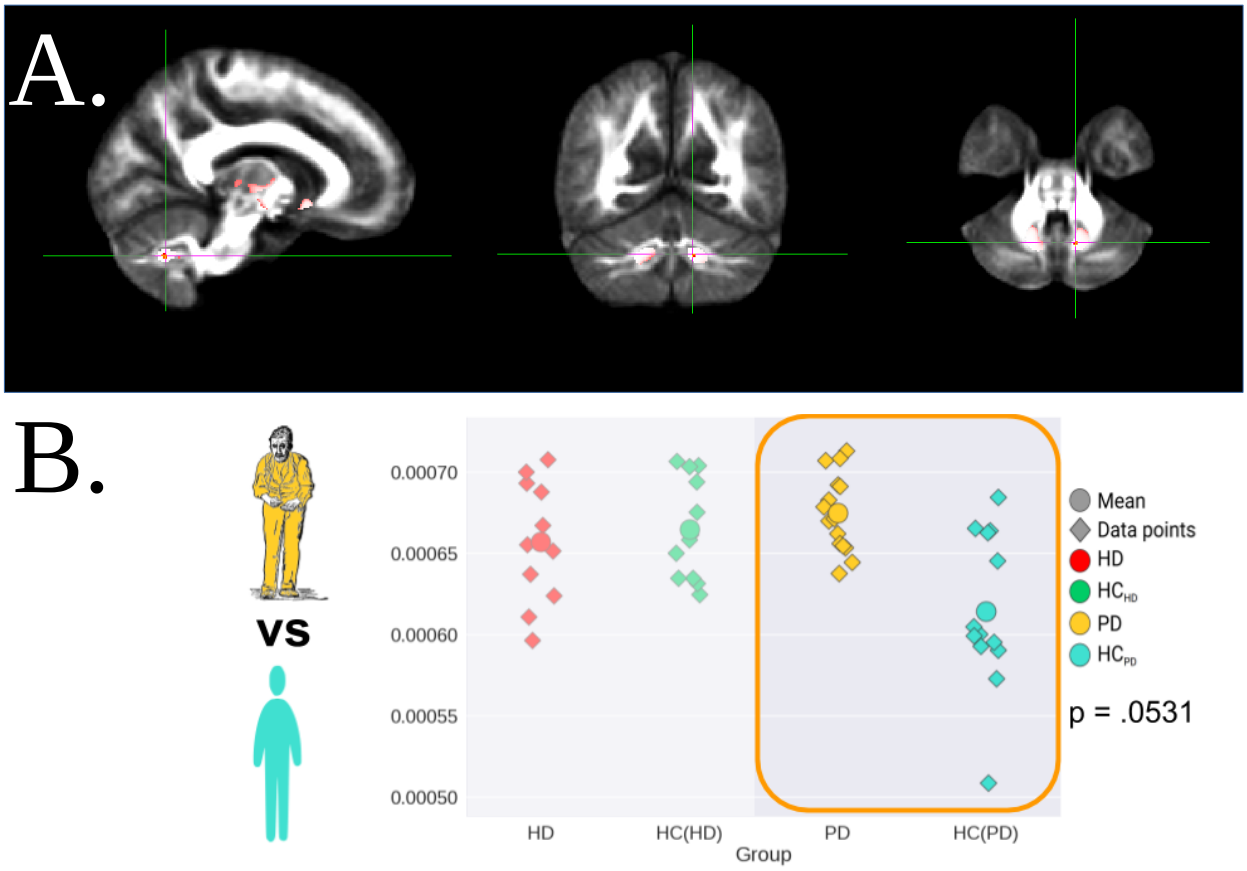

Figure 4.4. Trend towards higher mean diffusivity in the left dentate nucleus in patients with Parkinson's disease compared with their age-/gender matched healthy controls. A. Statistical non-parametric map showing the trend in the left dentate nucleus, thresholded at p = 0.55, corrected for multiple comparisons using TFCE in red, and the uncorrected voxel-wise map including the bilateral dentate nucleus in pink, overlaid on the average FA image across all subjects in standard space. B. Dispersion plots showing the average mean diffusivity over all voxels thresholded at p = 0.1 (as shown above) for the contrast PD vs. age-/gender-matched HC. The orange frame indicates the trend found in the voxel-wise analysis of diffusion metrics.

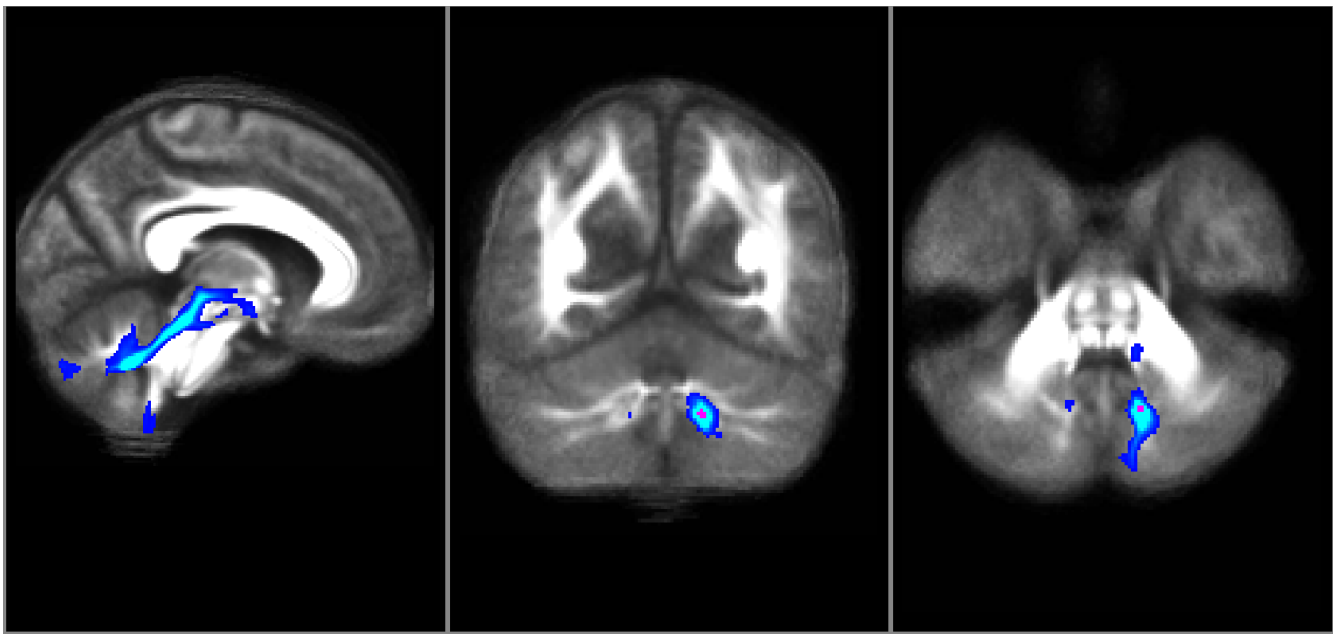

Figure 4.5. Probabilistic tractography using the significant cluster from the comparison between patients with PD and healthy controls as a seed (shown in pink), showing that the dentate nucleus is mainly connected with the subthalamic regions of the diencephalon, and the tegmentum of the mesencephalon through the brachium conjunctivum (superior cerebellar peduncle, shown in blue-lightblue).

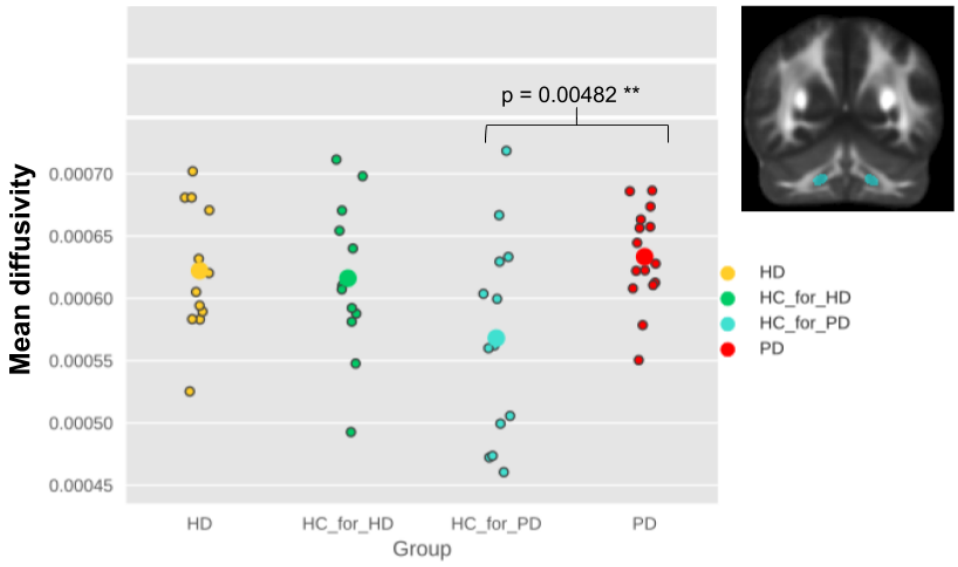

Figure 4.6. Mean diffusivity in the dentate nucleus showing a significant difference between the Parkinson's disease group and their age-matched controls.

4.3.2. Sparse PCA of UHDRS and UPDRS questionnaire scores

4.3.2.1. Decomposition of UHDRS and UPDRS questionnaire scores into sparse main components

Sparse PCA of UHDRS could not clearly distinguish between motor, neuropsychiatric, and cognitive components underlying the observed questionnaire scores. Most components showed high loadings on at least two of these three main symptomatic dimensions (see **Figure 4.8**).

The first UHDRS component had high loadings on questionnaire scores that are indicative of problems with activities of daily living, including various functional capacity scores, and psychiatric symptoms of disoriented and angry behavior, as well as a smaller group of questionnaire scores measuring oro-bucco-lingual and occular motor symptoms. The second component showed high loadings on motor symptoms including chorea and dsytonia, and a smaller group of loadings on questionnaire scores associated with behavior initiation such as apathy, and perseverance. The third UHDRS component predominantly comprises neuropsychiatric symptoms associated with mood disorders, that are also associated with impaired horizontal eye movements. The fourth UHDRS component showed high loadings on questionnaire scores including movement rigidity, postural stability, and irritability as a psychiatric symptom. Components 5, 8, and 9, only showed few loadings on questionnaire scores,

so we post-hoc decided to discard these components from further analyses. The sixth component shows high loadings on various cognitive scores, and interestingly the Lurija motor assessment which is one of the more cognitive complex motor tasks shows high loadings on this component as well. The 7th UHDRS component shows high loadings on motor assessments involving hand movements, as well as the symbol digit modalities test, which might be due to the fact that this cognitive task involves having the patient do some writing. The 10th UHDRS component showed high loadings on the questionnaire scores covering functional assessment of daily living activities, and verbal intelligence, as well as questionnaires assessing facial and complex motor movements (Lurija).

Since the UPDRS questionnaire mainly covers aspects of motor dysfunction and problems with daily activities seen in Parkinson's disease, it is more difficult to interpret the components as various expressions of motor, cognitive and neuropsychiatric symptoms. Indeed, the psychiatric symptoms of depressed and anxious mood did not load on any of the sparse components. Apathy showed high loadings on component 3, and cognitive impairment showed high loadings on component 7 together with various dysfunctions from the motor domain. Component 8 was only loading on one questionnaire score (rigidity neck), so we post-hoc decided to discard this component from further analyses. Scree-plots showing how much of

the variance is explained by each UHDRS/UPDRS principal component are shown in **Figure 4.7.** A heat-maps of UHDRS/UPDRS questionnaire scores loading on sparse principal components are shown in **Figures 4.8 and 4.9** respectively.

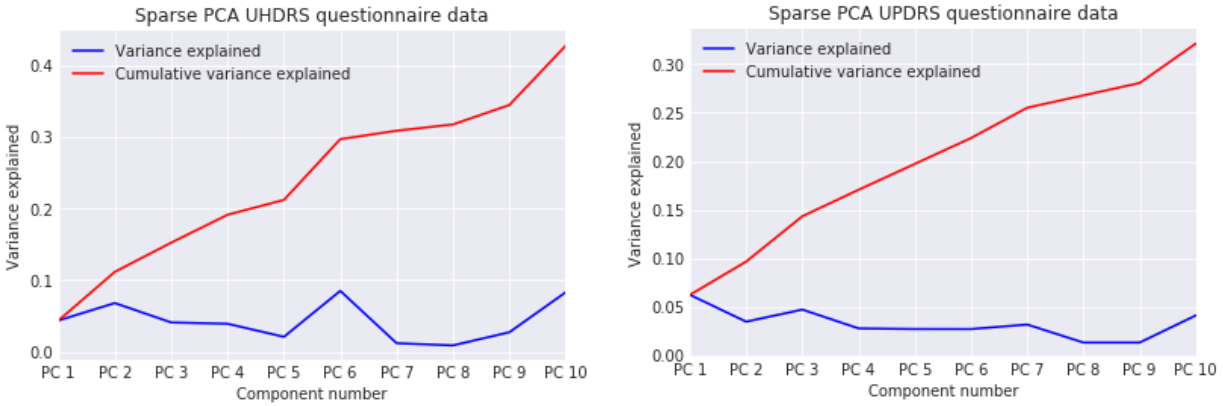

Figure 4.7. Variance explained and cumulative variance explained for sparse principal components extracted from UHDRS questionnaire scores (left), as well as UPDRS questionnaire scores (right).

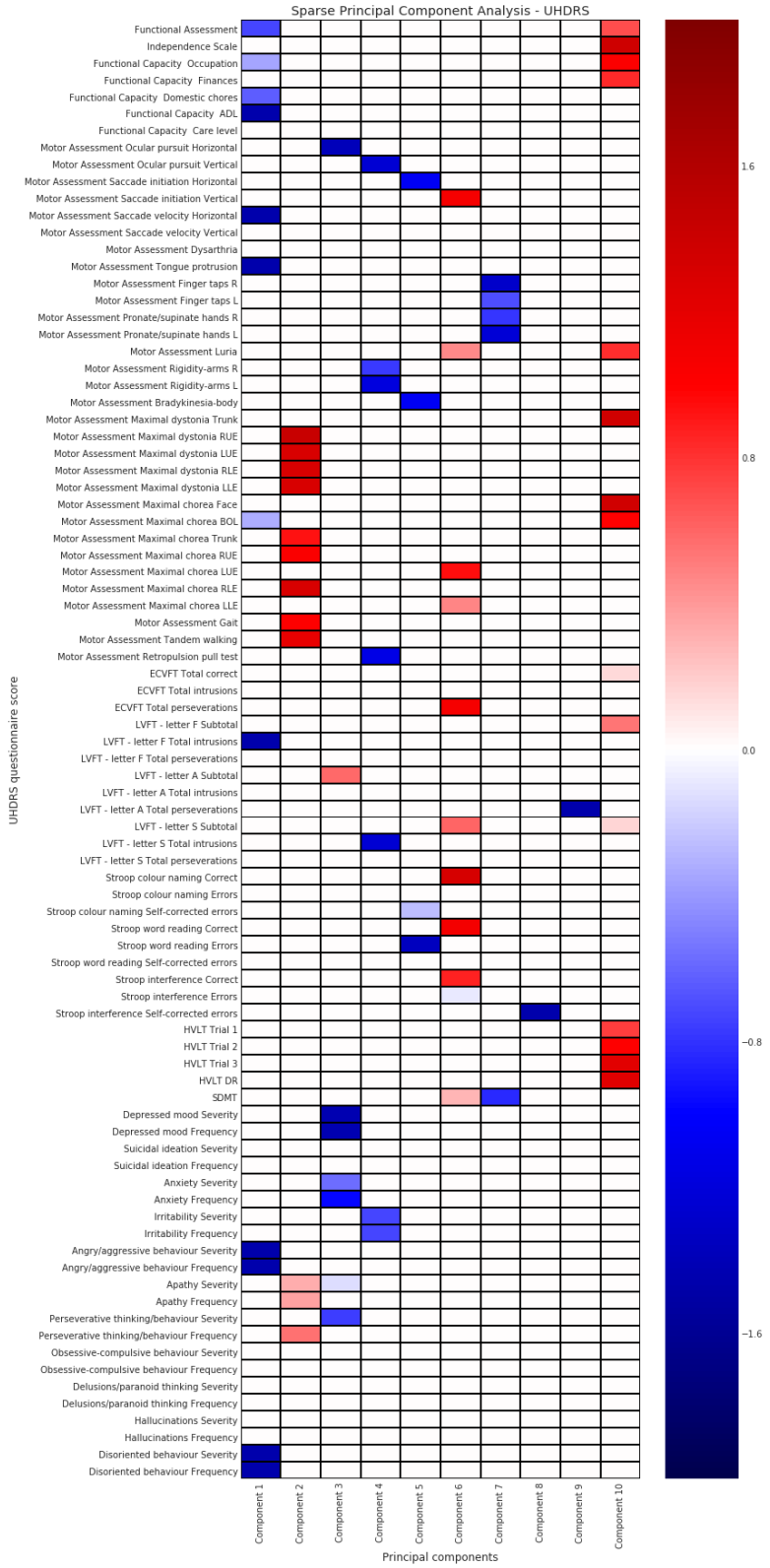

Figure 4.8. Loadings of UHDRS questionnaire scores on sparse principal components.

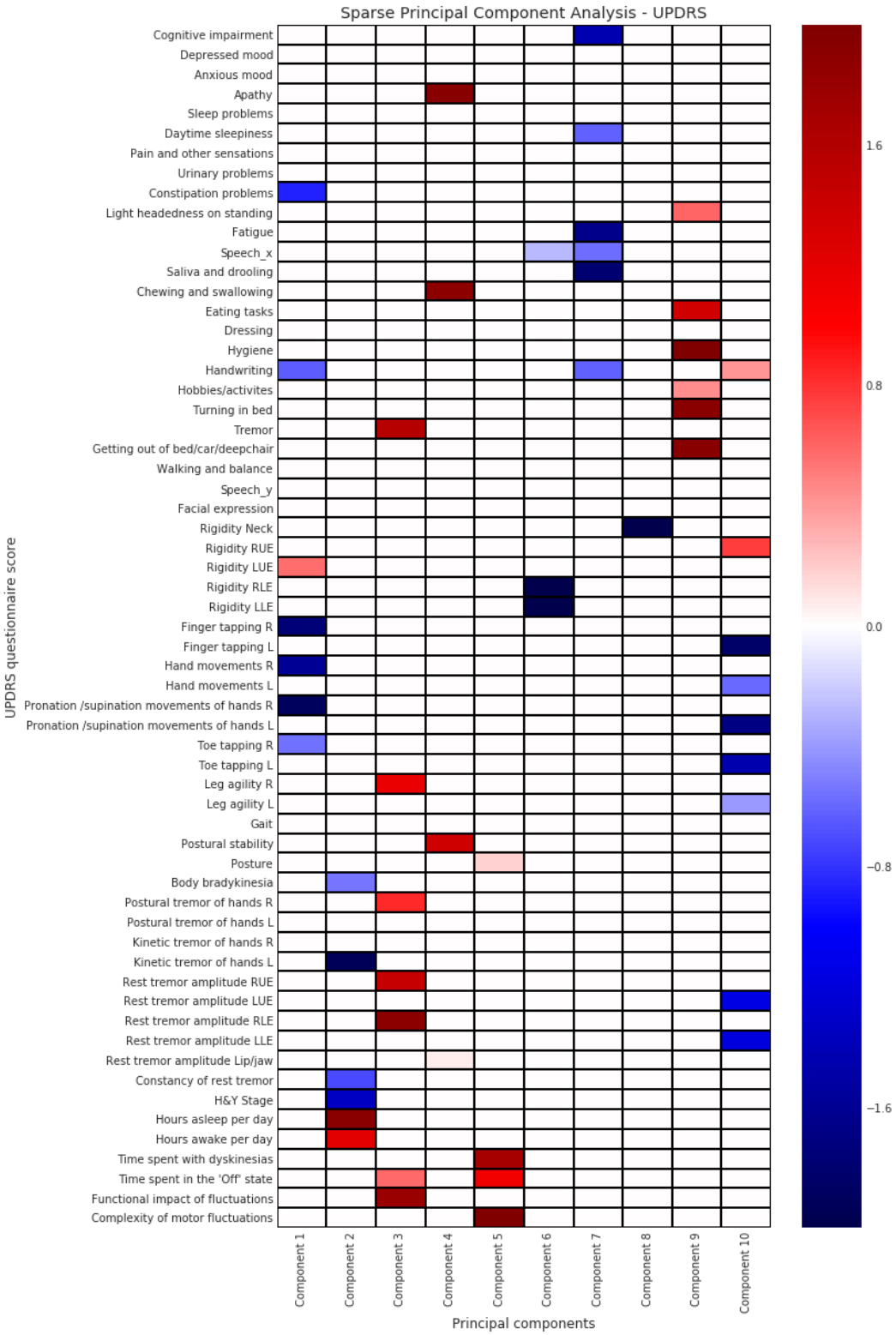

Figure 4.9. Loadings of UPDRS questionnaire scores on sparse principal components.

4.3.2.2. Correlation between imaging outcomes and UHDRS/UPDRS sparse principal components

Finally, we wanted to investigate whether the alterations in diffusion metrics seen in the voxel-wise analysis could be related to the clusters of motor, cognitive or psychiatric symptoms that were revealed using sparse principal component analysis.

There was a significant correlation between MD, extracted from the trend spatial map of the difference in mean diffusivity between HD and HC and UHDRS component 7 (Pearson's $r = -0.679$, $p = 0.015$), as well as UHDRS component 10 (Spearman's $\rho = 0.748$, $p = 0.005$, **Figure 4.10**). No significant correlations were found for the trend difference in mean diffusivity between patients with PD and their matched controls seen in the dentate nucleus.

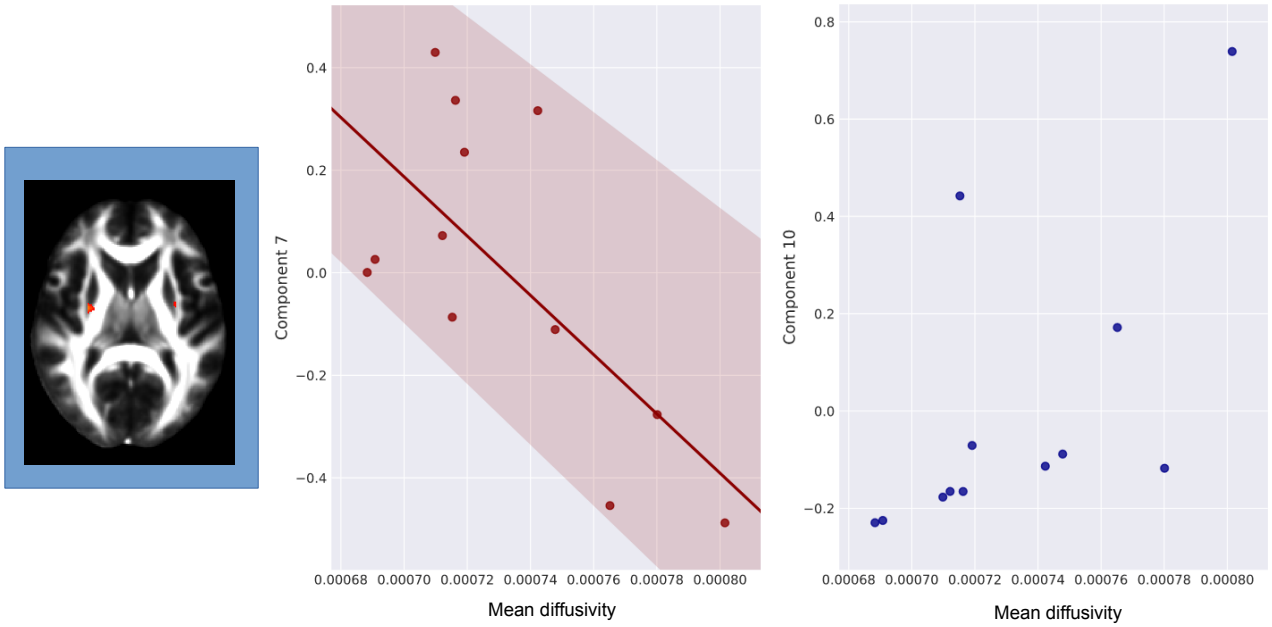

Figure 4.10. Scatter-plots showing the significant correlations between UHDRS sparse principal components 7 (left) and 10 (right) and the average mean diffusivity values across the trend voxel-wise cluster for the comparison between the patient group with Huntington's disease and the healthy control groups (HD < HC) in the caudal part ot the pallidum and GPi/GPe.

4.3.3. Exploratory factor analysis of UHDRS and UPDRS questionnaire scores

4.3.3.1. Decomposition of UHDRS and UPDRS questionnaire scores into latent factors

Using exploratory factor analysis we could retain over 80% of the variance in both UHDRS and UPDRS questionnaire scores, at the expense of lower interpretability when compared with the sparse PCA. Scree plots of the variance explained by each latent variable are shown in **Figure 4.11.** Plots of the factor loadings on latent variables, both unthresholded and thresholded (at 0.4) are shown in **Figures 4.12, 4.13, 4.14, and 4.15.**

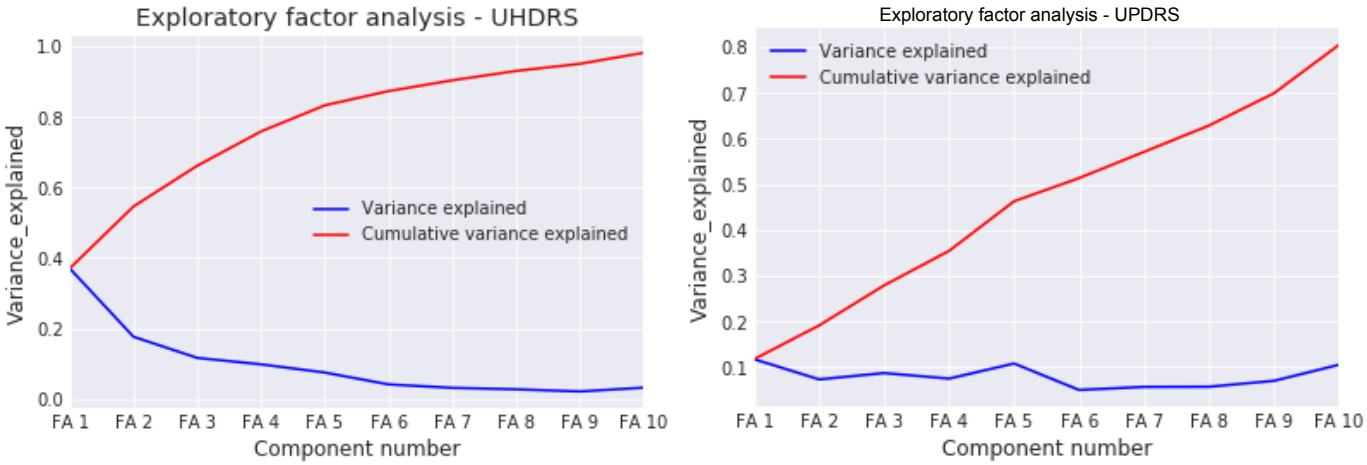

Figure 4.11. Variance explained and cumulative variance explained for latent variables from exploratory factor analysis of UHDRS questionnaire data (left), and UPDRS questionnaire data (right).

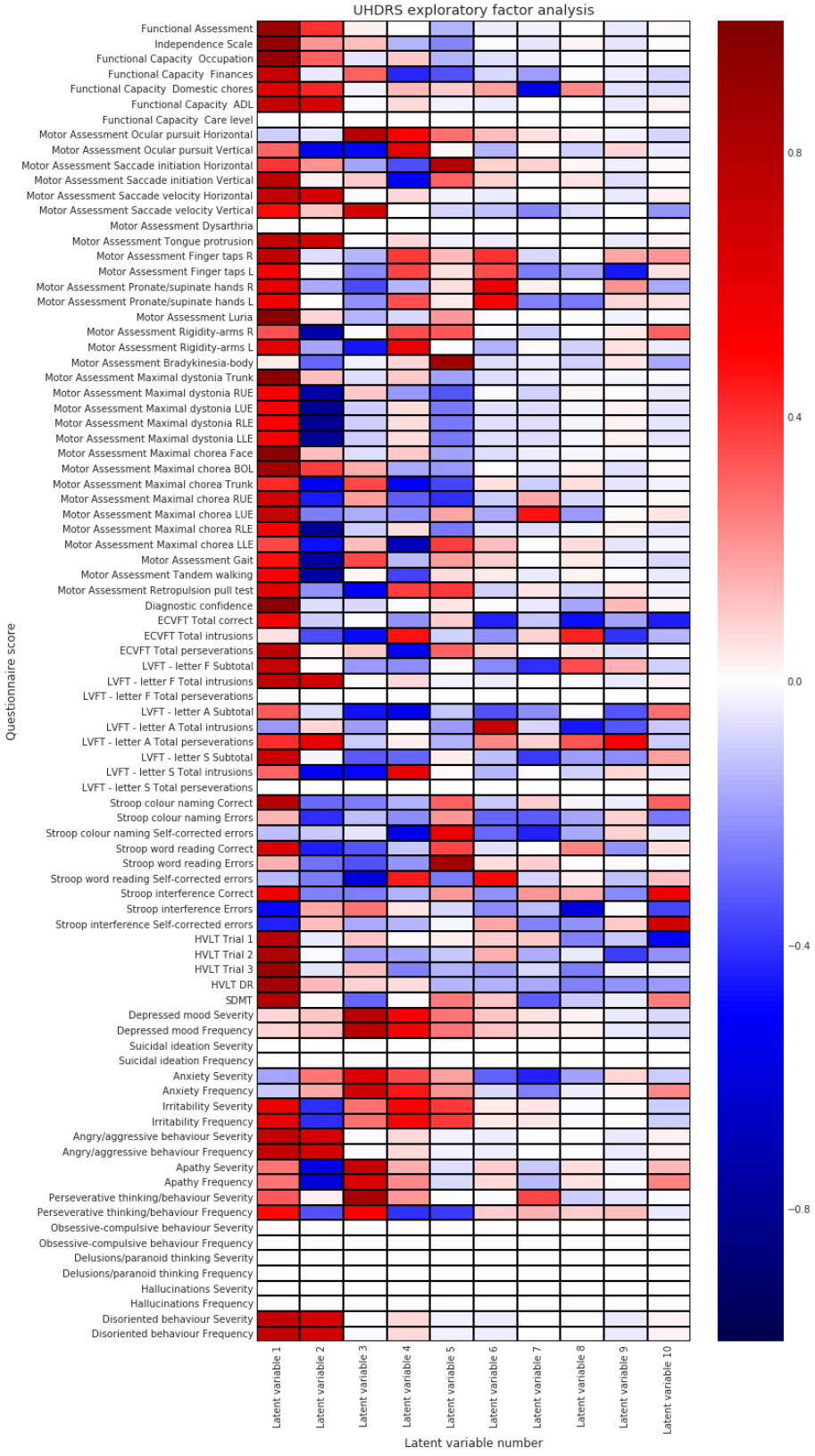

Figure 4.12 Loadings of UHDRS questionnaire scores on exploratory factors.

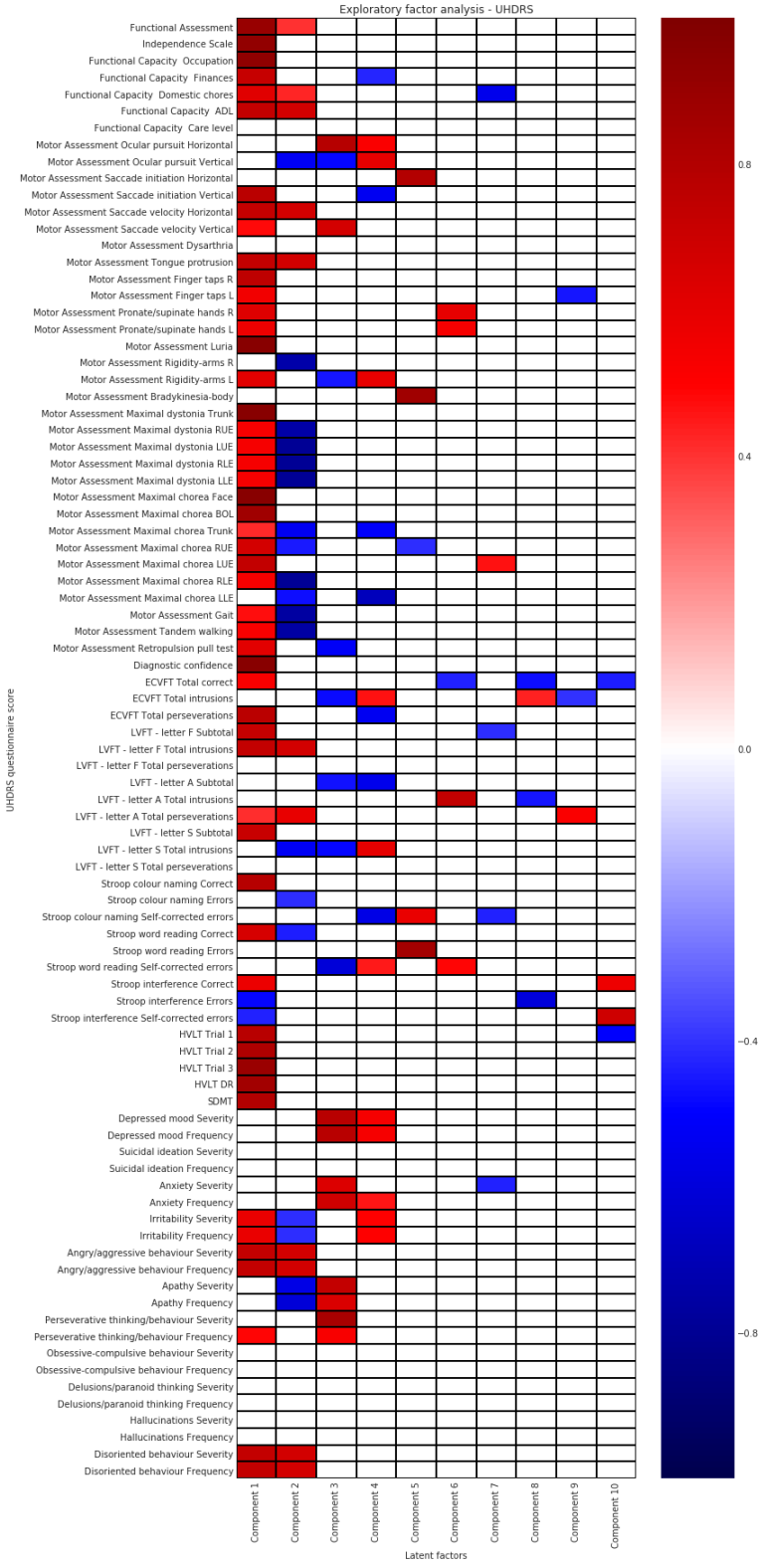

Figure 4.13. Loadings of UHDRS questionnaire scores on exploratory factors (loadings below 0.4 are considered to be insignificant have been thresholded).

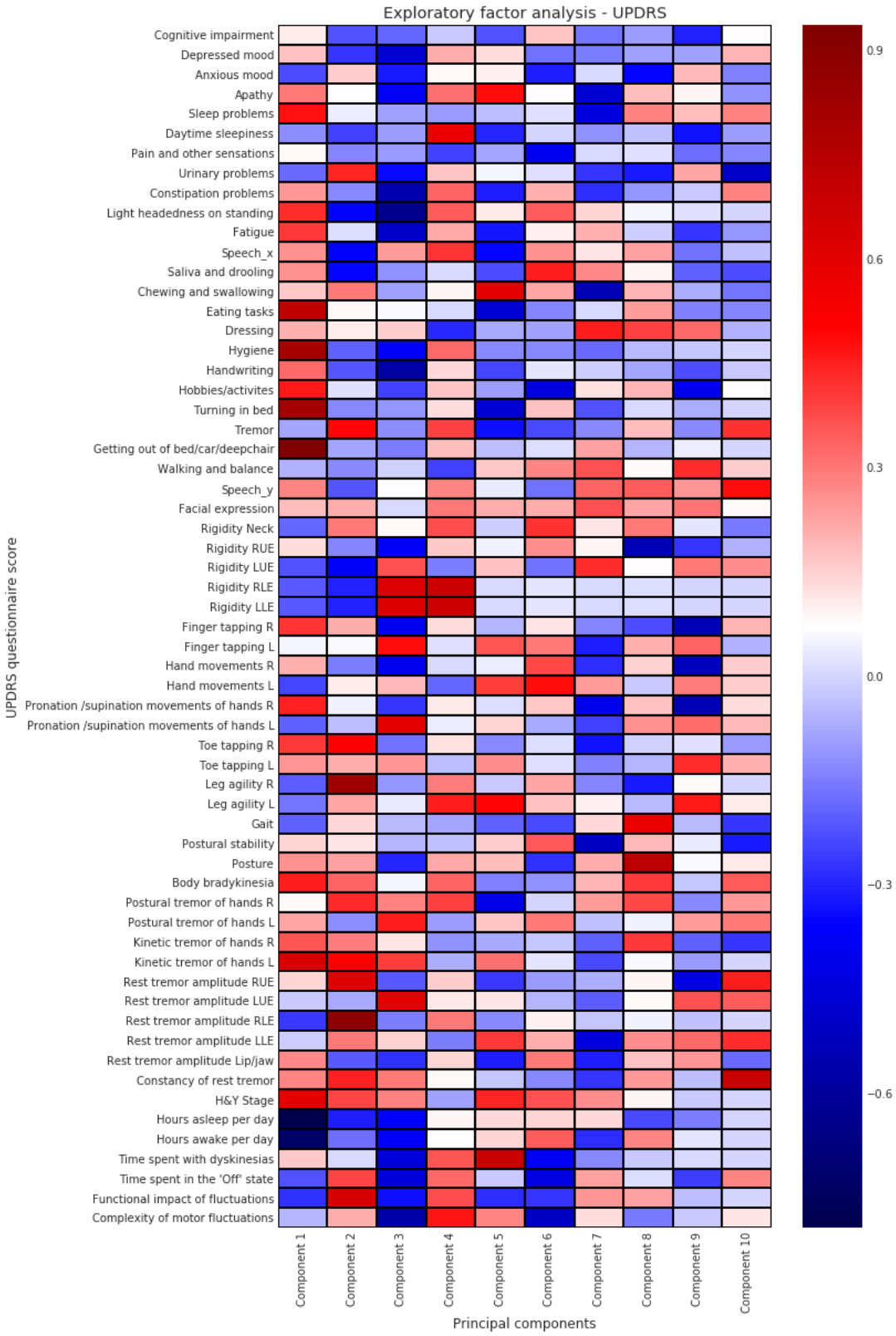

Figure 4.14. Loadings of UPDRS questionnaire scores on exploratory factors.

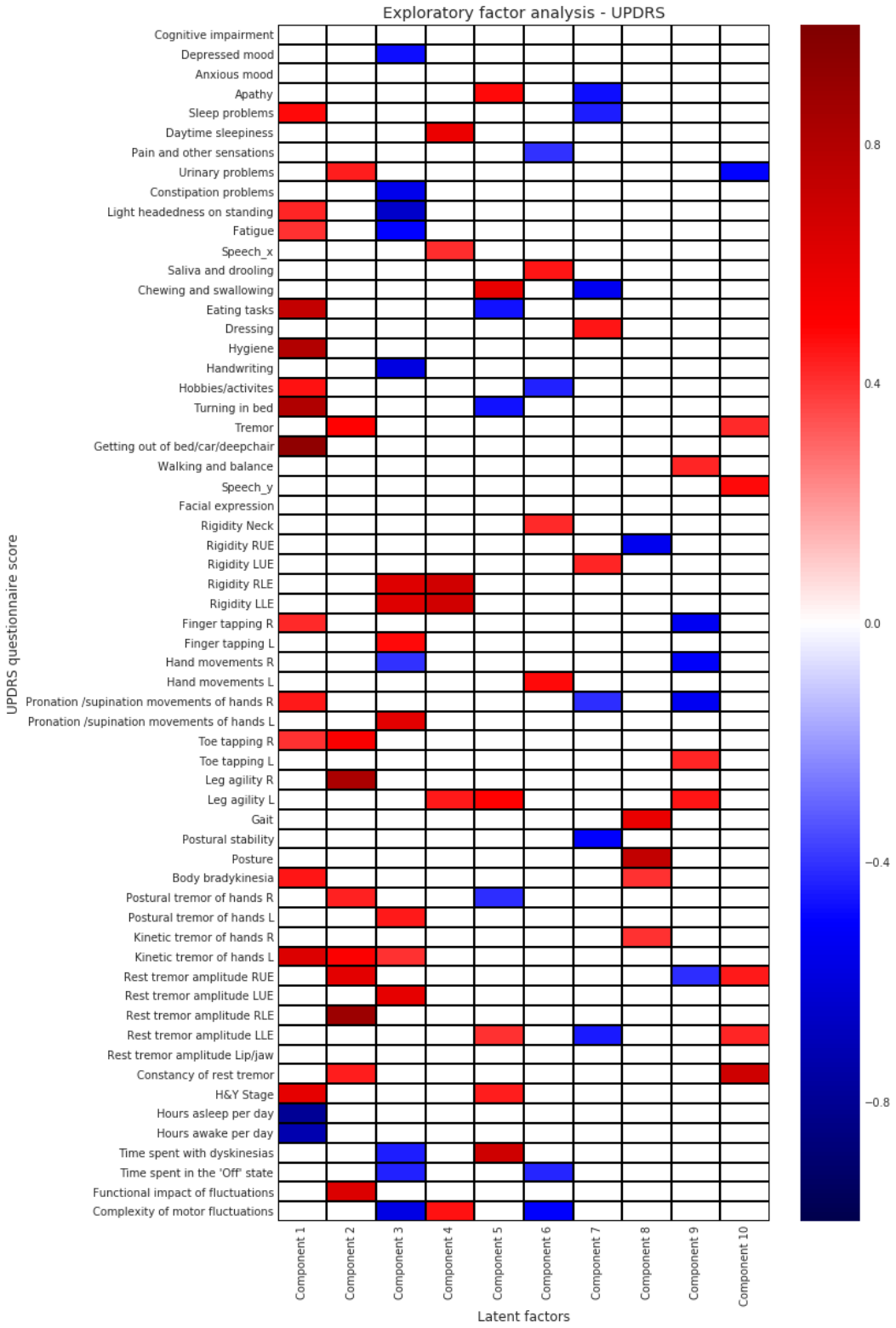

Figure 4.15. Loadings of UPDRS questionnaire scores on exploratory factors.

4.3.3.2. Correlation between imaging outcomes and UHDRS/UPDRS latent variables from exploratory factor analysis

There was a trend towards a correlation between FA, extracted from the significant spatial map (right posterior thalamus) for the difference between HC and HD and UHDRS component 5 (Spearman's ρ = -0.503, p = 0.095, **Figure 4.16**).

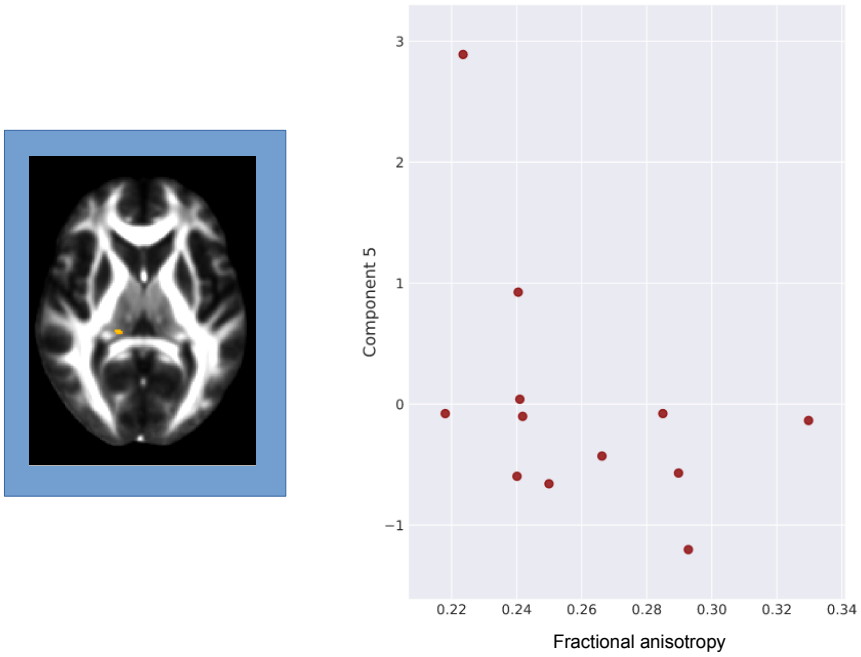

Figure 4.16. Scatter plot showing a trend towards a correlation between UHDRS latent variable 5 from exploratory factor analysis and the average fractional anisotropy values across the significant voxel-wise cluster (blue inset on far left) for the comparison between patients with Huntington's disease and matched healthy controls in posterior thalamic nuclei group.

Mean diffusivity extracted from the spatial map (dentate nucleus) for the trend difference PD vs HC was found to be correlated with UPDRS component 1 (Spearman's ρ = 0.546, p = 0.035), and UPDRS component 7 (Spearman's ρ = -0.642, p = 0.009, **Figure 4.17**).

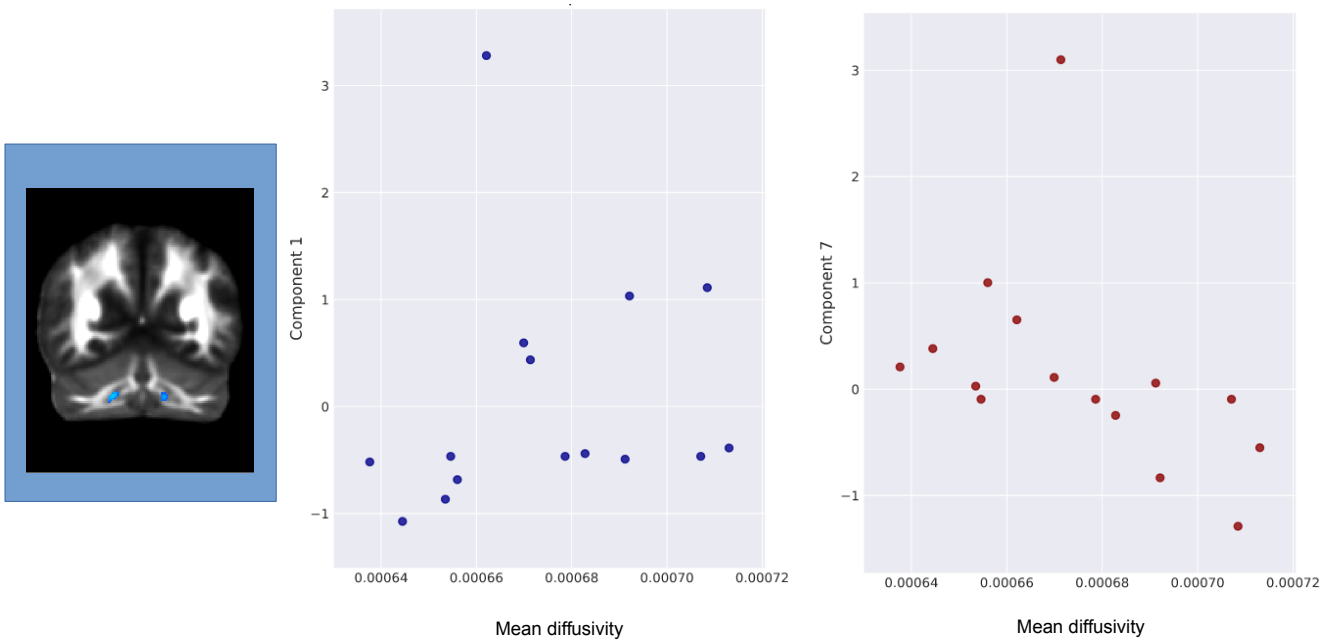

Figure 4.17. Scatter plots showing the significant correlations between UPDRS latent variables 1 and 7 from exploratory factor analysis and the average mean diffusivity across the trend voxel-wise cluster including the dentate nucleus of the cerebellum (blue inset on far left), testing for significant differences between patients with Parkinson's disease compared with matched controls (PD > HC).

4.4. Discussion

In this chapter, I have investigated abnormalities in the microstructure of deep cerebral/cerebellar relay nuclei of the basal ganglia system, and associate nuclei such as the dentate nucleus using diffusion tensor imaging in two neurodegenerative diseases found at the opposite ends of the spectrum of movement disorders: Parkinson's and Huntington's disease. A summary of key findings for this thesis chapter can be found in **Figure 4.last.** To the best of our knowledge, this is the first study that directly compared both diseases using ultra-highfield (7T) diffusion MRI.

When investigating which deep cerebral brain structures are affected by both diseases using a conjunction analysis, no significant effects were found. This finding suggests that early Huntingont's and Parkinson's disease, are two distict basal ganglia disoders that don't show detectable communalities at this stage of the diease at least at the voxel-wise level. It should however be noted that the approach for testing for similar diffusion metric alterations in both dieases using a conjunction analysis based on the infinum statistic of 1-P values is in itself a very conservative approach (Friston, 2009).

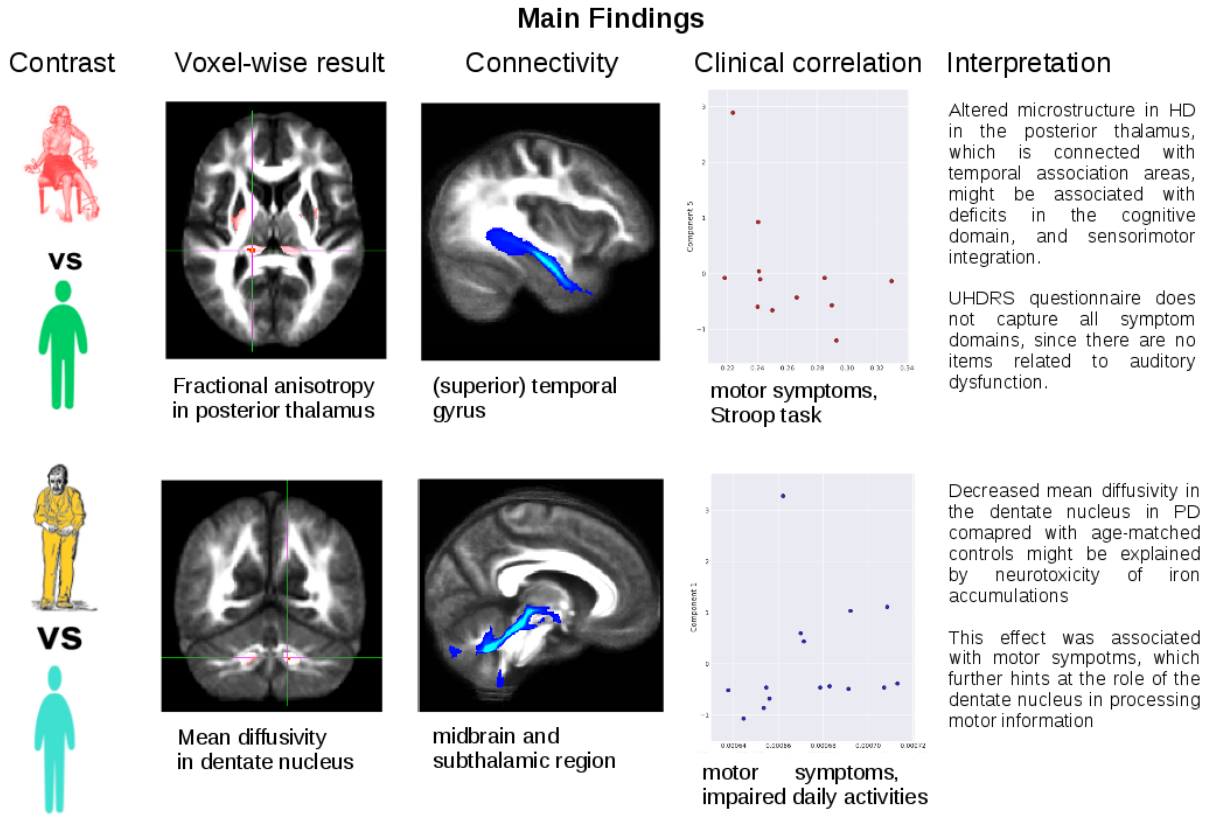

Figure 4.last Chapter summary showing the various analysis approaches used in this chapter and the key findings.

There was significantly lower FA in the right posterior thalamic nuclei group in HD compared with HC. The thalamus is the final subcortical relay nucleus of the basal ganglia loops before reentry in the cortex occurs, and therefore plays a major role in sensorimotor integration. Previous research using VBM showed that thalamic atrophy in HD was associated with cognitive symptoms (Kassubek *et al.*, 2005).

Using probabilistic tractography we found that this specific part of the thalamus is connected to the middle and superior temporal gyrus. This finding is in accordance with neuroanatomical studies in non-human primates using retrograde tracing (Yeterian and Pandya, 1989, 1991; Schmahmann and Pandya, 2009).

The average MD values from the significant voxel-wise cluster in the posterior thalamus showed a trend towards a correation with latent variable 5 from factor analysis that has high loadings on various motor symptoms, and the Stroop task. Taken the findings from probabilistic tractography and the correlational analysis together, it seems to be likely that the result found in posterior thalamus corresponds to abnormal thalamic connectivity with multi-modal association areas in the superior temporal gyrus that then result in deficits in the cognitive domain, and in sensorimotor integration. A further explanation might be that this altered connectivity to the superior temporal gyrus could be related to known auditory symptoms in Huntington's disease (e.g. {Formatting Citation} that are not captured using the UHDRS rating scale, since it does not include any auditory items.

However, given the small spatial extent of the effect seen in the posterior thalamus, and that it was only found unilaterally, the effect should be interpreted with caution, as it might correspond to a non-specific finding. Further research is necessary to determine, if this effect can be replicated.

We found a trend towards higher mean diffusivity in PD compared with HC in the dentate nucleus. At first sight the difference in mean diffusivity seems to be driven by lower MD in the matched healthy control group. However, previous research using susceptibility-weighted imaging in healthy subjects showed that the susceptibility signal decreases with age, which is indicative of accumulation of iron in older healthy subjects (Maschke *et al.*, 2004). Previous research in PD also showed increased susceptibility, indicative of increased iron accumulation, in the dentate nucleus in Parkinson's disease compared with healthy controls (He *et al.*, 2017). In PD, these iron accumulations in the dentate nucleus become neurotoxic due to altered cellular metabolism in dopaminergic cells (Hare and Double, 2016). As a result neurons are lost, and MD is higher in PD when compared with age-matched controls. By contrast, MD is lower in healthy elderly due to increased diffusion restrictions resulting from iron accumulation, and/or an increase T2-shine through on the diffusion-weigthed images due to iron accumulation. A previous study using resting-state fMRI found disrupted functional connectivity of the DN in PD (Liu *et al.*, 2013). A further study that used diffusion imaging to compare patients with multiple system atrophy and patients with PD found higher MD in the dentate nucleus in patients with multiple system atrophy compared with PD, which is similar to our findings when comparing PD patients with healthy controls (Tsukamoto *et al.*, 2012).

Mean diffusivity within the significant PD cluster in the dentate nucleus also showed high correlations with several latent variables from factor analysis, that showed high loadings on motor symptoms and impairments of daily activities (factor 1), various motor symptoms and apathy/sleep (factor 7), and mainly axial motor symptoms (factor 8). Using probabilistic tractography we have seen that this part of the dentate nucleus is predominantly connected with the subthalamic region and the tegmentum mesencephali, that both show close links to the motor system. Overall, these findings are indicative that this alteration in the micro-structure of the dentate nucleus might be a possible explanation for motor symptoms seen at an early stage of PD.

The present study has certain limitations that merit discussion. The sample size in both patient groups (N(HD) = 12, N(PD) = 15) is rather small, which inevitably decreases the likelihood that the statistically detected effects reflect true effects, and are generalizable to the population of HD/PD patients (Button *et al.*, 2013).

The present study did not detect any effect in the substantia nigra neither when looking at the conjunction analysis nor when testing for individual patient group differences nor when directly comparing the Parkinson's disease group with their age-matched controls. To further investigate any alterations in the substantia nigra, we ran a post-hoc region-of-interest analysis using customized masks of the substantia nigra from multi-modal image segmentation (Visser *et al.*, 2016), and did not detect

any effect either. These findings are at variance with previous diffusion imaging studies that showed lower FA in the substantia nigra in patients with PD compared with controls (Chan *et al.*, 2007b; Vaillancourt *et al.*, 2009b). Possible explanations of these discrepancies among studies are differences in the disease stages between studies (e.g. mainly stage 1 in our study vs. mainly stage 2, and to a lesser extent stage1 in Vaillancourt et al., 2009, vs. stages 1-4 in Chan et al., 2007), differences in sample size (e.g. 73 patients in Chan et al., 2007), as well as differences in the scanning protocol and data acquisition (e.g. 7 Tesla in our study vs. 3 Tesla in Vaillancourt et al., 2009 vs. 1.5 Tesla in Chan et al., 2007).

For the sparse principle component analysis, and factor analysis, it should be noted that since the number of subjects was much less than the number of features the resulting latent variables are most likely not estimates of the true factor structure of symptoms in HD, and PD. The general recommendation for PCA and FA is that N >> observed variables. This makes the meaning of the latent variables hard to interpret, and they most likely reflect idiosyncrasies inherent to this specific sample of patients. Indeed, the factor/component structure we detected for the UPDRS data is at variance with previous research that was based on larger sample sizes (Evans *et al.*, 2011; Vassar *et al.*, 2012), for example we could not clearly distinguish between limb bradykinesia, tremor, and limb rigidity, and components were loading on several

domains. Likewise, our components could often not distinguish lateralization (left vs. right), and lower/upper extremity. One possible solution to overcome this problem would have been to derive the latent variables from a larger data set, and then apply the resulting loading matrix to our data set to yield the reduced data set.

Neither PCA nor EFA could clearly distinguish between motor, cognitive, and psychiatric domains as orthogonal factors of symptoms, and latent variables were a mixture of these dimensions. This is most likely because the UPDRS/UHDRS questionnaire scores mainly contain items that are in the motor domain, whereas the cognitive and psychiatric symptoms are already under-sampled in observed variables, as a result a similar pattern of high loadings on motor scores in the factor space is expected.

Nevertheless, both PCA and EFA are valuable data reduction techniques, that helped us to overcome the curse of dimensionality when correlating multiple questionnaire scores with imaging data. Bearing these limitations in mind it should be noted that the UHDRS components were similar to previous components found in another imaging study that also used PCA in a small sample size (N = 22) but only using the motor domain of the UHDRS. Similar, to our findings maximal dystonia, maximal chorea, and gait loaded on the same component (our component 2), and

rigidity arms, ocular pursuit and retropulsion test loaded on the same component (our component 4) (Galvez *et al.*, 2018).

In conclusion, when using diffusion MRI as an imaging marker of brain micro-structure we found similar abnormalities between both basal ganglia disorders in the globus pallidus, as well as disease-characteristic micro-structural abnormalities in the posterior thalamus in HD and the dentate nucleus in PD. These imaging outcomes were associated with various clinical scores from motor, cognitive, and psychiatric domains.

Chapter II.5: Comparison of the white matter micro-structure in early Huntington's and Parkinson's disease using ultra high-field diffusion MRI

5.0. Abstract

Rational. Huntington's disease and Parkinson's disease are both movement disorders characterized by alterations in the white matter tract in the brain. Huntington's disease has been described as a cortical disconnection disease. In Parkinson's disease white matter loss has been suggested to precede gray matter alterations.

Objectives. To investigate microstructure alteration in the white matter in patients with Huntington's and Parkinson's disease, and compare the patient groups with age- and gender-matched control groups.

Methods. Tract-based spatial statistics was used to investigate changes in the white matter skeleton in patients with Parkinson's disease and Huntington's disease and matched controls without the need for introducing any bias by selecting a specific tract or region of inters.

Results. Both patient groups, patients with Huntington's and Parkinson's disease, showed similar abnormalities in mean diffusivity and fractional anisotropy relative to their matched controls in the posterior limb of the internal capsule, that contains

descending fibers of the cortico-spinal and cortico-striatal tract, known to degenerate in these diseases. Patients with Huntington's disease showed widespread decreases in fractional anisotropy in the white matter, including the corpus callosum, further indicating that it is a cortical disconnection disease. Higher mean diffusivity was found in the Huntington's disease compared with their matched control group in the right internal capsule, external/extreme capsule, and right, the superior longitudinal fasciculus. No significant differences in mean diffusivity or fractional anisotropy were found in the Parkinson's disease group compared with their matched control group. A trend for similar fractional anisotropy alterations was found in the genu of the corpus callosum, that is know to harbor the inter-hemispheric connections between the motor cortices.

Conclusions. Huntington's disease is cortical disconnection disease characterized by wide-spread degenerations in the white matter microstructure of the brain that are even detectable at the early stage of the disease. By contrasts, alteration in white matter microstructure in early Parkinson's disease are much more confined to tracts involved in the processing of motor signals including the posterior limb of the internal capsule and the genu of the corpus callosum.

5.1. Introduction

"How nerves sometimes operate by themselves without any command from other functioning parts of the soul. This is clearly apparent, for you will see paralytics and those who are shivering and benumbed by cold move their trembling parts such as head or hands without the permission of the soul; which soul with all its forces cannot prevent these parts from trembling."

Leonardo da Vinci[2]

The focus of the present chapter is to compare HD and PD with respect to abnormalities in the white matter micro-structure as revealed by diffusion MRI. Huntington's disease has been putatively described as a cortical disconnection disease with widespread white matter degenerations including the corpus callosum (Rosas *et al.*, 2010). These WM degenerations are most likely due to myelin breakdown as

2 Cited by Lees, A. J. (2007). Unresolved issues relating to the shaking palsy on the celebration of James Parkinson's 250th birthday. Movement Disorders : Official Journal of the Movement Disorder Society. United States. https://doi.org/10.1002/mds.21684

shown using multi-modal imaging research and post-mortem research (Bartzokis *et al.*, 2007; Bourbon-Teles *et al.*, 2017) .

Despite being characterized by antagonistic symptoms when compared with HD (as discussed in previous chapters), microstructural white matter alterations were also detectable in Parkinson's disease. In early stages of Parkinson's disease widespread micro-structural white matter damage has been found using diffusion MRI (Gattellaro *et al.*, 2009), and micro-structural WM damage might be used as an biomarker for cognitive dysfunction in Parkinson's disease (Melzer *et al.*, 2013; Kalia, 2018). Besides this initial strong associated between white matter damage and cognitive dysfunctioning, more recent research found that white matter aerations inter alia in the internal and external capsule, were already present in PD patients who did not show any cognitive symptoms, and that these WM alterations preceded gray matter loss (Rektor *et al.*, 2018). The underlying pathophysiological mechanism of this WM damage in PD is not completely known, however a strong link to anxonal degeneration has been hypothesized (Burke and O'Malley, 2013; Tagliaferro and Burke, 2016). WM micro-structural changes were also shown to be associated with systemic markers of inflammation (Chiang et al., 2017).

Whereas previous diffusion MRI studies demonstrated WM micro-structural alterations in either Huntington's or Parkinson's disease, this is the first study to

directly compare both diseases with respect to the WM micro-structure. Such a direct comparison is highly desirable as it has the potential to shed light on two model disorders found at the opposite end of the spectrum of movement disorders.

A detailed description of the demographic data of all participants enrolled in the study, as well as the study design can be found in section 4.2.1. The data acquisition follows the same protocol as described in section 4.2.2. The software packages used for data analysis and visualization are the same as cited in chapter 4.2.3 and 4.2.4.

5.2.1. Tract-based spatial statistics

The TBSS analysis was used to investigate white matter microstructural abnormalities unconfounded by the choice of a specific ROI, as TBSS is a voxel-wise method (Smith et al., 2006). After having fitted a diffusion tensor model for each subject, and each voxel in native space using the FSL tool dti_fit (see chapter 4.2 for details), FA images were slightly eroded, and the end slices were zeroed (to remove likely outliers from the diffusion tensor fitting).

In the acquired diffusion data there was signal drop out in the cerebellar hemispheres and temporal lobes. To account for this signal dropout an optimized linear registration with customized masks for each subject's hyperintensities in the temporal lobes, cerebellum, and if necessary in the cortex was used to improve the registration to a 1x1x1mm standard space using the FMRIB58-FA template as target (see **Figure 5.1** for an illustration how the optimized protocol improved the

registration). The average FA image, and the TBSS skeleton were derived from the average across all subjects, and a probabilistic mask for the signal dropout in the cerebellar hemispheres, and temporal lobes for all subjects was used to confine the skeleton to WM tracts without signal dropout. The same projection procedure estimated from the average fractional anisotropy images was used for the projection of the corresponding mean diffusivity difference images onto the TBSS skeleton.

A. Nonlinear registration into standard space without signal dropout masks for a single subject

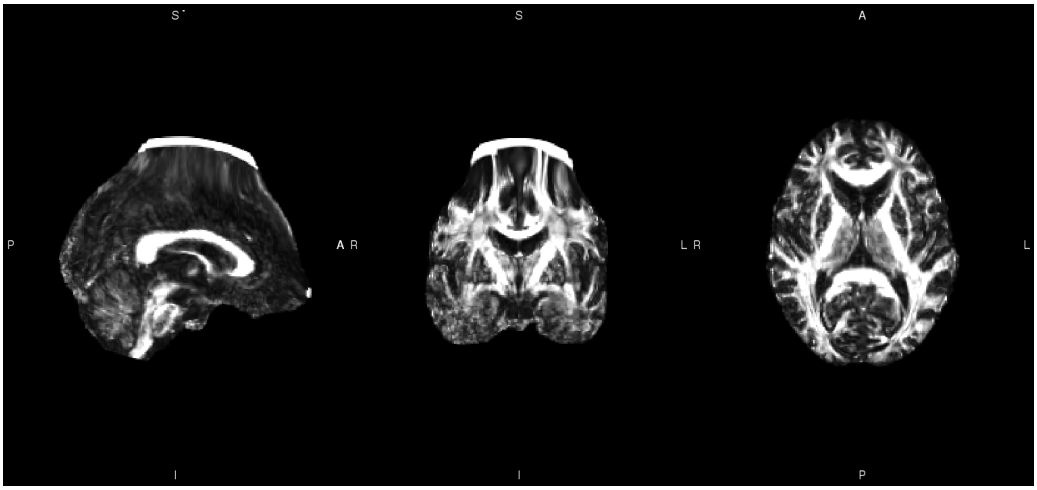

B. Signal dropout masks for a single subject in native space

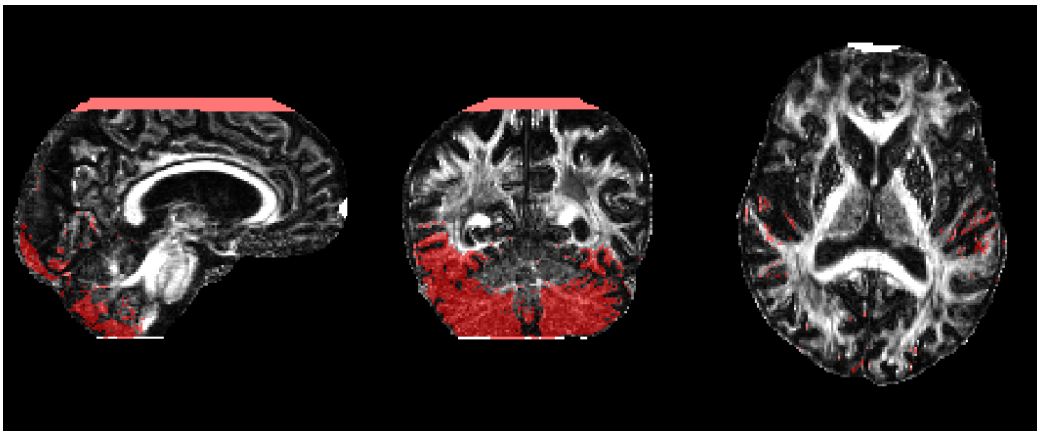

C. Improved registration into standard space using signal dropout masks (as shown in B)

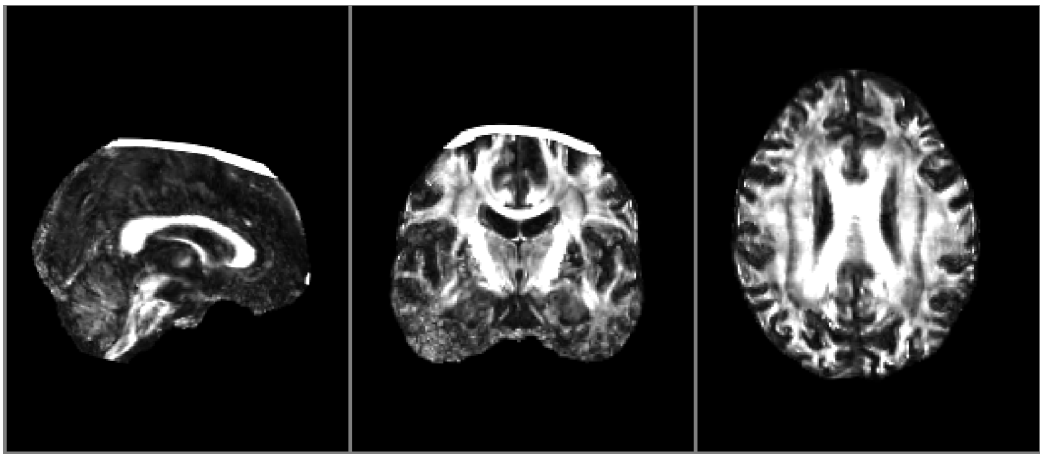

Figure 5.1 Using signal dropout masks to improve the non-linear registrations into standard space. A. Non-linear registration into standard space using the standard FSL pipeline results in parts of the cerebral cortex and the cerebellum, that are affected by signal dropout, to be deformed. B. Fractional anisotropy image of a single subject in native space with a thresholded and binarized signal dropout mask in red (transparent) covering parts of the central cortex and the cerebellum. These parts of the brain are then warped together as a whole in the modified registration algorithm (C) to avoid a loss of topology (as seen in A). C. Improved registration into standard space using signal dropout masks.

5.2.2. Statistical analyses

5.2.2.1 Voxel-wise statistical analyses

For voxel-wise statistics, permutation-based non-parametric inference (5,000 permutations) was used to test for overall effects of group, differences in mean diffusivity and fractional anisotropy alterations between patients and their age-/gender-matched healthy controls, as well as using customized one-tailed linear contrast for simultaneous comparisons of multiple patient groups with their age-/gender-matched healthy controls as described in more detail in section 4.2.4 (Nichols and Holmes, 2002). The demeaned age was entered as a co-variate of no-

interest in the model. Results were considered to be significant for $P < 0.05$, and corrected for multiple comparisons using threshold-free cluster enhanct with 2D optimization (Smith and Nichols, 2009). Generalized linear hypotheses on adjusted means were carried out to test for differences between single patient groups and healthy control groups, as well as use-defined linear contrasts.

5.2.2.2 Post-hoc correlation analysis between neuroimaging data and sparse PCA/factor analysis components

We have run post-hoc correlations between extracted diffusion metrics from the significant/trend TBSS clusters, and the sparse PCA/factor analysis components for each patient group separately (see section 4.2 for details about sparsePCA/factor analysis). The spatial maps of the significant/trend TBSS statistics were binarized, thresholded at 0.95, or 0.90 respectively, and used to calculate the average of the diffusion metric over all voxels within the map. D'Agostoni-Pearson K^2 test was used to test if the data were normally distributed. We have used the Pearson's product moment correlation for normally distributed data, and Spearman's rank order correlation for non-normally distributed data to test for a linear relationship or a

monotonic relationship respectively between extracted diffusion metrics on one hand, and sparse principal components and latent variable from exploratory factor analysis.

5.3. Results

5.3.1. Voxel-wise comparisons of diffusion metrics

5.3.1.1. Linear contrasts comparing multiple patient groups with age-/gender-matched healthy controls

There were significant differences in mean diffusivity alterations in both HD and PD patients compared with their matched control groups in the bilateral posterior limb of the internal capsule, and the right external/extreme capsule ($p = 0.042$, **Figure 5.2**), whereby MD was significantly higher in the patient groups (HD, PD), whereas FA was lower within these white matter regions (not significant). These findings of higher MD and lower FA are indicative of alterations within fibers that correspond to the predominate fiber direction within these brain regions, in this case the corticospinal and corticostriatal tracts.

There was a trend towards similar fractional anisotropy alterations in both HD and PD relative to their control groups in the posterior limb of the internal capsule and the genu of the corpus callosum ($p = 0.052$, **Figure 5.3**).

No significant differences in mean diffusivity alterations were found when comparing HD and PD relative to their age matched controls (p =.0682). There were significant differences in fractional anisotropy alterations in HD compared with PD relative to their age-/gender matched healthy controls in several parts of the corpus callosum, the internal capsule, the corona radiata, and the bilateral superior longitudinal fasciculus. (p = 0.019). Here HD had lower FA compared to their matched controls, and PD had higher FA.

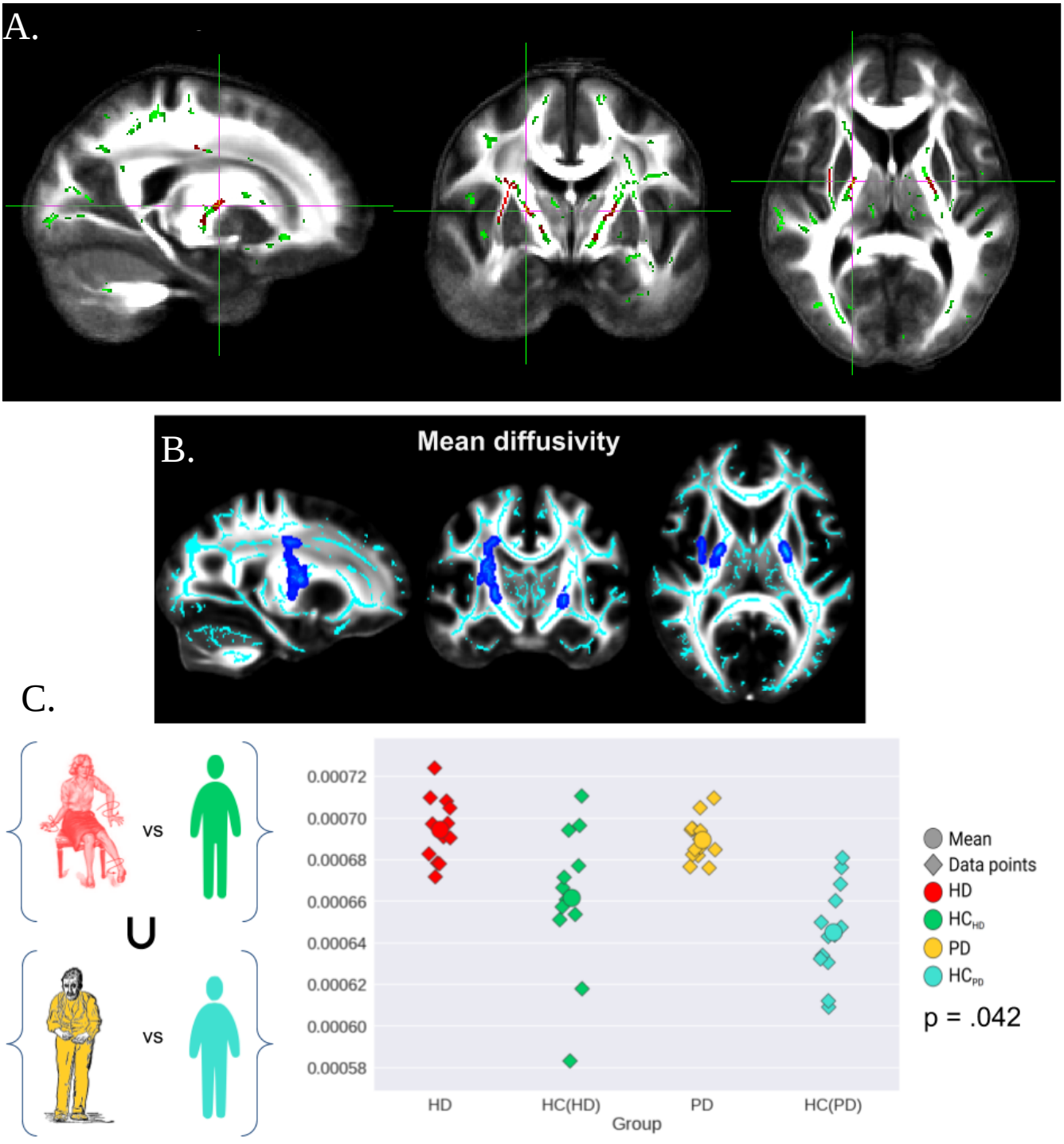

Figure 5.2. Significant differences in mean diffusivity alterations in the bilateral posterior limb of the internal capsule, and the left external/extreme capsule in both patients with Huntington's and Parkinson's disease relative to their age-/gender

matched healthy controls. A. Statistical non-parametric map showing the significant effect in the bilateral posterior limb of the internal capsule, and the right external/extreme capsule, corrected for multiple comparisons using TFCE in red, and the uncorrected voxel-wise map including the right superior longitudinal fasciculus in green, overlaid on the average FA image across subjects in standard space. B. Dilated/De-projected map showing only the significant voxels for the same contrast. C. Dispersion plot showing the average mean diffusivity over all significant voxels of the voxel-wise map (shown in A). On average both patient groups had higher mean diffusivity relative to their healthy controls.

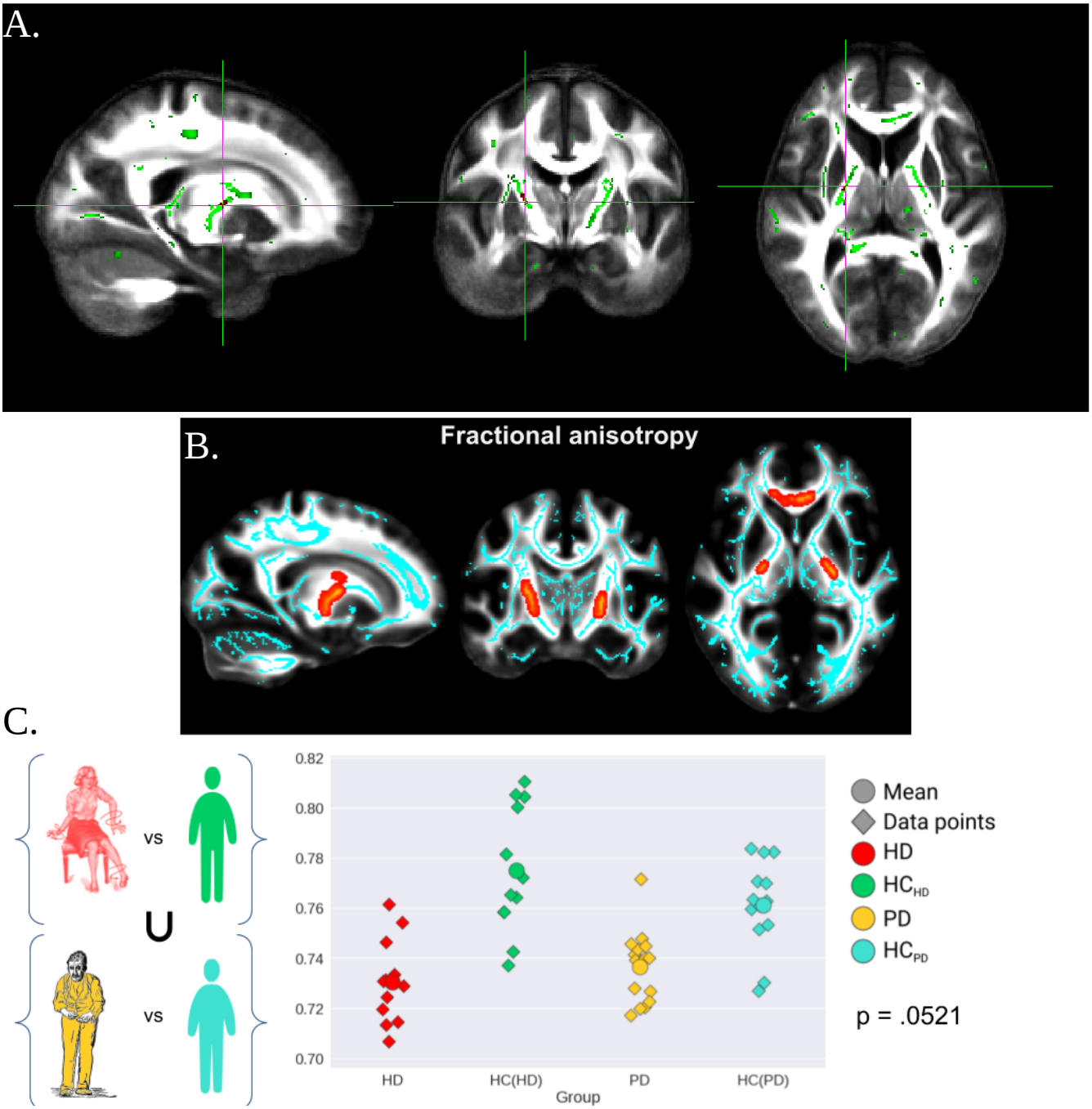

Figure 5.3. Trend towards similar fractional anisotropy alterations in the bilateral/right posterior limb of the internal capsule, and the genu of the corpus callosum in patients with both Huntington's and Parkinson's disease. A. Statistical

non-parametric map showing the trend in the right posterior limb of the internal capsule, thresholded at 0.06 corrected for multiple comparisons using TFCE in red, and the uncorrected voxel-wise map including the bilateral posterior limb of the internal capsule and the genu of the corpus callosum in green, overlaid on the average FA image across all subjects in standard space. B. Dilated/De-projected of the same contrast thresholded at the trend level ($p < 0.10$). C. Dispersion plots showing the average fractional anisotropy across all voxels thresholded at $p = 0.10$ (as shown in the map seen in B), indicating that fractional anisotropy was lower in both patients with Huntington's and Parkinson's disease relative to their healthy control groups.

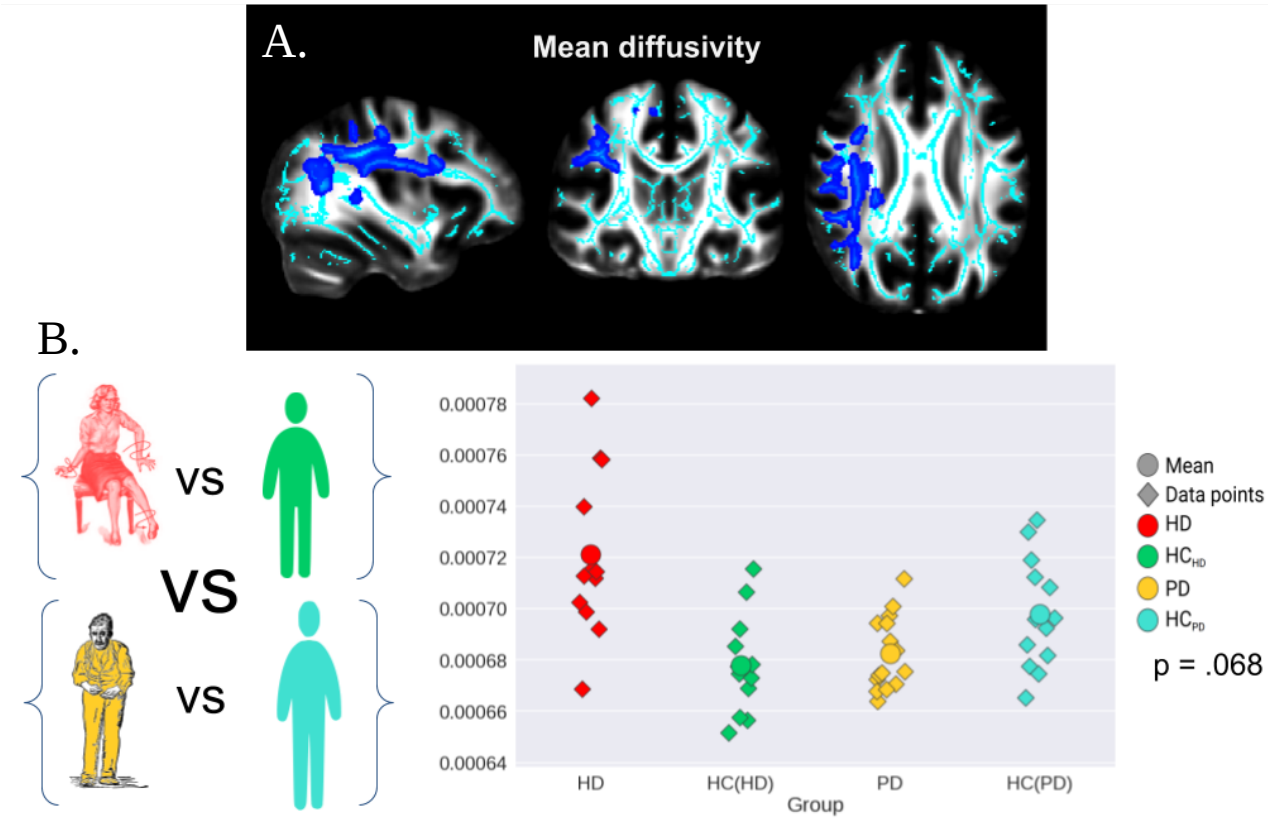

Figure 5.4. Trend towards differences in mean diffusivity alterations in patients with Huntington's disease and patients with Parkinson's disease relative to their matched controls the widespread parts of the white matter including the right superior longitudinal fasciculus. **A.** Dilated statistical non-parametric map showing the trend in the superior longitudinal fasciculus thresholded at 0.10 corrected for multiple comparisons using TFCE in blue. **B.** Dispersion plots showing the average fractional anisotropy across all voxels thresholded at p = 0.1 (as shown in the map above), indicating that mean diffusivity was higher in both patients with

Huntington's disease and lower in Parkinson's disease relative to their healthy control groups.

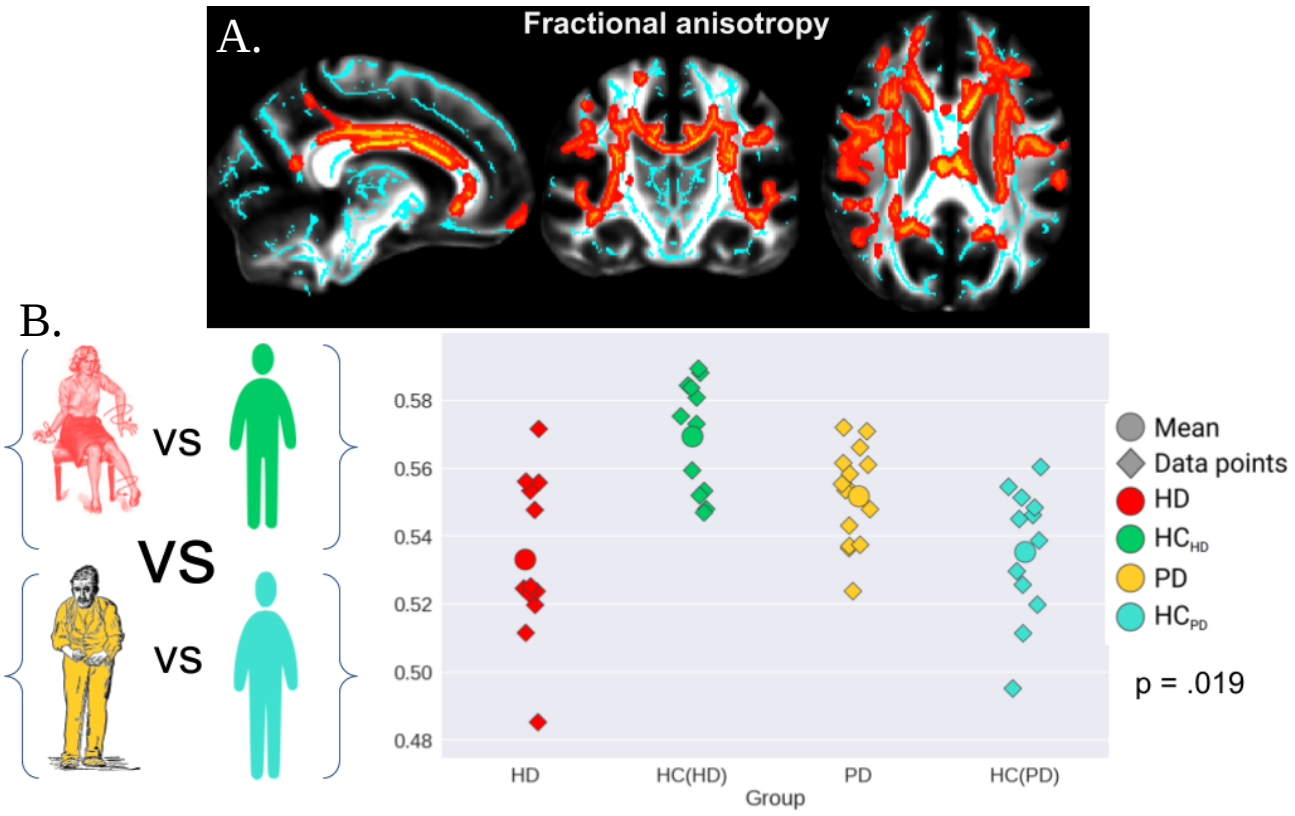

Figure 5.5. Significant differences in fractional anisotropy alteration in patients with Huntington's disease compared with patients with Parkinson's disease relative to their age matched controls in widespread parts of the white matter including the corpus callosum. **A.** Dilated/De projected statistical non-parametric map showing the significant effect in the corpus callosum and other parts of the white matter corrected for multiple comparisons using TFCE in blue. **B.** Dispersion plots showing the average fractional anisotropy across all voxels thresholded at p = 0.05 (as shown in the map above), indicating that fractional anisotropy was lower in the

Huntington's disease group, but higher in the Parkinson's disease group relative to their age -matched controls.

5.3.1.2. Comparing single patient groups with their age-/gender matched healthy controls

Significantly higher MD was found in patients with HD compared with their age-/gender matched controls in the posterior limb of the right internal capsule, the right external/extreme capsule, and the right superior longitudinal fasciculus ($p = 0.015$, **Figure 5.6**).

Significantly lower FA was found in patients with HD compared with their age-/gender matched controls in wide-spread parts of the white matter, including the corpus callosum, the right superior longitudinal fasciculus, the posterior limb of the right internal capsule, the right external/extreme capsule, and ($p = 0.003$), **Figure 5.7**).

No significant group differences in MD or FA were found when comparing patients with PD and their matched HC ($p = 0.083$, $p = 0.228$, respectively).

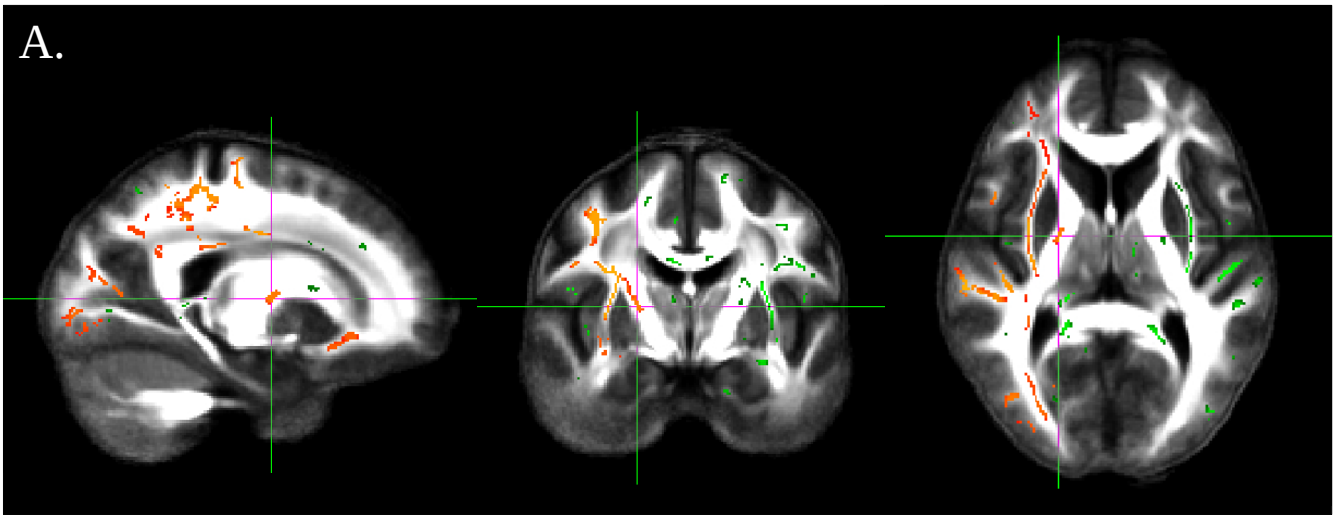
A.

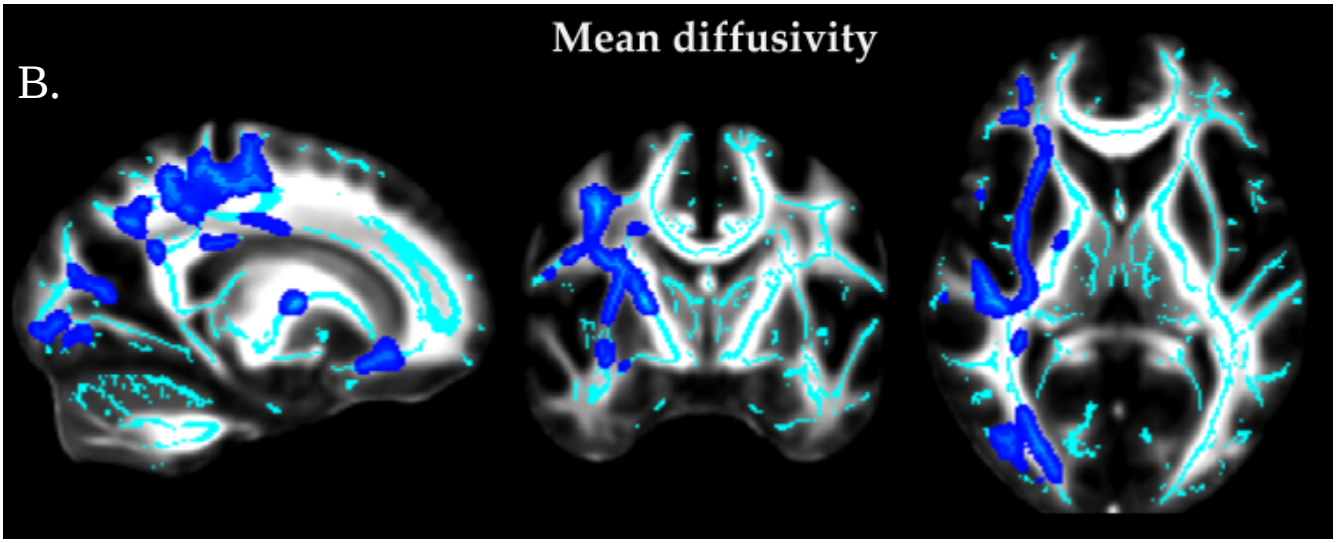
Mean diffusivity
B.

C.

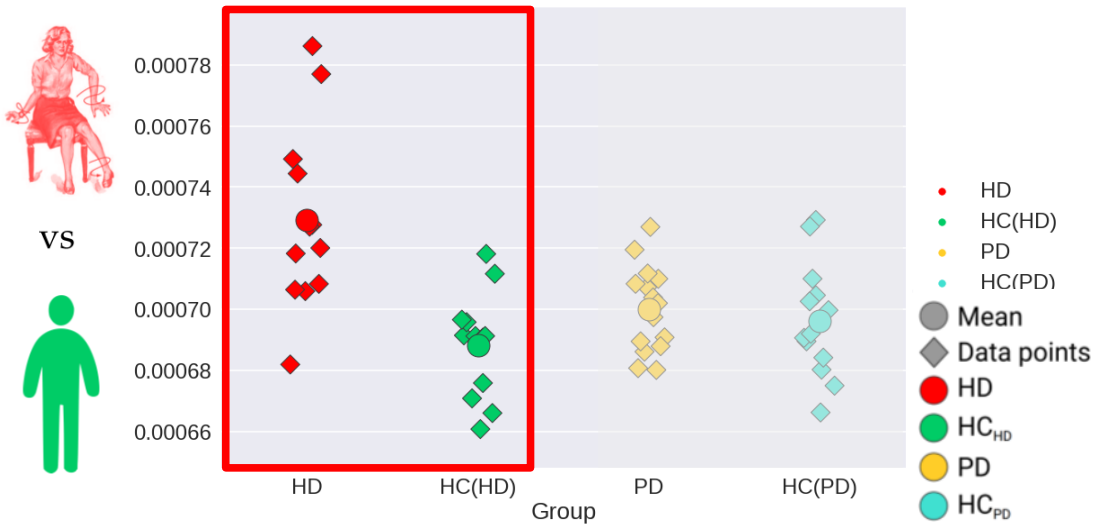

Figure 5.6. Higher mean diffusivity in the right posterior limb of the internal capsule, right external/extreme capsule, and right superior longitudinal fasciculus in

patients with Huntington's disease compared with age-/gender matched HC. **A.** Statistical non-parametric map of higher mean diffusivity showing the significant effect in the right posterior limb of the internal capsule, right external/extreme capsule, and right superior longitudinal fasciculus in red, and the uncorrected voxel-wise map in green, overlaid on the average FA image across all subjects in standard space. **B.** Dilated/Deprojected maps of the significant voxels for the same contrast (as shown in A). **C.** Dispersion plots showing the average mean diffusivity across all voxels thresholded at $p = 0.05$ (as shown in the map above in B), indicating that mean diffusivity was higher in the Huntington's disease group compared with their age-/gender matched controls. Mean diffusivity in Parkinson's disease group and their matched control group is only shown for illustrative purposed and masked out.

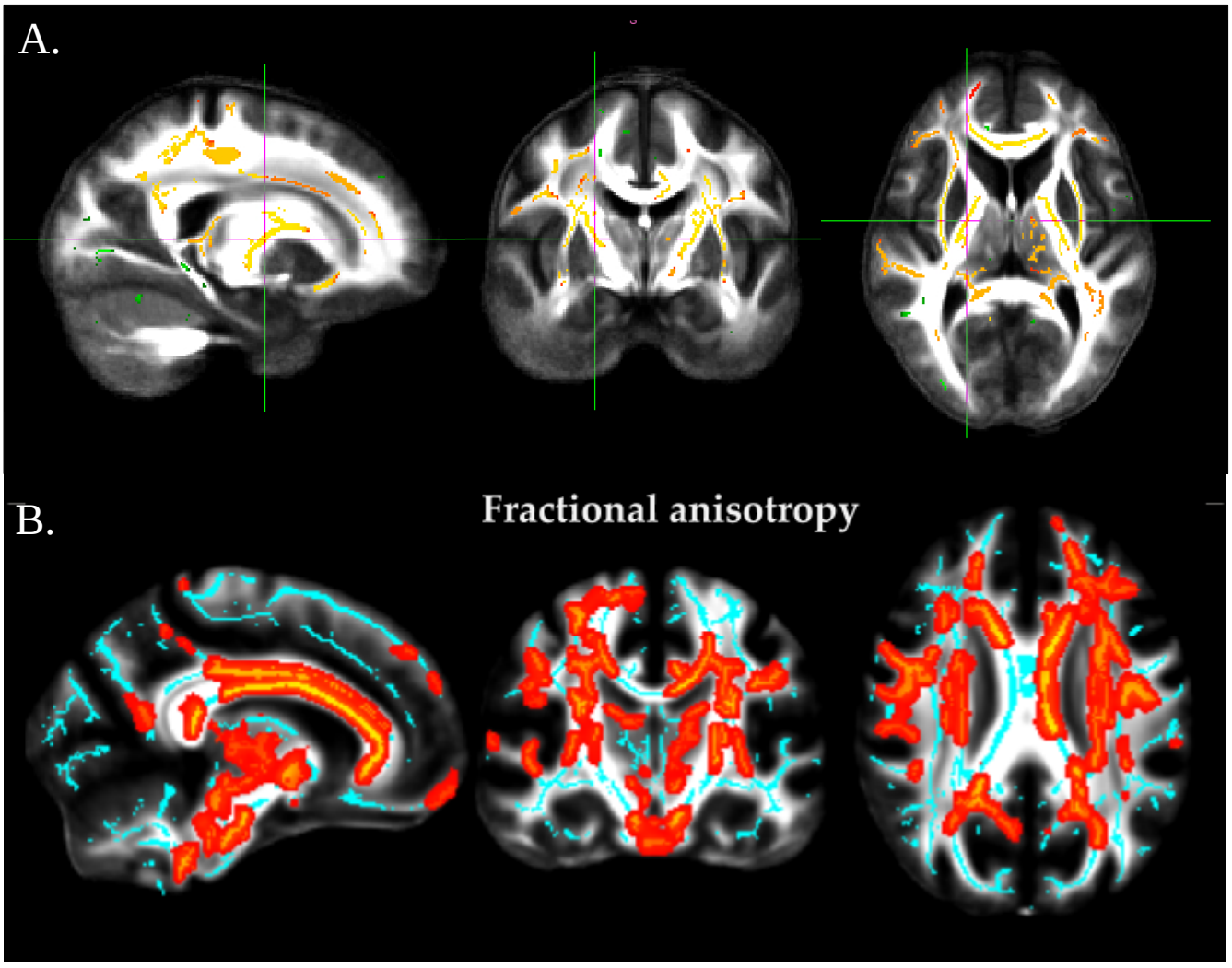
A.
B.
Fractional anisotropy

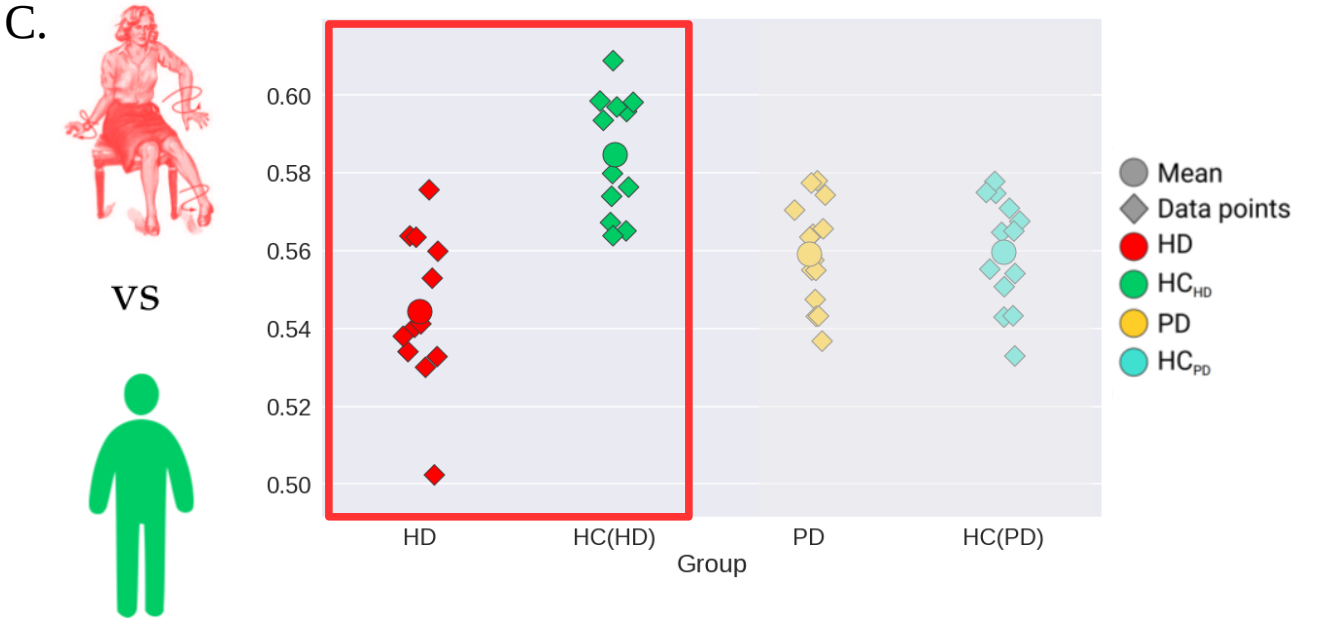
C.
VS
0.60
0.58
0.56
0.54
0.52
0.50
HD
HC(HD)
PD
HC(PD)
Group
Mean
Data points
HD
HC$_{HD}$
PD
HC$_{PD}$

Figure 5.7. Lower fractional anisotropy in widespread parts of the white matter including inter alia the corpus callosum, the bilateral posterior limb of the internal capsule, the bilateral external/extreme capsule, and the bilateral superior longitudinal fasciculus in patients with Huntington's disease compared with age-/gender matched HC. **A.** Statistical non-parametric map of lower fractional anisotropy showing the significant effect in wide-spread parts of the white matter at the level of the internal, and external/extreme capsules in yellow-orange when comparing patients with Huntington's disease with age-/gender matched healthy controls. **B.** Dilated/De-projected maps of the significant voxels for the same contrast (as shown in A) at the level of the corpus callosum. **C.** Dispersion plots showing the average fractional anisotropy across all voxels thresholded at $p = 0.05$ (as shown in the map above in B), indicating that fractional anisotropy was lower in the Huntington's disease group compared with their age-/gender matched controls. Fractional anisotropy in Parkinson's disease group and their matched control group is only shown for illustrative purposed and masked out.

5.3.2 Correlations of imaging outcomes with components from sparse PCA

There were significant correlations between the average FA extracted from the significant TBSS cluster for the difference between HD compared with matched HC, and UHDRS component 6 (Pearson's r = -0.627, p = 0.028), and UHDRS component 7 (Pearson's r = 0.612, p = 0.034, **Figure 5.8**).

There were significant correlations between the average MD, extracted from the significant TBSS cluster for the comparisons between patients with HD and matched healthy controls, and UHDRS component 7 (Pearson's r = -0.666, p = 0.017), and the UHDRS component 10 (Spearman's ρ = 0.685, p = 0.013, **Figure 5.9**).

There were significant correlations between the average FA extracted from the significant TBSS cluster testing for differences between patients with Parkinson's disease, and Huntington's disease relative to their age-matched control groups ($PDvsHC_{PD}$ vs $HDvsHC_{HD}$) and UHDRS component 5 (Spearman's ρ = 0.552, p = 0.062), component 6 (Pearson's r = -0.680, p = 0.014), component 7 (Pearson's r = 0.677, p = 0.015), and component 10 (Spearman's ρ = -0.671, p = 0.016, **Figure 5.10**).

There was a significant correlation between the average mean diffusivity extracted from the significant TBSS cluster testing for differences in both patient groups

HD/PD relative to their controls, and UHDRS component 7 (Pearson's r = 0.723, p = 0.007, **Figure 5.11**).

There were significant correlations between the average mean diffusivity, extracted from the trend TBSS cluster testing for significant difference between patients with Huntington's and Parkinson's disease relative to their healthy controls, and UHDRS component 7 (Pearson's r = -0.758, p = 0.004), and UHDRS component 10 (Spearman's ρ = 0.650, p = 0.022, **Figure 5.12**).

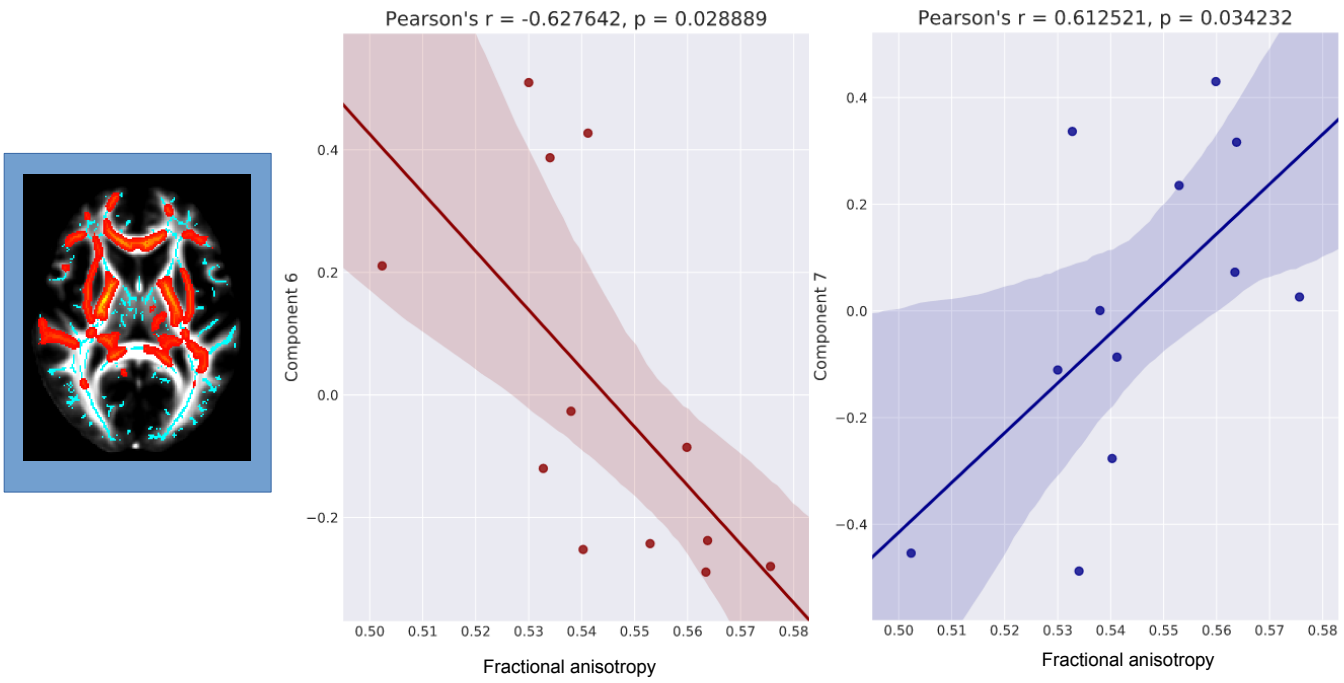

Figure 5.8. Scatter plots of the significant correlations between UHDRS sparse principal components 6 , and 7, and the average fractional anisotropy values across the significant TBSS cluster (blue inset on far left) for the comparison between patients with Huntington's disease and healthy controls in widespread parts of the white matter including the posterior limb of the internal capsule, and the genu of the corpus callosum.

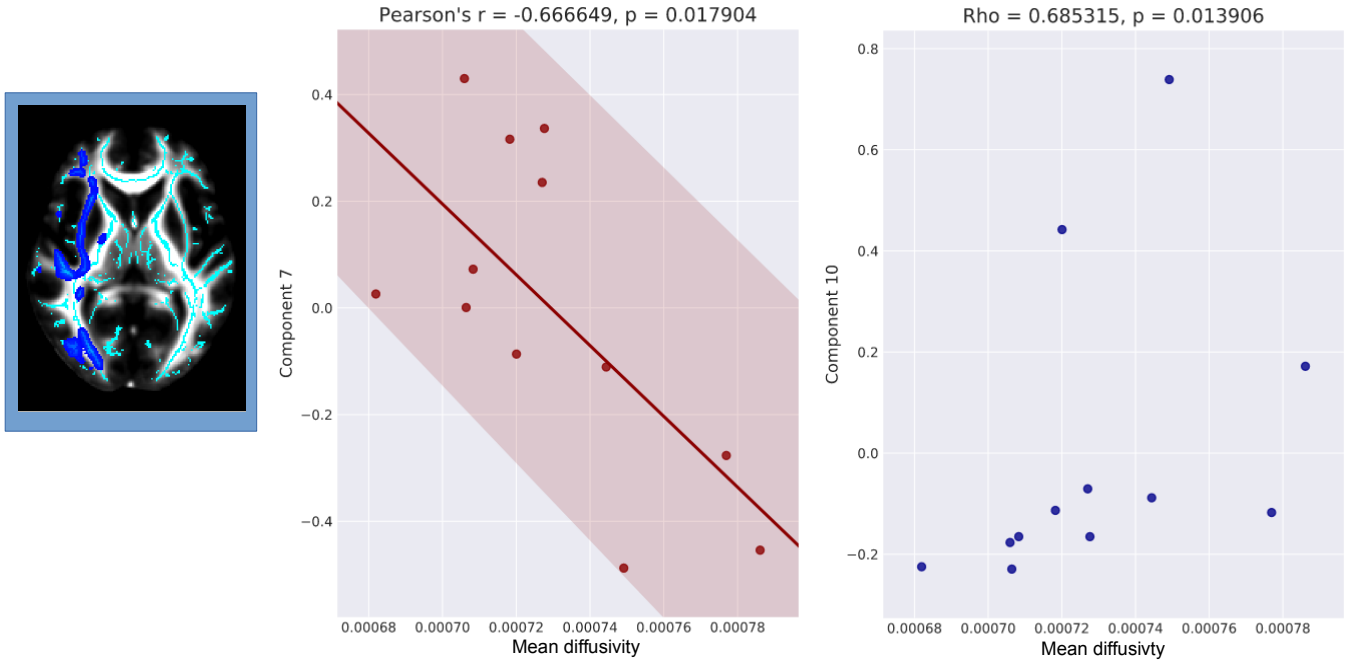

Figure 5.9. Scatter plots of the significant correlations between UHDRS sparse principal components 7 and 10, and the average mean diffusivity values across the significant TBSS cluster (blue inset on far left) for the comparison between patients with Huntington's disease and healthy controls in the right posterior limb of the internal capsule, the right external/extreme capsule, and the right superior longitudinal fasciculus.

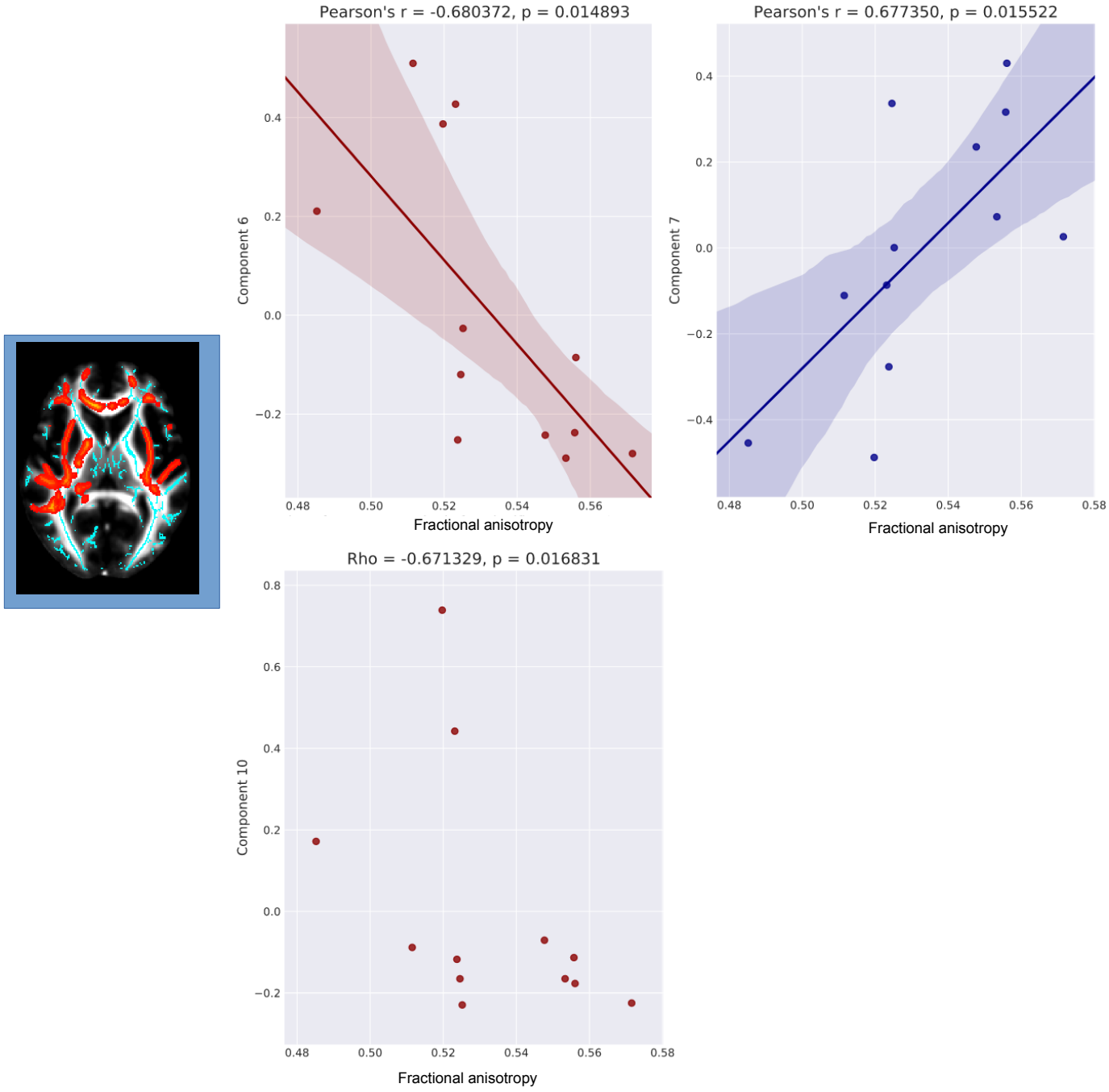

Figure 5.10. Scatter plots of the significant correlations between UHDRS sparse principal components 6 , 7, and 10 and the average fractional anisotropy values across the significant TBSS cluster (blue inset on far left) testing for significant differences between patients with Huntington's disease and Parkinson's disease

relative to their healthy controls. This TBSS cluster comprises wide-spread parts of the white matter including the posterior limb of the internal capsule, and the genu of the corpus callosum.

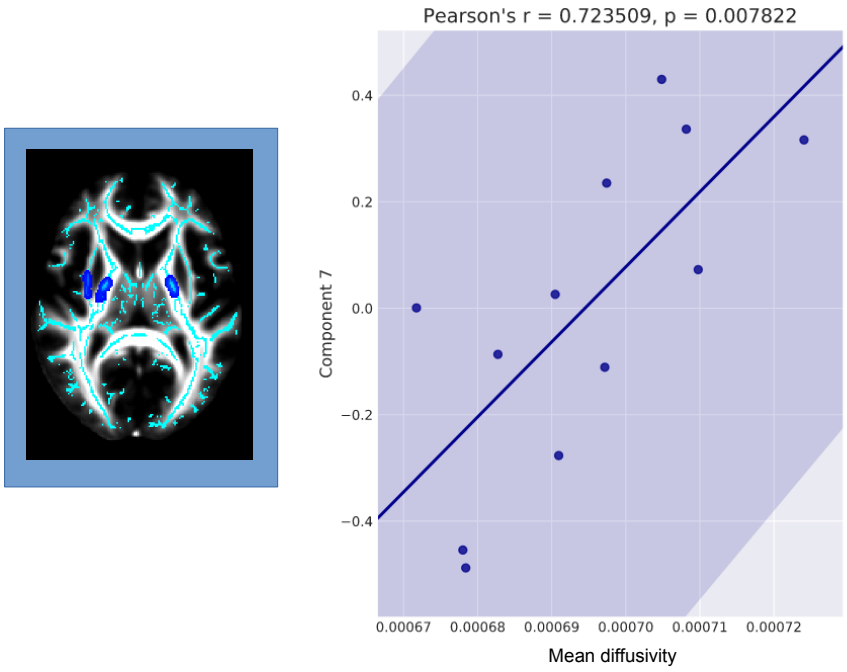

Figure 5.11. Scatter plot of the significant correlation between UHDRS sparse principal component 7 and the average mean diffusivity values across the significant TBSS cluster (blue inset on far left) testing for significant differences in both patient groups, i.e. Huntington's disease and Parkinson's disease, compared with both healthy control groups. This TBSS cluster comprises the posterior limb of the internal capsule, and the external/extreme capsule.

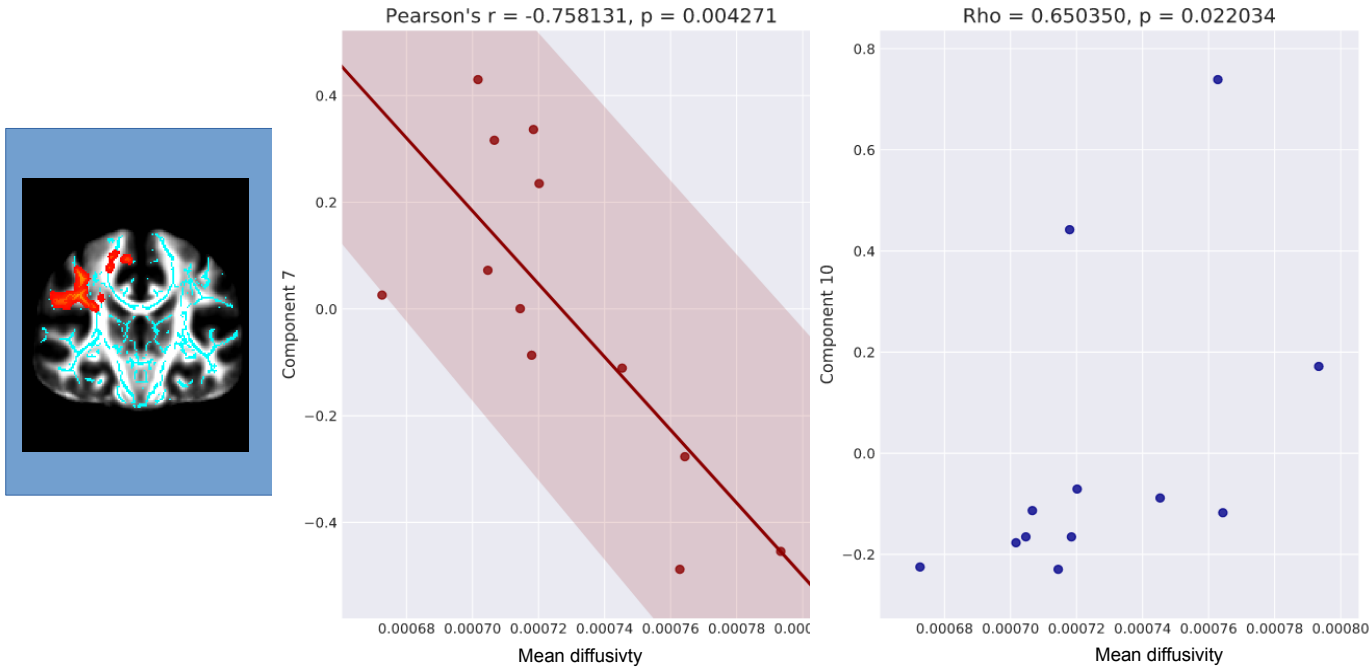

Figure 5.12. Scatter plots of the significant correlations between UHDRS sparse principal components 7 and 10, and the average mean diffusivity values across the trend TBSS cluster (blue inset on far left) testing for significant differences between patients with Huntington's disease and Parkinson's disease relative to their matched control groups in widespread parts of the white matter including the superior longitudinal fasciulus.

There was a trend towards a significant correlation between the average FA from the trend TBSS cluster testing for differences between both patient groups, i.e. Huntington's and Parkinson's disease, and their healthy controls and UPDRS component 9 (Pearson's $r = -0.456$, $p = 0.087$, **Figure 5.13**). There was a significant correlation between the average MD from the trend TBSS cluster testing for differences between patient groups with Huntington's disease and Parkinson's disease relative to their healthy controls and UPDRS component 10 (Spearman's $\rho = -0.550$, $p = 0.033$, **Figure 5.14**).

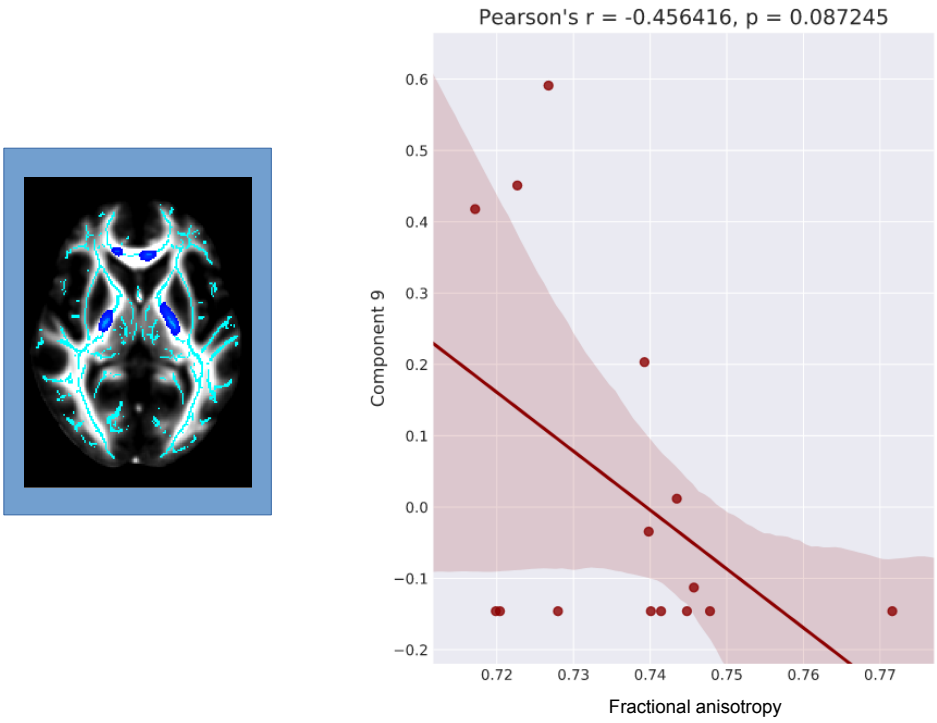

Figure 5.13. Scatter plot of the trend correlation between UPDRS sparse principal component 9 and the average fractional anisotropy across the trend TBSS cluster (blue inset on far left) testing for significant differences between both patient groups, i.e. patients with Huntington's disease and Parkinson's disease, relative to their matched control groups in the bilateral posterior limb of the internal capsule, and the genu of the corpus callosum.

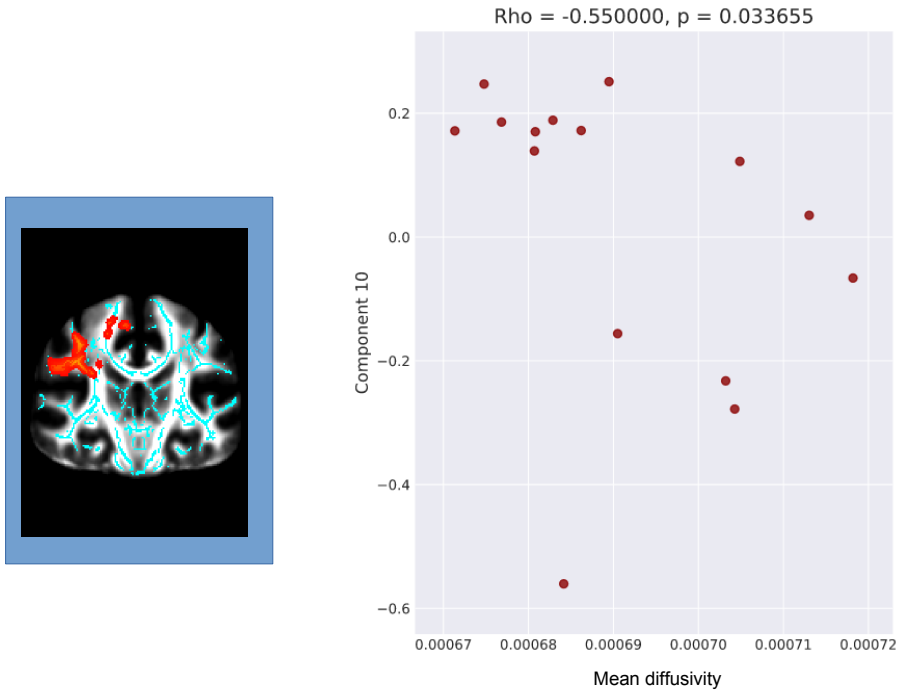

Figure 5.14. Scatter plot of the significant correlation between UPDRS sparse principal component 10 and the average mean diffusivity across the trend TBSS cluster (blue inset on far left) testing for significant differences between patients with Huntington's disease and Parkinson's disease relative to their matched control groups in the superior longitudinal fasciculus.

5.3.3 Correlations of imaging outcomes with latent variables from exploratory factor analysis

5.3.3.1 Correlations of imaging outcomes with latent variables from exploratory factor analysis within the Huntington's disease group

There was a significant correlation between the average FA extracted from the significant TBSS cluster for the difference between patients with HD and matched controls, and the UHDRS component 3 (Spearman's $\rho = 0.643$, $p = 0.024$, **Figure 5.15**).

There was a significant correlation between the average FA extracted from the trend TBSS cluster testing for differences in both patient groups, i.e. patients with Huntington's disease and Parkinson's disease and the matched control groups, and the UHDRS component 6 (Pearson's $r = 0.670$, $p = 0.017$, **Figure 5.16**).

There were trends towards correlations between the average FA extracted from the significant TBSS cluster testing for differences between patients with Parkinson's disease and Huntington's disease relative to their matched controls (PdvsHC vs HdvsHC), and the UHDRS component 1 (Spearman's $\rho = -0.545$, $p = 0.066$), the UHDRS component 3 (Spearman's $\rho = 0.510$, $p = 0.089$), and the UHDRS component 9 (Spearman's $\rho = -0.517$, $p = 0.084$, **Figure 5.17**).

There was a significant correlation between the average MD, extracted from the significant TBSS cluster for the difference between patients with HD and matched controls, and the UHDRS component 3 (Spearman's $\rho = -0.601$, $p = 0.038$), as well as a trend towards a correlation between MD from the same cluster and UHDRS component 8 (Pearson's $r = -0.514$, $p = 0.086$, **Figure 5.18**).

There was a significant correlation between the average MD, extracted from the significant TBSS cluster testing for differences in both patient groups, i.e. patients with Huntington's and Parkinson's disease compared with controls, and the UHDRS component 10 (Spearman's $\rho = -0.580$ $p = 0.047$, as well as a trend towards a correlation between MD from the same cluster and UHDRS component 1 (Spearman's $\rho = -0.551$, $p = 0.058$, **Figure 5.19**).

There was a significant correlation between MD, extracted from the the trend TBSS cluster testing for differences between patients with Huntington's disease, and Parkinson's disease relative to their matched controls, and the UHDRS component 3 (Spearman's $\rho = -0.636$, $p = 0.026$, **Figure 5.20**).

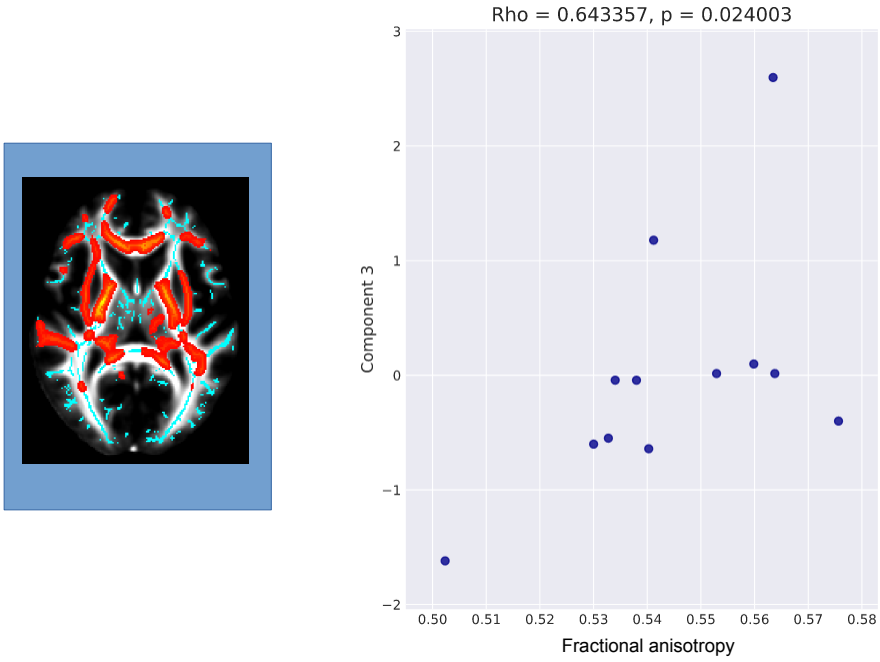

Figure 5.15. Scatter plot of the significant correlation between UHDRS latent variable 3 from factor analysis and the average fractional anisotropy values across the significant TBSS cluster (inset with the blue border on far left) for the comparison between patients with Huntington's disease and healthy controls in widespread parts of the white matter including the posterior limb of the internal capsule, and the genu of the corpus callosum.

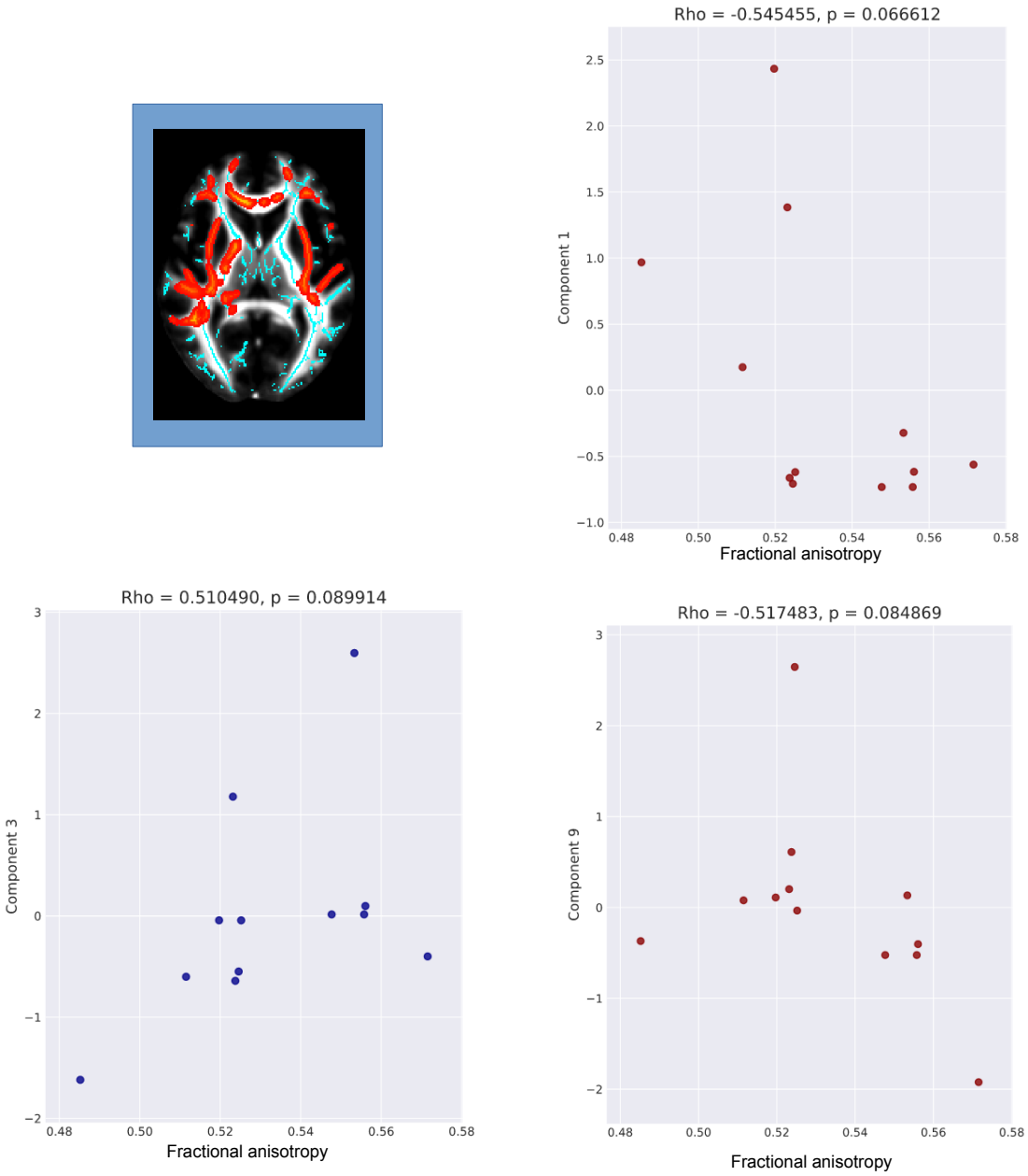

Figure 5.16. Scatter plots of the trends towards correlations between latent variables 1, 3 , and 9 from UHDRS factor analysis and the average fractional anisotropy values across the significant TBSS cluster (upper left inset with the blue border) testing for significant differences between patients with Huntington's disease

and Parkinson's disease relative to their healthy controls. This TBSS map comprises wide-spread parts of the white matter including the posterior limb of the internal capsule, and the genu of the corpus callosum.

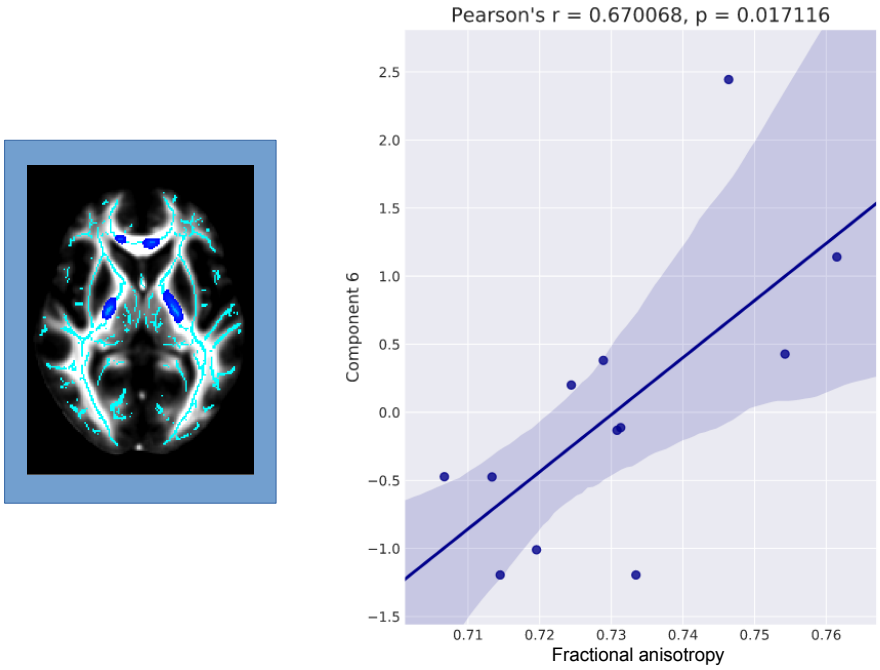

Figure 5.17 Scatter plot of the significant correlation between latent variable 6 from UHDRS factor analysis, and the average fractional anisotropy values across the trend TBSS cluster (inset with the blue border on far left) testing for significant differences in both patient groups, i.e. Huntington's disease and Parkinson's disease, compared with both healthy control groups. This TBSS cluster comprises the posterior limb of the internal capsule, and parts of the genu of the corpus callosum.

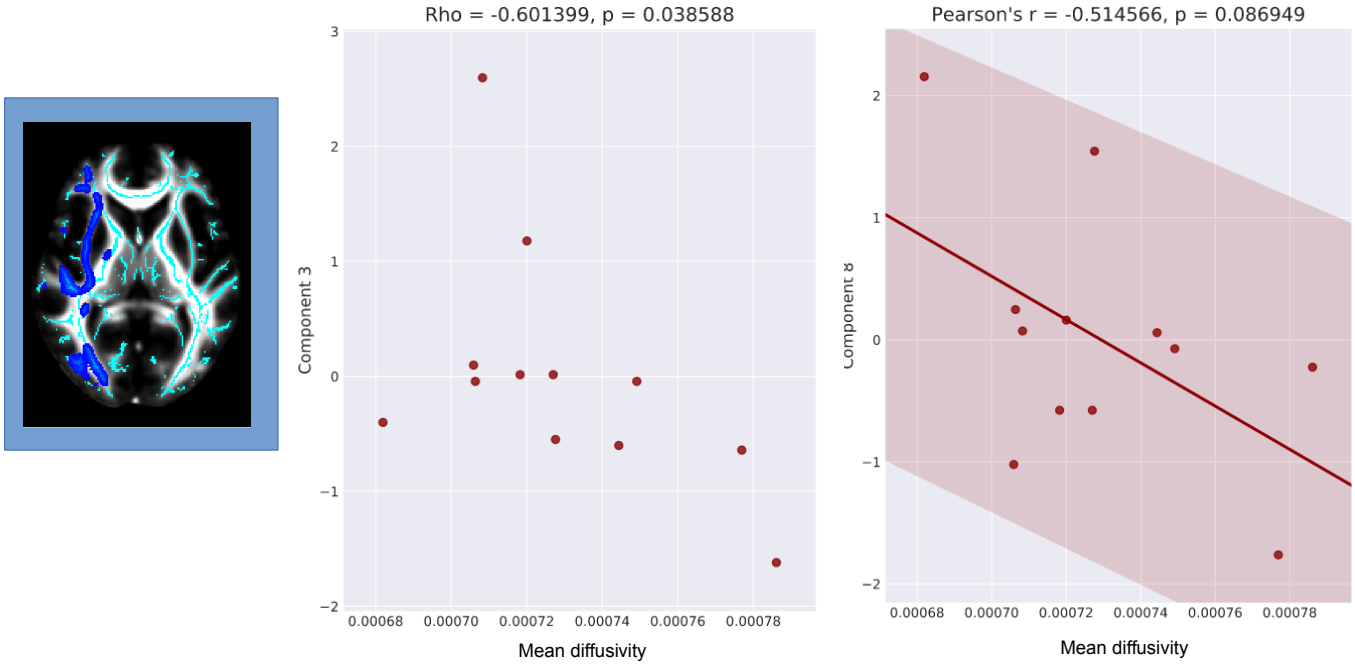

Figure 5.18. Scatter plots of the significant/trend correlations between latent variables 3 and 8 from factor analysis, and the average mean diffusivity values across the significant TBSS cluster (blue inset with the blue border on far left) for the comparison between patients with Huntington's disease and healthy controls in the right posterior limb of the internal capsule, the right external/extreme capsule, and the right superior longitudinal fasciculus.

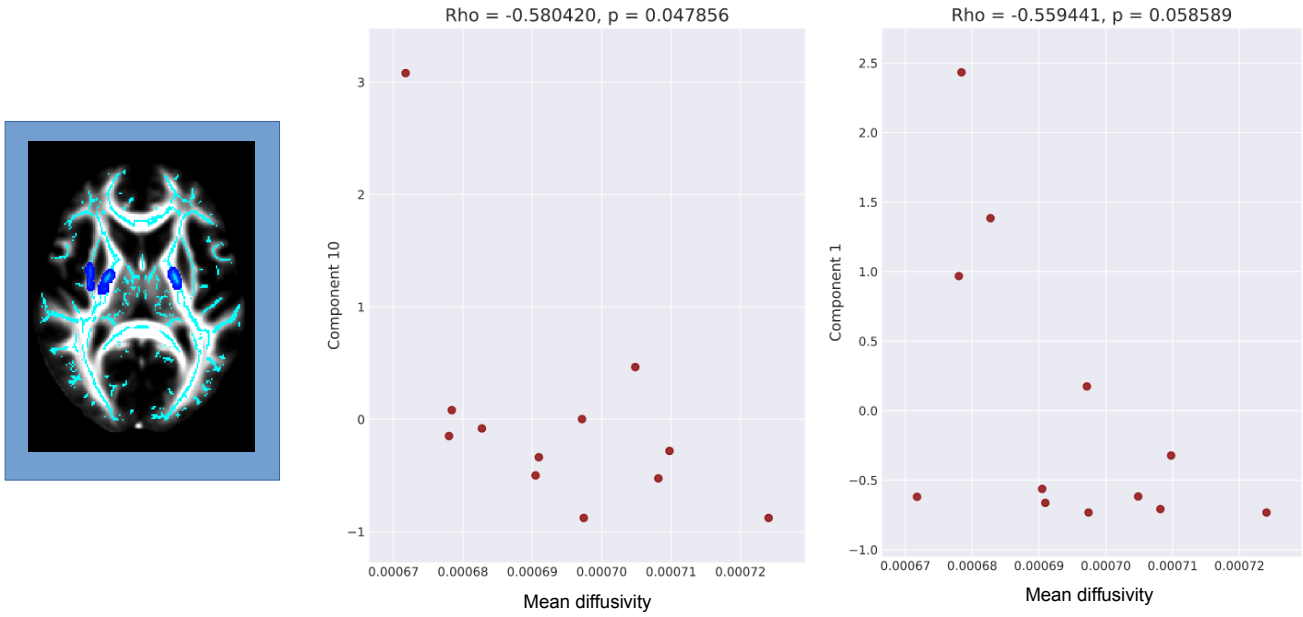

Figure 5.19 Scatter plot of the significant/trend correlations between latent variables 10 and 1 from the UHDRS factor analysis, and the average mean diffusivity values across the significant TBSS cluster (inset with the blue border on the far left) testing for significant differences in both patient groups, i.e. Huntington's disease and Parkinson's disease, compared with both healthy control groups. This TBSS cluster comprises the posterior limb of the internal capsule, and the external/extreme capsule.

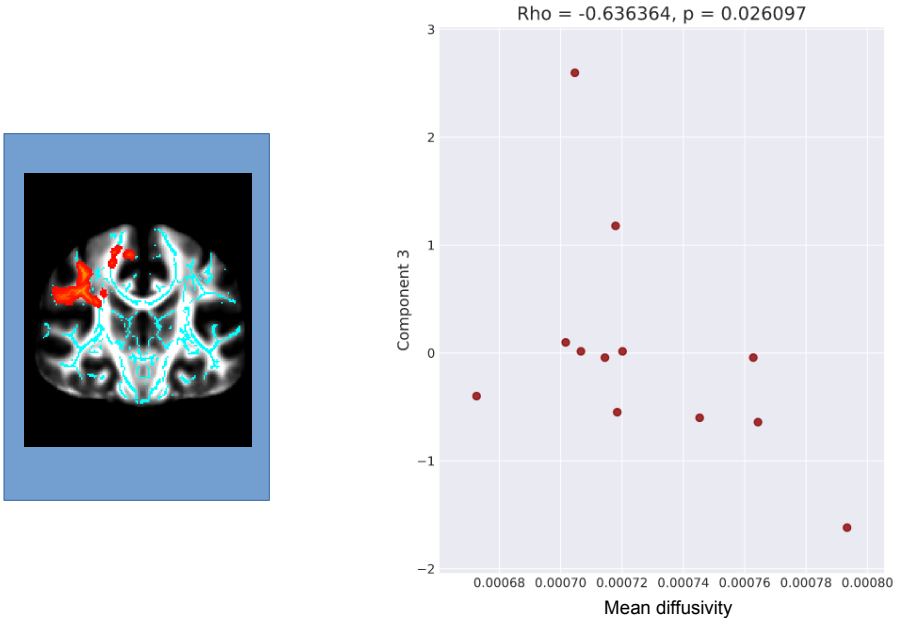

Figure 5.20 Scatter plot of the significant correlation between latent variable 3 from UHDRS factor analysis, and the average mean diffusivity values across the trend TBSS cluster (inset with the blue border on far left) testing for significant differences between patients with Huntington's disease and Parkinson's disease relative to their matched control groups in widespread parts of the white matter including the superior longitudinal fasciculus.

5.3.3.2 Correlations of imaging outcomes with latent variables from exploratory factor analysis within the Parkinson's disease group

There was a significant correlation between the average FA, extracted from the significant TBSS cluster, testing for differences between patients with Parkinson's and Huntington's disease relative to their matched controls ($PDvsHC_{PD}$ vs $HDvsHC_{HD}$) and the UPDRS component 2 (Spearman's ρ = -0.535, p = 0.039, **Figure 5.21**). There was a significant correlation between the average FA, extracted from the trend TBSS testing for differences in both patients groups, i.e. patients with Huntington's and Parkinson's disease relative to their matched controls (HC vs HD and PD), and the UPDRS component 4 (Spearman's ρ = -0.753, p = 0.001, **Figure 5.22**).

There was a significant correlation between the average MD, extracted from the significant TBSS cluster testing for differences in both patients groups, i.e. patients with Huntington's and Parkinson's disease relative to their control groups (HD and PD vs. HC) and the UPDRS component 3 (Pearson's r = 0.673, p = 0.005, **Figure 5.23**). There were trends towards a correlation between the average MD, extracted from the trend TBSS cluster testing for differences between patients with PD and age-matched controls (PD vs HC), and the UPDRS component 3 (Pearson's r = 0.464, p = 0.080, as well as the UPDRS component 8 (Spearman's ρ = -0.450 p =

0.092, **Figure 5.24**). There was a significant correlation between the average MD, extracted from the trend TBSS cluster, testing for differences between patients with Huntington's disease and Parkinson's disease relative to their matched controls ($HDvsHC_{HD}$ vs $PDvsHC_{PD}$), and the UPDRS component 3 (Pearson's r = 0.603, p = 0.017, **Figure 5.25**).

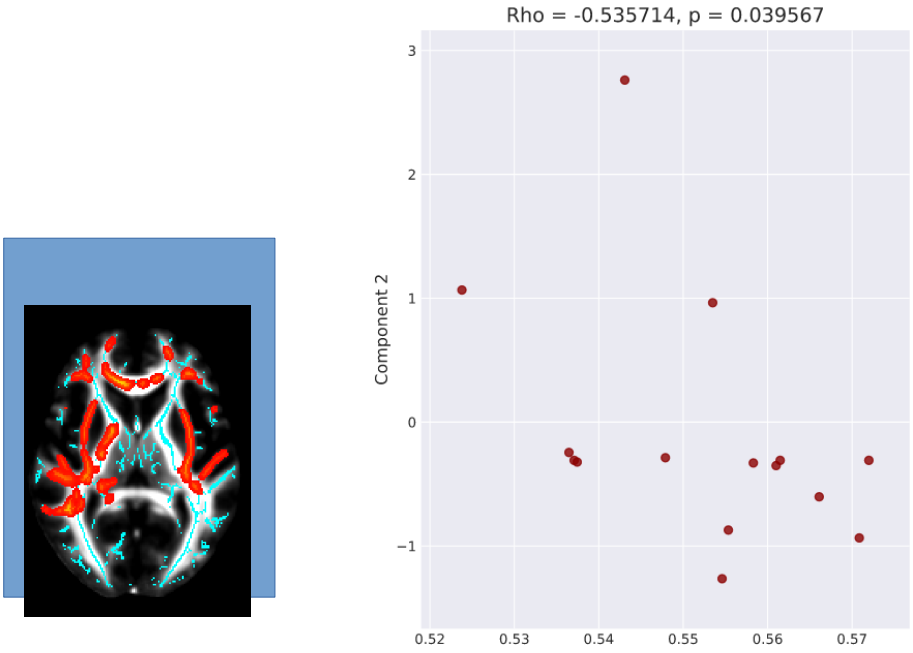

Fractional anisotropy

Figure 5.21. Scatter plot of the significant correlations between latent variable 2 from UPDRS factor analysis and the average fractional anisotropy values across the significant TBSS cluster (inset with the blue border on far left) testing for significant differences between patients with Huntington's disease and Parkinson's disease relative to their healthy controls. This TBSS comprises wide-spread parts of the white matter including the posterior limb of the internal capsule, and the genu of the corpus callosum.

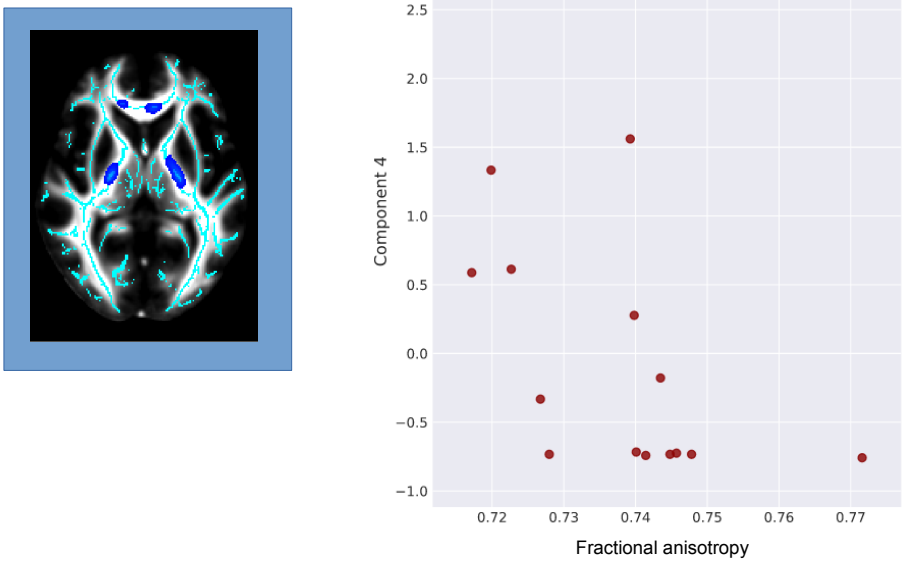

Figure 5.22. Scatter plots of the significant correlation between latent variable 4 from UPDRS factor analysis and the average fractional anisotropy across the trend TBSS cluster (blue inset with the blue border on far left) testing for significant differences between both patient groups, i.e. patients with Huntington's disease and Parkinson's disease, relative to their matched control groups in the bilateral posterior limb of the internal capsule, and the genu of the corpus callosum.

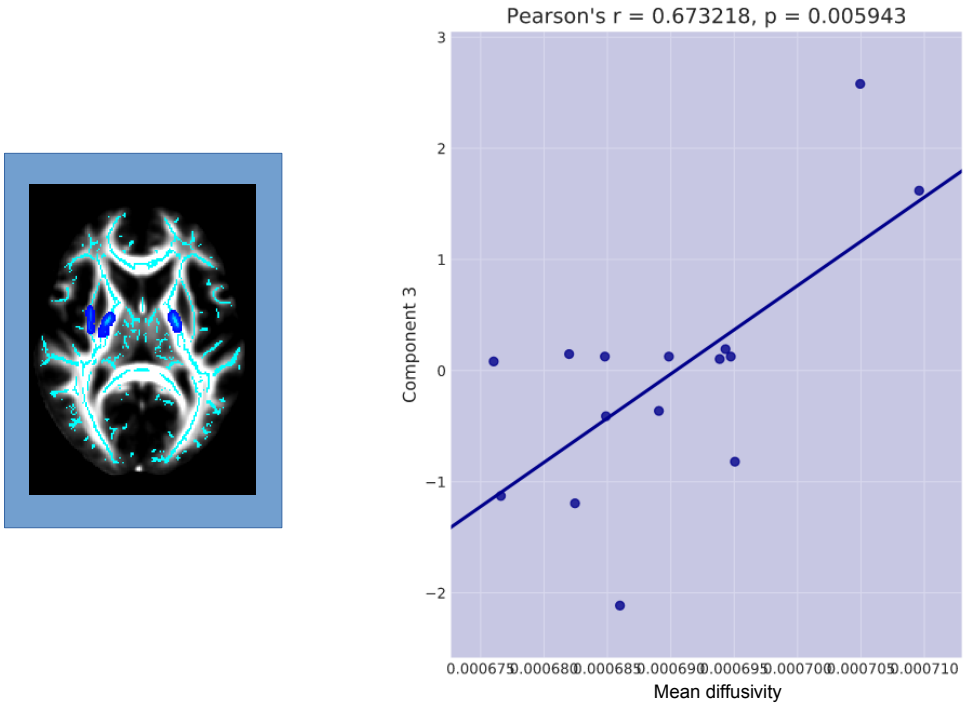

Figure 5.23. Scatter plot of the significant correlations between latent variable 3 from UPDRS factor analysis the average mean diffusivity values across the significant TBSS cluster (blue inset with the blue border on far left) testing for significant differences in both patient groups, i.e. Huntington's disease and Parkinson's disease, compared with both healthy control groups. This TBSS cluster comprises the bilateral posterior limb of the internal capsule, and the left external/extreme capsule.

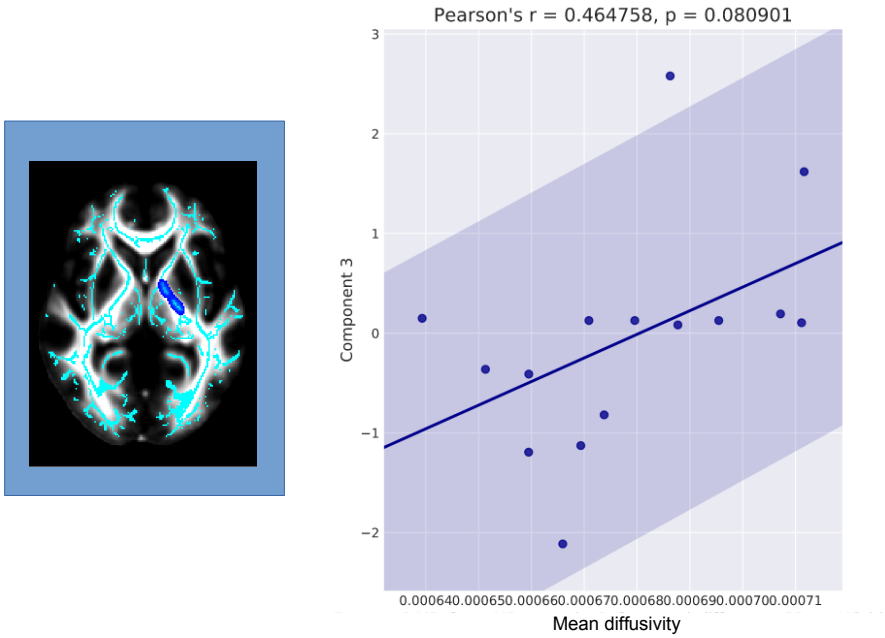

Figure 5.24. Scatter plot of the trend towards a significant correlation between latent variables 3 from UPDRS factor analysis and the average mean diffusivity across the trend TBSS cluster (inset with the blue border on far left) for the comparison between patients with Parkinson's disease and matched healthy controls in the left posterior limb of the internal capsule.

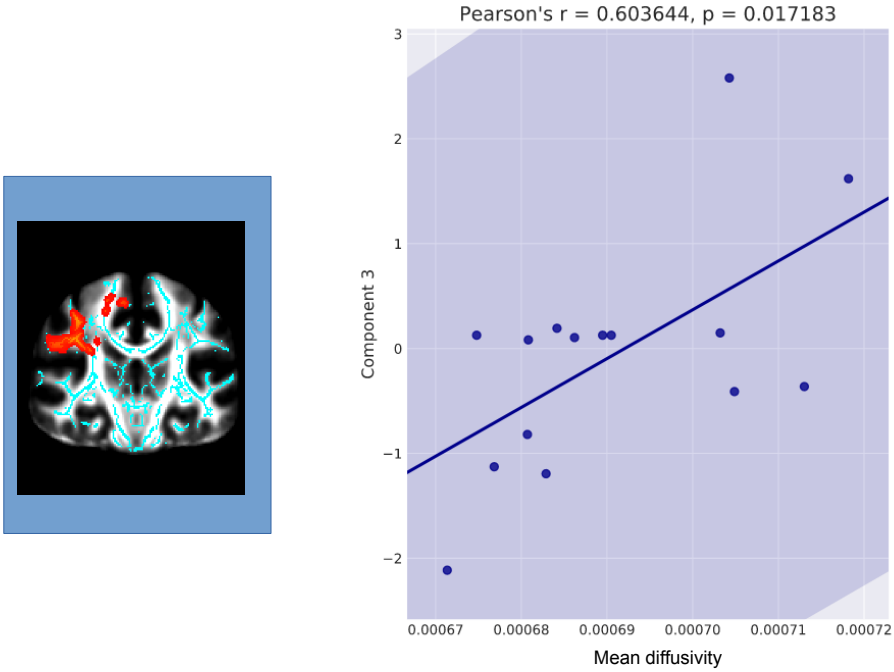

Figure 5.25. Scatter plot of the significant correlation between latent variable 3 from UPDRS factor analysis, and the average mean diffusivity values across the trend TBSS cluster (inset with the blue border on far left) testing for significant differences between patients with Huntington's disease and Parkinson's disease relative to their matched control groups in widespread parts of the white matter including the superior longitudinal fasciulus.

5.4. Discussion

In this chapter, I have investigated alterations in the micro-structure of the white matter in two basal ganglia disorders that are found at the opposite end of the spectrum of movement disorders: Huntington's, and Parkinson's disease. To the best of our knowledge, this is the first diffusion MRI study that directly compared both patient groups. This is also one of the few studies (e.g. (Plantinga *et al.*, 2018)) that used ultra-high-field diffusion imaging at 7 Tesla in Parkinson's disease, and the only 7 Tesla diffusion MRI study in Huntington's disease.

The strong, widespread abnormalities in both diffusion metrics, mean diffusivity and fractional anisotropy, seen in HD when compared with age matched controls are similar to previous research with respect to their correlative neuroanatomy. Indeed, the posterior limb of the internal capsule and the external capsule contain corticostriatal fibers (Schmahmann and Pandya, 2009). These fibers are part of the direct and indirect basal ganglia pathway and known to degenerate in HD. Widespread decreases in FA have been previously found in early HD and patients with presymptomatic HD (Rosas *et al.*, 2006a; Della Nave *et al.*, 2010b). However, it should be noted that the significant difference in MD between patients with HD and age-matched controls seen in the right external/extreme capsule should be

interpreted with caution, since the external and extreme capsules cannot be distinguished using single-shell DTI data (Oishi *et al.*, 2010; Qiu *et al.*, 2012), they can only be distinguished from each other using multi-shell (i.e. with several b-values) diffusion spectrum imaging (q-space imaging) (Mars *et al.*, 2016). In addition, the effect might also be driven due to a partial volume effect that involves the gray matter of the claustrum (not seen on DTI images).

The posterior limb of the internal capsule also contains fibers of the pyramidal tract (cortico-spinal tract) that is known to degenerate in animal models of HD. These alterations in both MD and FA were found to be associated with components from the UHDRS sparse PCA analysis and the exploratory factor analysis, that were combinations of both cognitive and motor symptoms. The right superior longitudinal fasciculus is involved in visuo-spatial attention, and higher aspects of motor behavior, including fine tuning of movements requiring somaesthetic information (via the connection between parietal cortex and SMA/PMC through SLF-I), whereas the left superior longitudinal fasciculus is part of the the language network(Schmahmann *et al.*, 2008; Thiebaut de Schotten *et al.*, 2011; Kljajevic, 2014). This might explain why the effect seen in the superior longitudinal fasciculus when looking at the MD was lateralized to the right hemisphere. Similarly, previous research showed that FA was lower when comparing preHD subjects with healthy controls in the right superior

longitudinal fasciculus, but bilaterally for the comparison between patients with clinical HD and healthy controls (Phillips *et al.*, 2014).

Significant differences in fractional anisotropy alterations were seen in HD and PD in widespread parts of the white matter and several parts of the corpus callosum, whereby HD had lower FA compared to their matched controls, and PD had higher FA. These findings are consistent with the hypothesis that HD is a cortical disconnection disease, characterized by widespread loss of connections in the corpus callosum (Rosas *et al.*, 2010). Here HD had lower FA compared to their matched controls, and PD had higher FA compared with their age-matched controls. The higher FA in PD might be associated with inflammatory processes that then render the white matter more isotropic. Indeed, previous research showed that white matter damage in PD was associated with systemic markers of inflammation, however FA was lower when compared with controls (Chiang *et al.*, 2017).

We found common abnormalities in HD and PD (only at uncorrected levels in PD) in the posterior limb of the internal capsule, which shows up both in FA and MD, as well as the right external capsule (MD). In the Huntington's disease group, higher mean diffusivity was associated with sparse principal component 7 that loaded on hand/finger movements and the symbol digit test (non-verbal intelligence), thereby

indicating that the effect seen in the imaging data is related to both motor and cognitive symptoms.

Since MD was significantly higher in the patient groups whereas the FA was slightly lower (trend), these findings are indicative of degeneration of the main tracts found in the posterior limb of the internal capsule, i.e. the corticospinal and corticostriatal tracts, rather than degeneration of the lenticulothalamic tract, which would have resulted in both higher MD, and FA due to the characteristic geometric properties underlying the tissue microstructure. Indeed, if the predominant tracts degenerate diffusion is less restricted (higher mean diffusivity) and less directed along the direction of the degenerated tracts (lower fractional anisotropy). By contrast, if the secondary fiber tracts degenerate diffusion is also less restricted (higher mean diffusivity), but even more directed along the directions of the degenerated tracts (higher fractional anisotropy, see **Figure 5.26**)

Similar to our findings, a meta analysis in PD showed altered MD in the internal capsule (Atkinson-Clement *et al.*, 2017), and fractional anisotropy has previously been found to be increased in presymptomatic/early Huntington's disease (Rosas *et al.*, 2006b),. In contradistinction to these previous studies, we have here provided for the first time a direct comparison of both HD and PD.

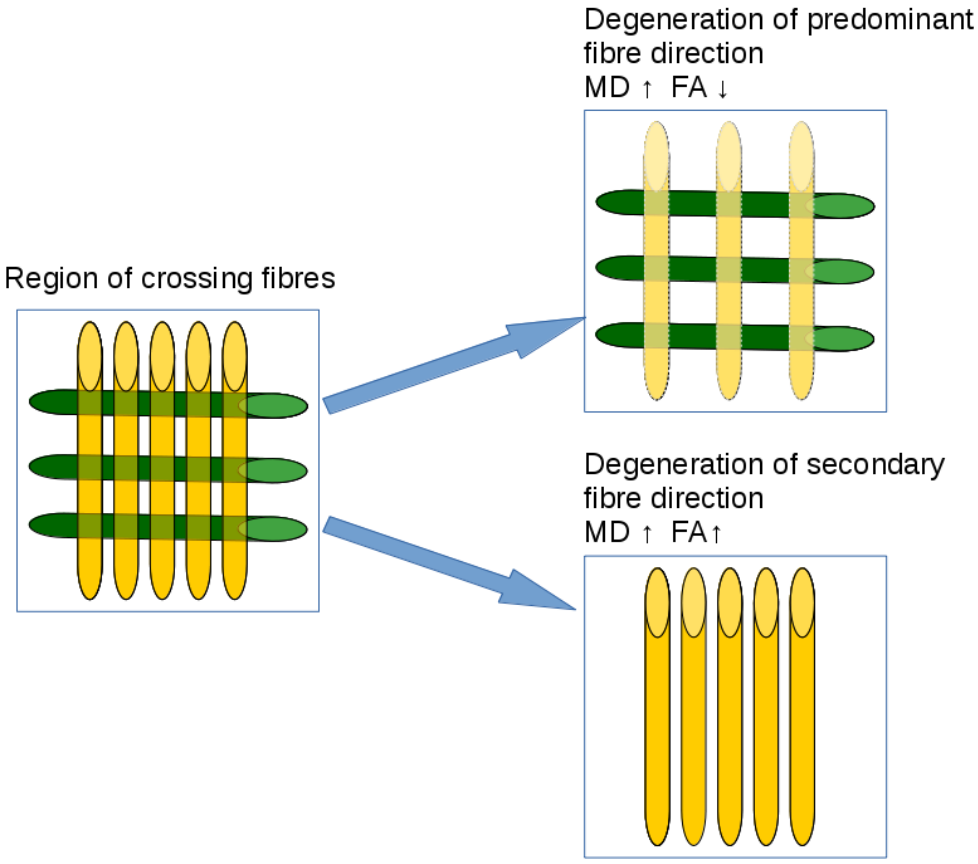

Figure 5.26. Schematic drawing explaining the change of diffusion metrics in regions of crossing fibers. In a region of crossing fibers, such as the posterior limb of the internal capsule, several fiber populations are present, and one of them is the predominant fiber direction, i.e. the cortico-spinal tract. As a result diffusion is highly restricted (low MD), and relatively highly anisotropic when compared with regions with no predominant fiber direction. In this case, degeneration of the predominant fiber direction, i.e. the cortico-spinal tract, results in less diffusion restrictions (higher MD), and lower anisotropy, since the fiber directions are now

relatively uniform (upper arrow). By contrast, degeneration of the secondary fiber direction also results in higher diffusion restrictions, but higher anisotropy, since there is now only one strong fiber direction, the predominant fiber direction left (lower arrow).

The decrease in FA in the genu of the corpus callosum is indicative of degeneration of inter-hemispheric connections among frontal areas. These findings are similar to what has been seen in the preHD study (chapter 2), where lower FA was found in the genu of the corpus callosum when looking at the data cross-sectionally, but longitudinal effects were confined to the splenium of the corpus callosum. Similar to our findings, previous cross-sectional research found lower FA in the genu of the corpus callosum in PD, but also in the splenium of the corpus callosum (Rosas *et al.*, 2010).

Despite these promising findings the present study has several limitations that should be mentioned. The sample size of the study is still small, because the recruitment of the full sample is still running. However, since we found significant effects despite the small sample size, it is likely that our study underestimates alterations in the white matter structure in Huntington's and Parkinson's disease, rather than being a false positive result (Friston, 2012). Since the sample size is still small, the post-hoc

correlations were not corrected for multiple comparisons, and should therefore be considered to be an exploratory analysis.

Since sparse principal components and latent variables from factor analysis were correlated with averaged values, extracted from statistical non-parametric maps, there is always the possibility of introducing a voodoo bias or circularity bias by carrying out interference on statical entities, rather then in an a-priori hypothesis-driven way. However, since correlations were carried out within patient groups that are orthogonal to the statistical hypotheses for the voxel-wise inference, i.e. they were carried out separately for Huntington's and Parkinson's disease patients, it is unlikely that our analysis approach would have caused voodoo correlations. By contrast, voxel-wise correlations of imaging data with sparse components and latent variables would have been hard to interpret due to the lack of any direct group inference.

A further limitation was the factor structure and loading matrix were derived from the given data set, rather than using a larger data set to derive the loading matrix, and apply it to the present data. This inevitability results in unreliable latent variables, since the number of features exceeds the number of subjects, therefore the factor structure we have identified rather reflects idiosyncrasies of this specific sample.

In conclusion, we have found distinct alterations in diffusion metrics in the right superior longitudinal fasciculus and in parts of the corpus callosum in two diseases at the opposite end of the spectrum of movement disorders: Huntington's and Parkinson's disease. Huntington's disease seems to be clearly a disconnection disease with lower FA in most parts of the corpus callosum. These alterations were associated with sparse principal components and latent factors from UHDRS/UPDRS exploratory factor analysis, thereby suggesting that they capture both symptoms in the motor and cognitive domain. Similar alterations in both diseases, i.e. Huntington's and Parkinson's disease, were found in the genu of the corpus callosum that is well known to have an integrative function in the motor system, because it provides inter-hemispheric connection to the motor cortices.

Chapter II.6: Probabilistic tractography of the hyper-direct pathway and connectivity-based parcellation of the subthalamic nucleus in early Huntington's and Parkinson's disease using ultra high-field diffusion MRI

6.0. Abstract

Rationale. The subthalamic nucleus is a central hub of extrapyramidal motor system, and receives direct input from the cortex through the hyperdirect pathway. In Parkinson's disease the subthalamic nucleus is known to be hyperactive, and deep brain stimulation of the subthalamic nucleus is used as a treatment option for non-responders to pharmacological therapies.

Objective. To reconstruct the hyperdirect pathway using probabilistic tractography of high-resolution 7T diffusion MRI data. To parcellate the subthalamic nucleus into motor, associative, and limbic territories based on its structural connectivity. To investigate alteration in the strength of connectivity of the hyperdirect pathway, and structural changes of the tripartite subregions of the subthalamic nucleus in two movement disorders, i.e. patients with Parkinson's disease and Huntington's disease relative to their healthy controls.

Methods. 7T structural and diffusion MRI data were acquired from 18 patients with early Parkinson's disease, and 12 patients with early Huntington's disease, and 25

healthy controls. Probabilistic tractography was used to reconstruct the hyperdirect pathway, and derive a connectivity-based parcellation of the subthalamic nucleus.

Results. Lower motor connectivity in the right hemisphere was found in the Huntington's disease group compared with their matched control group, indicating that the hyperdirect pathway might play an important role in the pathophysiology of Huntington's disease. Patients with Huntington's disease and Parkinson's disease differed in their associative territory in the left hemisphere, with the Huntington's disease being lower than their control group, and the Parkinson's disease group being higher than their matched control group. This finding might be characteristic of an under-influence of the subthalamic nucleus in basal ganglia control in Huntington's disease, and an over-influence of the subthalamic nucleus in Parkinson's disease, leading to their disease characteristic symptoms. Motor and associative territories underwent disease-specific changes in their coordinates.

Conclusions. Alteration in the subthalamic nucleus and the hyperdirect pathway were detectable using 7T diffusion MRI in early Huntington's and Parkinson's disease. These findings indicate that this pathway might play an important role in these diseases, and were consistent with a theoretical hypothesis about over-activity of the subthalamic nucleus in Parkinson's disease, and under-activity of the subthalamic nucleus in Huntington's disease.

6.1. Introduction

"Le grand lobe limbique existe, plus ou moins distinct, plus ou moins volumineux et plus ou moins complet, chez tous les mammiferes."

Paul Broca (1878) - Anatomie comparee des circonvolutions cerebrales. Le grand lobe limbique et la scissure limbique dans la serie des mammiferes

The subthalamic nucleus (STN) is a small ellipsoid-shaped deep cerebral nucleus that is found in the caudal part of the diencephalon, ventral to the zona incerta and the dorsal thalamus, dorsal to the substantia nigra and the cerebral peduncles, medial to the posterior limb of the internal capsule, and lateral to the red nucleus (**Figure 6.1**). It was first described by the French neurologist Jules Bernard Luys in 1865 (Luys, 1865; Parent, 2002) and therefore the eponyms body of Luys or corpus Luysii (French: corps de Luys) were used as synonyms for the subthalamic nucleus (**Figure 6.1**).

The STN receives inhibitory, GABAergic input from the external segment of the globus pallidus (GPe), which is part of the indirect pathway (Kita, Chang and Kitai, 1983), and excitatory, glutamatergic input from the prefrontal and limbic cortex (Kunzle and Akert, 1977; Kunzle, 1978; Monakow, Akert and Kunzle, 1978; Kitai and Deniau, 1981; Nakanishi, Kita and Kitai, 1988). The STN itself contains

excitatory, glutamatergic neurons projecting to the GPi, GPe and the SNr (Carpenter, Fraser and Shriver, 1968; Nauta and Cole, 1978; Smith, Hazrati and Parent, 1990; Parent and Hazrati, 1995).

Since the first half of the 20th century it is known that the STN plays a crucial role in movement disorders, and that unilateral lesions of the STN are at the root of hemiballism of the contra-lateral limbs, a unilateral form of involuntary, choreatic, large amplitude (ballistic) movements, as shown in post-mortem findings (Martin, 1927) and non-human primates (Whittier, 1949; Carpenter, Whittier and Mettler, 1950). Recent research indicates that the subthalamic nucleus plays a crucial role in the pathogenesis of Parkinson's disease, and showed that neurons in the subthalamic nucleus showed increased and more synchronous firing rates in patients with Parkinson's disease (Yokoyama *et al.*, 1998). By contrast, postmortem research in Huntington's disease revealed that patients exhibit 20–30% loss of neurons in the subthalamic nucleus (Lange *et al.*, 1976; Guo *et al.*, 2012), and within the framework of the basal ganglia loops lowered activity in the subthalamic nucleus in Huntington's disease has been suggested.

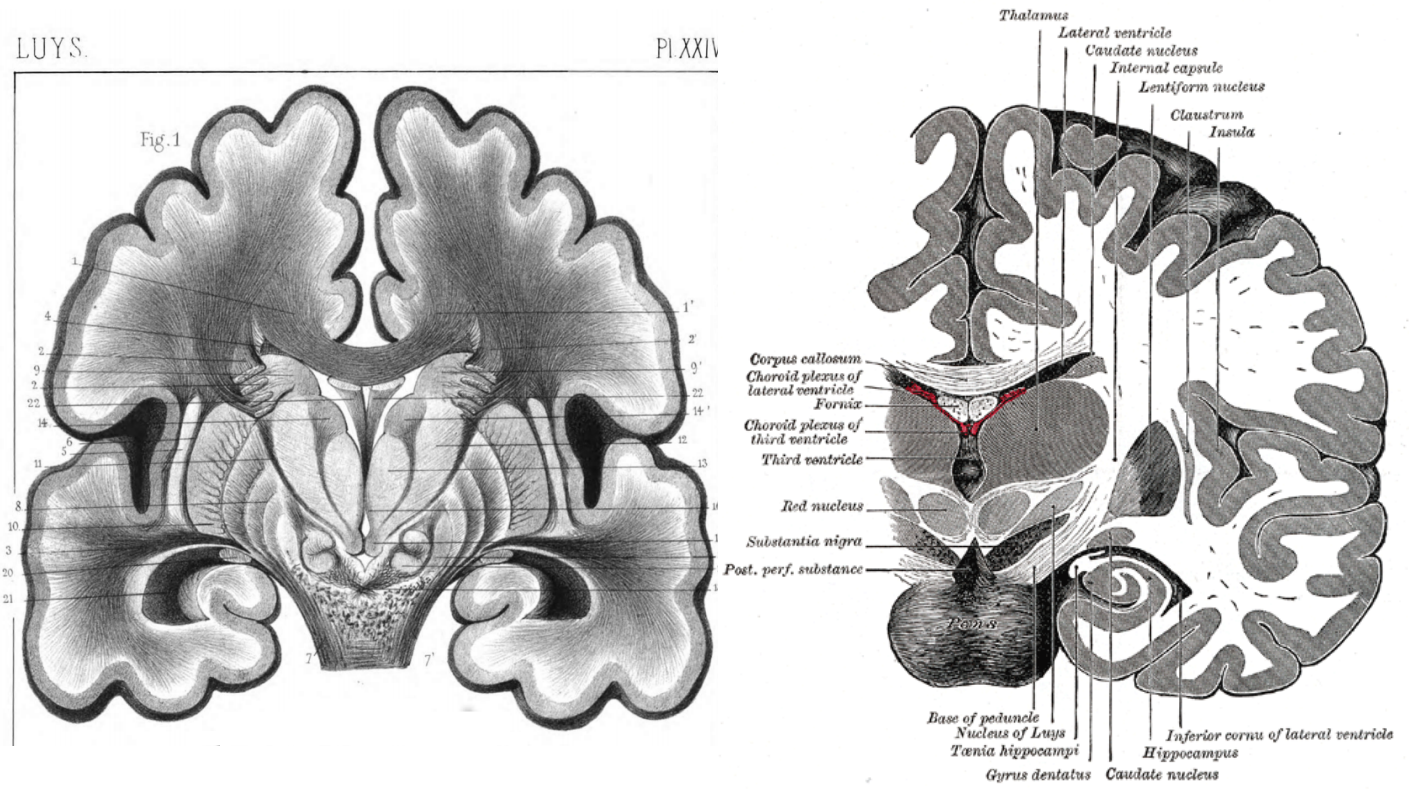

Figure 6.1. Left. Plate XXIV from Bernard Luys anatomy textbook "Recherches sur le système nerveux cérébro-spinal" (Investigations on the cerebro-spinal nervous system) (Luys, 1865). Number 19 shows the subthalamic nucleus, however, Luys incorrectly described it as "substance grise accessoire des olives superieures" (accessory gray substance of the superior olives), because he wrongly identified the red nucleus of the mesencephalon (Number 17) as the superior olive (discussed in more detail in (Parent, 2002)). Right. Figure 717 of the 1918 edition of Henry Gray's textbook "Anatomy of the human body" (more commonly know as "Gray's anatomy"). Henry Gray used the eponym "Nucleus of Luys" to refer to the subthalamic nucleus. Both figures are in the public domain.

Deep brain stimulation of the subthalamic nucleus is an effective treatment option for late-stage Parkinson's disease, however it causes various cognitive and behavioral side effects (Benabid *et al.*, 2009). The subthalamic nucleus is known to receive direct afferent input from the primary motor cortex (M1) and supplementary motor area (SMA) (Monakow, Akert and Kunzle, 1978; Nambu et al., 2000), however this hyperdirect pathway has been long-time neglected in classical models of basal ganglia dysfunctioning in movement disorders (Nambu, 2008a), and only recently direct connections from the prefrontal cortex to the subthalamic nucleus have been described in non-human primates (Kunzle and Akert, 1977; Kunzle, 1978; Monakow, Akert and Kunzle, 1978; Haynes and Haber, 2013). These connections are of limbic and associative nature, and might provide a conceptual framework explaining various side-effects associated with deep brain stimulation, such as its controversial effects on cognitive function (Wang *et al.*, 2016).

Deep brain stimulation in PD was shown to be most effective if the dorsolateral sensorimotor part of the subthalamic nucleus was targeted (Bot *et al.*, 2018). By contrast, the ventromedial part of the STN corresponds to the associative territory, and the medial part to the limbic territory (Benarroch, 2008). It has also been hypothesized that the therapeutic effect of DBS of the STN in PD is mediated by antidromal stimulation of the hyperdirect motor pathway (Chen *et al.*, 2018).

However, the description of these functional territories on the basis of stereotactic and neuroanatomical information alone does not take inter-individual differences and disease related alterations into account.

Here we have used probabilistic tractography to reconstruct the hyerdirect pathway in patients with Parkinson's and Huntington's disease, and healthy subjects, and used this information to delineate motor, limbic, and associative territories within the subthalamic nucleus, and how they are affected by disease. Probabilistic tractography is a promising tool that can be used for non-invasve connectivity-based parcellation of subcortical nuclei, i.e. the description of sub-territories within subcortical nuclei based on their structural connectivity probability with cortical areas (Behrens, Johansen-Berg, *et al.*, 2003). Using probabilistic tractography of ultra-high-field diffusion MRI data it has become feasible for the first time to reconstruct the sensorimotor, limbic, and associative hyperdirect pathways in-vivo, and this information can be used for connectivity-based parcellation of the STN which provides valuable information about the precise location of the motor territories, as well as their variability in movement disorders, and in healthy individuals.

6.2. Methods

6.2.1. Participants and study design

A detailed description of the demographic and clinical data of the patient groups, as well as the study design can be found in section 4.2.1. Compared with the sample size in chapter 4, 3 additional patients with Parkinson's disease were recruited, making the overall sample size of the Parkinson's disease group N = 18.

6.2.2. Data acquisition

The protocol and the parameters for the data acquisition are the same as already described in section 4.2.2.

6.2.3. Data processing: Probabilistic tractography

A probabilistic diffusion model was fit on the distortion and eddy-current corrected data, and crossing fibers were modeled within each voxel of the brain using bedpostx (part of FSL, with default settings) (Behrens, H. Johansen Berg, *et al.*, 2007). Probabilistic tractography was run for each subject and each hemisphere two times for each pathway (motor, limbic, associative) tracking from the cortical area to the subthalamic nucleus, and then tracking from the subthalamic nucleus to the cortical

area to yield a symmetric estimation of the streamlines that are part of the hyperdirect pathway. This approach was used to overcome the drawback that fibre tracking is a non-commutative procedure, i.e tracking from the endpoint of a tract will not automatically yield the pathway back to the intial seed region and vice-versa (D.K. Jones, 2010; Van Hecke, Emsell and Sunaert, 2015). This directly follows from the mathematical properties of fitting a streamline by integrating over a tensor field with the initial condition set to the seed voxel. Tracking in both directions and then adding the probabilistic fibre tracts will therefore give a more robust estimate of the hyperdirect pathways. Even though it is know that both inter-telencephalic neurons (IT neurons) and projection neurons (PT neurons) give rise to the basal ganglia pathways, the data analysis was confined to the reconstruction of hyperdirect pathway for each hemisphere seperately, because even at 7T single-shell diffusion MRI is most likely not suitable to correctly reconstruct the geometry of these axon collaterals due to the inability to distinguish the fiber geometry of crossing, bending, kissing, fanning, and branching fibers (Jbabdi and Johansen-Berg, 2011a).

Probtrackx2 GPU (as implemented in FSL) was run with 5,000 particles per seed voxel for the motor/associative pathway, and 100,000 particles per seed voxel for the limbic pathways using the following default settings (number of steps per sample = 2000, steplenth = 0.5, fiber threshold = 0.01, distance threshold = 0.0). To speed up

computation time of the tractography analysis, probtrackx2 was run on a graphical processing unit (GPU) using multi-thread and parallel computing (Hernandez-Fernandez *et al.*, 2016). A higher number of particles was used for the limbic pathway to account for the fact that the limbic pathway is longer when compared with the motor and associative pathways, and because a customized midsaggital exclusion mask (described below) was used for the limbic pathway thereby decreasing the chance of streamlines to reach the limbic cortex.

Each probtrackx2 run included a seed mask and way-point mask set either to the STN or to the relevant cortical mask (i.e. motor, limbic or associative cortex, as described below), as well as target masks and waypoint stop masks set to both the STN and relevant cortical masks. Waypoint stop masks were used to avoid tracking beyond the cortical or sub-cortical targets, i.e. to exclude fibers connecting e.g. the motor and the associative cortex, or fibers that descend beyond the subthalamic nucleus. An exclusion mask was used for both tractography runs to exclude fibers, (1) that go through the striatum, putamen, GPe, or GPi/SNr and are therefore part not part of the hyperdirect pathway, but part of the direct/indirect basal ganglia pathway, (2) that go through the thalamus and are therefore part of corticopetal projections of the basal ganglia system, (3) that go through the SN and are therefore part of the corticonigral/nigrocortical system, (4) that terminate or go through

cortices not used as either seed or target masks (e.g. in case of the the motor hyerdirect pathway, the limbic cortex and associative cortex were used as exclusion masks), and (5) that go through the optic nerves, fornix, or cingulum bundle in case of the limbic pathway.

The sub-cortical masks used for tractography were obtained using multi-modal image segmentation (Visser *et al.*, 2016) as described in chapter 4. The motor cortex mask consisted of the primary motor cortex (Brodmann area 4a and 4p, i.e. area gigantopyramidalis) , and the premotor cortex (Brodmann area 6, i.e. area agranularis frontalis) from the Juelich Histological Atlas (Eickhoff *et al.*, 2010). The Juelich Histological Atlas was used for the motor and premotor cortex because it is based on tissue probability maps derived from the cytoarchitectonic characteristics of these areas (Eickhoff *et al.*, 2010). The associative cortex mask consisted of area 9, area9/46dorsal, area 9/46ventral, and area 46 from the connectivity-based dorsal-frontal parcellation atlas (Sallet *et al.*, 2013), and these areas taken together form the dorsolateral prefrontal cortex in humans. The limbic cortex consisted of the inferior part of the anterior cingulate gyrus (ACC) (below z = 72), the medial-frotal cortex (MFC) from the Harvard-Oxford cortical atlas, and the subcallosal cortex from the Harvard-Oxford cortical atlas (Desikan *et al.*, 2006). These cortical masks were thresholded at the 20th percentile of the intensity range.

6.2.4. Connectivity strength

The number of successful streamlines that start at the seed mask, and reach the target mask without being discarded when fulfilling an exclusion criterion (e.g. step length, curvature threshold, fibre threshold) or hitting the exclusion masks, are commonly referred to as the waytotal. We have added the waytotals from both tractography runs, going from the subcortical seed to the cortex, and from the cortical seed to the subcortical mask to get a robust estimate of the strength of connectivity. In a second step, the sum of the waytotals was divided by the number of voxels in the subcortical seed to yield a measure of connectivity that is not biased by inter-subject variability in the seed size, i.e. to account for the fact that a higher number of seed voxels automatically results in more streamlines seeded.

6.2.5. Connectivity-based parcellation, volumetric analysis, and centre of gravity

The streamline images (called fdt paths in FSL) from both tractography runs, going from the sub-cortical seed to the cortex, and from the cortical seed to the sub-cortical target, were added to yield a combined reconstruction of the hyerdirect pathway that is not biased by asymmetrical properties of the tensor field of the fiber orientation distribution. This was done for each of the 3 functional hyper-direct

loops, i.e. the motor, limbic, and associative loop. The resulting images were then divided by the sum of the way-totals from both tractography runs, and intersected with the subthalamic nucleus, to yield a probabilistic map of connectivity strength with the relevant cortex for each voxel in the subthalamic nucleus.

Given that at a voxel size of 1x1x1 mm, voxels in the STN most likely correspond to several functional territories at the same time, a probabilistic threshold was used for the volumetric analysis rather than running a hard segmentation. For each and every subject the motor, limbic, and associative connectivity maps were thresholded at the 10th percentile of the robust intensity range of non-zero voxels. This threshold was chosen to remove voxels with low probabilities of being connected to the target cortical region from the connectivity-based parcellation maps. The volume of the functional territories within the STN was computed using these thresholded territories, and in a second step normalized by the total STN volume to account for inter-individual differences in the overall STN volume. The overlap was calculated for each combination of functional territories. The Jaccard index was calculated for each combination of functional territories as a normalized measure of similarity using the volume of the intersection of two functional territories divided by the volume of the set union of these two territories (Jaccard, 1901).

The centre of gravity (COG) was calculated for each unthresholded map as the weighted arithmetic mean of the connectivity strength (p_n) along each of the main axis of the MNI coordinate system x, y, and z, i.e. x-coordinate COG = $x_1 * p_1 \ldots + x_n * p_n$., using the FSL tool fslstats. The COG for each main axis was normalized (divided) by the length of the subthalamic nucleus along this main axis.

6.2.6. Spatial regression of tracts against diffusion metric images

Spatial regression of the combined probabilistic reconstructions of the hyper-direct pathways against the diffusion metric images (from dti fit, see chapter 4 for details) was carried out for each of the three functional loops, each hemisphere, and each diffusion metric (MD, FA, MO). Since the diffusion tensor model is not informative in regions of crossing fibers, a mask of crossing fibers was created by thresholding the FA image at 0.3. This resulted in weighted averages of diffusion metrics across the entire tract, that were used to test for between-subjects effects.

6.2.7 Statistical inference

Statistical analyses were carried out using R (version 3.2.3, The R Foundation for Statistical Computing, 2015), and python's statistical computing, machine learning packages scipy (Oliphant, 2007; McKinney, 2010), and scikit-learn (Pedregosa *et al.*,

2012), as well as python's statistical models package (stats models) (Seabold and Perktold, 2010). Permutational analyses of covariance were carried out using R's aovp() package with age as covariate, group as categorical, exogenous variable, and imaging metrics (volumes, COG, overlap indices) as endogenous variable. Generalized linear hypotheses on adjusted means were then carried out to test for differences between single patient groups and age-matched healthy control groups, as well as user-defined linear contrasts.

Generalized linear contrasts were used to test the null hypotheses that patients with HD/PD did not differ when compared with their age-matched controls:

H_0: $\mu(HD) - \mu(HC_{HD}) = 0$

$\mu(PD) - \mu(HC_{PD}) = 0$

Linear contrasts were used to test for the main effect of diagnosis, i.e. that patients did not differ when compared with healthy controls:

H_0: $[\mu(HD) + \mu(PD)] - [\mu(HC_{HD}) + \mu(HC_{PD})] = 0$

Linear contrasts were used to test for interaction effects between the diagnosis and age groups, i.e. if patients with HD differed from patient with PD when compared with their age-/gender matched healthy controls:

H_0: $[\mu(HD) - \mu(HC_{HD})] - [\mu(PD) - \mu(HC_{PD})] = 0$

Sparse PCA was used to reduce the dimensionality of the UHDRS and UPDRS questionnaire scores as previously described in chapter 4.2.4.2. In addition, we have also used exploratory factor analysis as implemented in python's scikit-learn package to reduce the dimensionality of the UHDRS and UPDRS questionnaire scores. In brief, factor analysis assumes that the UHDRS/UPDRS questionnaire scores are caused by linear transformations of lower dimensional latent factors, and random Gaussian noise. The factor analysis algorithm performs a maximum likelihood estimate of the so-called loading matrix (questionnaire scores by components matrix), the transformation of the latent variables to the observed ones, using expectation-maximization. Factor analysis was run with the following settings: number of components = 10, stopping tolerance for EM algorithm = 1e-15, maximum number of iterations = 1000000.

If significant group differences were found using the general linear contrasts, imaging outcomes were correlated with the principal components from the sparse PCA analysis. D'Agostino-Pearson K2-test was used to test if data were normally distributed. In the case of bivariate normality the Pearson product moment correlation coefficient was used, if one or both of the variables were not normally distributed the Spearman rank-order correlation was used.

6.3. Results

No significant differences in the volume of the entire left or right subthalamic nucleus were found when comparing both patient groups relative to the control groups, or when directly comparing each patient group with their matched control group (all $p > 0.05$, **Figure 6.2**). **Figure 6.3.** shows a probabilistic reconstruction of the tripartite hyperdirect pathways averaged over all subjects (both patients and healthy controls).

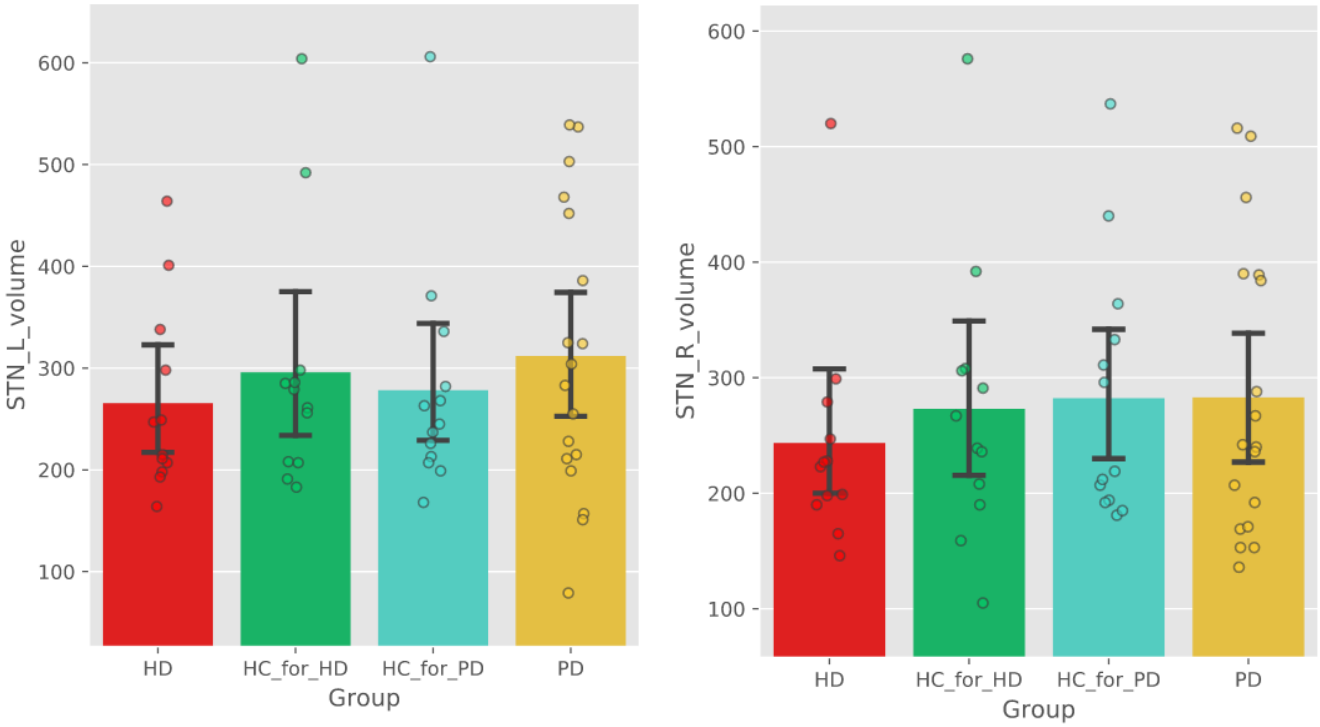

Figure 6.2. Volume (in mm^3) of the left and right subthalamic nucleus for patients with Huntington's and Parkinson's disease and their control groups.

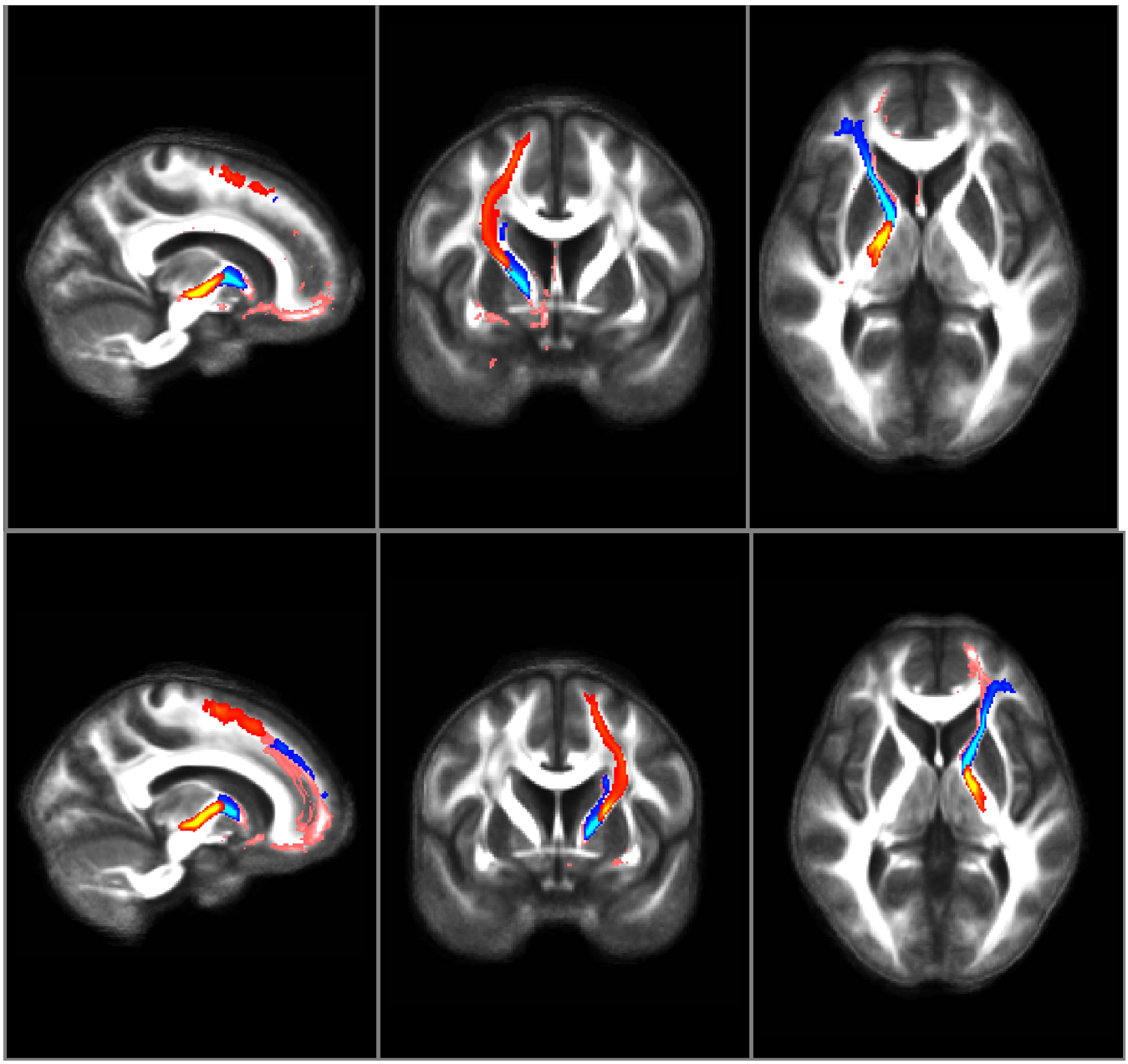

Figure 6.3. Probabilistic reconstruction of the hyperdirect pathway going from the cortex to the subthalamic nucleus in the right hemisphere (upper panel), and the left hemisphere (lower panel), average over all subjects including patient groups and healthy controls. Motor pathway (red-orange), associative pathway (blue-lightblue), and limbic pathway (pink-white).

6.3.1. Strength of connectivity in motor, limbic, and associative hyperdirect pathways

There were significant differences in the motor loop strength of connectivity, as measured by the streamline counts, in both HD and PD relative to their matched controls, lateralized to the right hemisphere (z = -2.079, uncorrected p = 0.037 *), that were also found when normalizing the motor strength of connectivity by the size of the STN seed mask (z = -2.339, uncorrected p = 0.019 *). When directly comparing HD/PD groups with their age-matched controls, it was found that this effect was mainly driven by significant differences in right motor loop connectivity between the HD group and their age-matched control group, both before (z = -2.684, p = 0.007 **), and after normalization by the STN size (z = -2.939, p = 0.003 **, see **Figure 6.4**).

No significant differences in alterations in connectivity strength were found for the left motor hyperdirect pathway before normalization or after normalization by the STN seed volume (p = 0.74, p = 1 respectively).

No significant differences in alterations of connectivity strength were found for the limbic or associative hyperdirect pathways (lowest uncorrected p-values = 0.060, and 0.066 respectively).

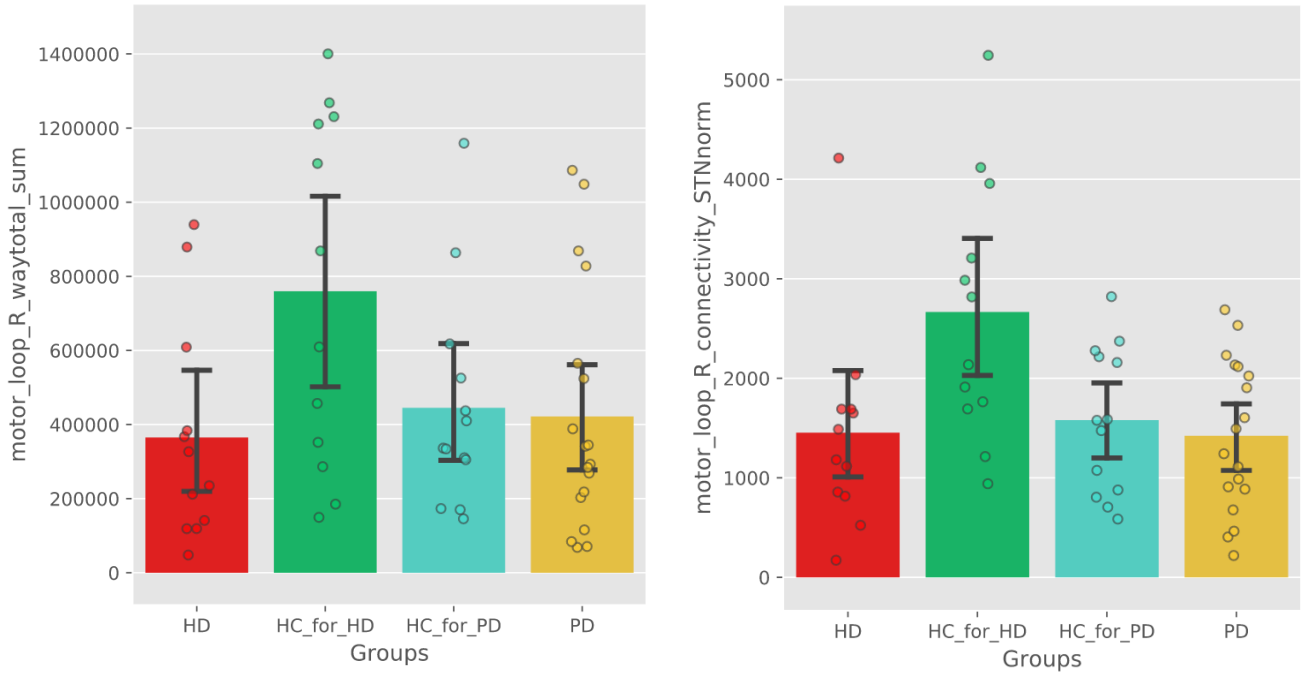

Figure 6.4. Connectivity strength, as measured by the streamline counts, in the motor hyperdirect pathway before (left), and after normalization by the subthalamic nucleus seed volume.

6.3.2. Volumetric measures of motor, associative, and limbic territories within the subthalamic nucleus

Figure 6.5 shows the probabilistic connectivity-based parcellation of the subthalamic nucleus into motor, associative, and limbic sub-territories for a typical control subject, a typical subject with Huntington's disease, and a typical subject with Parkinson's disease.

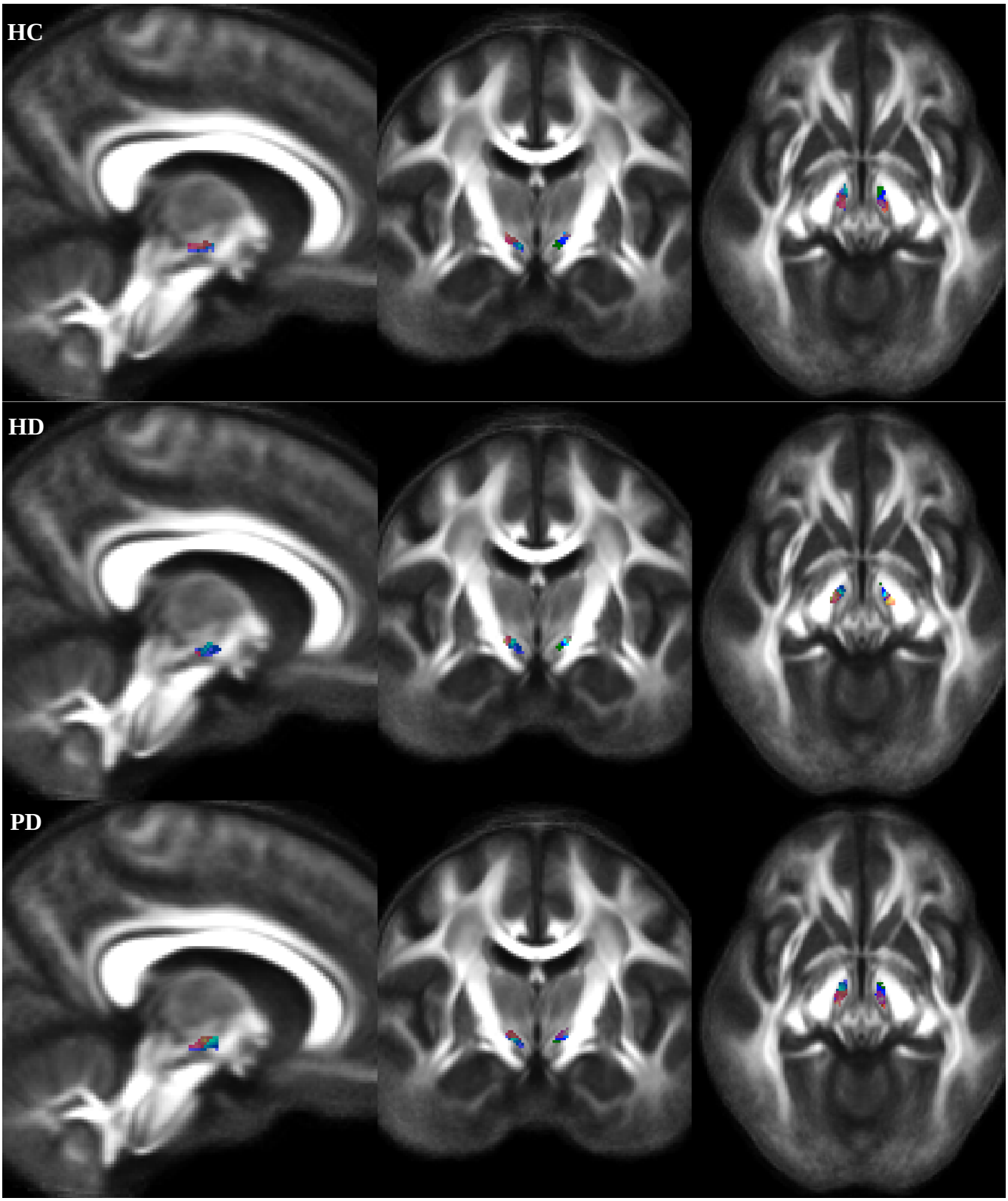
HC
HD
PD

Figure 6.5. Connectivity-based parcellation of the subthalamic nucleus into tripartite functionally segregated territories, i.e. motor (red), associative (blue), limbic (green) overlaid on the average fractional anisotropy image in standard space. HC: a typical control subject, HD: a typical subject with Huntington's disease, PD: a typical subject with Parkinson's disease

No significant differences in alterations of the volume or the volume ratio were found for the motor territory of the subthalamic nucleus in neither the left nor right hemisphere (lowest $p = 0.12$ and $p = 0.61$ respectively).

There were significant differences between the patients with HD and PD relative to their age-matched control groups in the volume of the associative territory ($z = -2.272$, $p = 0.023$ *), and the associative volume to total STN volume ratio ($z = -2.226$, $p = 0.026$ *) in the left hemisphere (**Figure 6.6**).

No significant differences between patients with HD and PD and their matched controls were found for the volume and volume ratio of the right associative territory (all $p > 0.05$).

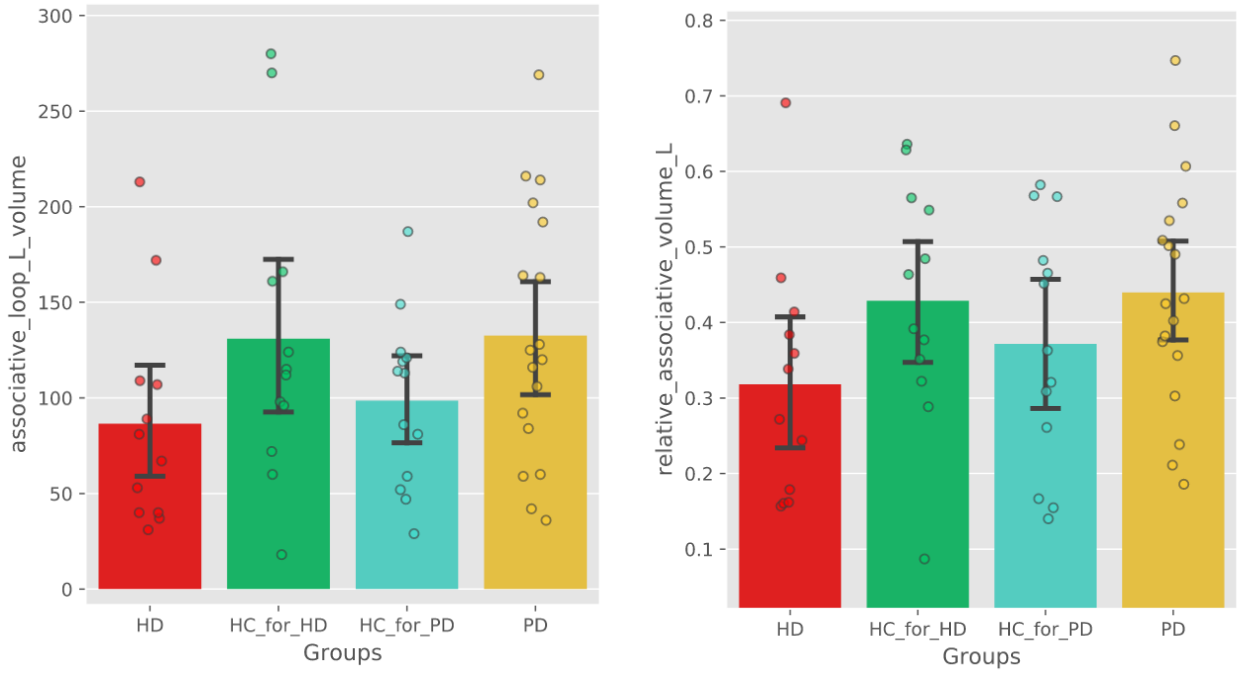

Figure 6.6. Significant differences in the volume in mm^3 (left) and volume ratio (right) of the associative territory within the subthalmaic nucleus in the left hemisphere between patients with HD and PD when compared with their age- and gender-matched controls.

There were significant differences between the patients with HD and PD relative to their age-matched control groups in the volume of the limbic territory (z = -2.486, p = 0.012 *), and the limbic volume to total STN volume ratio (z = -2.359, p = 0.018*) in the left hemisphere (**Figure 6.7**). When directly comparing the HD/PD patient groups with their age-/gender matched healthy controls, significant differences were found between the PD group and their matched controls in both the volume of the

limbic territory (z = 2.033, p = 0.042*), and the limbic volume to total STN volume ratio (z= -2.359, p = 0.018*) in the left hemisphere (**Figure 6.7**).

No significant differences between patients with HD and PD and their matched controls were found for the volume and volume ratio of the right limbic territory (all $p > 0.05$).

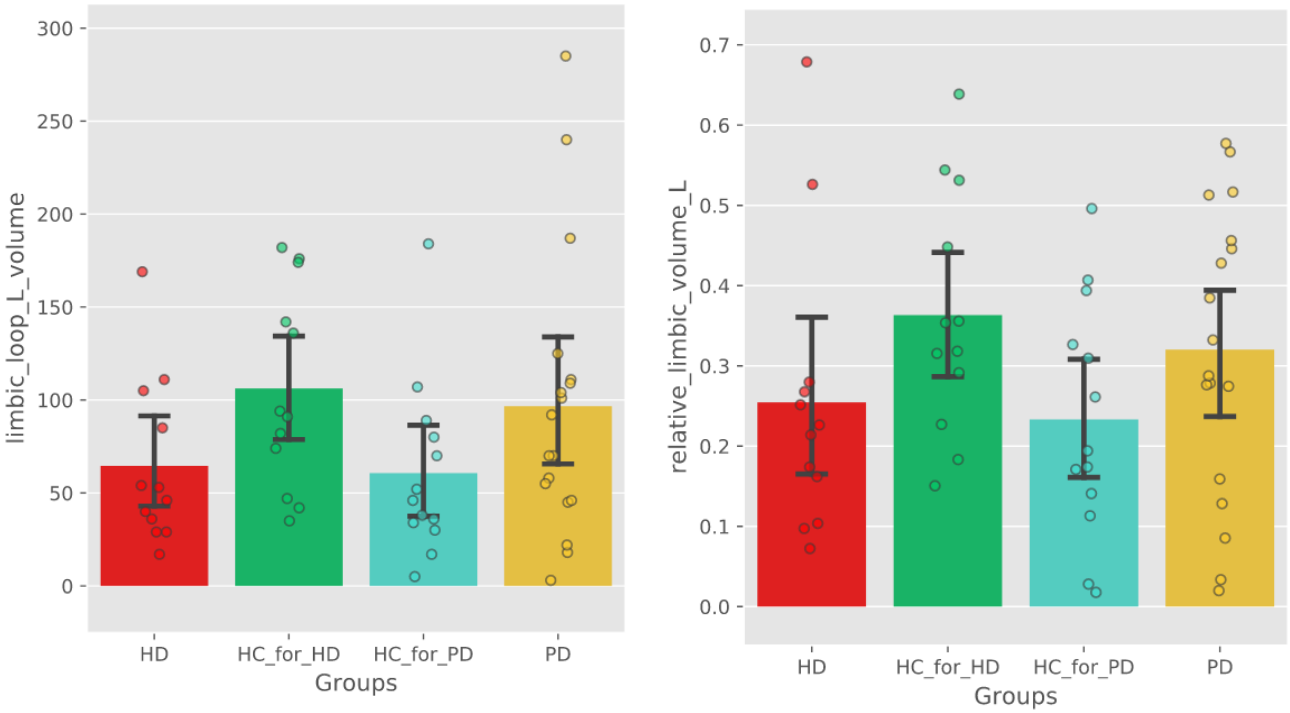

Figure 6.7 Significant differences in the volume in mm^3 (left) and volume ratio (right) of the limbic territory within the subthalamic nucleus in the left hemisphere between patients with HD and PD when compared with their age- and gender-matched controls.

6.3.3. Measures of overlap and similarity for the motor and associative territories

When calculating the overlap between limbic and motor/associative territories, and the Jaccard index using a threshold at the 10th percentile of the streamline intensity at the single subject level, several subjects did not show any overlap or had a Jaccard index of zero. Subsequently, various thresholds were tried, at both the single subject, and group level, including the 2.5th, 5th, 7.5^{th} percentiles. Even with a threshold at the 2.5th percentile, several subjects did not show any overlap or similarity, while other subjects showed perfect overlap/similarity. We therefore post-hoc decided to discard the limbic territory from the analysis of overlap/similarity, and only focus on the motor and associative territory.

There were significant differences between the patients with HD and PD relative to their age-matched control groups in the overlap between motor and associative territories (z = -2.107, p = 0.035 *) in the left hemisphere, and a strong trend towards significant differences between the patients with HD and PD relative to their age-matched control groups in the overlap between motor and associative territories normalized by the volume of the subthalamic nucleus (z = -1.957, p = 0.050, **Figure 6.8**).

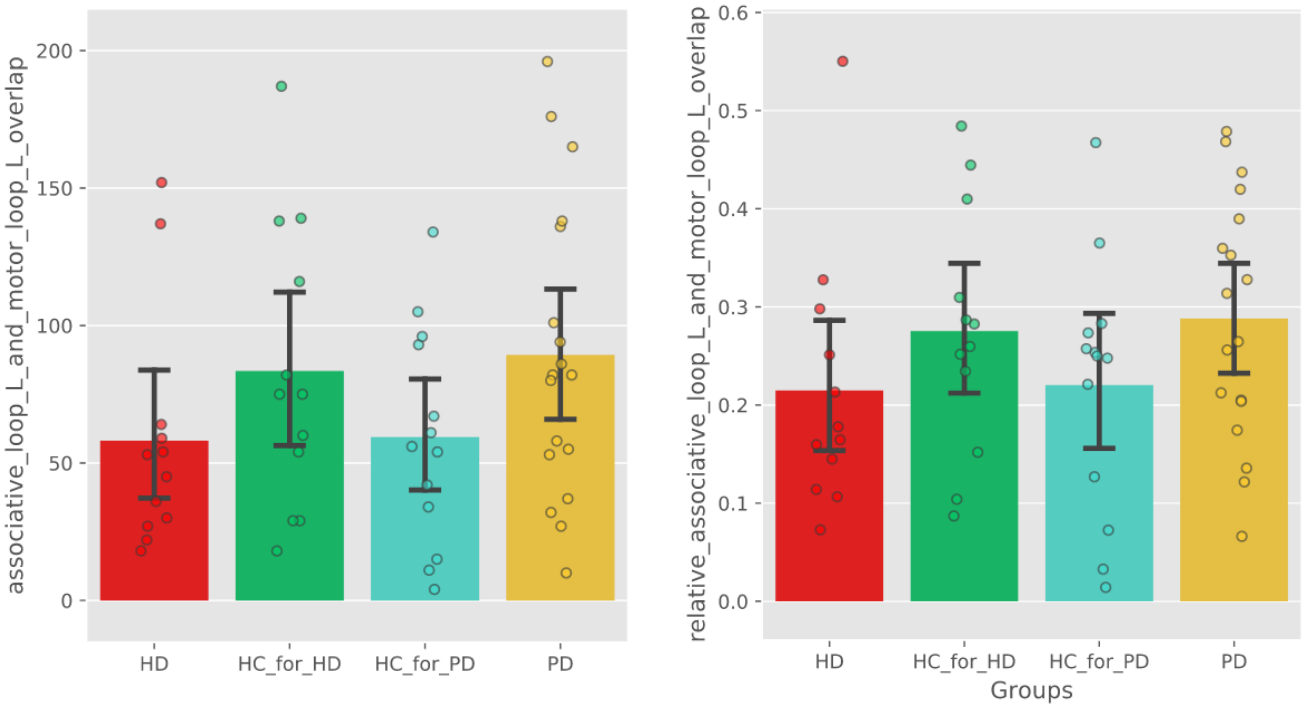

Figure 6.8. Significant differences in the overlap in mm^3 between motor and associative territories (left) and the relative overlap (normalized by the total STN volume) in the left hemisphere between patients with HD and PD when compared with their age- and gender-matched controls.

No significant differences between patients with HD and PD and their matched controls were found for the Jaccard index as measure of similarity between the motor and associative territories (all $p > 0.05$).

No significant differences between patients with HD and PD and their matched controls were found for the Pearson correlation as a continuous measure of similarity between the motor, limbic, and associative territories (lowest uncorrected p-value = 0.091, for the contrast PD vs. age-matched HD when looking for differences in the right limbic and associative subthalamic territories).

6.3.4. Centre of gravity (mass) statistics for the motor, limbic and associative connectivity-based parcellations

No significant differences between patients with HD and PD relative to their age-matched control groups were found for the normalized x-coordinates and y-coordinates of the motor COGs of the STN in either hemisphere. When directly comparing the HD/PD patient groups with their age-matched controls a significant difference was found for the normalized x-coordinate of the motor COG between patients with PD and their matched controls that was lateralized to the right hemisphere ($z = 2.066$, uncorrected $p = 0.038$, **Figure 6.9**, right).

There were significant differences in both HD and PD relative to their matched controls in the normalized z-coordinate of the motor COG in the right STN ($z = 2.861$, $p = 0.004$). Post-hoc comparisons of the individual patient groups revealed that this effect was mainly driven by a significant difference in the normalized z-

coordinate of the motor COG between the HD group compared with the matched control group (z = 2.614, p = 0.008).

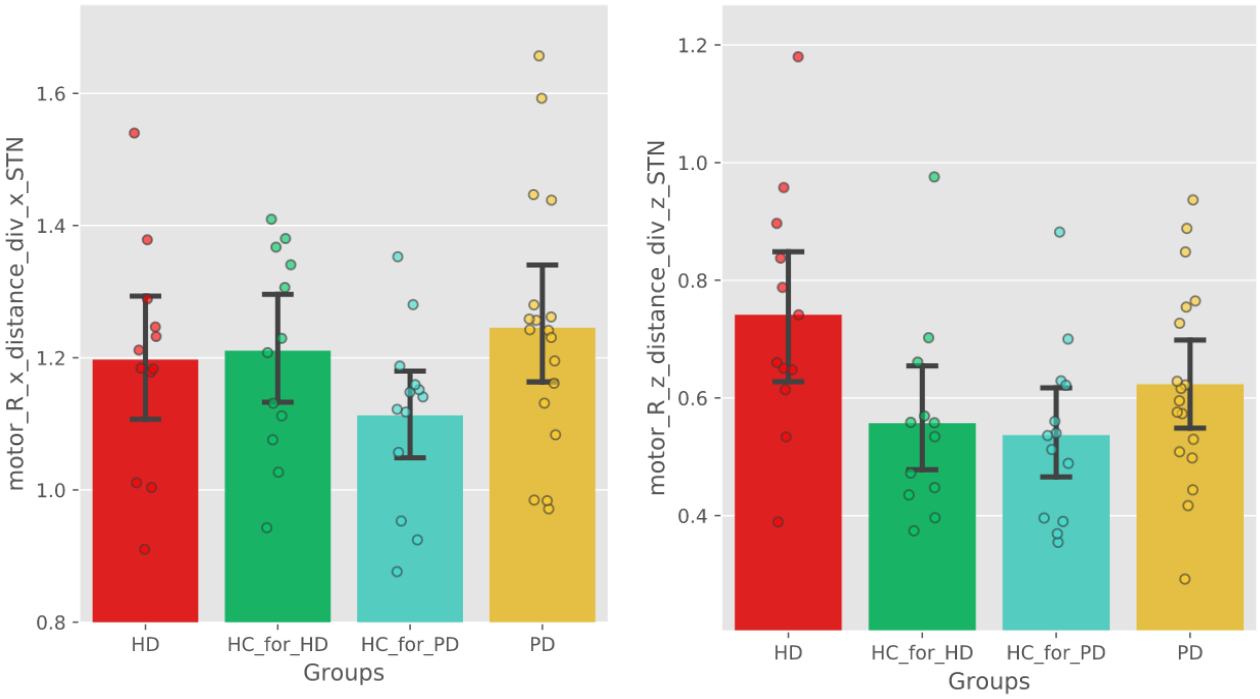

Figure 6.9. Significant differences between patients with PD and matched-controls in the normalized x-coordinate of the COG of the right STN (left). Significant differences in both patients with PD and HD relative to their matched controls in the z-coordinate of the COG of the right STN (right).

No significant differences between patients with HD and PD relative to their age-matched control groups were found for any motor, limbic, or associative COG coordinates in the left hemisphere (all $p > 0.05$).

There was a strong trend towards differences in both HD and PD relative to their matched controls in the normalized x-coordinate of the limbic COG in the right STN ($z = 1.959$, $p = 0.050$). When directly comparing patient groups with their control groups a significant difference was found between the PD group and their matched controls in the normalized x-coordinate of the limbic COG in the right STN ($z = 2.187$, $p = 0.028$, **Figure 6.10**). No significant differences between patients with HD and PD relative to their age-matched control groups were found for any y- or z-coordinates of the left limbic COG (all $p > 0.05$).

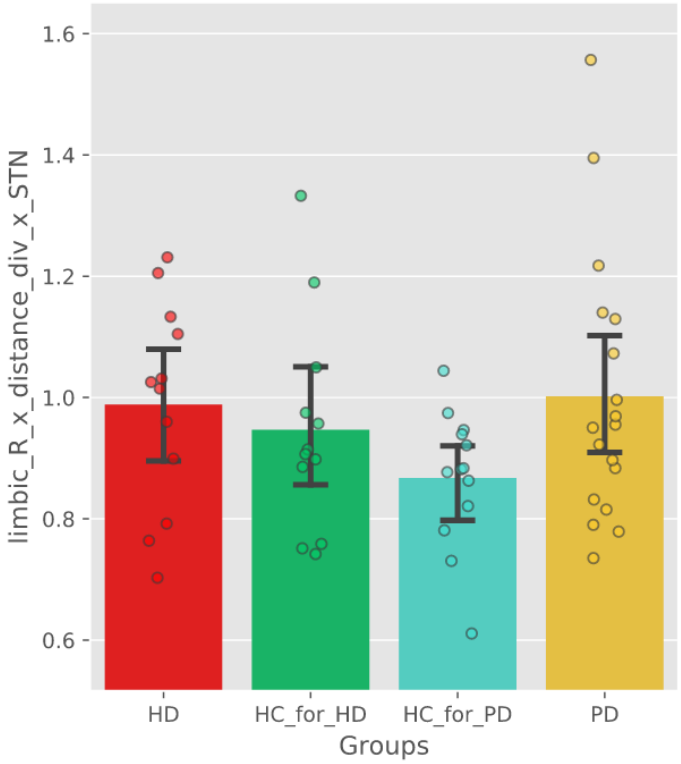

Figure 6.10. Significant differences between patients with PD and matched-controls in the normalized x-coordinate of the limbic COG of the right STN (left).

No significant differences between patients with HD and PD relative to their age-matched control groups were found for the normalized x-coordinates and y-coordinates of the associative COGs of the STN in either hemisphere (all $p > 0.05$). When directly comparing the HD/PD patient groups with their age-matched controls a significant difference was found for the normalized x-coordinate of the associative COG between patients with PD and their matched controls that was lateralized to the right hemisphere ($z = 2.185$, uncorrected $p = 0.028$, **Figure 6.11**).

There were significant differences in both HD and PD relative to their matched controls in the normalized z-coordinate of the motor COG in the right STN ($z = 2.552$, $p = 0.010$). Post-hoc comparisons of the individual patient groups revealed that this effect was mainly driven by a significant difference in the normalized z-coordinate of the motor COG between the HD group compared with the matched control group ($z = 2.428$, $p = 0.015$, **Figure 6.11**).

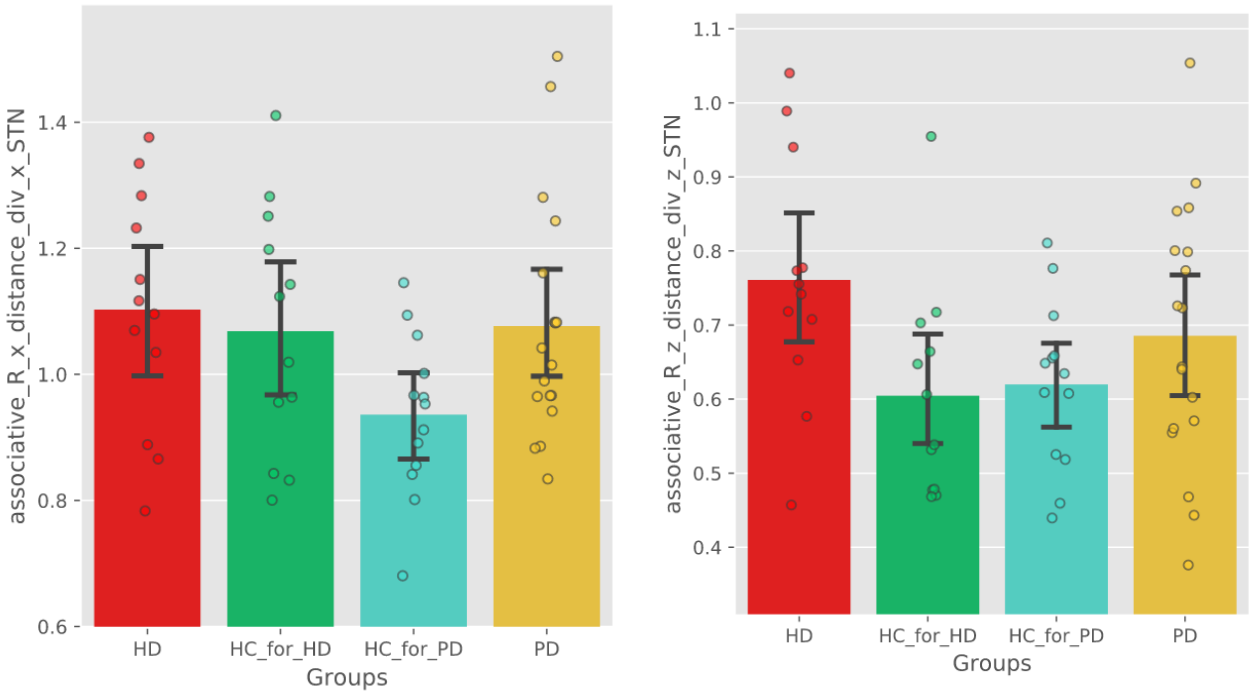

Figure 6.11. Significant differences between patients with PD and matched-controls in the normalized x-coordinate of the associative COG of the right STN (left). Significant differences in both patients with PD and HD relative to their matched controls in the z-coordinate of the associative COG of the right STN (right).

6.3.5. Correlation of imaging data with UHDRS/UPDRS sparse components

6.3.5.1. Post-hoc correlation of strength of connectivity and volumetric measures with UHDRS sparse components

There was a significant correlation between the relative volume of the left associative STN territory and the UHDRS components 3 (Spearman's $\rho = -0.671$, $p = 0.016$), as well as component 7 (Pearson's $r = 0.596$, $p = 0.040$). There was a significant correlation between the relative volume of the left limbic STN territory and the UHDRS component 4 (Spearman's $\rho = 0.589$, $p = 0.043$). There was a trend towards correlation between volume of the left limbic STN territory and the UHDRS component 1 (Spearman's $\rho = 0.560$, $p = 0.058$), and UHDRS component 4 (Spearman's $\rho = 0.560$, $p = 0.057$). There was a significant correlation between volume of the left associative STN territory and UHDRS component 3 (Spearman's $\rho = -0.721$, $p = 0.008$). There was a significant correlation between the overlap of the associative and motor STN territories and UHDRS component 3 (Spearman's $\rho = -0.706$, $p = 0.010$).

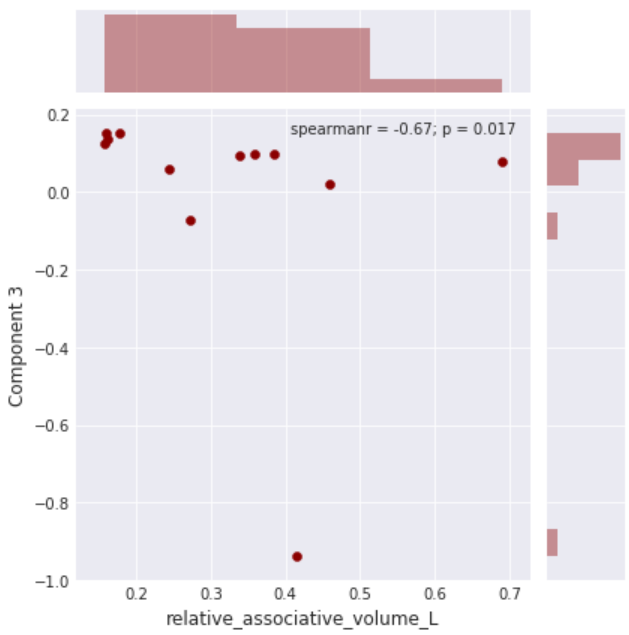
spearmanr = -0.67; p = 0.017
Component 3
relative_associative_volume_L

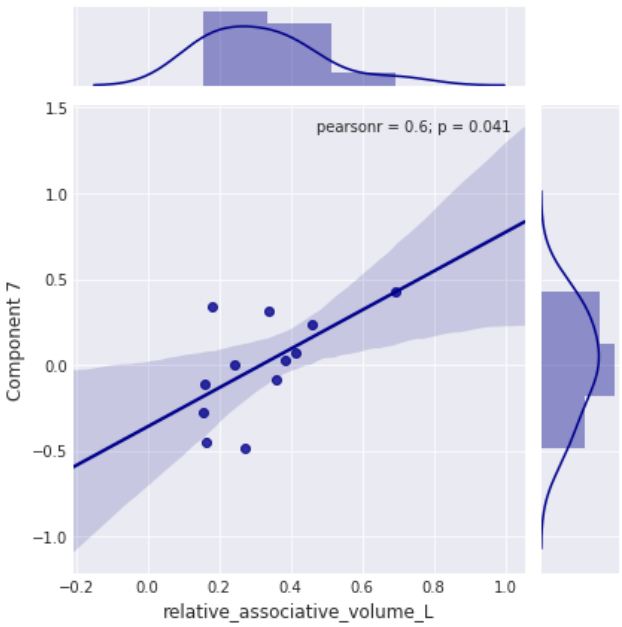
pearsonr = 0.6; p = 0.041
Component 7
relative_associative_volume_L

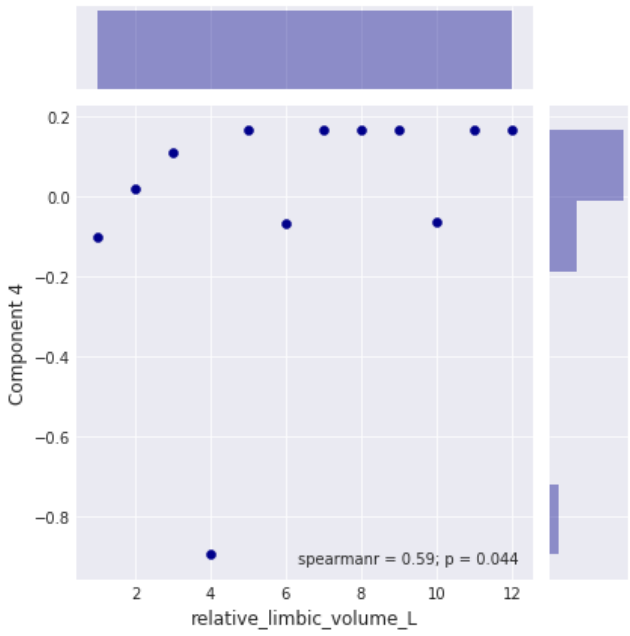
spearmanr = 0.59; p = 0.044
Component 4
relative_limbic_volume_L

Figure 6.12. Scatter plot showing the significant correlation between the relative associative volume of the left subthalamic nucleus and UHDRS components 3 and 7, as well as the significant correlation between the relative limbic volume of the left subthalamic nucleus and UHDRS component 4.

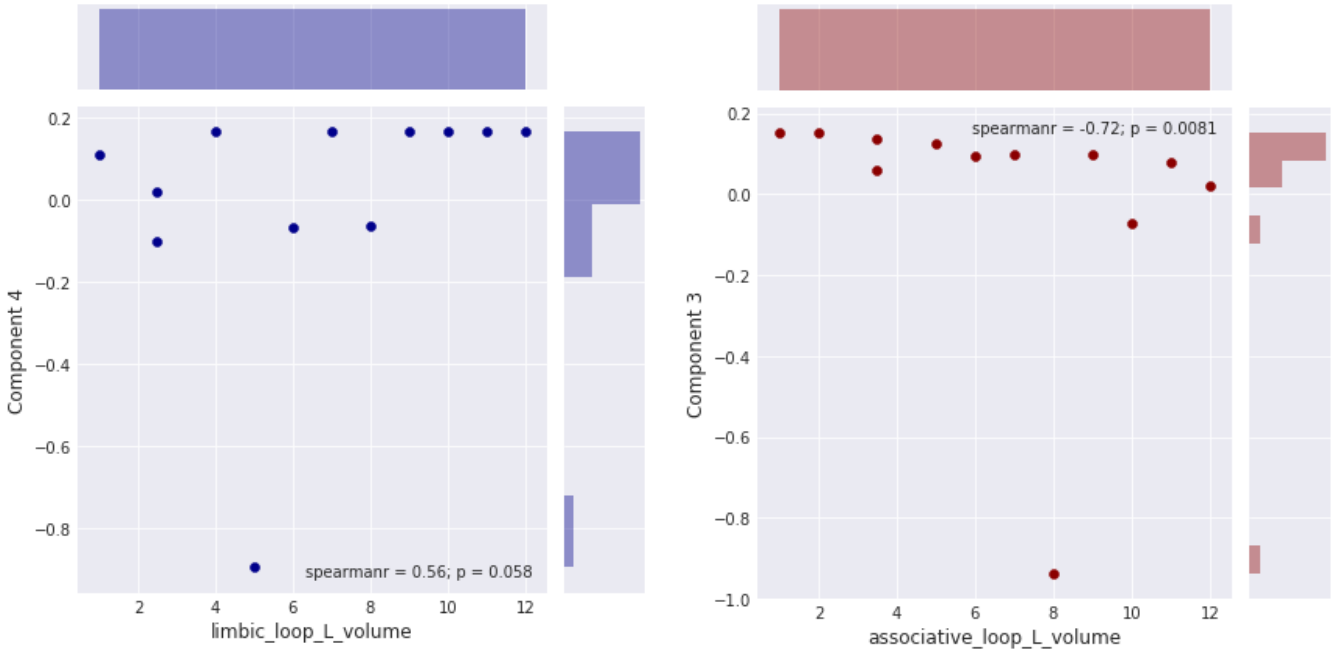

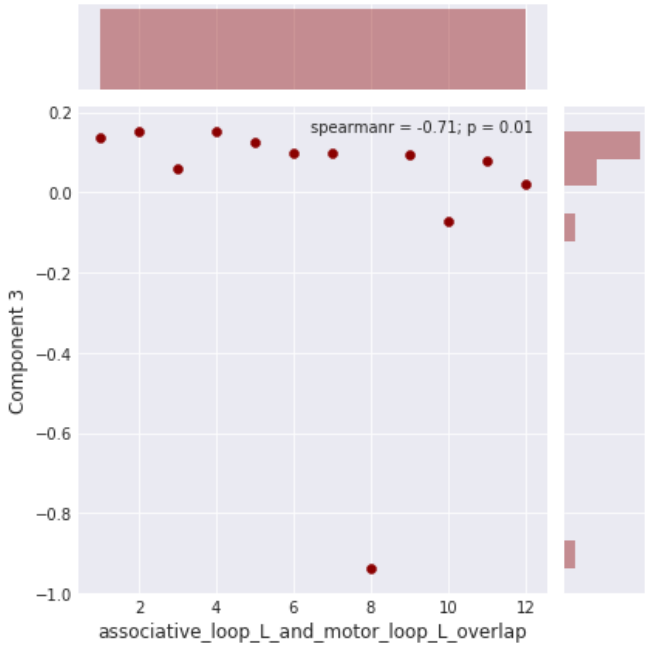
spearmanr = -0.71; p = 0.01
Component 3
associative_loop_L_and_motor_loop_L_overlap
0.2
0.0
−0.2
−0.4
−0.6
−0.8
−1.0
2
4
6
8
10
12

Figure 6.13. Scatter plots showing the trend towards a significant correlation between the volume of the left limbic subthalamic nucleus and UHDRS component 4, the significant correlation between the volume of the left associative subthalamic nucleus and UHDRS component 3, as well as the overlap between the left associative and motor territories and UHDRS component 3.

6.3.5.2. Post-hoc correlation of centre of gravity statistics with UHDRS sparse components

No significant effects or trends found for correlations between UHDRS sparse components and the normalized z-coordinate of the right motor COG, the normalized z-coordinate of the right associative COG (all $p > 0.1$).

6.3.5.3. Correlations between latent variable from exploratory factor analysis of UHDRS data and STN connectivity and volumetric metrics

There was a trend towards correlation between strength of connectivity of the right motor hyperdirect pathway and UHDRS latent variable 9 (Pearson's $r = 0.557$, $p = 0.059$). There was a significant correlation between UHDRS latent variable 3 and the absolute and relative volume of the associative territory of the subthalamic nucleus

(Spearman's $\rho = 0.811$, $p = 0.001$, and Spearman's $\rho = 0.690$, $p = 0.013$ respectively), as well as the overlap between the left associative and motor territories of the subthalamic nucleus. There was a trend towards correlation between the overlap between the left associative and motor territories and UHDRS latent variable 2 (Spearman's $\rho = 0.510$ $p = 0.089$).

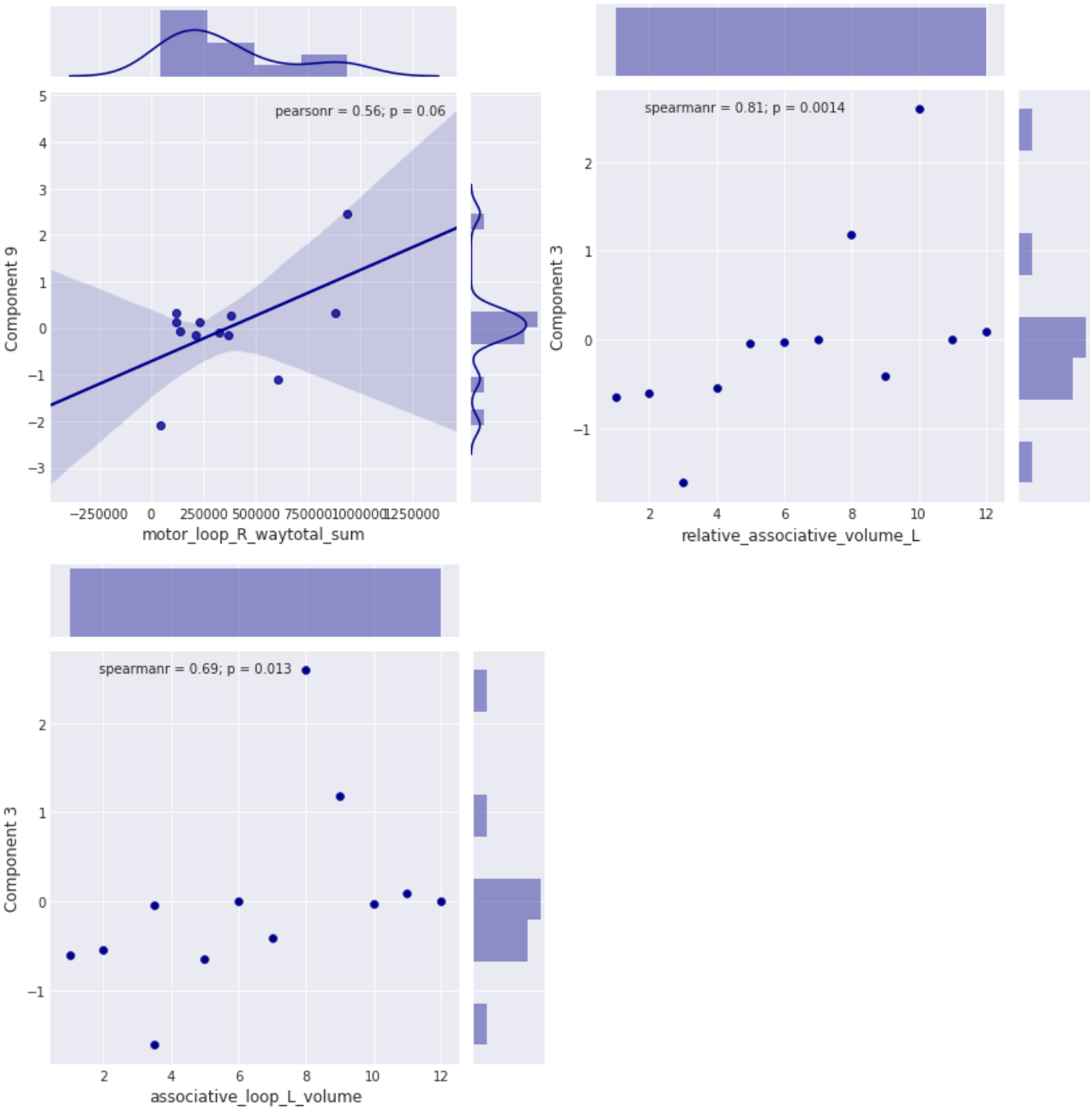
pearsonr = 0.56; p = 0.06
Component 9
motor_loop_R_waytotal_sum
spearmanr = 0.81; p = 0.0014
Component 3
relative_associative_volume_L
spearmanr = 0.69; p = 0.013
Component 3
associative_loop_L_volume

Figure 6.14. Scatter plots showing the trend towards a significant correlation between the strength of connectivity of the right motor hyperdirect pathway and UHDRS latent variable 9, as well as the significant correlations between the absolute/relative volumes of the left associative territory of the subthalamic nucleus and UHDRS latent variable 3.

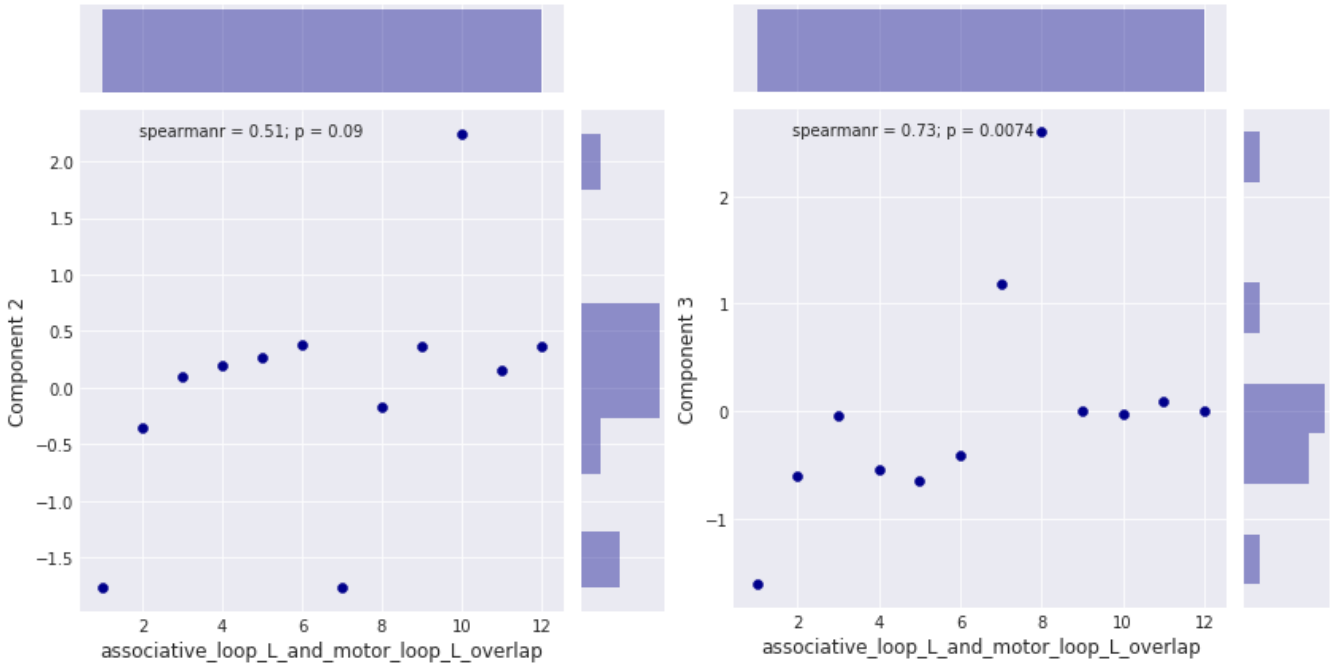

Figure 6.15. Scatter plots showing the significant/trend correlations between the overlap of the left associative and motor territories of the subthalamic nucleus and UHDRS latent variables 2 and 3.

6.3.5.4. Correlations between latent factors from exploratory factor analysis of UHDRS data and centre of gravity statistics from STN tractography

No significant effects or trends found for correlations between the latent variables from UHDRS factor analysis and the normalized z-coordinate of the COG of the right motor STN, or the normalized z-coordinate of the COG of the right associative STN (all $p > 0.1$).

6.3.5.5. Post-hoc correlation of strength of connectivity and volumetric measures with UPDRS sparse components

There was a significant correlation between UPDRS sparse principal component 2 and the relative associative volume of the left subthalamic nucleus (Spearman's ρ = 0.576, p = 0.012), the absolute/relative limbic volumes of the left subthalamic nucleus (Spearman's ρ = 0.550, p = 0.017, Spearman's ρ = 0.654, p = 0.003 respectively). There was a trend towards correlation between the overlap between the left associative and motor subthalamic nucleus and UPDRS component 5 (Spearman's ρ = -0.454, p = 0.058).

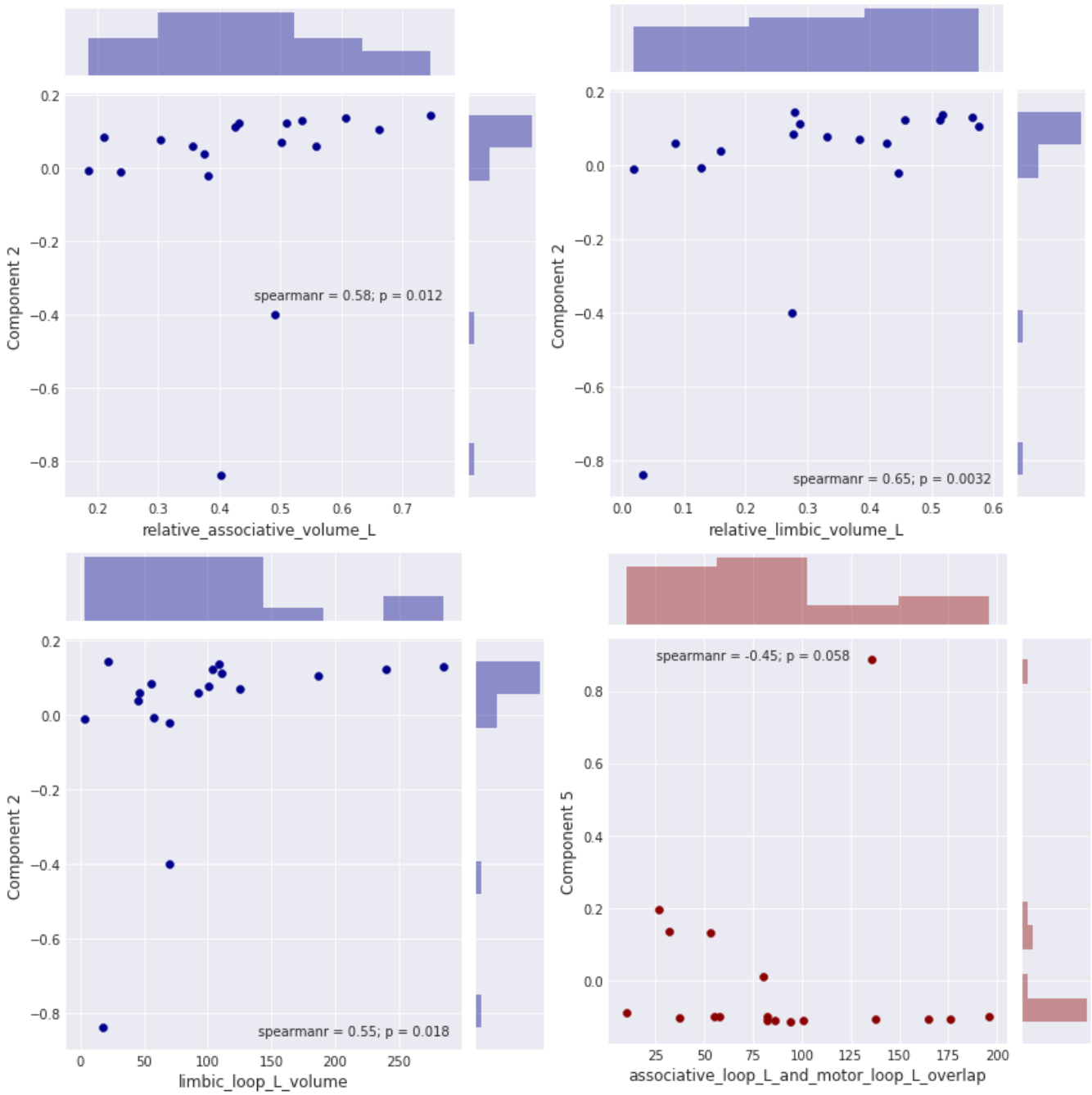

Figure 6.16. Scatter plots showing the significant correlations between UPDRS Component 2 and the relative associative volume of the left subthalamic nucleus, absolute/relative limbic volume of the left subthalamic nucleus, as well as the trend

towards a significant correlation between the overlap between the left associative and motor subthalamic nucleus.

6.3.5.6. Post-hoc correlation of centre of gravity statistics with UPDRS sparse components

There was a significant correlation between the right motor x-coordinate (normalized by the x-length of the STN) and UPDRS component 4 (Spearman's $\rho = 0.531$, $p = 0.023$). There was a trend towards a significant correlation between the right motor z-coordinate (normalized by the z-length of the STN) and UPDRS component 3 (Spearman's $\rho = -0.426$, $p = 0.077$). There was a significant correlation between the normalized right motor z-coordinate and UPDRS component 5 (Spearman's $\rho = -0.594$, $p = 0.009$). There was a significant correlation between the normalized richt limbic x-coordinate and UPDRS component 1 (Spearman's $\rho = -0.496$, $p = 0.036$). There was a significant correlation between the normalized right associative x-coordinate and UPDRS component 1 (Spearman's $\rho = -0.558$, $p = 0.016$). There was a trend towards correlation between the normalized right associative z-coordinate and UPDRS component 1 (Spearman's $\rho = 0.440$, $p = 0.067$). There was a significant correlation between the normalized right associative z-coordinate and

UPDRS component 3 (Spearman's ρ = -0.483, p = 0.042). There was a trend towards correlation between the normalized right associative z-coordinate and UPDRS component 7 (Spearman's ρ = -0.438, p = 0.068).

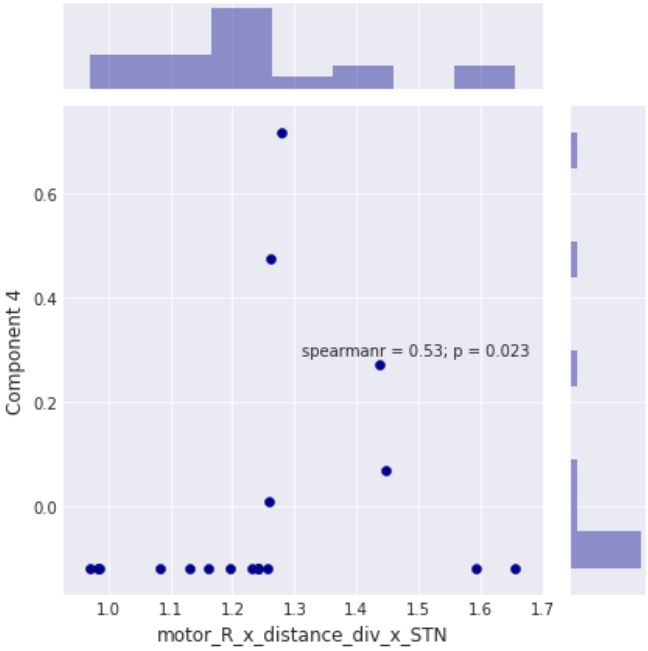
spearmanr = 0.53; p = 0.023
Component 4
motor_R_x_distance_div_x_STN

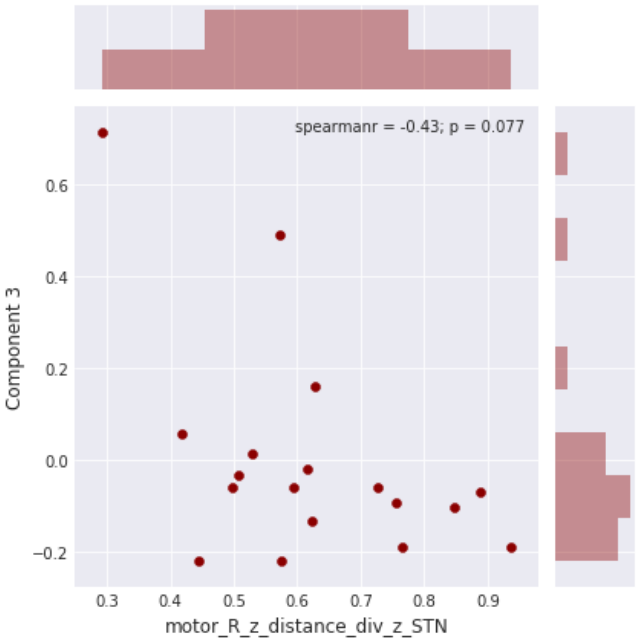
spearmanr = -0.43; p = 0.077
Component 3
motor_R_z_distance_div_z_STN

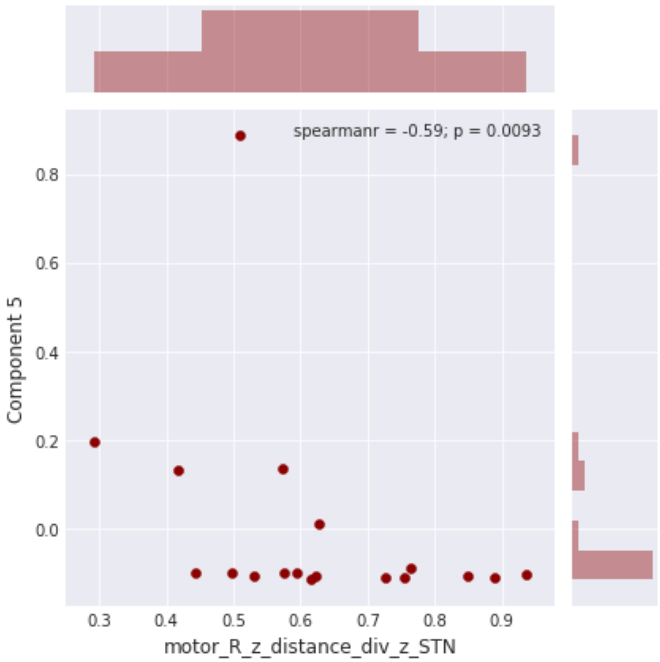
spearmanr = -0.59; p = 0.0093
Component 5
motor_R_z_distance_div_z_STN

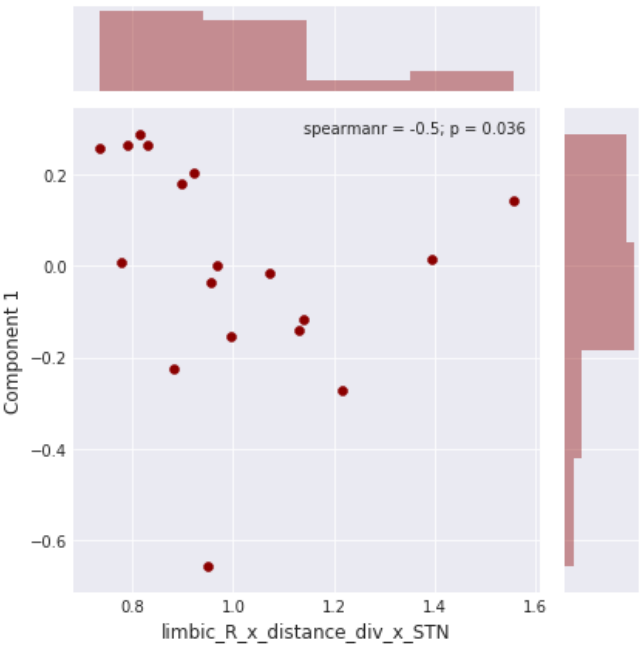
spearmanr = -0.5; p = 0.036
Component 1
limbic_R_x_distance_div_x_STN

Figure 6.17. Scatter plots showing the significant correlation between the normalized right motor x-coordinate of the subthalamic nucleus and UPDRS component 4, the trend towards a insignificant correlation between between the normalized right motor z-coordinate and UPDRS component 3, the significant correlation between the the normalized motor z-coordinate and UPDRS component 5, as well as the significant correlation between the normalized right limbic x-coordinate and UPDRS component 1.

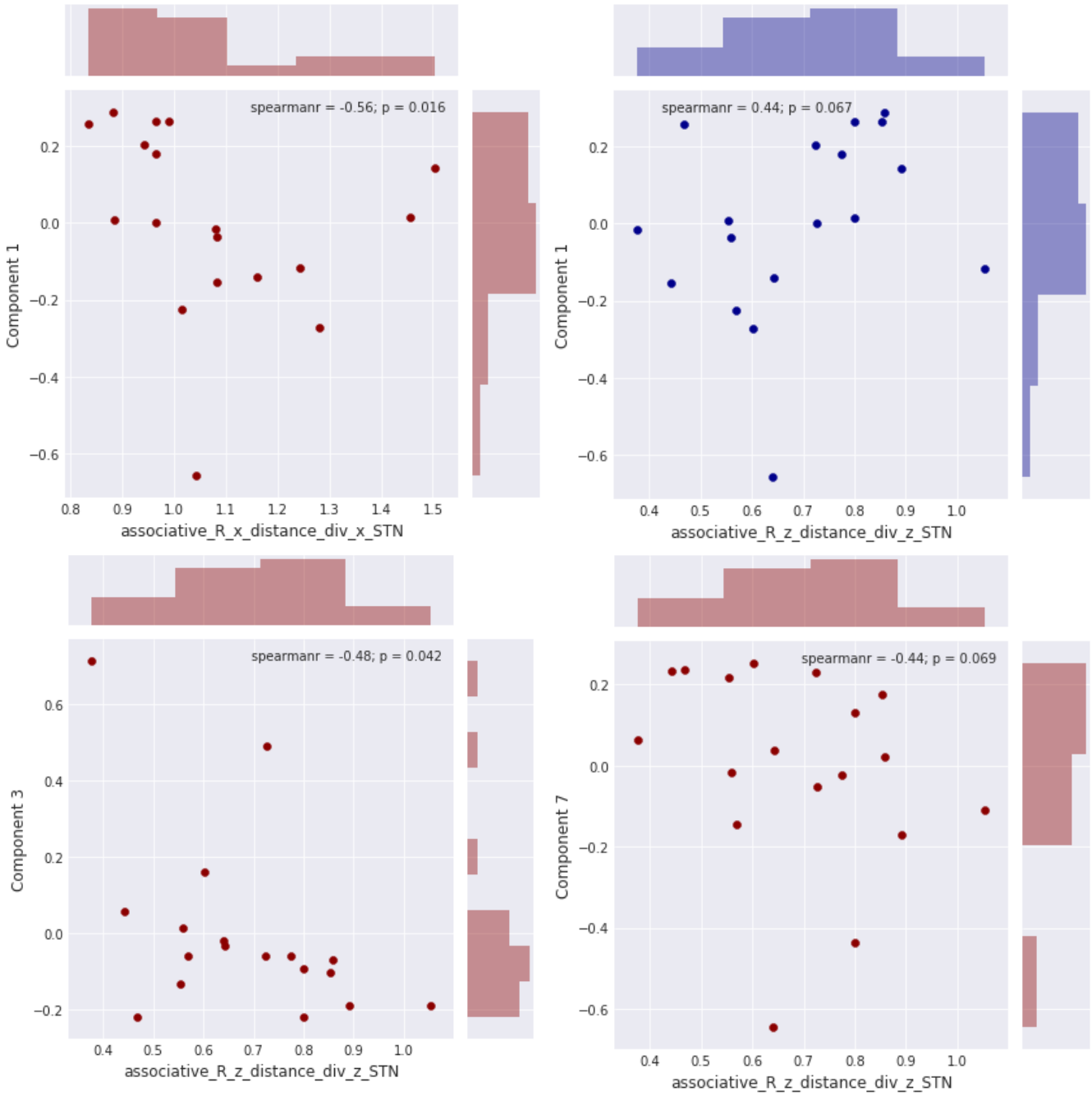
spearmanr = -0.56; p = 0.016
Component 1
associative_R_x_distance_div_x_STN
spearmanr = 0.44; p = 0.067
Component 1
associative_R_z_distance_div_z_STN
spearmanr = -0.48; p = 0.042
Component 3
associative_R_z_distance_div_z_STN
spearmanr = -0.44; p = 0.069
Component 7
associative_R_z_distance_div_z_STN

Figure 6.18. Scatter plots showing the significant/trend correlations between the normalized right associative x/z-coordinates and UPDRS component 1, as well as between the normalized right associative z-coordinate and UPDRS components 3 and 7.

6.3.5.7. Correlations between latent factors from exploratory factor analysis of UPDRS data and STN connectivity and volumetric metrics

There was a significant correlation between the strength of connectivity of the right hyperdirect motor pathway and UPDRS latent variable 5 (Pearson's r = -0.559, p = 0.0156).There was a significant correlation between the left relative associative volume and UPDRS latent variable 10 (Pearson's r = -0.524, p = 0.025). There was a trend towards a significant correlation between the left relative limbic volume and UPDRS latent variable 9 (Pearson's r = -0.409, p = 0.091).

There were trends towards significant correlations between UPDRS latent variable 6 and the left associative volume (Pearson's r = 0.447, p = 0.062) and the overlap between the left associative and motor territories(Pearson's r = 0.437, p = 0.069).

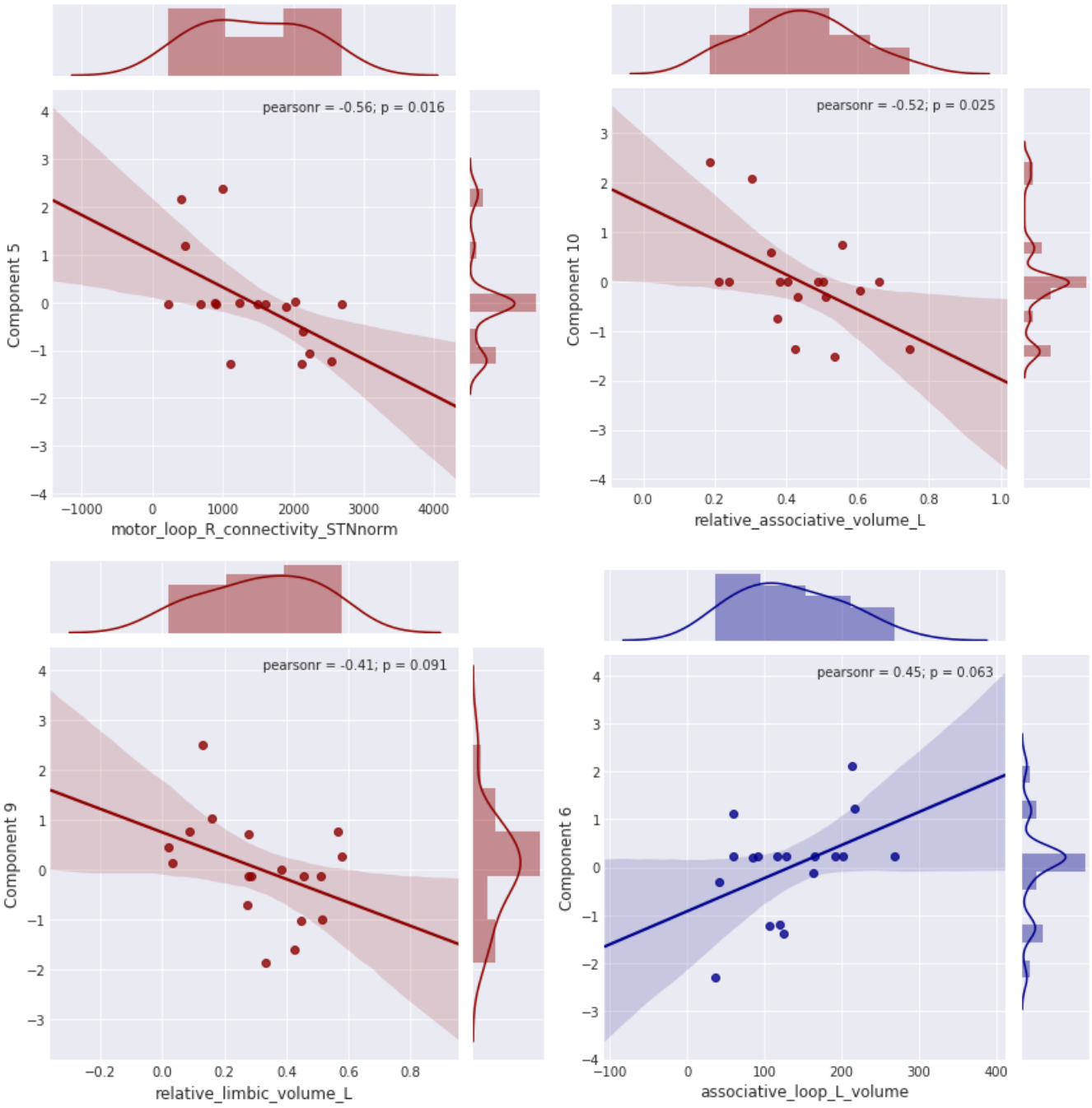
pearsonr = -0.56; p = 0.016
Component 5
motor_loop_R_connectivity_STNnorm
pearsonr = -0.52; p = 0.025
Component 10
relative_associative_volume_L
pearsonr = -0.41; p = 0.091
Component 9
relative_limbic_volume_L
pearsonr = 0.45; p = 0.063
Component 6
associative_loop_L_volume

Figure 6.19. Scatter plots showing the significant correlations between strength of connectivity of the right hyperdirect motor pathway and UPDRS latent variable 5, the significant correlation between the relative associative volume of the left subthalamic nucleus and UPDRS latent variable 10, the trend correlation between the relative limbic volume of the left subthalamic nucleus and UPDRS latent variable 9, and the trend correlation between the associative volume of the left subthalamic nucleus and UPDRS latent variable 6.

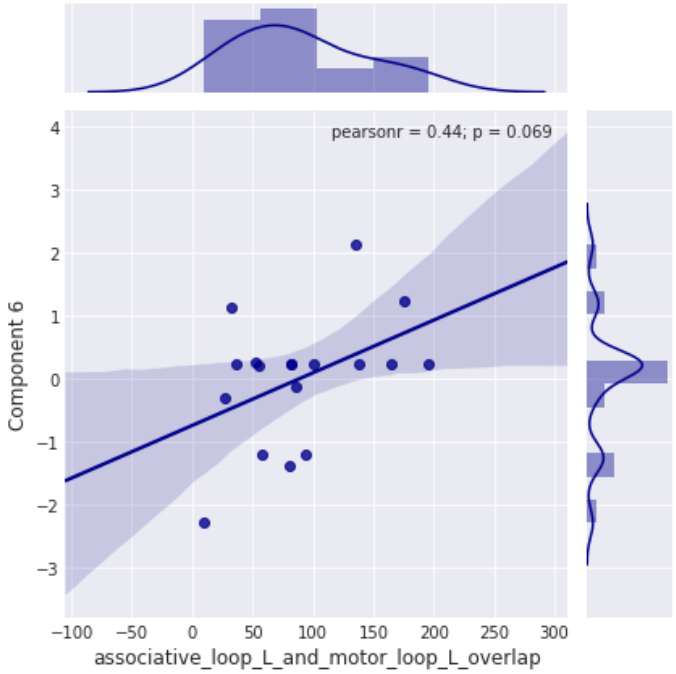

Figure 6.20. Scatter plot showing the trend toward a significant correlation between the overlap between the left associative and motor territories and UPDRS latent variable 6.

6.3.5.8. Correlations between latent variable from UPDRS exploratory factor analysis and centre of gravity statistics from STN tractography

There was a trend towards a correlation between normalized right motor z-coordinate and the UPDRS latent variable 3 (Pearson's r = 0.406, p = 0.094, **Figure 6.21**). There was a trend towards a correlation between the normalized right associative x-coordinate and the UPDRS latent variable 5 (Pearson's r = 0.428, p = 0.076, **Figure 6.21**).

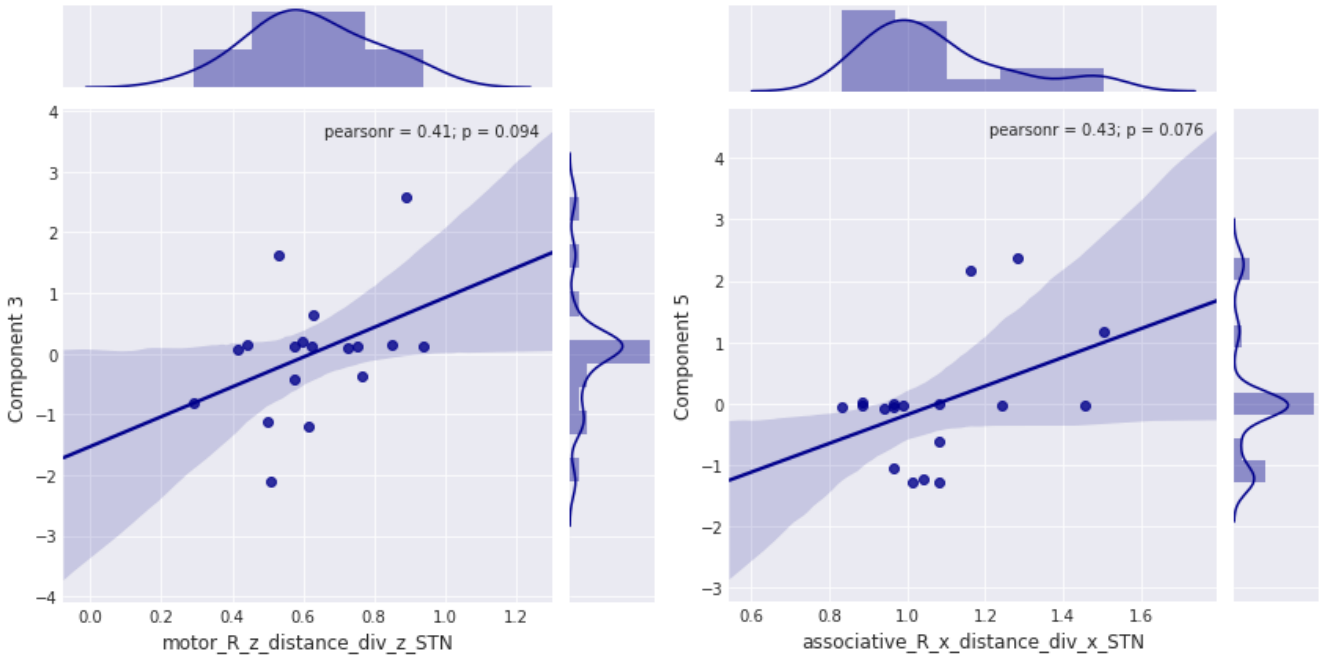

Figure 6.21. Scatter plots showing the trend towards a significant correlation correlation between the normalized right motor z-coordinate and UPDRS latent

variable 3, as well as between the normalized right associative x-coordinate and UPDRS latent variable 5.

6.4. Discussion

In this chapter, we have used probabilistic tractography to reconstruct the hyper-direct pathway going from the cortex directly to the subthalamic nucleus, and have used this information to derive a connectivity-based parcellation of the subthalamic nucleus into motor, limbic, and associative territories. Similar to previous descriptions of the neuroanatomy of these subregions of the subthalamic nucleus, we were able to identify a dorsolateral motor territory, a ventromedial associative territory, and a medial limbic territory (Parent and Hazrati, 1995; Benarroch, 2008; Haynes and Haber, 2013). However, there was also a lot of inter-subject variability with respect to the spatial extent of these territories. This the first study that directly compares the strength of connectivity of the hyperdirect pathway, as well as the volumes of these 3 territories in both Huntington's and Parkinson's disease.

A previous 7T diffusion MRI study in patients with Parkinson's disease found different STN territories based on connectivity-based parcellation of the STN, and described the motor territory as the posterolateral part of the STN, the associative as the central part of the STN, and the limbic territory as the anteromedial part of the STN (Plantinga *et al.*, 2018). Since the aforementioned study did not include a healthy control group, no inferential

statistics were reported. The study did not use an exclusion mask for the striatum, pallidum, or thalamus, and was thereby effectively not only looking at the hyper-direct pathway, but the entire cortico-subthalamic connections, including the cortico-caudatoputaminal-pallidal-subthalamic connections.

A further 3T diffusion MRI study in healthy subjects used a data-driven connectivity based parcellation algorithm looking at both cortical and sub-cortical targets, and identified the motor territory as being posterior, the limbic territory as being anterior, and the associative territory as being in the middle, in-between the limbic and motor territories (Lambert et al., 2012). When looking at the overlap between the motor and the limbic territory we found that it was zero in several subjects, where this was driven by the fact that the associative territory was in-between the motor and limbic territory both along the rostro-caudal axis, and the dorso-ventral axis. This might suggest that the limbic and motor territories actually do not overlap, however, there was also a large variability and several subject did show some overlap probably due to the low threshold we have used. We found that the motor territory and associative territory overlapped in all subjects, which is consistent with neuroanatomical descriptions of STN neurons receiving input from both the motor and prefrontal cortices in non-human primates (Haynes and Haber, 2013). **Table**

6.1. provides an overview of current research on the subthalamic nucleus and hyperdirect pathway with a focus on papers that are relevant for the thesis.

Authors	Subject characteristics	Study design	Data acquistition	Analysis method	Key findings	Interpretation,implications, comments
Plantinga et al. (2018)	17 PD 1 HC	Quantitaitve descriptive study without group inferential statistics due to lack of control group and incon-sistent scanning protocol	7T 1.5 mm^3 Single-shell (b=1500 or b=2000) 50 dir or 60 dir 2 phase encod. dir.	Probabilistic tractography (FSL) of connections between cortex (motor, associative, limbic, residual) and STN ("hyperdirect pathway") Connectivity-based parcellation of STN	Parcellation of STN into a posterolateral motor territory, a central associative territory, and an anteromedial limbic territory	First parcellation of STN using 7T diffusion data No exclusion mask was used for striatum, pallidum, or thalamus thereby not excluding cortico-caudatoputaminal-pallidal subthalamic connections
Lambert et al. (2012)	12 HC	Quantitaitve descriptive study without group inferential statistics Methodological study implemeting a data-driven method to derive a connec-tivity-based parcellation of the STN	3T 1.7 mm^3 Single-shell (b=1000) 61 dir average over two aquisitions	Probabilistic tractography (FSL) between 11 seed regions including STN and 202 cortical, sub-cortical and cerebellar targets Agglomerative hierarchical clustering of probability of con-nectiviy index images to derive STN territories	Data-driven validation of the existence of three distinct regions within STN Parcellation of STN into a posterior (and lateral) motor territory, a mid associative territory, and an anterior (and medial) limbic territory	Surgical implication of connectivity-based parcellation for DBS patients is mentioned. Strongly implied the existence of three regions in STN based on empircal data. Tractography on its own cannot prove the existance of three subthalamic territories
Forstmann et al. (2010)	9 HC	Correlational study design based on behavioural and imaging data	7T structurals 3T diffusion data 1.5 mm^3 Single-shell (b=1000) 60 dir HARDI	Probabilistic tractography (FSL) between STN/striatum as seeds and M1, preSMA, ACC, and IFG(BA44) as targets Strength of conectivity was calculated as: p(STN)/p(any other target) Correlation with behavioural data	Flexibility in switching between the speed and accuracy conditions in a continous performance task (outside the scanner) was correlated with strength of connectivity between striatum and preSMA	Favours the striatal hypothesis over the subthalamic hypothesis, i.e. that response thresholds are dreceased by increasing activation from cortex to the striatum, not to the STN Findings are inconclusive, since striatum or STN were not used as exclusion masks for the reconstructions of the direct, indirect or hyperdirect cortico-fugal segments respectively
Haynes & Haber (2013)	4 Macaca nemestrina 39 Macaca fascicularis	Descriptive neuroanatomical tracing study in monkeys	Injection of anterograde/bidirectional tracers into vmPFC (BA14, 25 & 32v), OFC (BA 11,13,12), dACC (BA24), DPFC (BA10,9&46), PMC/SMA (BA6), M1 (BA4) Immunohistochemical staining of brain slices 3D reconstruction of STN to identify projection sites of cortical areas within STN and evaluate their convergence		Limbic projections enter STN at the medial tip and rostrally, associative projections at the medial half, and motor projec-tions at the lateral half and more caudally	Neuroanatomical proof of topographically organized and convergent limbic and prefrontal parts of the hyperdirect pathway
Chen et al. (2018)	11 DBS patients with PD	Correlational study design with inferential stats using a split into groups based on symptom improvement	3T 2 x 2 x 2 mm Single-shell (b=1000) 30 dir	Deterministic tractography (StealthViz) of hyperdirect pathway using motor cortex and STN as ROI (using a FA=0.2 threhold) Localization of DBS electrodes using postsurgical CT	Distance between DBS elec-trode and reconstructed hyper-direct pathway was negatively correlated with improvement in UPDRS symptoms Similar findings using a split into groups based on less/more than 50% improvement in symptoms	Deterministic tractography does not model uncertainty that accu-mulates along tract, and principal diffusion direction is inaccurate in regions of crossing fibres (e.g. centrum semiovale) where the hyperdirect pathway goes through STN ROI at 3T MRI might be inaccurate, since resolution is too low to distinguish STN from SN
Akram et al. (2018)	20 PD	Correlational study design using connectivity strength as predictors for improve-ment in clinical data pre- and post-DBS surgery	3 T 1.5 x 1.5 mm^3 Single-shell(b=1500) 128 dir 2 phase encode dir.	Probabilistic tractography (FSL) between DBS-VTA area and M1, SMA, PFC as targets using IC as waypoint, and STR, THAL as exclusion masks Connectivity ratio between STN voxels activated by DBS and STN voxels not activated by DBS was used as connectivity strength	Connectivity to M1 predicted improvement in tremor; con-necitivity to SMA predicted improvement in bradykinesia/ rigidity, and connectivity to PFC predicted improvement in rigidity	Identification of subregions within the motor STN as optimal targets for DBS to improve specific symptoms
Vanegas-Arroyave et al. (2016)	22 DBS patients with PD	Correlational study design group comparisons between effective and non-effective DBS contacts in strength of connectivity	3T 2 x 2 x 2 mm^3 Single-shell (b=1000) 32 dir	Probabilistic tractography (AFNI) between DBS-VTA area and various cortical and subcortical targets of interest Connectivity strength as fraction of total number of tracts from DBS-VTA area to target regions.	Sites of clinically-effective electrodes within STN were connected with brainstem, thal, STN, SN, and SFG Higher strength of connectivity with SFG and thal for effective electrodes compared with ineffective electrodes	Tractography might be used to identify effective contacts for DBS

Table 6.1. A Summary of relevant literature on the subthalamic nucleus and hyperdirect pathway from diffusion imaging and neuroanatomical studies. (Abbreviations: ACC: anterior cingulate cortex, DBS: deep-brain stimulation, dir:

directions, DPFC: dorsal prefrontal cortex, HC: healthy control, IC: internal capsule, IFG: inferior frontal gyrus, HD: Huntington's disease, PD: Parkinson's disease, GPe: globus pallidus, pars externa, GPi: globus pallidus, pars interna, M1: primary motor cortex, PFC: prefrontal cortex, PMC: premotor cortex, PPN: pedunculo-pontine nucleus, S1: primary somato-sensory cortex, SFG: superior frontal gyrus, SMA: supplementary motor area, SN: substantia nigra, STN: subthalamic nucleus, STR: striatum, THAL: thalamus, vmPFC: ventromedial prefrontal cortex, VTA:Volume of tissue activated during deep-brain stimulation).

There were significant differences in both patients with Huntington's and Parkinson's disease in the motor connectivity of the right hyperdirect pathway (both before and after normalization by the STN volume), but this effect was mainly driven by differences between patients with HD and their matched controls. Noteworthy, strength of motor connectivity in the hyperdirect pathway was lower in the older control group when compared with the younger control group. The Parkinson's disease group did not differ from the matched control group in motor connectivity strength (or the strength of connectivity of any other territory), which was an unexpected finding due to the known role of the hyperdirect pathway in Parkinson's disease. More specifically, overactivity of the hyperdirect pathway (Nambu, Tachibana and Chiken, 2015) and/or overactivity and increased synchronization of neurons in the subthalamic nucleus (Yokoyama *et al.*, 1998; Obeso *et al.*, 2014) has been found in patients with Parkinson's disease, and might explain hypokinetic symptoms by means of increased inhibition of motor programs sent from the cortex to the basal ganglia through the cortico-subthalamic-pallidal projections. The discrepancy in these findings with our present finding might be that we have looked here at the structural connectivity of the hyperdirect pathway, whereas such a hyeractivity of the STN was suggested on functional considerations based on micro-electrode recordings in patients with Parkinson's disease (Yokoyama *et al.*, 1998).

A possible explanation of the decrease in the strength of connectivity seen in HD might be that it reflects a loss of executive inhibitory control exerted by the motor cortex through the hyperdirect pathway that then results in both hyperkinetic motor symptoms, and a cognitive deficit. Indeed, previous neurocognitive research and behavioral research based on animal studies suggests that the hyperdirect pathway exerts a top-down control over behavioral and motor programs sent from the cortex through the basal ganglia feedback loops by imposing decisional thresholds on movement selection (Cavanagh *et al.*, 2011; Herz *et al.*, 2016). More specifically, during movement initiation the motor cortex might send a corollary signal through the cortico-subthalamic-pallidal hyperdirect pathway that results in inhibition of the motor programs via the corticopedal GPi-thalamus-cortex connections (Nambu, Tokuno and Takada, 2002). Then, another corollary signal is sent from the motor cortex through the cortico-striato-pallidal direct pathway to disinhibit the thalamus and the cortex, and release only the selected appropriate motor program (Nambu *et al.*, 2000). Based on this model, hypokinetic symptoms in Parkinson's disease have been explained by overactivity of the hyperdirect pathways and the subthalamic nucleus, resulting in overly conservative thresholds imposed on the motor program selections, and ultimately in symptoms of bradykinesia, akinesis, and rigidity. Given this conceptional framework of the functioning of the hyperdirect pathway the

decrease in motor connectivity in Huntington's disease group we have seen here might result in lowering of thresholds imposed on the selection of appropriate motor programs, and thereby in early hyperkinetic symptoms, such as chorea.

Patients with Huntington's disease and Parkinson's disease differed relative to their age matched controls in both the relative and absolute volumes of the limbic and associative territories, whereby in the Huntington's disease group the limbic and associative volume was decreased, and by contrast in the Parkinson's disease group the limbic and associative volumes were increased. In Huntington's disease this decrease in the associative volume was associated with less psychiatric symptoms (component 3), but more motor symptoms in hand/finger movement (component 7). In Huntington's disease the decrease in the limbic volume was associated with more motor symptoms (especially rigidity), and irritability as a psychiatric symptom (component 4). In Parkinson's disease the increase in the associative volume was associated positively with sparse PCA component 3, consisting primarily of motor symptoms including tremor, as well as agility of the right leg, thereby indicating that the increase was maladaptive. The fact that the volumes of the associative territory correlated with motor symptoms further indicates the integrative role of motor and associative processes that has also been neuroanatomically shown based on convergent projection from the DLPFC and motor cortices on the subthalamic

neurons (Haynes and Haber, 2013). Furthermore, the DLPFC (i.e. the cortical area that gives rise to the associative hypterdirect pathway) is known to play an important role in motor integration (Miller and Cohen, 2001; Hoshi, 2006), and cognitive action selection in healthy subjects (Cieslik *et al.*, 2013). The loop of the basal ganglia pathway and the hyperdirect pathway has been suggested to play a crucial role in goal-directed and habitual inhibition, and that imbalances in this network might lead to symptoms associated with Parkinson's disease (Jahanshahi *et al.*, 2015). The present knowledge about the role of hyperdirect pathway during movement initiation suggests that it conveys a corollary signal from movement and behavioral programs, that are initiated by the prefrontal cortex, and this signal then inhibits the parts of the thalamus and the cortex that process the selected and competing motor programs, thereby inhibiting the release of ballistic movements (Nambu, Tokuno and Takada, 2002). Within this conceptional framework of role of subthalamic nucleus suggested by (Nambu, Tokuno and Takada, 2002; Nambu, Tachibana and Chiken, 2015), the lower volume of the associative territory in Huntington's disease might result in less inhibition exerted from the STN on motor and behavioral programs, sent from the cortex through the direct basal ganglia pathway, thereby resulting in hyperkinetic motor symptoms. By contrast, the higher volume of the associative territory in Parkinson's disease might result in more

inhibition exerted from the STN on motor and behavioural programs, sent from the cortex through the direct basal ganglia pathway, thereby resulting in hypokinetic motor symptoms.

There were significant differences between patients with Huntington's disease, and patients with Parkinson's disease relative to their control groups in the absolute and relative overlap between the associative and the motor territories in the left hemisphere. Here the Huntington's disease group showed less overlap than their matched healthy controls (not significant), whereas the Parkinson's disease group showed more overlap (trend) than their matched healthy controls. These changes in the overlap may be driven by the corresponding changes in the relative associative volume. In the Huntington's disease group the overlap was negatively correlated with sparse component 3 that showed low loadings on psychiatric symptoms and horizontal eye movements, hence the lower overlap in Huntington's disease corresponds to less psychiatric symptoms and probably has an adaptive function. In the Parkinson's disease group the sparse PCA could not clearly distinguish if the increase in overlap was compensatory or maladaptive, since positive correlations were found with both sparse component 2 (low loadings on body bradykinesia, tremor, and H&Y stage, thereby suggesting compensatory function), as well as component 3 (high loadings on tremor and leg agility, thereby suggesting maladaptive function).

There were significant differences in right STN motor and associative territories in the COG coordinates. In the Parkinson's disease group the centre of gravity of the right motor and the right associative territory was shifted laterally. This effect might be either driven by a lateral shift of the motor/associative territory, or by a gradient of atrophy in the connectivity of the STN voxels running from medial to lateral. However, it is not possible to distinguish between these two possible interpretations. In both patient groups, i.e. patients with Huntington's and Parkinson's disease the centre of gravity of the right motor territory and the right associative territory was shifted dorsally. In the Parkinson's disease group these shifts were associated with the clinical data (sparse PCA components 3, 4 and 5) that are primarily indicative of an increase in motor symptoms.

This finding indicates that the functional territories of the STN undergo a shift in coordinates themselves, and this might be a reason why DBS sometimes fails or needs to be revised in Parkinson's disease. These shifts in the COG of the tripartite STN territories are inherently hard to interpret, and there was also a large variability in patient groups that probably reflects individual idiosyncrasies. However, since the patient groups differed significantly from the matched control groups in their motor COG coordinates in the right hemisphere, the motor territory might undergo neurodegenerative changes due to disease. This information might be relevant in the

clinical setting as additional guidance for deep brain stimulation in Parkinson's disease; the present gold standard for neurosurgery is to base the insertion of the electrode on altlas-based stereotactic coordinates of the motor STN, but these coordinates themselves as we have seen are affected by the disease state. Indeed, the precision of the electrode placement has been reported as an important factor determining the success of DBS in Parkinson's disease (Paek *et al.*, 2013). Further research is needed to replicate these changes in the centre of gravity of the tripartite STN territories, and to investigate if such information can be translated into the clinical context, and improve the outcomes of DBS surgery.

Despite these promising findings the present study has several limitations that merit discussion. The results presented here are preliminary results and not as thoroughly investigated as the other results sections, and the sample size of the study is still quite low, because the recruitment of the full sample is still running. Certainly, since we have detected significant effects despite a small sample size, we would expect that the significance of these effects would be even larger in a larger sample (Friston, 2012). However, due to the small sample size the effects seen are less generalizable to the entire population of patients with Huntington's and Parkinson's disease, and the probability that an observed significant effect reflects a true population effect, i.e. the positive predictive value, is lower than with a larger sample size (Button *et al.*,

2013). A further limitation was that the data acquisition only included single-shell data with one b-value, which might be problematic when tracking through regions of crossing fibers where multi-shell data might be required, due to the complex geometry of crossing, bending, and fanning fibres (Jbabdi and Johansen-Berg, 2011b). Indeed, the subthalamic nucleus is surrounded by various white matter tracts including the ansa lenticularis, the lenticular fasciculus, the distal part of the dentato-rubro-thalamic tracts, and cortico-subthalamic connections might be mainly formed by axon collaterals of the pyramidal tract running through the internal capsule. Further research is needed to validate if these complex fiber geometries in the internal capsule and the white matter surrounding the subthalamic nucleus can be reliably reconstructed using single-shell probabilistic tractography.

In conclusion, we have found alteration in the subthalamic nucleus and the hyperdirect pathway using 7T diffusion MRI in early Huntington's and early Parkinson's disease. These findings indicate that this pathway might play an important role in these diseases, and were consistent with a theoretical hypothesis about over-activity of the subthalamic nucleus in Parkinson's disease, and under-activity of the subthalamic nucleus in Huntington's disease.

Chapter II.7: Probabilistic tractography of the motor, limbic, and associative basal ganglia loops and connectivity-based parcellation of the globus pallidus pars interna in early Huntington's and Parkinson's disease using 7Tesla diffusion MRI

7.0. Abstract

Rationale. The globus pallidus, pars interna, is the final common pathway of 3 basal ganglia loops, i.e. the direct pathway (cortex-striatum-GPi), the indirect pathway (cortex-striatum-GPe-STN-GPi), and the hyerdirect pathway (cortex-STN-GPi), where various aspects of motor signal processing is integrated, and the combined signal is then send to thalamus to loop back to the cortex. In both Parkinson's disease and Huntington's disease the internal segment of the globus pallidus is a target for deep brain stimulation in patients whose symptoms are not amenable to other therapeutic options. Here we have investigated alterations in the structural connectivity of the cumulative corticofugal connections between the cortex and the globus pallidus, pars interna, as well as functionally segregated subregions of the globus pallidus, pars interna.

Objective. To reconstruct the cumulative basal ganglia loops converging on the globus pallidus, pars interna, using probabilistic tractography of high-resolution 7Tesla

diffusion MRI data. To parcellate the globus pallidus into the tripartite, i.e. motor, associative, and limbic territories based on its structural connectivity. To investigate alterations in the strength of connectivity of the tripartite corticofugal connections between the cortex and globus pallidus, pars interna, and structural changes of the tripartite subregions of the globus pallidus, pars interna, in two movement disorders, i.e. patients with early Parkinson's disease and early Huntington's disease relative to their healthy controls.

Methods. 7Tesla structural and diffusion MRI data were acquired from 18 patients with early Parkinson's disease, and 12 patients with early Huntington's disease, and 25 healthy controls. Probabilistic tractography was used to reconstruct the corticofugal connections between motor, associative and limbic regions of the cortex and the globus pallidus, pars interna, and derive a connectivity-based parcellation of the globus pallidus, pars interna.

Results. Lower strength of motor connectivity in the right hemisphere was found in patients with Huntington's disease compared with their matched control group. A clear contrast between patients with Huntington's and Parkinson's was found in the relative volume of the motor territory, particularly in the left hemisphere (but to a lesser extent also in the right hemisphere), with Parkinson's disease being lower than their matched control groups, and Huntington's disease being higher than their

matched control groups. An increase in the relative overlap of the motor and associative territories was found in patients with Huntington's disease in the left hemisphere. Centre of gravity statistics of the motor, associative and to a lesser extent the limbic territories underwent changes related to the diseases. Imaging outcomes correlated with dimensionality-reduced clinical data from UHDRS/UPDRS. *Conclusions.* Probabilistic tractography detected disease-specific alterations in the strength of connectivity of functionally segregated basal ganglia loops, as well as volumetric changes in the motor territory of the globus pallidus that are consistent with the role of these structures within the framework of the basal ganglia loop. Motor and associative territories within the globus pallidus, pars interna, undergo shifts due to disease, that are of clinical importance.

7.1. Introduction

The globus pallidus, pars interna, (GPi) plays a crucial role in the pathophysiology of both Huntington's and Parkinson's disease, and it is a central hub in the basal ganglia system, as it is the final common pathway of the classical direct, indirect, and the novel hyperdirect pathway. Imbalances in the direct pathway going from the cortex to the caudate and putamen and then to the GPi, and the indirect pathway going from the cortex to the caudate and putamen and then to the globus pallidus, pars externa, (GPe), from the GPe to the STN, and from the STN to the GPi, have been hypothesized as a potential pathophysiological mechanism underlying Parkinson's disease (Obeso *et al.*, 2002; Nelson and Kreitzer, 2014). More specifically, the well known degeneration of dopaminergic, nigrostrial neurons differentially modulates the direct pathway (excitatory D1 modulation), and the indirect pathway (inhibitory D2 modulation) in Parkinson's disease (Nelson and Kreitzer, 2014). The information from the hyperdirect pathway going from the cortex to the subthalamic nucleus, is ultimately also integrated in the GPi.

Cortico-subcortical connections through these pathways are functionally segregated in motor, limbic, and associative loops that are somatotopically organized (Obeso *et al.*, 2008), and show a high convergence in the basal ganglia. Using diffusion imaging it has been shown that motor, limbic, and associative territories can be reconstructed

in the striatum, and are altered in Huntington's disease (Bohanna *et al.*, 2008) More recently, a fourth pathway has been suggested on the basis of diffusion MRI research that provides direct afferent input from the cortex to the pallidum (Magaudda *et al.*, 2013; Demetrio *et al.*, 2014). The GPi is also one of the targets for deep brain stimulation in Parkinson's disease (Okun, 2012). More recently, deep brain stimulation of the GPi, has also been suggested as a treatment option for Huntington's disease (Gonzalez *et al.*, 2014; Wojtecki *et al.*, 2016).

Here we have used probabilistic tractography to reconstruct the cumulative connections from the cortex to the GPi that are part of the direct, indirect, hyper-direct pathway, and the cortico-pallidal tract. These basal ganglia loops are organized in functionally segregated cortico-basal reentry circuits, that can be mainly subdivided into motor, limbic and associative loops (Jahanshahi *et al.*, 2015), based on which part of the cortex gives rise to the loop. More specifically, the motor cortex, including primary (M1) and premotor cortex (PMC), the dorsolateral prefrontal cortex (DLPFC), as well as the orbitofrontal and anterior cingulate cortex, give rise to motor, associative, and limbic loops respectively that ultimately project to distinct territories within the GPi (Krack *et al.*, 2010; Saga, Hoshi and Tremblay, 2017). The information from probabilistic tractography was then used to derive a probabilistic

connectivity-based parcellation of the GPi into these motor, limbic, and associative territories as shown in **Figure 7.1.**

A. Probabilistic connectivity-based parcellation of the globus pallidus, pars interna (GPi) into topographic distinct, functionally segregated sub-territories

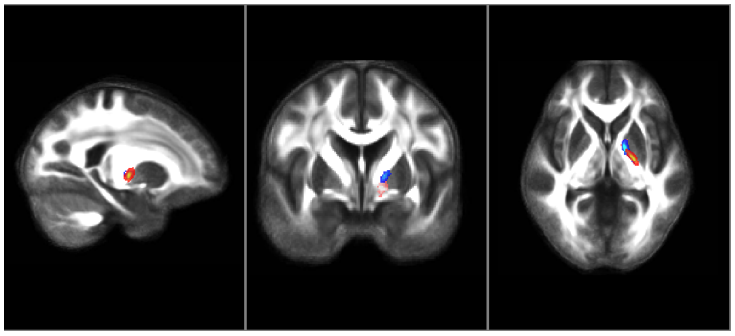

Red: motor , pink: limbic, blue: associative

B. Hard segmentation of the connectivity-based parcellation of the striatum into topographic distinct, functionally segregated sub-territories

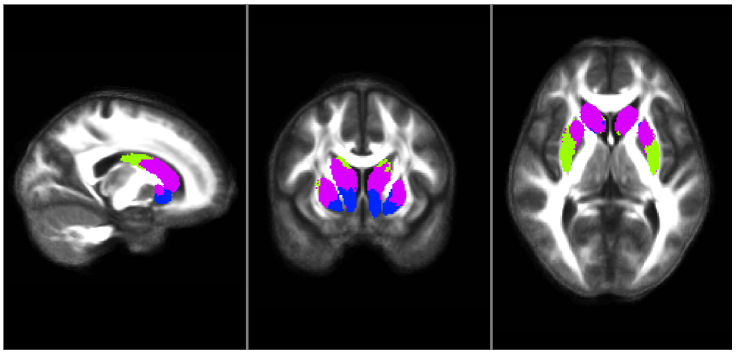

Green: motor, violett: associative, blue: limbic

C. Schematic drawing of topographically organized, functionally segregated cortico-basal ganglia circuits based on research in non-human primates (from Saga, Hoshi and Tremblay, 2017).

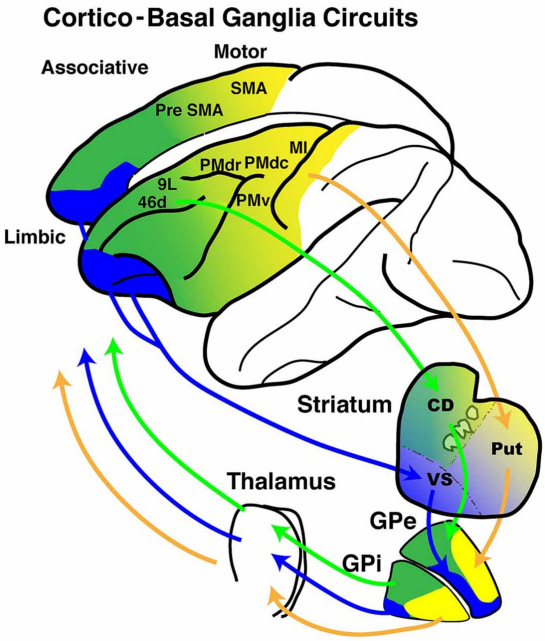

Yellow: motor, Blue: limbic, Green: associative

(from Saga, Hoshi and Tremblay, 2017)

Figure 7.1. Organization of the basal ganglia system into topographically organized, functionally segregated circuits as a framework for the interpretation of the results in this chapter. **A.** Probabilistic connectivity-based parcellation of the globus pallidus, pars interna (GPi), into topographically distinct, functionally segregated sub-territories, i.e. a caudodorsal motor territory (red), rostroventral limbic territory (pink), and a rostrodorsal associative territory (blue). An average of the probabilistic segmentation over all subjects and patient groups from the present study is shown.

B. Hard segmentation of the connectivity-based parcellation of the striatum (caudatoputamen) including the nucleus accumbens into the same sub-territories, thereby showing that the topographic organization can be found in humans at this level of the basal ganglia circuit. An average over all subjects and patient groups from the present study is shown. **C.** Schematic drawing of topographically organized, functionally segregated cortico-basal ganglia circuits based on research in non-human primates (from (Saga, Hoshi and Tremblay, 2017)). This figure illustrates how the tripartite topographical organization of the basal ganglia into motor, limbic and associative loops is reflected at various levels of the cortico-subcortical reentry circuits. (Figure 7.1C is originally copyrighted by Saga, Hoshi and Tremblay (2017) under the terms of the Creative Commons Attribution License [CC BY]).

7.2. Methods

A detailed description of the demographic and clinical data of the patient groups, as well as the study design can be found in section 4.2.1. Compared with the sample size in chapter 4, 3 additional patients with Parkinson's disease were recruited, making the overall sample size of the Parkinson's disease group N = 18.

7.2.1. Data processing: Probabilistic tractography

Data pre-processing and the probtrackx2 settings were the same as described in section 6.2. In brief, probabilistic tractography was used to track in both directions from cortex to the GPi, and from the GPi to cortex for each of the three basal ganglia loops: motor, limbic, and associative. The exclusion mask used for both tractography runs was modified to only comprise the thalamus and the cortices not used as either seed or target masks (e.g. in case of the the motor loop, the limbic and associative cortex was used as exclusion masks), and a customized mask for the limbic loop (see below). This exclusion mask was used to exclude fibers, (1) that go through the thalamus and are therefore part of corticopetal projections of GPi to the cortex, rather than the corticofugal projections from the cortex to the GPi, and (2) that terminate or go through cortices not used as either seed or target masks (e.g. in case of the the motor hyper-direct pathway, the limbic and associative cortex was

used as exclusion masks), and (3) that go through the optic nerves, fornix, or cingulum bundle in case of the limbic pathway. Seed, target and exclusion masks for the motor, limbic and associative basal ganglia loops are displayes in Figure Nn. The sum of the streamline images from both tractography runs was calculated, and divided by the waytotal to yield the final reconstruction of the cumulative direct, indirect, and hyerdirect corticofugal projections.

7.2.2. Connectivity strength

As described in chapter 6.2.4. the connectivity strength between the GPi and the cortex was calculated as the sum of the waytotals from the tractography runs going from the seed cortex to the GPi, and the GPi to the target cortex. A normalized measure of connectivity was calculated by dividing the sum of the waytotals by the number of voxels in the GPi mask for each subject.

7.2.3. Connectivity-based parcellation, volumetric analysis, and centre of gravity

Connectivity-based parcellation, volumetric analysis, and calculation of the centre of gravity was carried out on the sum of the streamline images from both tractography

runs that were normalized by the sum of the waytotals, and intersected with the GPi seeds. This was done using the same settings as described in chapter 6.2.5.

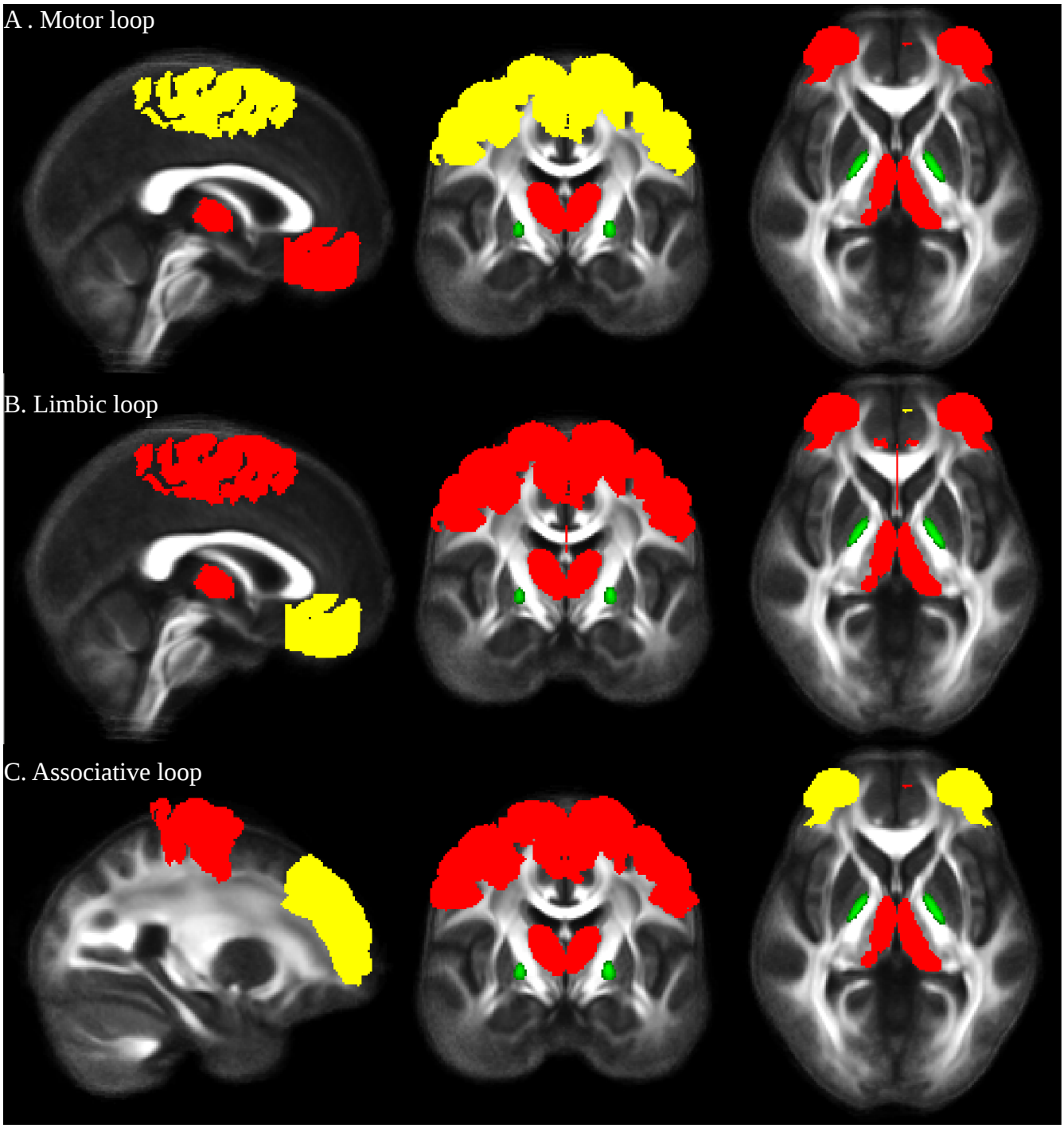

Figure 7.2. Seed, target, and exclusion masks for the motor (A), limbic(B), and associative (C) basal ganglia loops overlaid on the average fractional anisotropy image in standard space. Green: probabilistic seed/target mask of the globus

pallidus, pars interna, average over all subjects. Yellow: Atlas-based cortical seed/target mask. Red: Exclusion masks.

7.2.4. Spatial regression of tracts against diffusion metric images

The weighted average MD, FA, and MO was calculated across the cumulative basal ganglia loops with regions of crossing fibers masked out as described in chapter 6.2.6, and used for group comparisons.

7.2.5 Statistical inference

The same statistical tests as described in chapter 6.2.6. were used to test for significant group differences. In brief, permutational ANCOVA was carried out with age as covariate of no interest and group as categorical factor, and generalized linear hypotheses were used as post-hoc tests. If linear contrasts were significant between groups, the imaging outcomes were correlated with the components from sparse PCA, and the latent factors from factor analysis.

7.3. Results

Patients with Huntington's disease and Parkinson's disease showed significant differences relative to their age-matched control groups in the left GPi seed volumes (z = -2.566, p = 0.0103 *). This effect was mainly driven by a significant difference between patients with Huntington's disease and their matched controls (z = -2.566, p = 0.0103 *).

Patients with Huntington's disease and Parkinson's disease showed significant differences relative to their age-matched control groups in the right GPi seed volumes (z = -2.141 p = 0.0323 *). There was a trend towards a significant difference between patients with Huntington's disease and their matched controls (z = -1.848, p = 0.0647). To adjust for these differences that were already present in the seed volumes, we have normalized (divided) the tractography outcomes (way-totals, volumes) by the GPi seed volume for each subject.

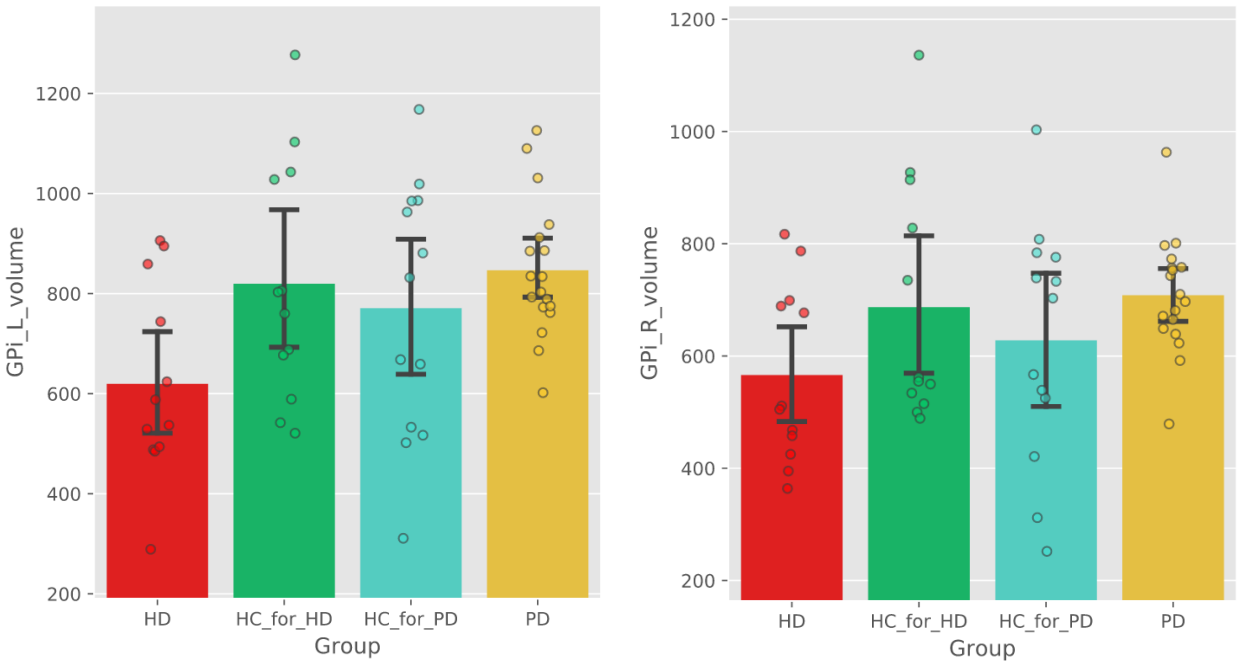

Figure 7.3. Bar plots of the GPi seed volumes for the left and right hemispheres. In both the left and right hemisphere there was a significant difference between patient groups relative to their matched controls. The difference between patients with Huntington's disease and healthy controls was significant in the left hemisphere, but only a trend in the right hemisphere.

7.3.1. Strength of connectivity in motor, limbic, and associative cumulative basal ganglia pathways

There were significant differences in the strength of connectivity of the motor cumulative basal ganglia loop in both HD and PD relative to their matched controls, lateralized to the right hemisphere ($z = -2.205$, uncorrected $p = 0.0275$ *). When normalizing the motor strength of connectivity by the size of the GPi seed mask, there was only a trend for significant differences in both HD and PD relative to their matched controls ($z = -1.887$, $p = 0.0591$). When directly comparing HD/PD groups with their age-matched controls, it was found that this effect was mainly driven by significant differences in right motor loop connectivity between the HD group and their age-matched control group before normalizing by the GPi volume ($z = -2.016$, $p = 0.0438$ *), but this effect did not survive the normalization by the GPi seed volume ($z = -1.258$, $p = 0.208$, see **Figure 7.4**).

No significant differences in alterations in connectivity strength were found for the left motor cumulative basal ganglia pathway before normalization nor after normalization by the GPi seed volume (lowest $p = 0.12$, and $p = 0.44$ respectively, **Figure 7.4**).

No significant differences in alterations of connectivity strength were found for the limbic or associative cumulative basal ganglia pathways (all $p > 0.05$).

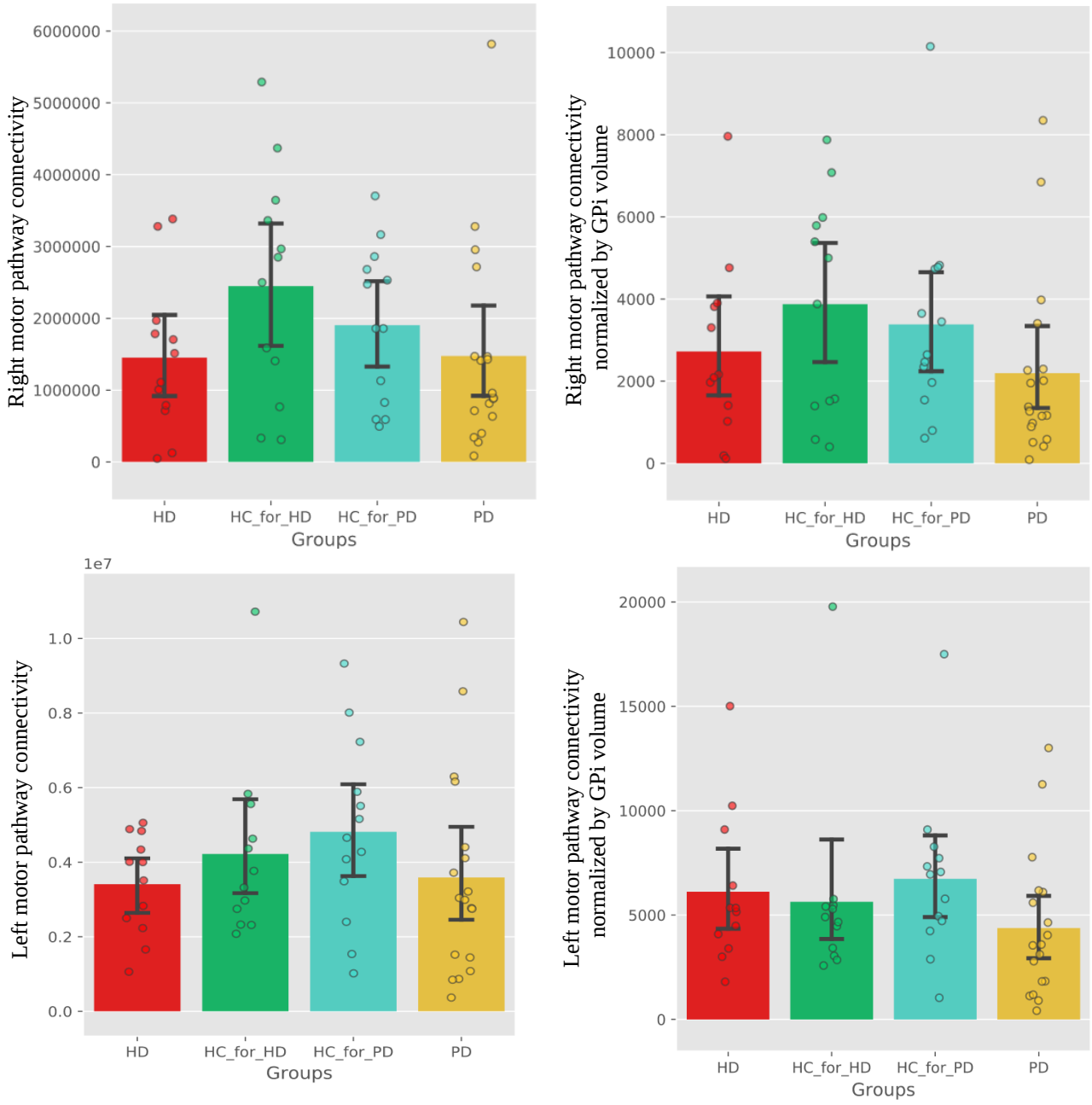

Figure 7.4. Significant differences in both HD and PD relative to their matched controls when looking at the strength of connectivity (i.e. the sum of the waytotals from both tractography runs) of the motor cumulative basal ganglia loop in the right hemisphere before normalization by the GPi seed/target volume (left column). After

normalization by the GPi seed/target volume, there is only a trend towards differences in both HD and PD compared with their age-matched control groups (right column).

7.3.2. Volumetric measures of motor, associative, and limbic territories within the globus pallidus, pars interna

The probabilistic segmentation of the globus pallidus pars interna was found to be in good accordance with previous neuroanatomical descriptions of these territories within the GPi with a ventromedial limbic territory, a rostrodorsal associative territory, and a dorsocaudal motor territory (see **Figure 7.5**).

No significant differences in alterations of the absolute volumes of the probabilistic motor, limbic or associative GPi territories (thresholded at the 10th percentile at the singe-subject level) were found in neither the left nor right hemisphere when comparing patients with HD/PD relative to their matched controls, or when comparing individual patient groups with their matched controls (all $p > 0.05$).

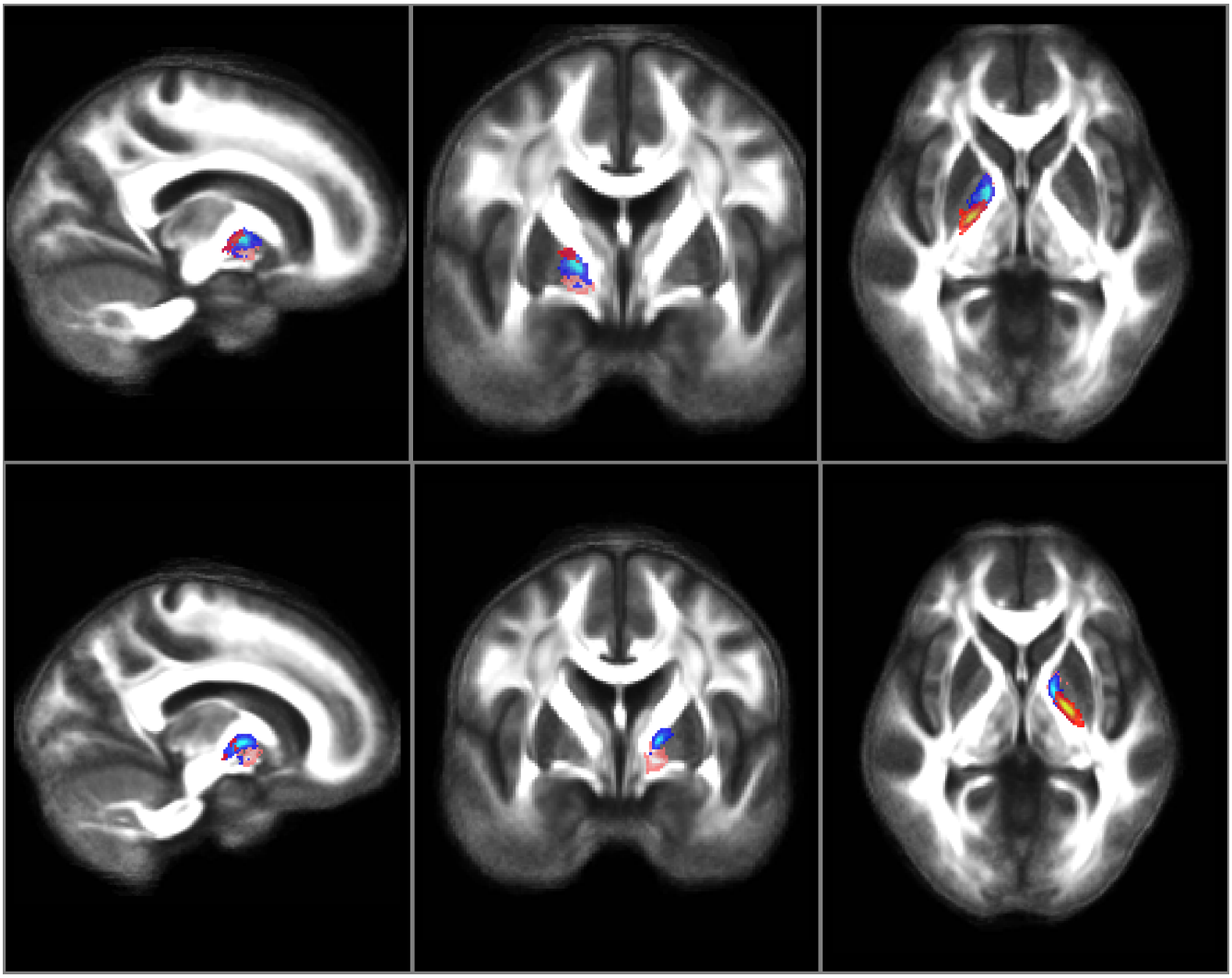

Figure 7.5. Probabilistic segmentation of the globus pallidus pars interna into motor (red-orange), limbic(pink-white), and associative territories (blue-lightblue) in the right (upper panel) and left hemisphere (lower panel).

There were significant differences between the patients with HD and PD relative to their age-matched control groups in the motor volume to total GPi volume ratio in the left hemisphere ($z = 2.365$, $p = 0.018$ *, **Figure 7.6**). When directly comparing each disease group (HD or PD) individually with their age/gender-matched controls, a significant difference between patients with PD and their matched controls was found in the motor volume ratio in both the left ($z = -2.046$, $p = 0.040$*) and the right hemisphere ($z = -2.148$, $p = 0.031$). Comparisons between the HD group and their matched control group were not significant (all $p > 0.05$).

No significant differences between patients with HD and PD and their matched controls were found for the limbic volume to total GPi volume ratios or the associative volume to total GPi volume ratios in either hemisphere (all $p > 0.05$).

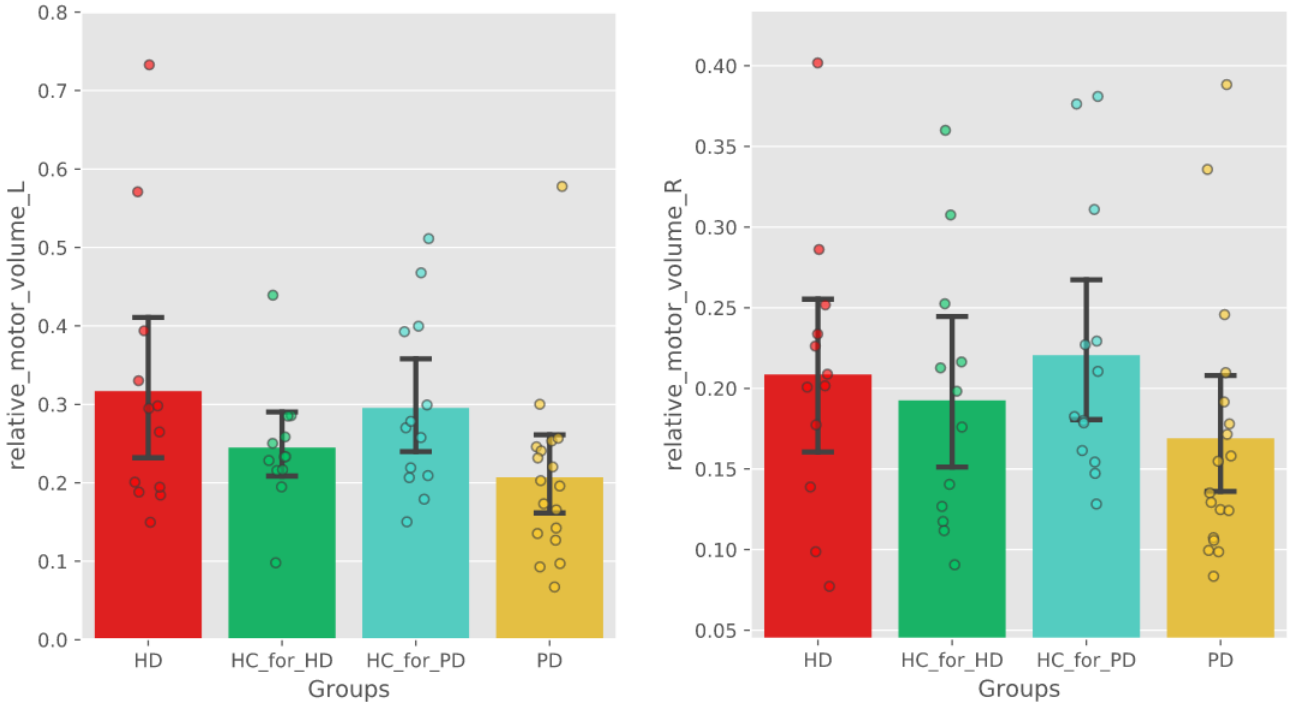

Figure 7.6. Significant differences in the volume ratio of the motor territory within the globus pallidus pars interna in the left and right hemispheres between patients with PD and their age-matched healthy controls.

7.3.3. Measures of overlap and similarity for the motor and associative GPi territories

When calculating the overlap between limbic and motor/associative territories, and the Jaccard index using a threshold at the 10th percentile of the streamline intensity at the single-subject level, several subjects did not show any overlap or had a Jaccard index equal to zero. We then subsequently tried various other thresholds at both the single-subject, and group level, including the 2.5^{th}, 5th, 7.5^{th} percentiles. Even with a threshold as low as the 2.5^{th} percentile, several subjects did not show any overlap or similarity between the limbic and the motor/associative territories, whereas other subjects showed nearly perfect overlap/similarity. We therefore post-hoc decided to discard the limbic territory from the analysis of overlap/similarity, and only focused on the overlap/similarity between motor and associative territories.

No significant differences between patients with HD and PD and their matched controls were found for the absolute volume of the overlap between the motor and associative GPi territories in either hemisphere, or the corresponding relative volume of the overlap normalized by the GPi seed volume (all $p > 0.05$). When directly comparing the HD/PD patient groups with their matched controls a significant difference between the patients with HD and their matched control group was found in the relative overlap between motor and associative territories normalized by the

volume of the GPi seed that was lateralized to the left hemisphere (z = 2.345, p = 0.0190 *, **Figure 7.7**). Similarly, when using the Jaccard index as a measure of similarity between the motor and associative territories, a significant difference between the patients with HD and their matched control group was found in the left hemisphere (z = 1.995, p = 0.0461 *, **Figure 7.7**).

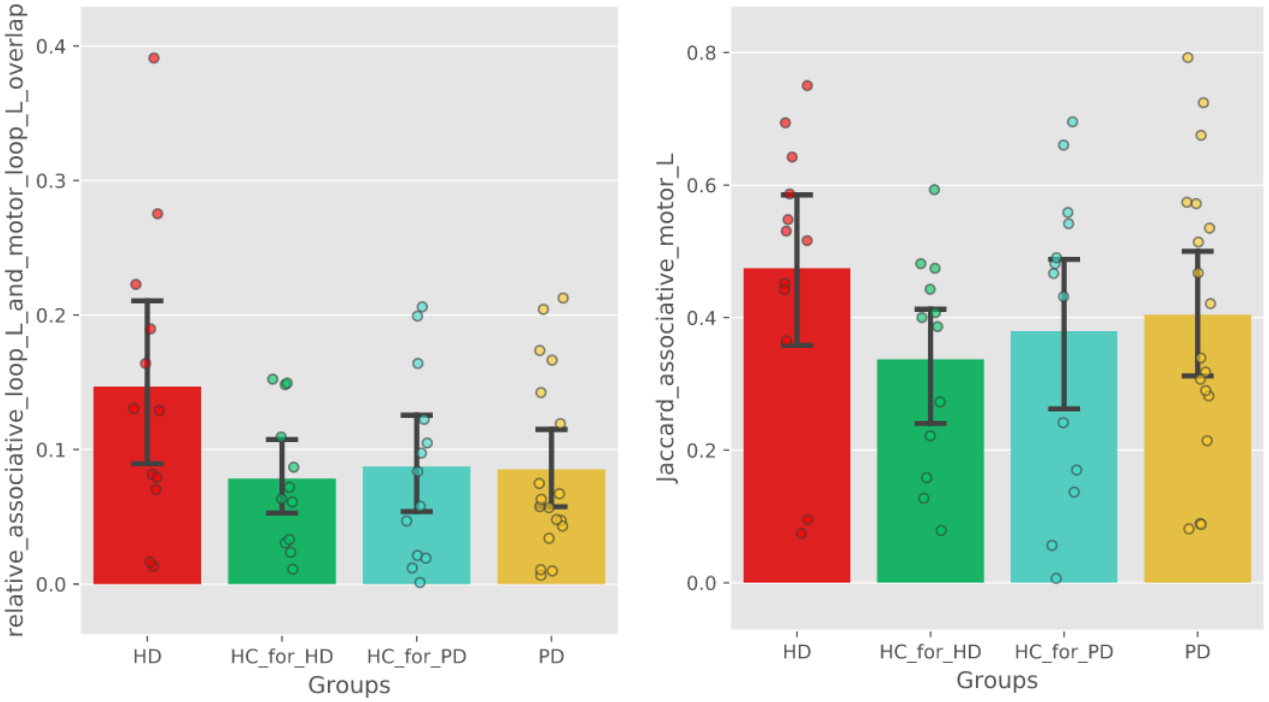

Figure 7.7. Significant differences between patients with HD and their age-matched healthy controls in the overlap between the associative and motor territories in the left GPi, normalized by the total GPi volume (left column), as well as in the Jaccard index as a measure of similarity between the associative and motor territories of the left GPi (right column).

When using Pearson correlation as a measure of similarity between motor and associative territories, significant differences in both HD and PD relative to their matched controls were found in the left hemisphere (z = 2.206, p = 0.027*) and there was a trend for the same effect in the right hemisphere (z = 1.932, p = 0.053). Post-hoc comparisons between individual patient groups and their control groups revealed a significant difference between patients with PD and their age/gender-matched controls in both the left (z = 3.002, p = 0.002**), and the right hemisphere (z = 1.966, z = 0.049*, **Figure 7.8.**).

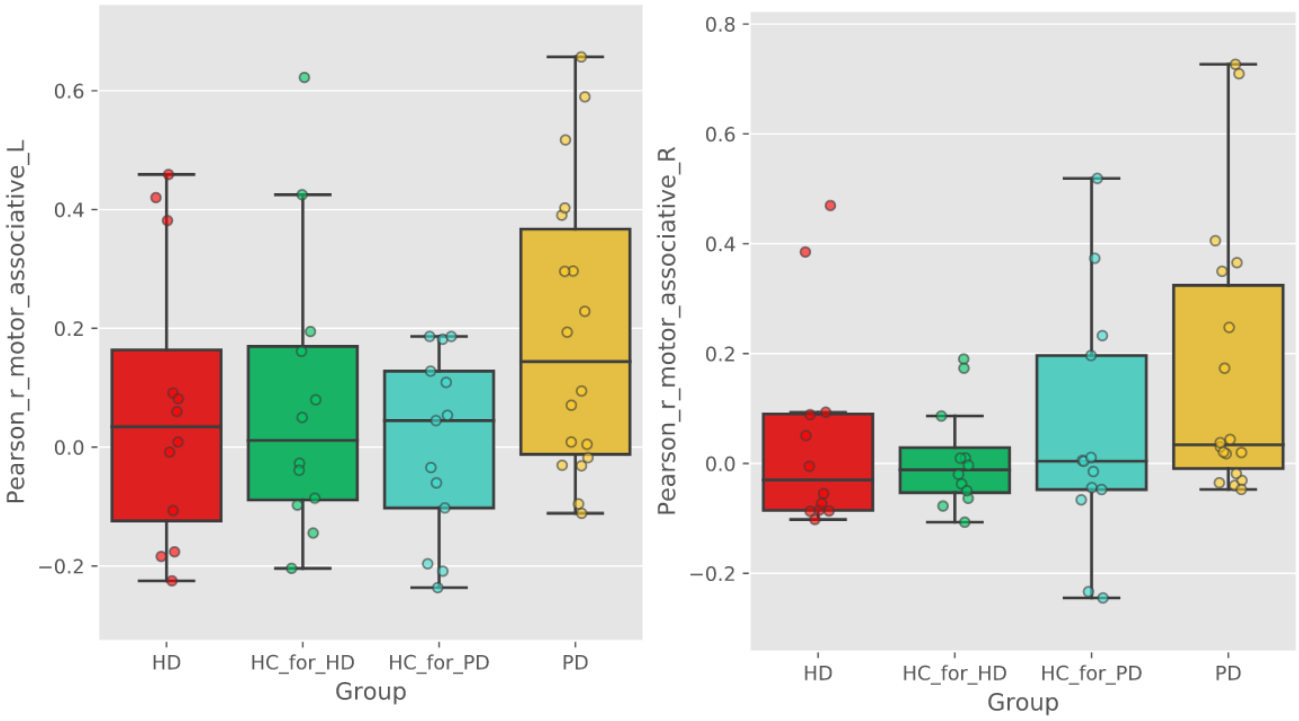

Figure 7.8. Significant differences between patients with PD and their age-matched healthy controls in the Pearson product moment correlations used as a measure of

similarity between the motor and associative territories within the GPi in the left and right hemispheres.

7.3.4. Centre of gravity (mass) statistics for the motor, limbic and associative connectivity-based parcellations

There were significant differences in both HD and PD relative to their matched controls in the normalized x-coordinate of the motor COG of the GPi that were lateralized to the right hemisphere ($z = -2.689$, $p = 0.007^{**}$, **Figure 7.9**). Post-hoc comparisons of the individual patient groups revealed that this effect was mainly driven by a significant difference in the normalized x-coordinate of the right motor COG between the HD group compared with the matched control group ($z = -2.108$, uncorrected $p = 0.03501$, **Figure 7.9**).

There were significant differences in both HD and PD relative to their matched controls in the normalized z-coordinate of the motor COG of the GPi that were lateralized to the left hemisphere ($z = 2.836$, $p = 0.004^{**}$, **Figure 7.9**). Post-hoc comparisons of the individual patient groups revealed significant differences in the normalized z-coordinate of the left motor COG between the HD group compared with the matched control group ($z = 2.080$, uncorrected $p = 0.037^{*}$, **Figure 7.13**). There was also a significant difference in the normalized z-coordinate of the left

motor COG between the PD group compared with the matched control group (z = 1.964, p = 0.049*, **Figure 7.9**).

No significant differences between patients with HD and PD relative to their age-matched control groups were found for the normalized y-coordinates of the motor COGs of the GPi in either hemisphere (all p > 0.05).

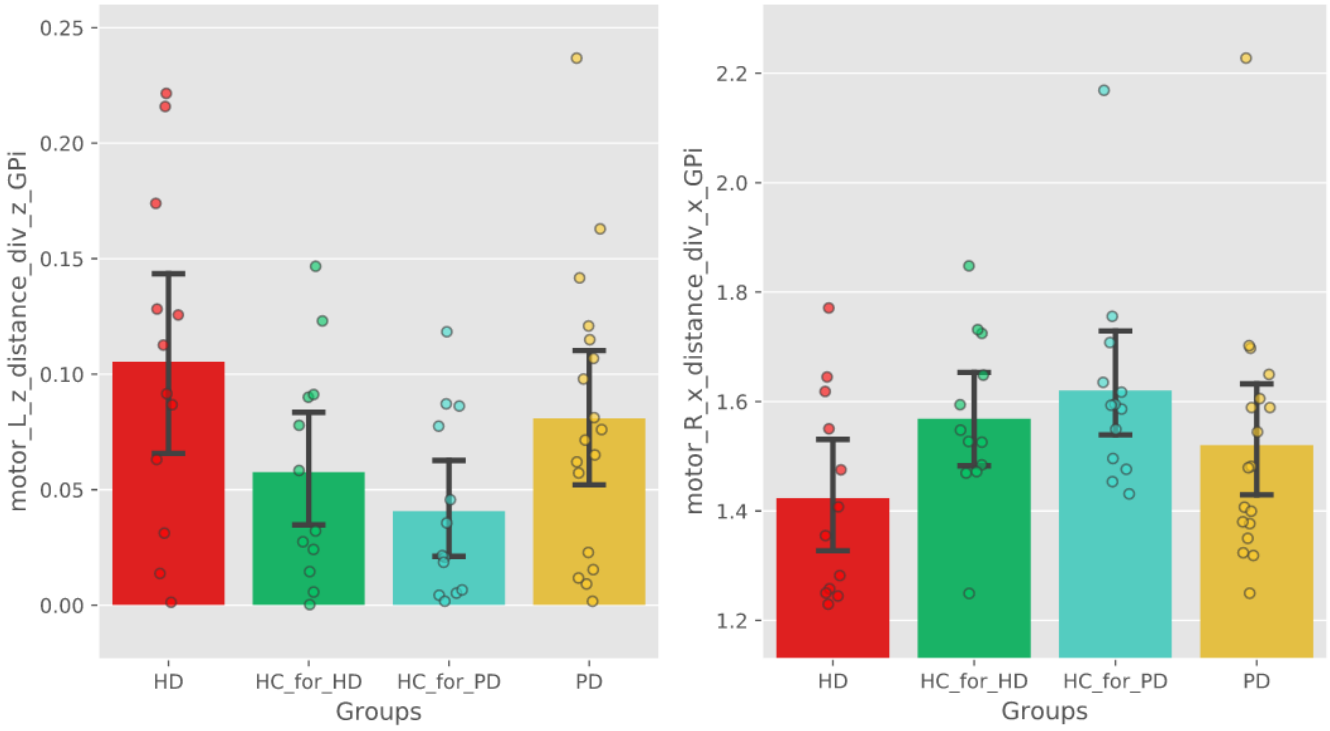

Figure 7.9. Significant differences between patients with HD and PD relative to their age-/gender-matched controls in the z-coordinate of the motor territory of the left GPi (left column), and in the x-coordinate of the motor territory of the right GPi (right column).

No significant differences between patients with HD and PD relative to their age-matched control groups were found for any limbic COG coordinate in either hemisphere (all $p > 0.05$). The only significant effect seen in the limbic COG coordinates was found when directly comparing patients with HD and their matched controls in the normalized x-coordinate of the limbic COG lateralized to the right hemisphere ($z = -1.986$, $p = 0.047$*, **Figure 7.10**.).

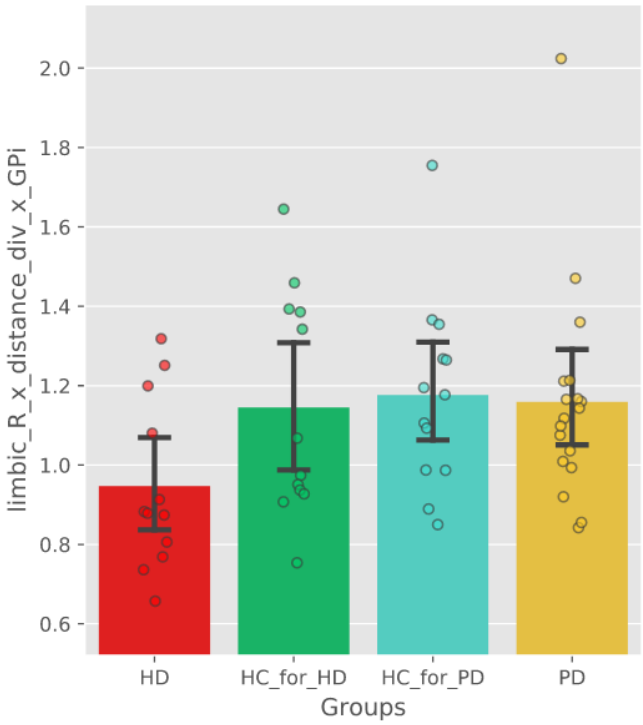

Figure 7.10. Significant differences between patients with HD and their age-/gender-matched controls in the x-coordinate of the limbic territory of the right GPi.

There were significant differences in both HD and PD relative to their matched controls in the normalized y- and z-coordinates of the associative COG in the left GPi (y-coordinate: z = 2.361, p = 0.018*; z-coordinate: z = 2.447, p = 0.014*, **Figure 7.11**.). Post-hoc comparisons of each individual patient groups with their age-/gender-matched control groups revealed that these effects were mainly driven by a significant difference in the normalized y- and z-coordinates of the associative COG between the HD group compared with their matched control group (y-coordinate: z = 2.578, p = 0.009**, z-coordinate: z= 2.224, p = 0.0261*, **Figure 7.11**.). No significant differences between the patient groups relative to their control groups were found for the x-coordinate of the left associative GPi COG (all p > 0.05).

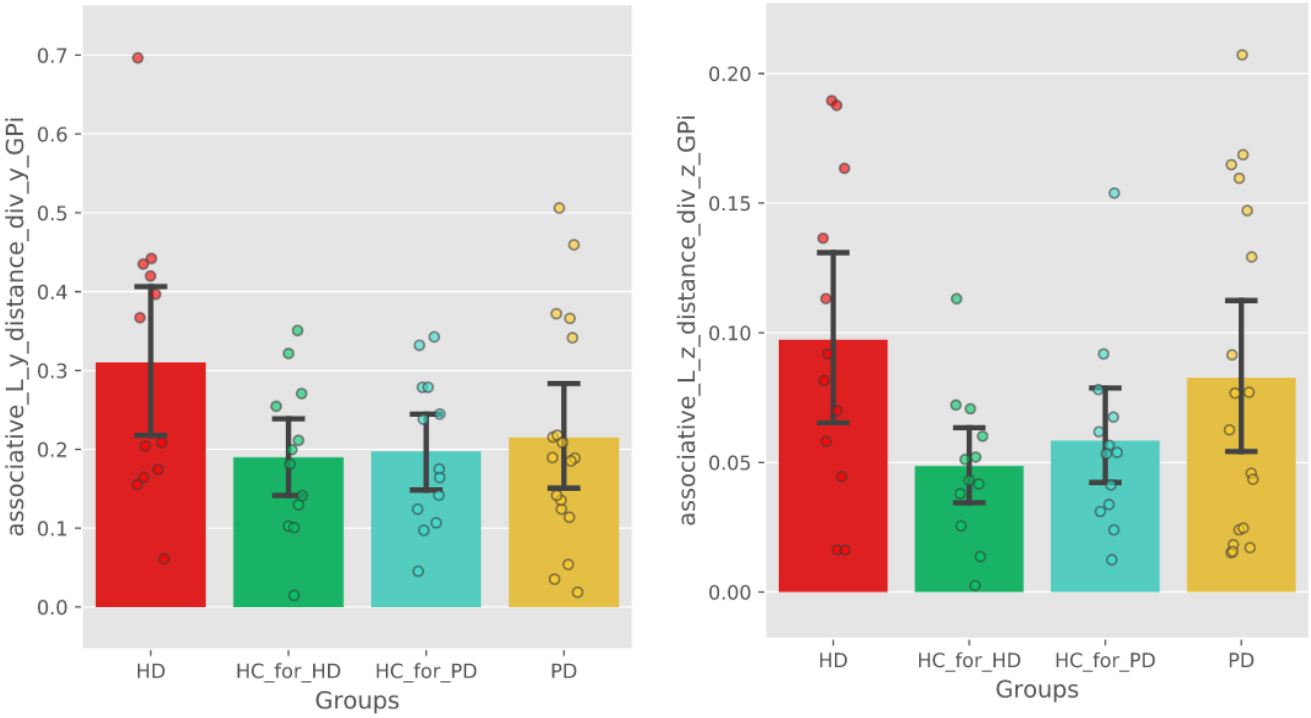

Figure 7.11. Significant differences between patients with HD and PD relative to their age- and gender-matched controls in the y-, and z-coordinates of the associative territory of the left GPi (left).

There were significant differences in both HD and PD relative to their matched controls in the normalized x- and z-coordinates of the associative COG in the right GPi (x-coordinate: z = -2.038, p =0.041*; z-coordinate: z = 2.485, p = 0.013, **Figure 7.12**). Post-hoc comparisons of the individual patient groups revealed that the effect seen in the z-coordinate was mainly driven by a significant difference between the HD group compared with their matched control group (z = 2.203, p = 0.0276*, **Figure 7.12**). No significant differences between the patient groups relative to their control groups were found between groups for the y-coordinate of the right associative GPi COG (all $p > 0.05$).

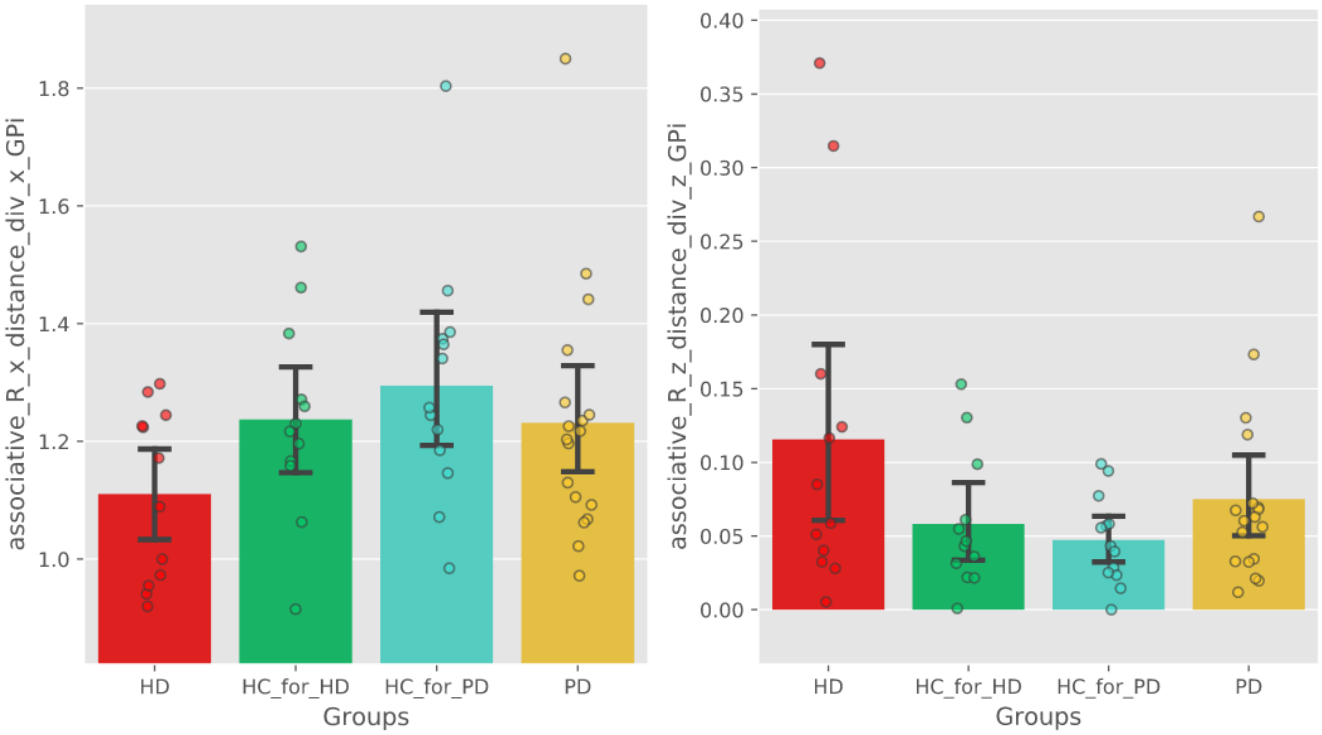

Figure 7.12. Significant differences in both patient groups, patients with HD and PD, compared with their age- and gender-matched controls in the x-, and z-coordinates of the associative territory of the right GPi.

7.3.5. Spatial regression of probabilistic reconstructions of the cumulative corticofugal basal ganglia pathway against diffusion metric images

An average over all subjects of the probabilistic reconstruction of the cumulative corticofugal basal ganglia pathways is shown in Figure Nn, and was found to be in good agreement with previous neuroanatomical descriptions.

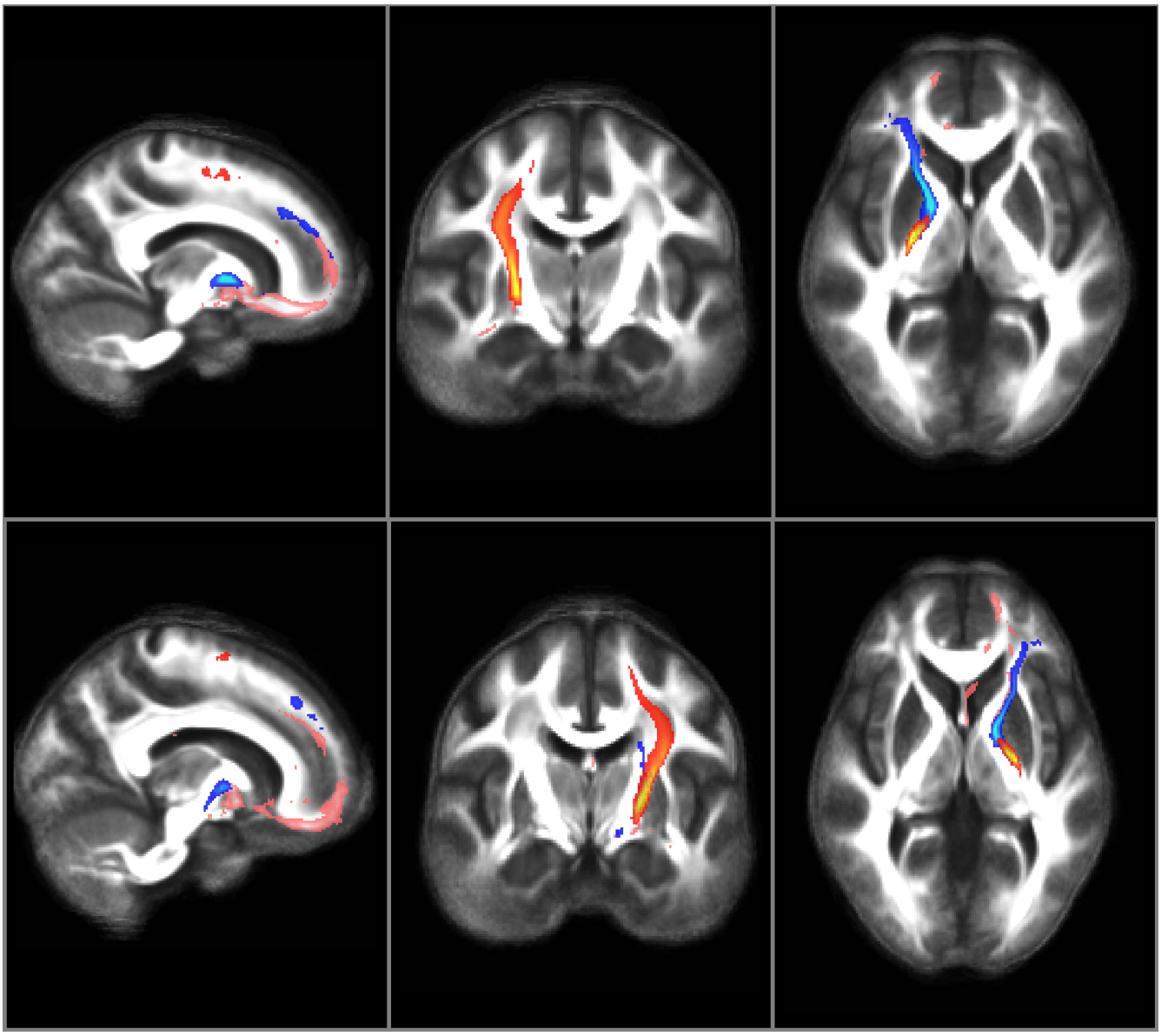

Figure 7.13. Probabilistic reconstruction of the corticofugal basal ganglia pathways going from the cortex to the GPi. Motor pathway (red-orange), associative pathway (blue-lightblue), and limbic pathway (pink-white).

There were significant differences between patients with HD and PD relative to their matched controls in MD, FA and MO in the limbic basal ganglia pathway in the right hemisphere ($z = -2.492$, $p = 0.013^{*}$; $z = -2.685$, $p = 0.007^{**}$; $z = -2.590$, $p = 0.009^{**}$ respectively, **Figure 7.14**). Post-hoc comparisons of the individual patient groups revealed that this effect was mainly driven by a significant difference between the PD group compared with their matched control group in the MD, FA, and MO in the limbic basal ganglia pathway in the right hemisphere ($z = 3.041$, $p = 0.002^{**}$, $z = 3.116$, $p = 0.001^{**}$, $z = 2.824$, 0.004^{**}, **Figure 7.14**).

No significant differences between the HD/PD groups relative to their patient groups were found in MD, FA, or MO in the motor and associative basal ganglia pathways in neither the right nor the left hemispheres (all $p > 0.05$).

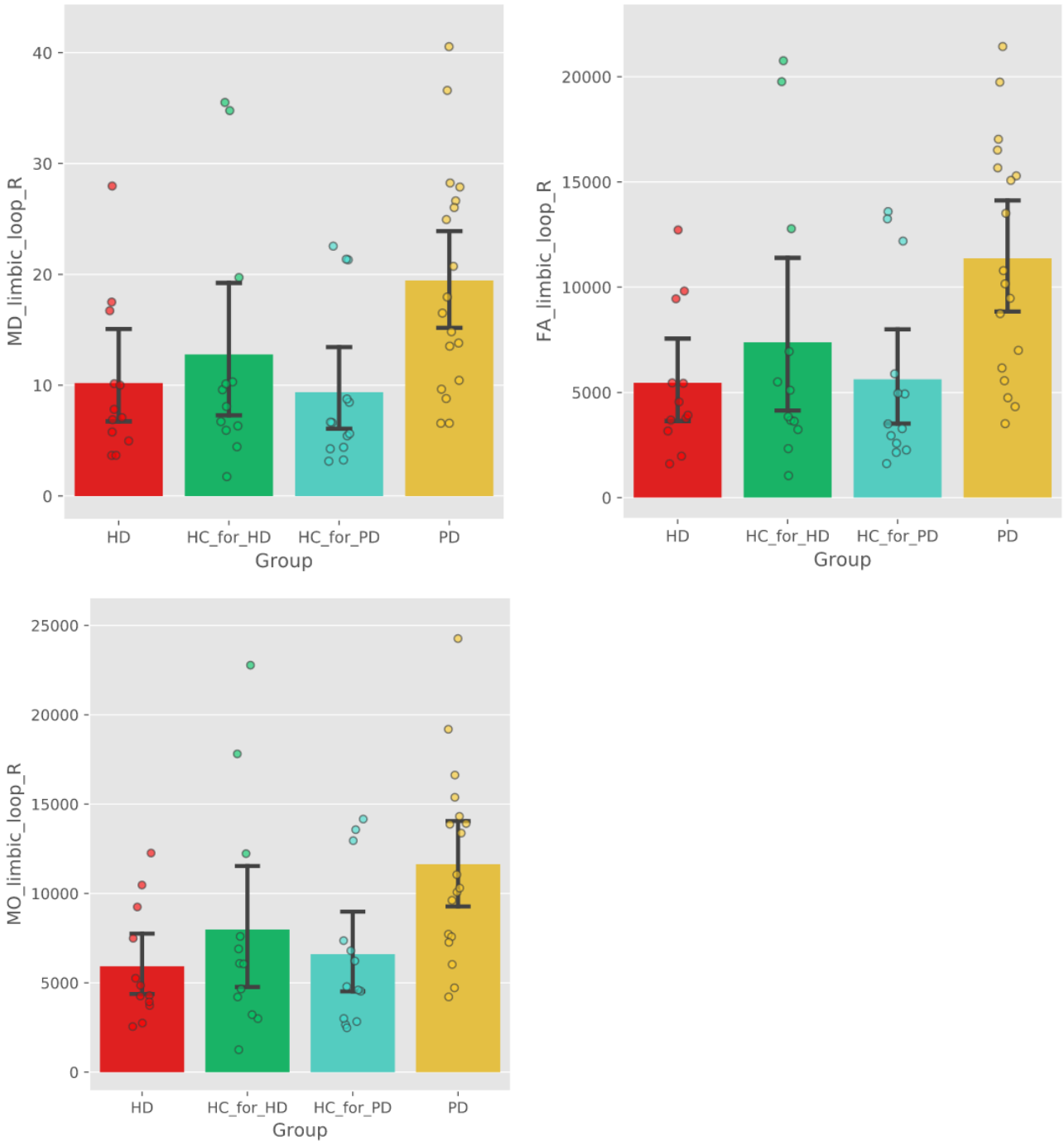

Figure 7.14. Significant differences between patients with HD and PD relative to their matched controls in mean diffusivity (MD, top left), fractional anisotropy (FA,

top right), and the mode of anisotropy (MO, bottom left) across the right limbic cumulative corticofugal basal ganglia pathway.

7.3.6. Correlation of imaging data with UHDRS/UPDRS sparse components

7.3.6.1. Correlations of strength of connectivity and GPi volumetric measures with UHDRS sparse components

There was a significant correlation between the relative motor volume of the left GPi and UHDRS component 4, consisting of motor symptoms of arm rigidity, ocular pursuit vertical, and postural instability, and irritability as a psychiatric symptom (Spearman's ρ = -0.641, p = 0.024, **Figure 7.15.**). There was a significant correlation between component 7, consisting of finger/hand movements and figural intelligence, and the relative motor volume of the left GPi (Spearman's ρ = -0.720, p = 0.008, **Figure 7.15.**), as well as a trend towards a correlation between UHDRS Component 7 and the relative overlap of the left associative and motor GPi (Pearson's r = -0.572, p = 0.051, **Figure 7.16.**).

There were trends towards a correlation between the relative motor volume of the left GPi and UHDRS component 2, mainly loading on chorea, dystonia and gait (Spearman's ρ = 0.573, p = 0.051, **Figure 7.15.**), as well as UHDRS component 10,

showing high loadings on functional assessment, proximal chorea/dystonia, and verbal intelligence (Spearman's $\rho = 0.503$, $p = 0.095$, **Figure 7.15.**).

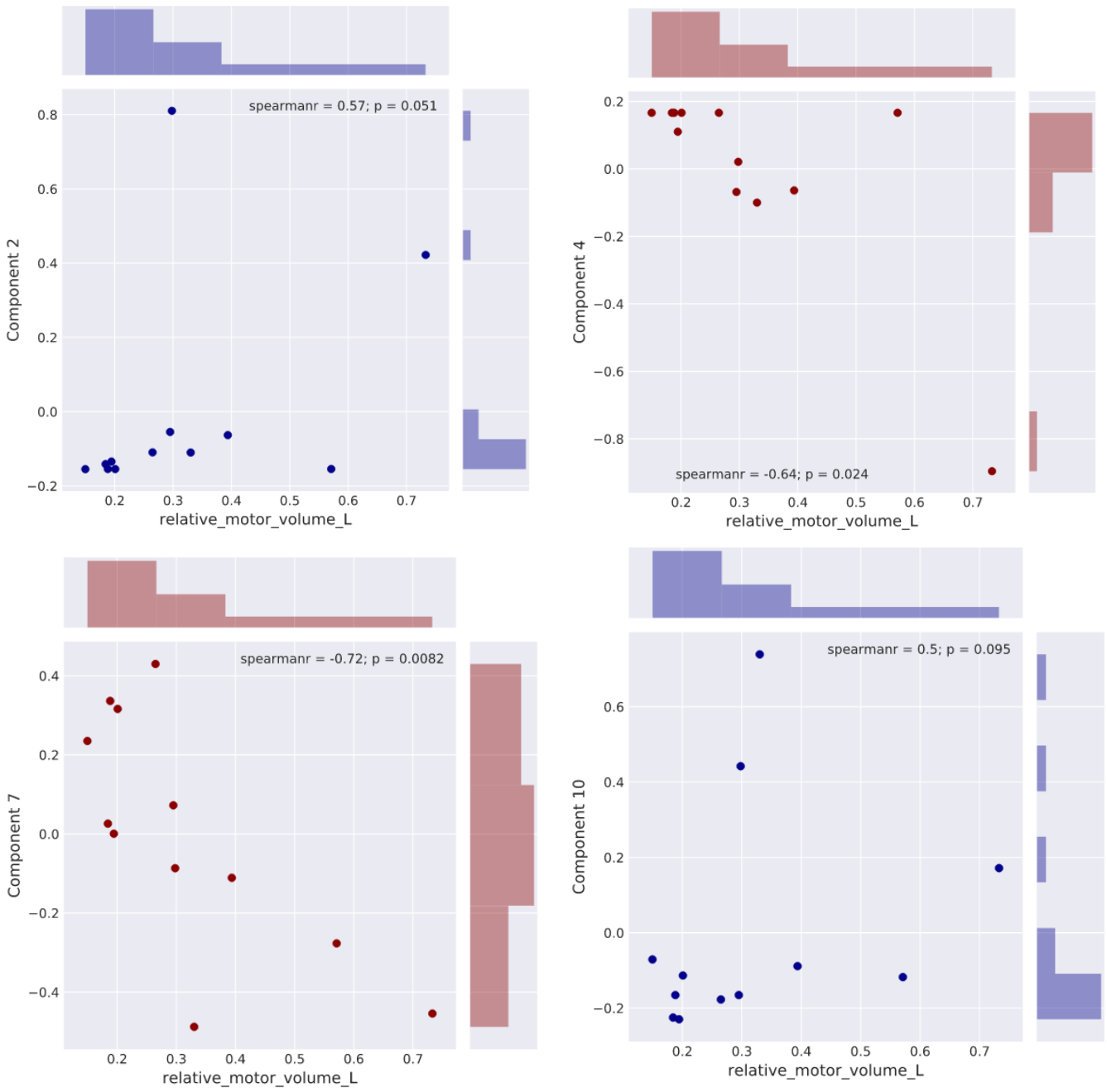

Figure 7.15. Scatter plots showing significant/trend correlations between the relative motor volume of the left GPi, and UHDRS components 2, 4 , 7, and 10.

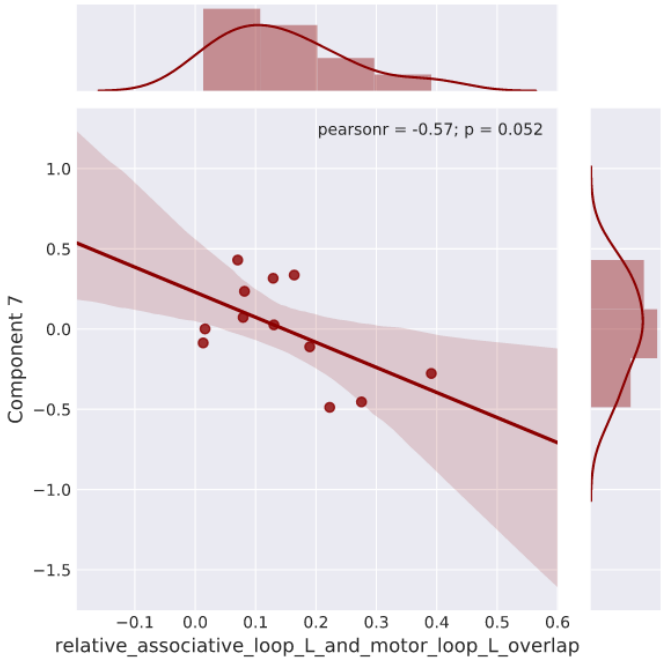

Figure 7.16. Scatter plot showing a trend towards a significant correlation between the relative motor volume of the right GPi and UHDRS component 7, mainly loading on finger/hand movements and figural intelligence.

7.3.6.2. Correlations between GPi centre of gravity statistics and UHDRS sparse components

There was a strong trend towards a correlation between the normalized z-coordinate of the left associative GPi and UHDRS component 3, mainly loading on psychiatric symptoms and ocular motor pursuit (Spearman's $\rho = 0.573$, $p = 0.051$, **Figure 7.17**).

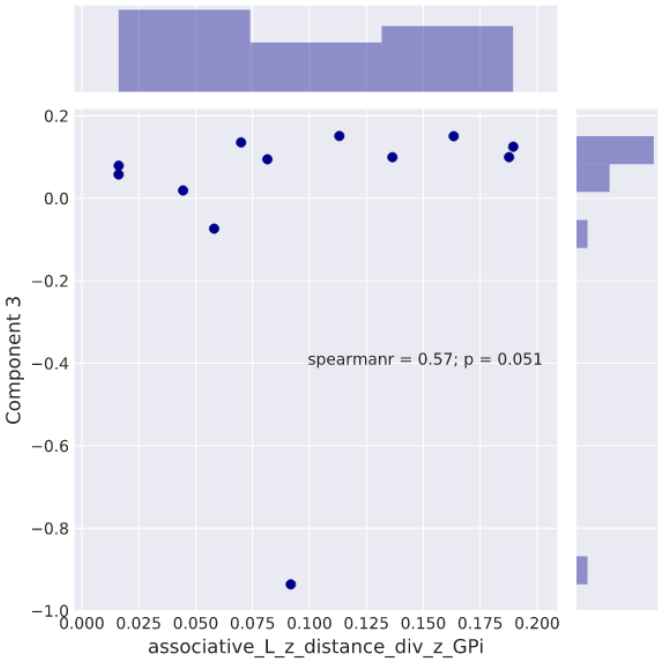

Figure 7.17. Scatter plot showing the trend towards a significant correlation between the z-coordinate of the left associative GPi and UHDRS component 3.

7.3.6.3. Correlations between latent factors from exploratory factor analysis of UHDRS data and strength of connectivity and GPi volumetric measures

There were significant/trend correlations between the strength of connectivity of the right motor pathway, and UHDRS latent variable 1 (Spearman's $\rho = 0.503$, $p = 0.095$, **Figure 7.18.**), latent variable 5, mainly loading on motor symptoms (bradykinesia, saccade movement) and Stroop (Spearman's $\rho = -0.622$, $p = 0.030$, **Figure 7.18.**), and latent variable 6, mainly loading on hand movements and verbal intelligence (Pearson's $r = 0.748$, $p = 0.005$, **Figure 7.18.**). There was a significant correlation between the relative volume of the left GPi motor territory and UHDRS latent variable 1 (Spearman's $\rho = 0.594$, $p = 0.041$, **Figure 7.19.**). There was a significant correlation between UHDRS latent variable 10 (verbal intelligence and Stroop interference) and the Jaccard index of similarity between the left motor and associative territories (Spearman's $\rho = -0.587$, $p = 0.044$, **Figure 7.20.**). There was a significant correlation between UHDRS latent variable 3 (psychiatric symptoms of low mood disorders, eye movements, and verbal intelligence), and the relative overlap between the left motor and associative territories (Spearman's $\rho = -0.790$, $p = 0.002$, **Figure 7.20.**), as well as a trend towards a significant correlation between the same

overlap metric and UHDRS latent variable 6 (hand movements, and verbal intelligence (Pearson's r = 0.516, p = 0.085, **Figure 7.20.**).

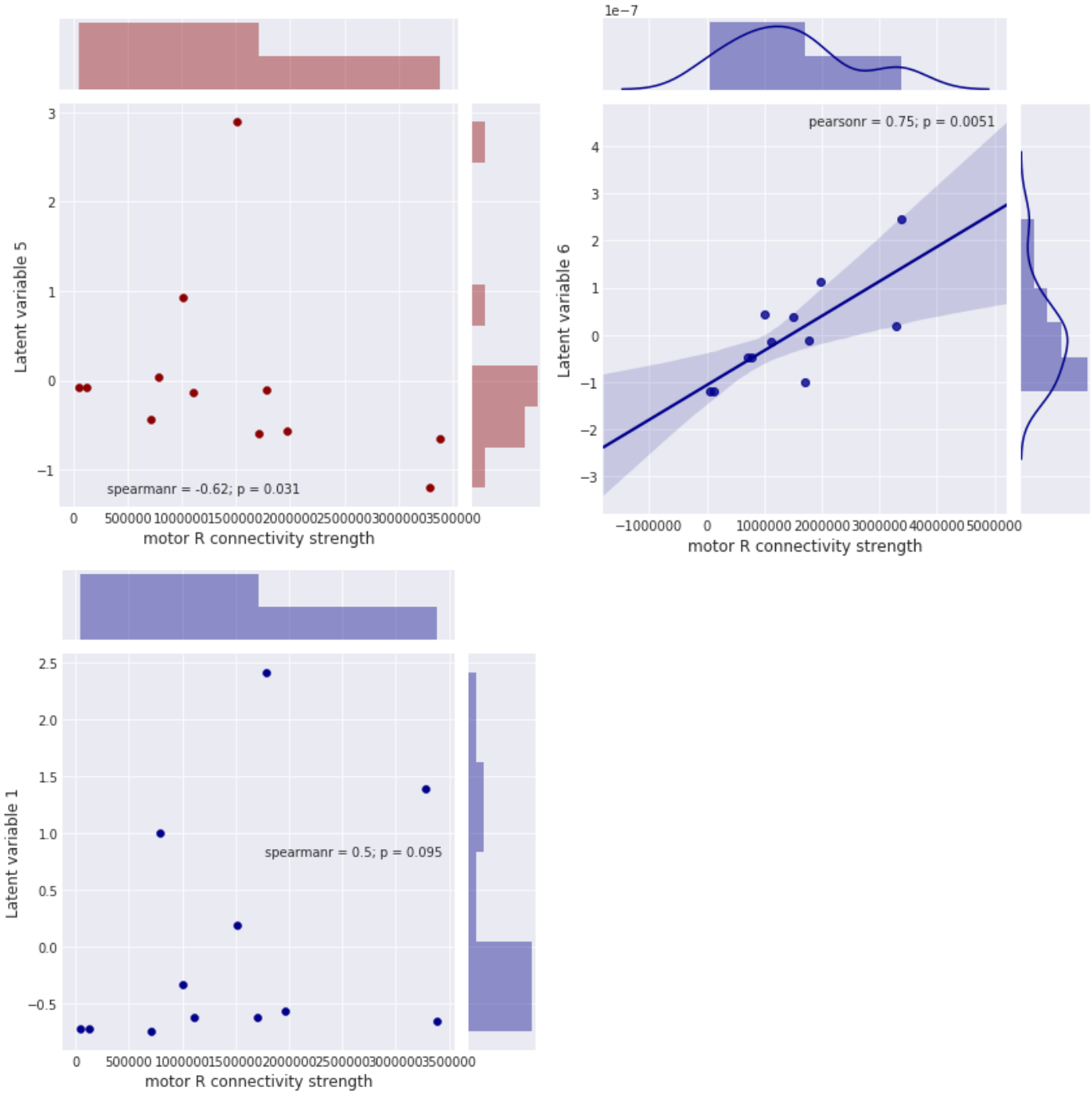

Figure 7.18. Scatter plots showing the significant/trend correlations between the connectivity strength of the right motor basal ganglia loop, and UHDRS latent variables 5, 6 and 1 from exploratory factor analysis.

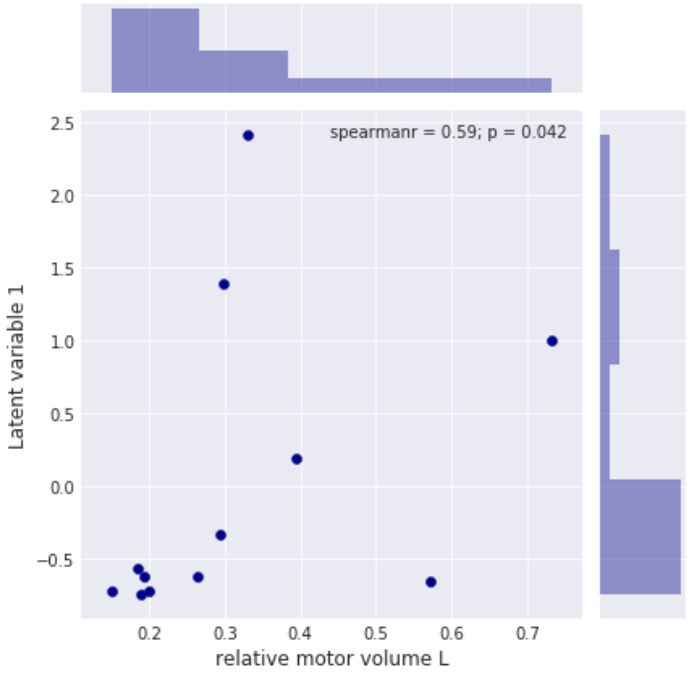

Figure 7.19. Scatter plot showing the significant correlations between relative volume of the motor territory of the left GPi, and UHDRS latent variable 1. from exploratory factor analysis.

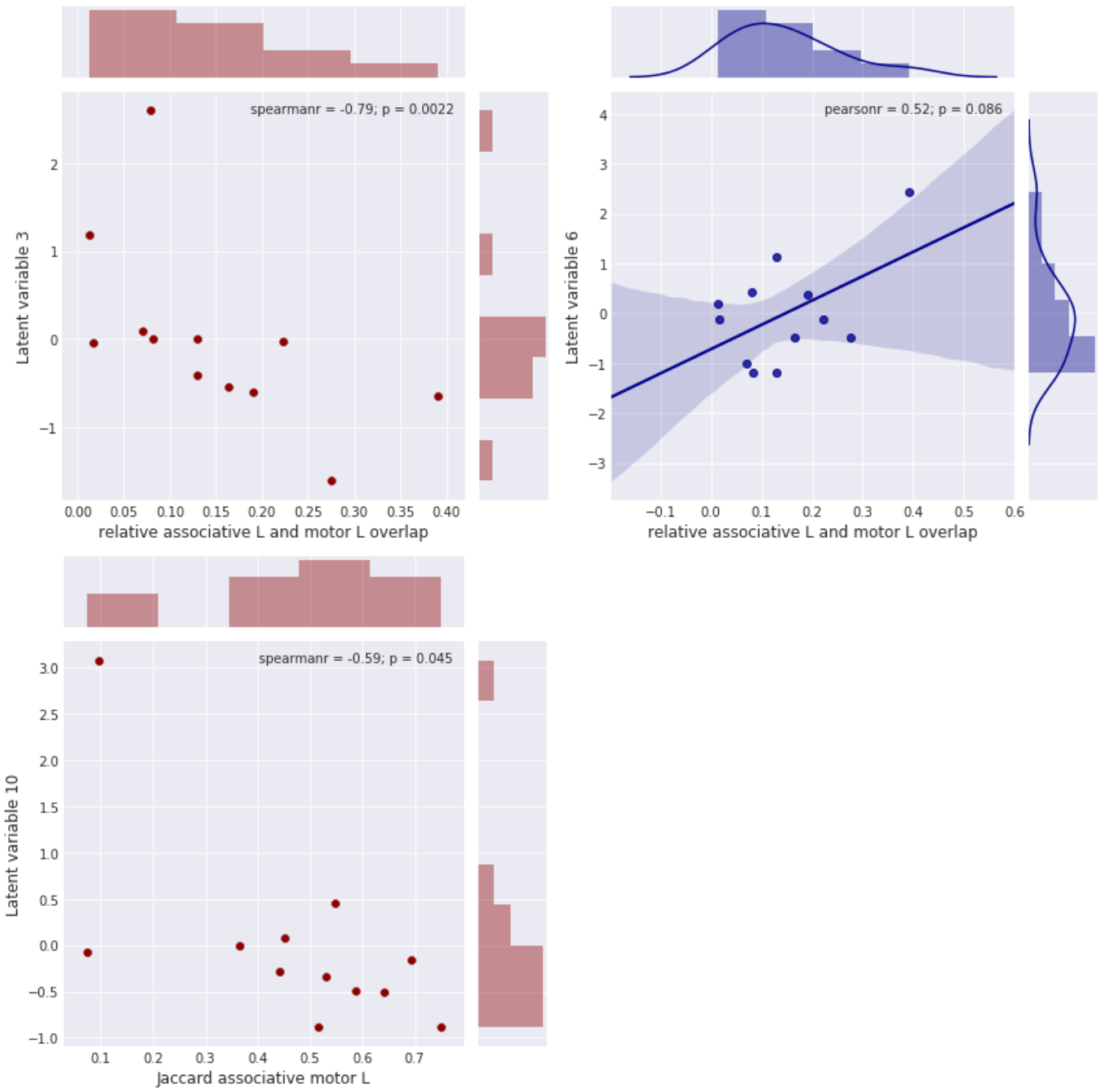

Figure 7.20. Scatter plot showing the significant/trend correlations between the overlap of the left GPi motor and associative territory, normalized by the total GPi volume, and UHDRS latent variables 3, and 6, as well as the significant correlation

between the motor-associative Jaccard index of the left GPi and UHDRS latent variable 10.

7.3.6.4. Correlations between latent factors from exploratory factor analysis of UHDRS data and GPi centre of gravity statistics

There was a significant correlation between UHDRS latent variable 4, mainly loading on oculumotor symptoms, verbal intelligence, and psychiatric symptoms, and the normalized x-coordinate of the right motor GPi (Pearson's r = 0.759, p = 0.004, **Figure 7.21**), as well as the normalized x-coordinate of the right limbic GPi (Pearson's r = 0.600, p = 0.038, **Figure 7.22**), as well as the normalized y-coordinate of the left associative GPi (Pearson's r = 0.591, p = 0.042, **Figure 7.23**). There was a significant correlation between the normalized z-coordinate of the left motor GPi and UHDRS latent variable 2 (Pearson's r = 0.623, p = 0.030, **Figure 7.21**). There was a trend towards a correlation between the normalized x-coordinate of the right limbic GPi and UHDRS latent variable 6 (Pearson's r = 0.572, p = 0.051, **Figure 7.22**). There was a significant correlation between the normalized associative y-coordinate of the left associative GPi and UHDRS latent variable 3 (Spearman's ρ = -0.692, p = 0.012, **Figure 7.23**). There was a significant correlation between normalized z-coordinate of the left associative GPi and UHDRS latent variable 6 (Pearson's r = 0.642, p = 0.024, **Figure 7.23**). There was a trend towards a correlation between normalized x-coordinate of the right associative GPi and UHDRS latent variable 9 (Spearman's ρ = 0.503, p = 0.095, **Figure 7.23**). There

was a significant correlation between the normalized z-coordinate of the right associative GPi and UHDRS latent variable 10 (Spearman's ρ = -0.748, p = 0.005).

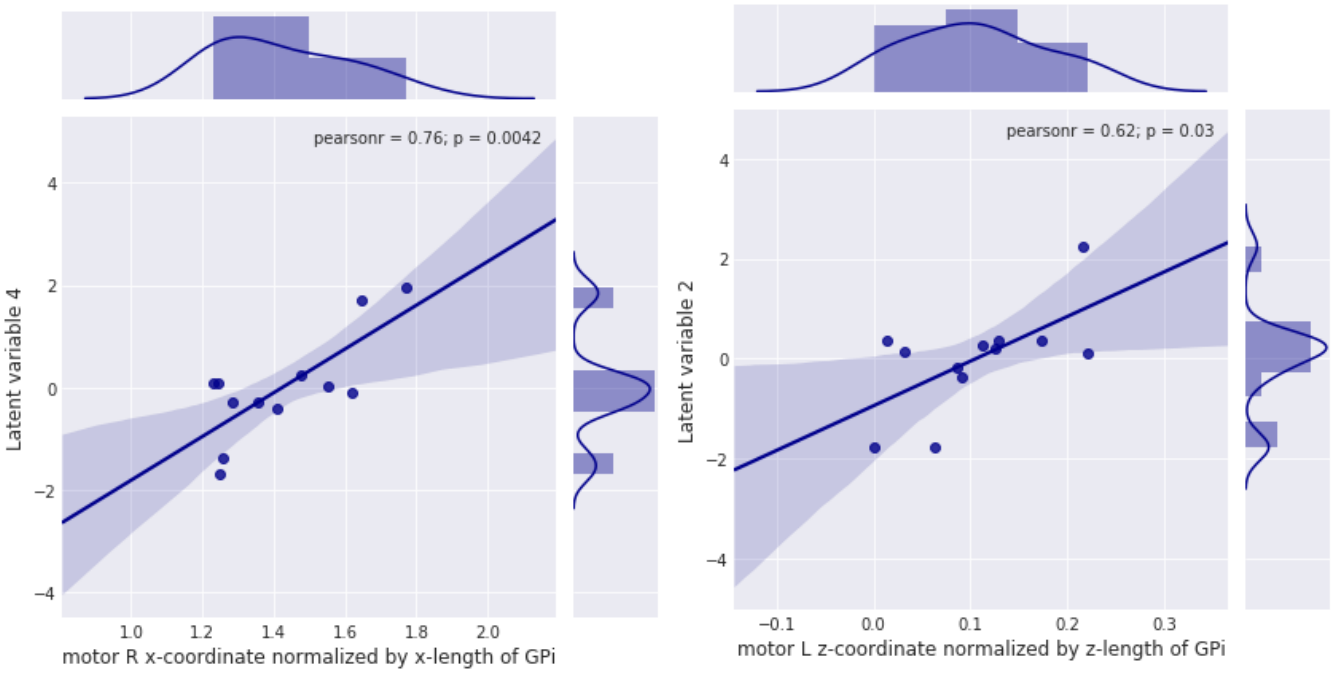

Figure 7.21. Scatter plots showing the significant correlation between the x-coordinate of the COG of the right motor territory and latent variable 4 from UHDRS exploratory factor analysis as well as the significant correlation between the z-coordinate of the COG of the left motor territory and latent variable 2 from UHDRS exploratory factor analysis.

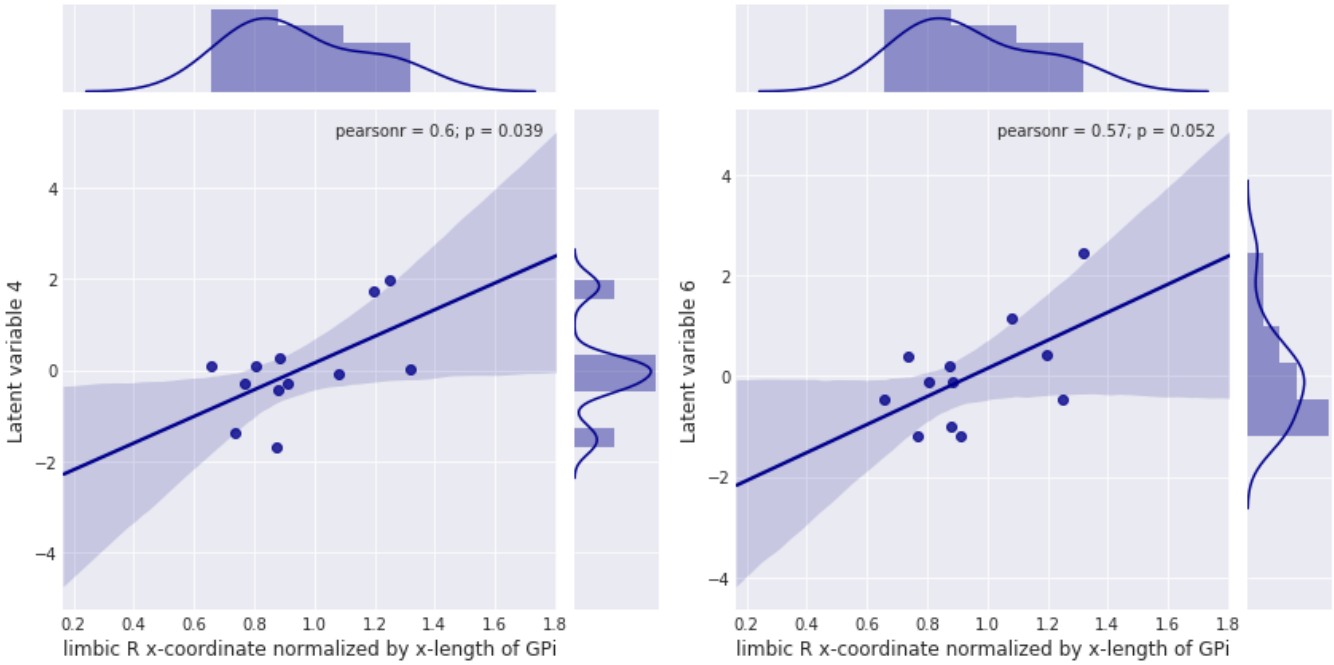

Figure 7.22. Scatter plots showing the significant correlation between the x-coordinate of the COG of the right limbic territory and latent variable 4 from UHDRS exploratory factor analysis as well as the trend correlation between the x-coordinate of the COG of the right limbic territory and latent variable 6 from UHDRS exploratory factor analysis.

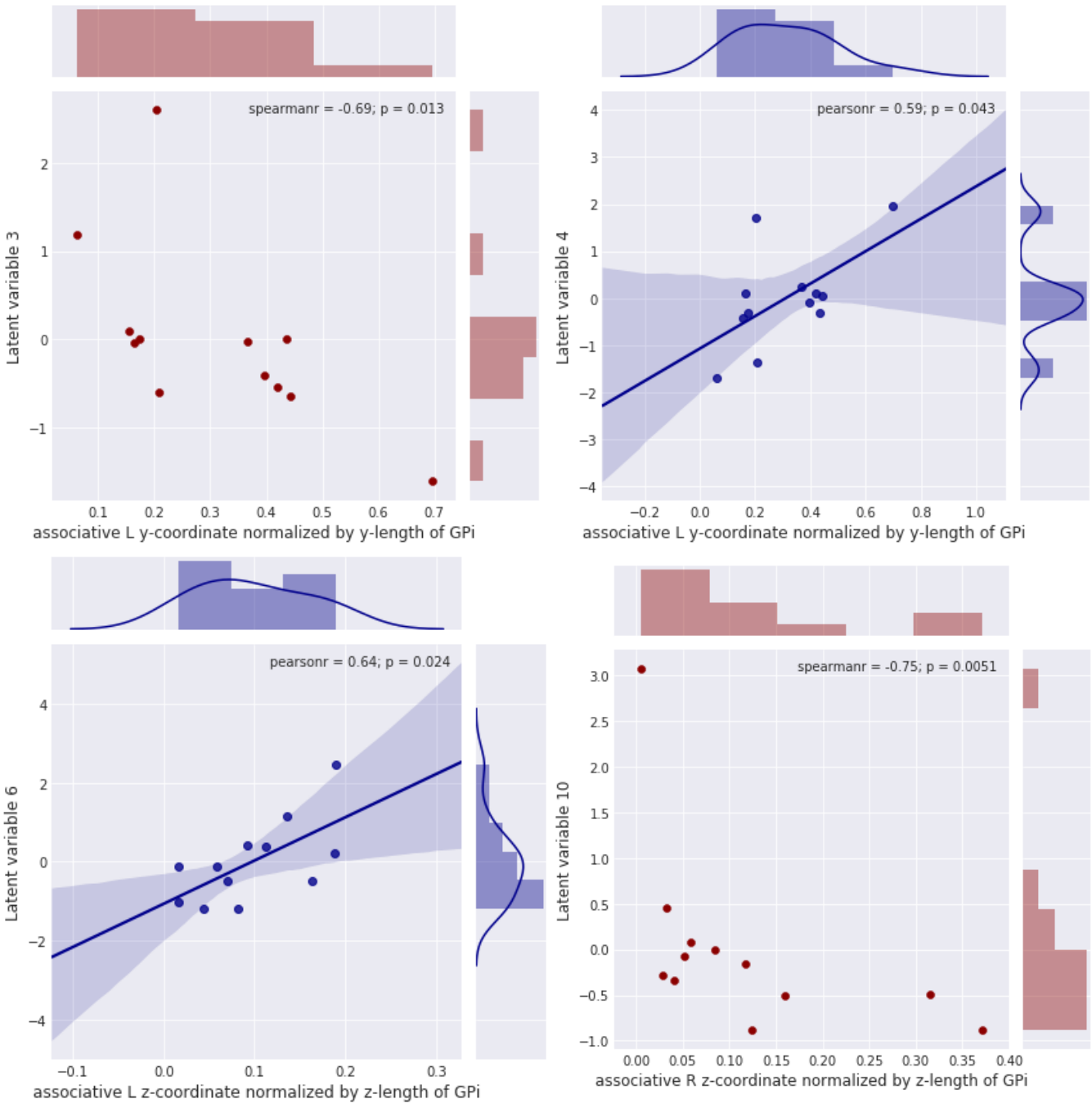

Figure 7.23. Scatter plots showing the significant correlation between the y-coordinate of the COG of the left associative territory and latent variables 3, and 4 from UHDRS exploratory factor analysis, the significant correlation between the z-

coordinate of the COG of the left associative territory and latent variable 6 from UHDRS exploratory factor analysis, as well as the significant correlation between the z-coordinate of the COG of the right associative territory and latent variable 10 from UHDRS exploratory factor analysis.

7.3.6.5. Correlation of strength of connectivity and GPi volumetric measures with UPDRS sparse components

There was a trend towards a correlation between the connectivity strength of the right motor loop and UPDRS component 2 that was mainly loading on tremor, body bradykinesia, H&Y stage, and hours asleep (Spearman's ρ = -0.446, p = 0.063, **Figure 7.24**). There was a trend towards a correlation between the relative motor volume of the right GPi and the UPDRS component 9 that was loading on impairments of daily activities (Spearman's ρ = 0.455, p = 0.057, **Figure 7.24**).

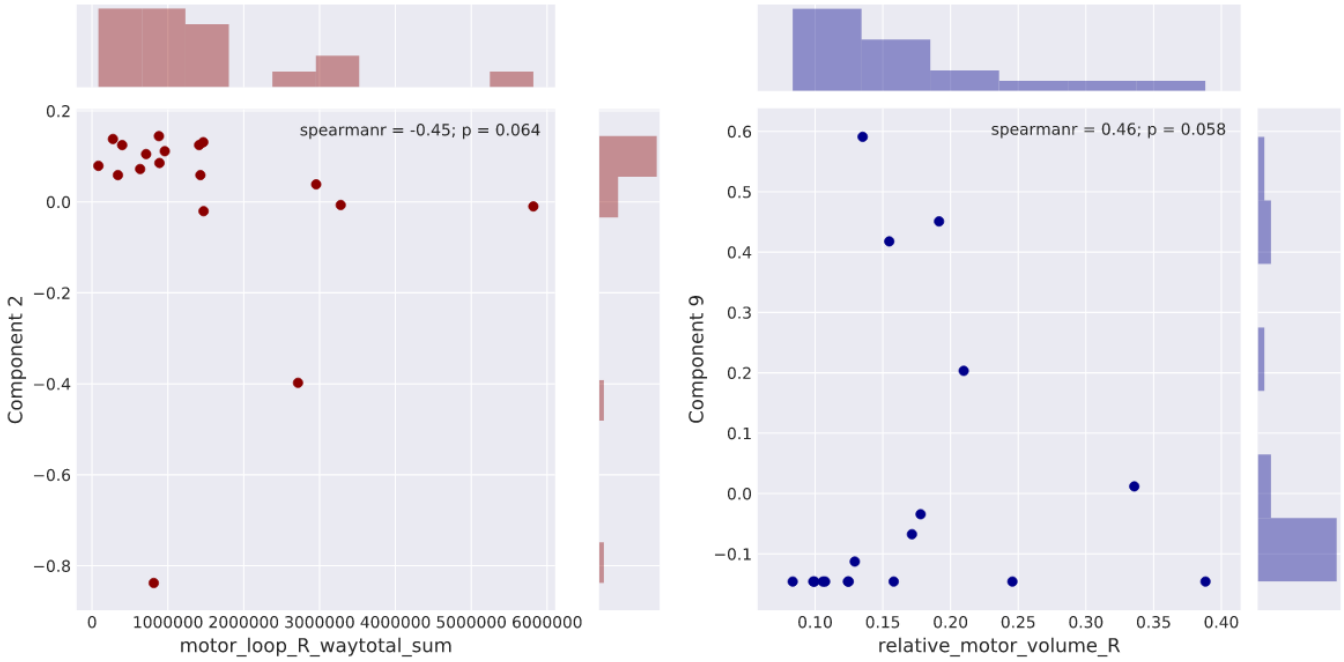

Figure 7.24. Scatter plots showing the trend correlations between connectivity strength of the right motor loop and UPDRS component 2, and between the right relative motor volumes and UPDRS component 9.

7.3.6.6. Correlation of GPi centre of gravity statistics with UPDRS sparse components

There was a significant correlation between the y-coordinate of the left associative GPi and the UPDRS Component 5, mainly loading on time spent with dyskinesias or in the off-state, and complexity of motor fluctuations (Spearman's ρ = -0.493, p = 0.037, **Figure 7.25**).

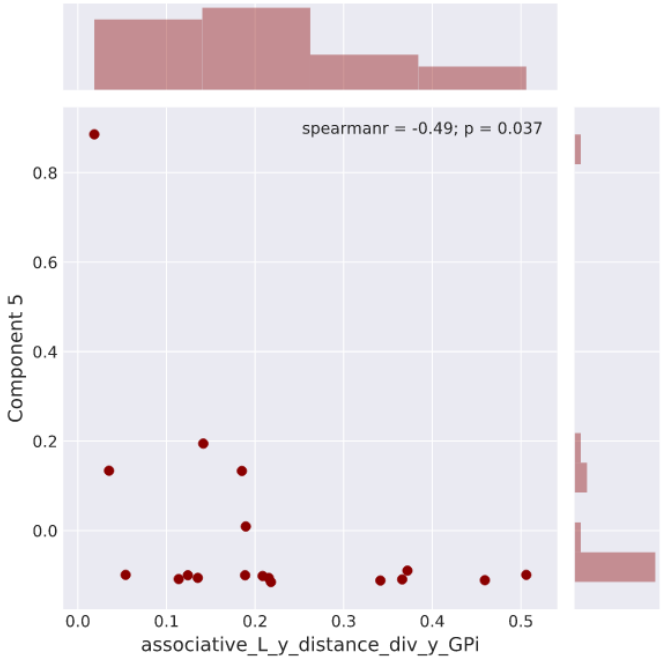

Figure 7.25. Scatter plot showing the significant correlation between the normalized y-coordinate (rostrocaudal/sagital coordinate) of the left associative GPi and UPDRS component 5.

7.3.6.7. Correlations between latent factors from exploratory factor analysis of UPDRS data and strength of connectivity and GPi volumetric metrics

There was a significant correlation between the motor strength of connectivity in the right hemisphere and UPDRS latent variable 6 (Spearman's $\rho = 0.593$, $p = 0.009$, **Figure 7.26**), as well as UPDRS latent variable 8, mainly loading on various motor symptoms (Spearman's $\rho = 0.688$, $p = 0.001$, **Figure 7.26**).

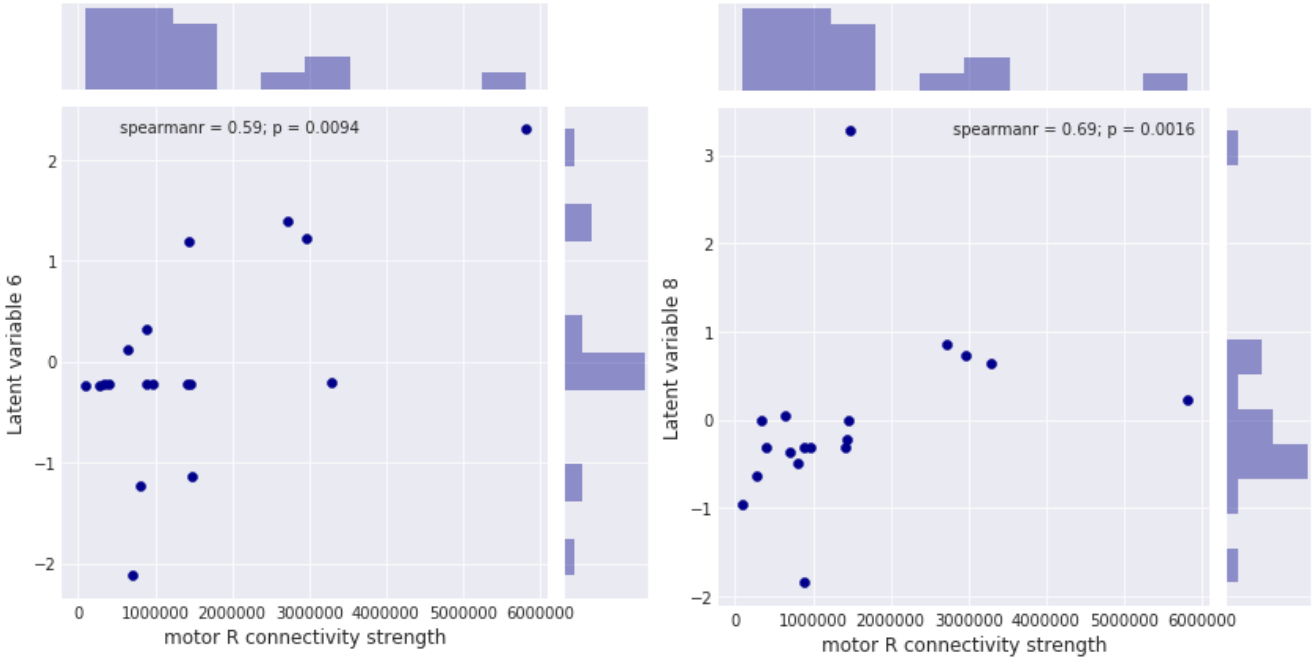

Figure 7.26. Scatter plots showing the significant correlations between the strength of connectivity of the right motor loop, and UPDRS latent variables 6 and 8 from exploratory factor analysis.

There were significant correlations of the UPDRS latent variable 6 with the Jaccard index for the associative and motor differences in the left hemisphere (Pearson's r = 0.478, p = 0.044, **Figure 7.27**), as well as with the relative overlap of the left associative and motor territories (Pearson's r = 0.489, p = 0.039).

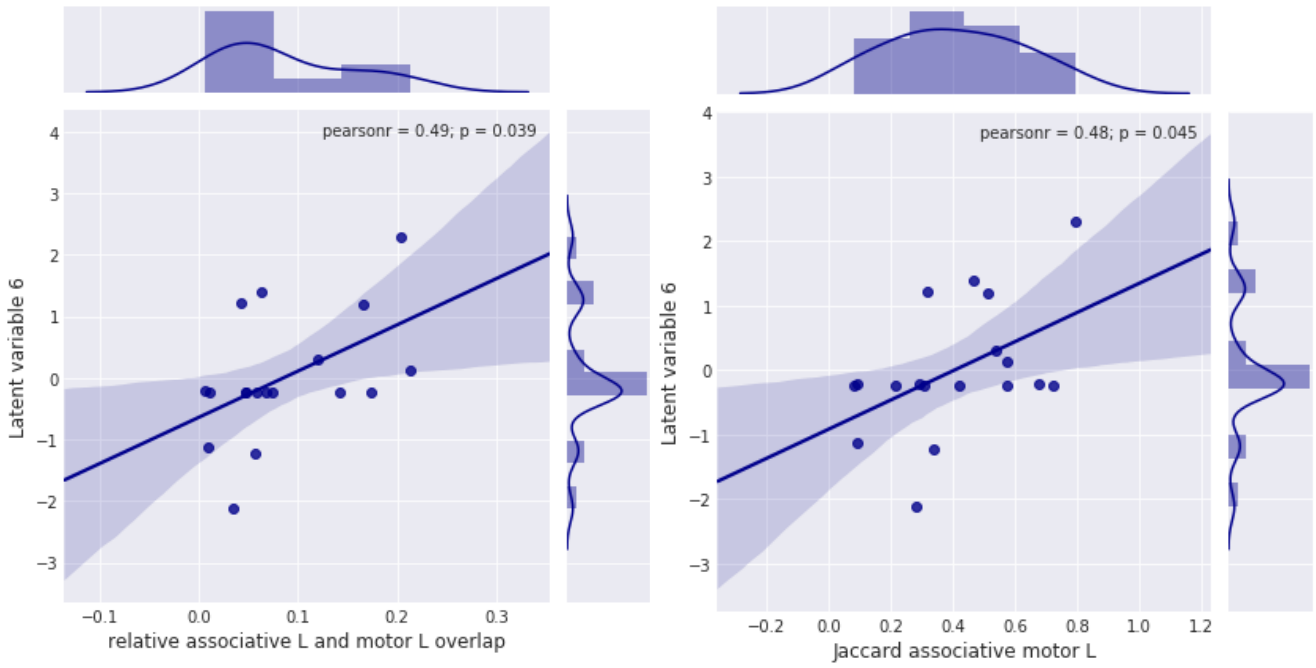

Figure 7.27. Scatter plots showing the significant correlation between the relative overlap between the associative and motor territories of the left GPi and UPDRS latent variable 6 (left), as well as the significant correlation between the associative-motor Jaccard index of the left GPi and UPDRS latent variables 6 (right).

7.3.6.8. Correlations between latent factors from UPDRS exploratory factor analysis and GPi centre of gravity statistics

UPDRS latent variable 9, that was mainly loading on distal motor symptoms and balance, was significantly correlated with the normalized x-coordinate of the right motor GPi (Spearman's $\rho = 0.543$, $p = 0.019$, **Figure 7.28.**), the normalized x-coordinate of the right limbic GPi and (Spearman's $\rho = 0.578$, $p = 0.011$, **Figure 7.29.**), and the normalized x-coordinate of the right associative GPi (Spearman's $\rho = 0.587$, $p = 0.010$, **Figure 7.30**). There was also a significant correlation between the normalized z-coordinate of the left motor GPi and UPDRS latent variable 7, loading on both psychiatric and motor symptoms, as well as activities of daily living (Spearman's $\rho = -0.496$, $p = 0.036$, **Figure 7.28.**).

There was a trend towards a correlation between UPDRS latent variable 3 (loading on motor symptoms as well as depressed mood) and the normalized y-coordinate of the left associative GPi (Pearson's $r = 0.415$, $p = 0.086$), as well as the normalized z-coordinate of the left associative GPi (Pearson's $r = -0.594$, $p = 0.009$, **Figure 7.30**). There was a trend towards a correlation between the normalized x-coordinate of the right associative GPi and UPDRS latent variable 5 (Spearman's $\rho = -0.463$, $p = 0.052$, **Figure 7.30**).

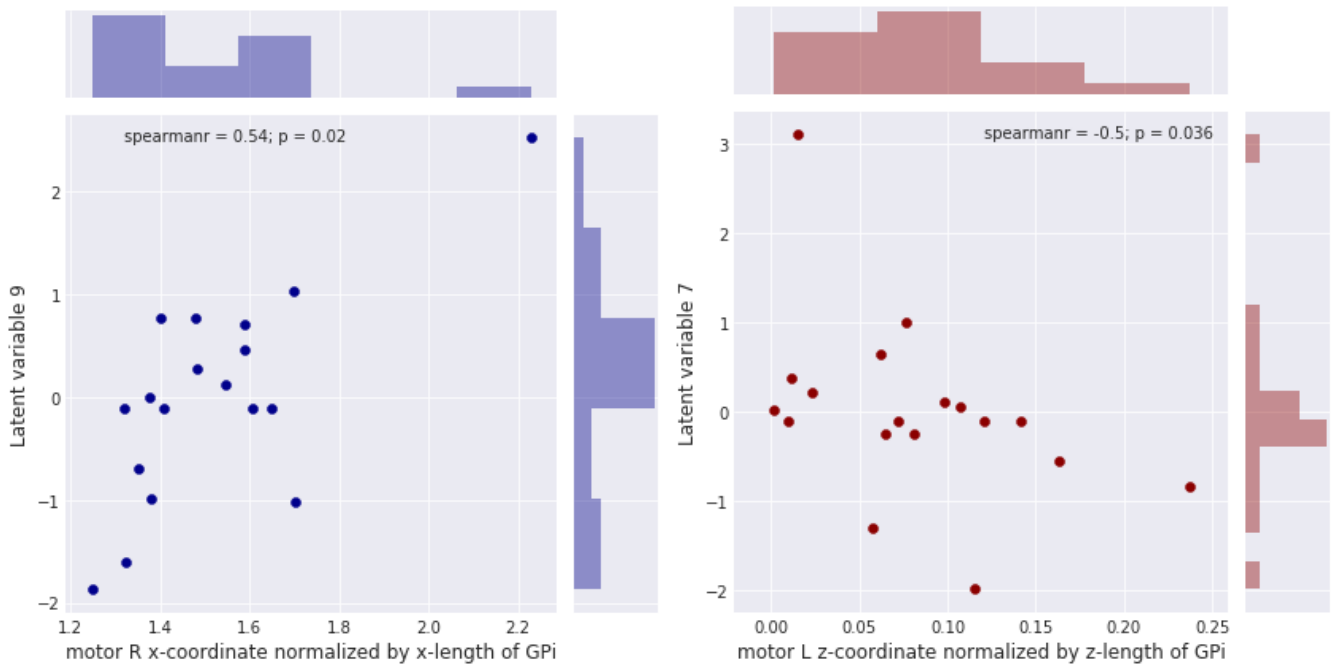

Figure 7.28. Scatter plots showing the significant correlations between the x-coordinate of the COG of the right motor GPi and UPDRS latent variable 9 (left), as well as the significant correlation between the z-coordinate of the COG of the left motor GPi and UPDRS latent variable 7 (right).

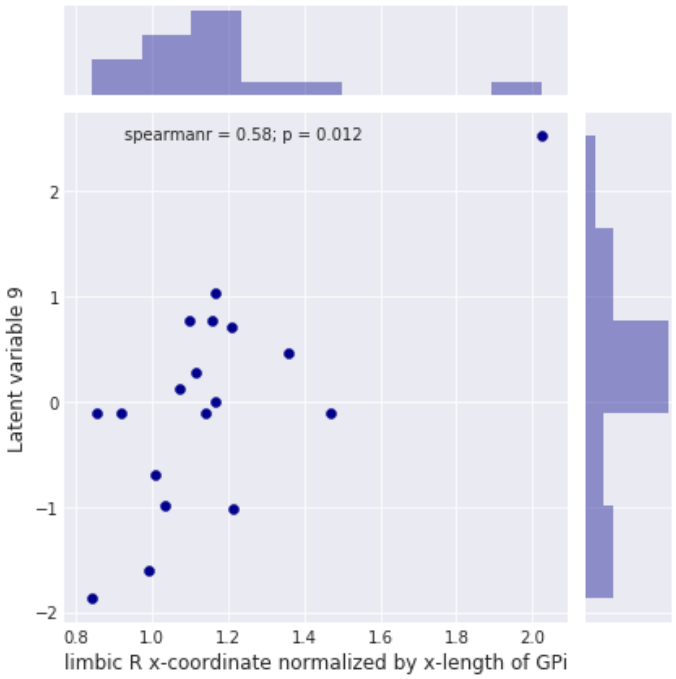

Figure 7.29. Scatter plot showing the significant correlation between the x-coordinate of the COG of the right limbic GPi and UPDRS latent variable 9 from exploratory factor analysis.

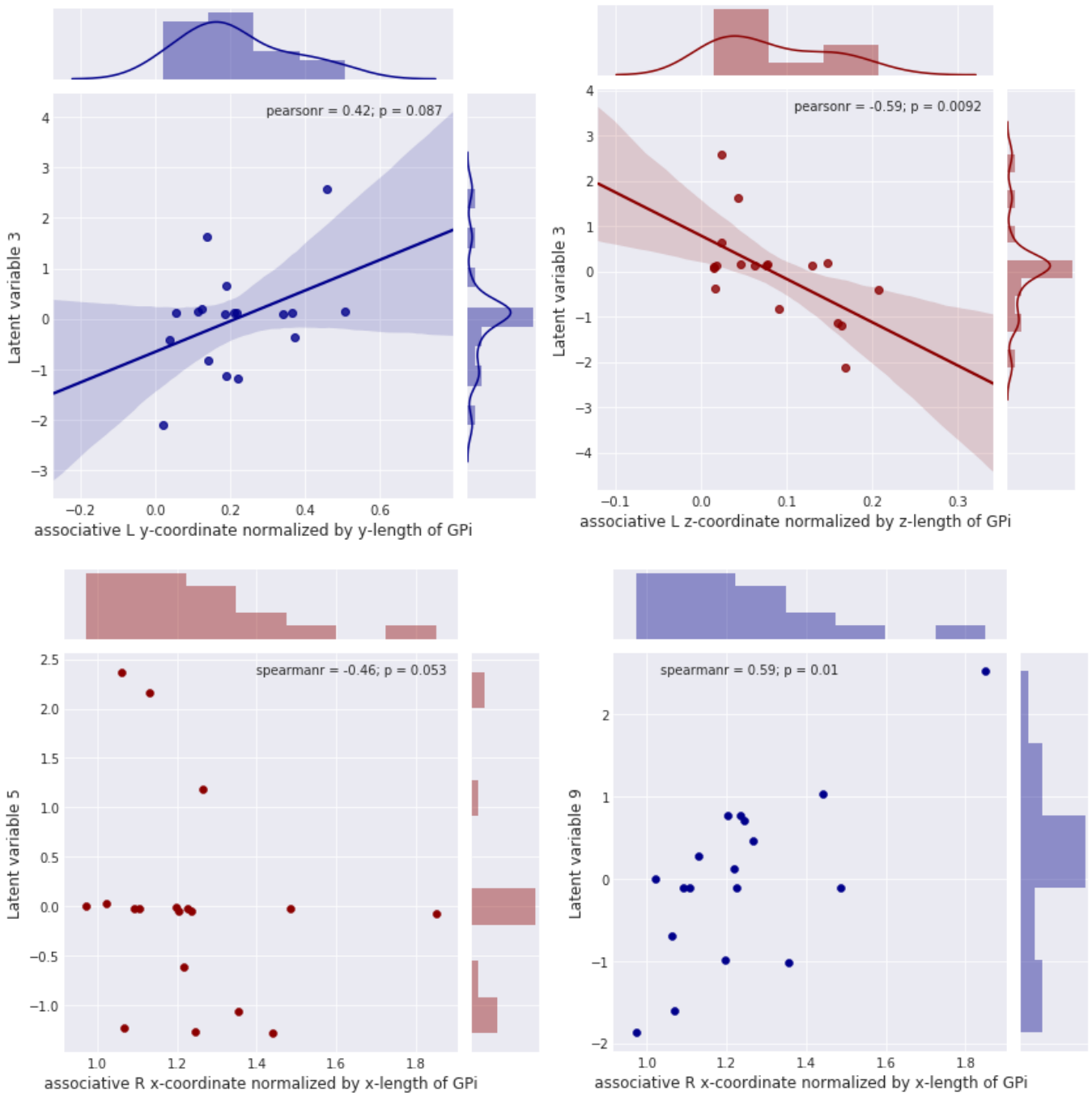

Figure 7.30. Scatter plots showing the significant correlations between the y-coordinate of the COG of the left associative GPi and UPDRS latent variable 3, the significant correlation between the z-coordinate of the COG of the left associative

GPi and latent variable 3, as well as the significant/trend correlations between the x-coordinate of the COG of the right associative GPi and UPDRS latent variables 5 and 9.

7.4. Discussion

Here we have used probabilistic tractography to reconstruct the connections between the motor, associative, and limbic cortices and the globus pallidus pars interna in patients with Huntington's and Parkinson's disease as well as healthy control subjects, and used these reconstructions to identify so-called tripartite parcellations of the GPi, i.e. motor, associative, and limbic territories within the GPi. Rather than using a hard segmentation of the connectivity profiles within the GPi we have used probabilistic parcellations of the GPi, thereby allowing an overlap between territories, because even at a resolution of 1x1x1 mm3 isotropic voxel size each GPi voxel is probably associated with various functional territories, as previously suggested by several research groups (Patriat *et al.*, 2018; Plantinga *et al.*, 2018). Previous research investigated if alterations in tractography outcomes were specific to a given part of the tripartite, functionally segregated basal ganglia loops at various other relay nuclei of the loops, including the caudate and putamen (Bohanna, Georgiou-Karistianis and Egan, 2011; Marrakchi-Kacem *et al.*, 2014) in Huntington's disease and the subthalamic nucleus in Parkinson's disease (Plantinga *et al.*, 2018). This is the first study that investigates such alterations at the level of the GPi, thereby leveraging the increased resolution of the 7T data, and directly compares both patients with Huntington's and Parkinson's disease with matched control groups.

Previous tractographic research carried out with the GPi as the sub-cortical relay nuclei of interest failed to include group inferences due to a lack of a control group (Middlebrooks *et al.*, 2018; Patriat *et al.*, 2018)

We have seen that various imaging outcomes were correlated with disease symptom severity, as measured using dimensionality-reduced UHDRS/UPDRS data. Overall, our study suggests that probabilistic tractography of the tripartite GPi basal ganglia loops might be a valuable tool to further differentiate imaging- and symptoms-based phenotypes of early PD/HD patients that could provide valuable indicators for a personalized medicine approach towards treatment.

Overall the reconstruction of the motor, limbic and associative territories are in good agreement with previous neuroanatomical research in non-human primates (McFarland and Haber, 2002; Saga, Hoshi and Tremblay, 2017), and diffusion neuroimaging research in humans (Draganski *et al.*, 2008; Patriat *et al.*, 2018). More specifically, we could clearly identify a contiguous rostroventral limbic territory, rostrodorsal associative territory, and a caudoventral motor territory (see **Figure 7.1**). A previous 7T probabilistic tractography study in patients with movement disorders (Parkinson's disease or dystonia) found a similar connectivity-based parcellation when compared with our research in terms of the neuroanatomy of the findings, but differed in the methodological approach, since corticopetal projections

were reconstructed in a two-step process going from the cortex to the thalamus, and then from the thalamus to the GPi (Patriat *et al.*, 2018). By contrast, we have looked at corticofugal projections that are part of the cortico-striato-pallidal tract or the cortico-pallidal tract which has only been recently described in humans using diffusion MRI (Magaudda *et al.*, 2013; Milardi *et al.*, 2015), as well as in monkeys using tracing techniques (Smith *et al.*, 2014; Smith and Wichmann, 2015). Thus we were effectively investigating the combined effect of the direct basal ganglia pathway going from the cortex(GLU) to the striatum(GABA), and then to the GPi(GABA), the indirect basal ganglia pathway going from the cortex(GLU) to the striatum(GABA) to the GPe(GABA) to the STN(GLU) and then to the GPi, and the cortico-pallidal tract going immediately from the cortex to the GPi presumably using glutamate (Smith *et al.*, 2014).

Taken together our findings and previous imaging research indicate that the basal ganglia is organized in topographic/topological organized, functionally segregated cortico-basal reentry circuits that are clearly reflected as distinct territories at the level of the GPi. Besides the aforementioned 7T study (Patriat *et al.*, 2018), our study is one of the few studies to show this in humans for the internal segment of the globus pallidus, and at the level of detai and resolution, i.e. 1x1x1mm^3 available at ultra-highfield MRI. **Table 7.1** gives an overview of previous research carried out in

the field of Huntington's or Parkinson's disease that used tractography or connectivity-based parcellation methods.

Authors	Subject characterisitcs	Study design	Data acquistition	Analysis method	Key findings	Interpretation, implications, and comments
Patriat et al. (2018)	15 DBS patients with PD 2 DBS patients with dystonia 1 HC	Quantitaitve descriptive study without group inferential statistics due to lack of control group	7T 1.5 mm^3 isotopic Single-shell (b=1500) 50 dir 2 phase encod. Dir	2-step probabilisitic tractography (FSL) with connectivity based parcellation: 1. parcellation of the thalamus based on thalamocortical connections 2. parcellation of GPi based on lenticulothalamic connections	Identification of functional GPi territories (motor, limbic, asso-ciaitive, residual) conistent with neuroanatomical descriptions Intra-subject validation using repeated scans and striatum-to-GPi tractography in a single control subject	Proof of concept for feasability of GPi parcellation based on probabilsitic tractography No group infterential statistics reported due to a lack of matched control group
Zhang et al. (2015)	50 unmedicated PD 27 matched HC	Case-control study with unbalanced sample size	3T 2 mm^3 isotopic Single-shell (b= 1,000) 64 dir	Deterministic tractrography (TrackVis) between SN and striatum Group comparison of diffusion metrics across tract	Abnormalities in FA,RD, AD across nigro-striatal tract in PD compared with HC FA, RD, AD correlated with UPDRS-III scores	Potential use of nigrostriatal tractography as a biomarker for PD stageing Limited to determinisitic fiber tracking that is likely inaccurate given the complex fibre architec-ture of nigrostrial tract
Marrakchi-Kacem et al. (2014)	18 HD 17 matched HC	Case-control study	3T Single-shell (b= 1,000) 50 dir	Probabilistic tractography (BrainVISA/ Connectomist-2.0) to reconstruct motor, limbic, associative cortico-striatal connections Group inference based on tripartite territories within striatum	Decrease in limbic territory of caudate(L) and putamen(R) in HD compared with HC Increase in associative territory of caudate(L) and putamen(L) in HD compared with HC	Lack of effect in the motor territory seems to be unexpected One of the few studies that compared volumes of functional subterritories in the striatum
Middle-brooks, et al. (2018)	17 PD (6 excuded from analysis)	Single-group pre-/post design with correlational inferential statitics Combined DBS/MRI study	3T 1.6 mm^3 isotropic Single-shell (b=1,000) 64 dir	Connectivity-based parcellation (FSL) of the GPi into territories connected to 10 targets, i.e. caudate, putamen, GPe, STN, SN, thalamus, PPN, M1, SMA/PMC, PFC Hard segmentation of territories	Volume of tissue activated within GPi territory, connected to M1, correlated with improve-ment in UPDRS-III scores post-DBS	GPi tractography might be useful for evaluation of accurate DBS targeting in PD
Bohanna et al. (2011)	12 clinical HD 14 HC	Case-control study	3T scanner 1.88 mm^3 28 dir Single-shell (b=1200)	Probabilistic tractography (FSL) between striatum and various cortical areas Connectivity-based parcellation of the striatum	Lower volume in parts of caudate/putamen connected to S1 and M1 in HD compared with HC	First study to show abnormalties in connectivity-based subterritor-ies of striatum in HD Small sample size

Table 7.1. A summary of probabilistic tractography and connectivity-based parcellation studies in Huntington's and Parkinson's disease. (Abbreviations: AD: axial diffusivity, DBS: deep-brain stimulation, dir: directions, FA: fractional anisotropy, HC: healthy control, HD: Huntington's disease, PD: Parkinson's disease, GPe: globus pallidus, pars externa, GPi: globus pallidus, pars interna, M1: primary motor cortex, PFC: prefrontal cortex, PMC: premotor cortex, PPN: pedunculo-pontine nucleus, RD: radial diffusivity, S1: primary somato-sensory cortex, SMA: supplementary motor area, SN: substantia nigra, STN: subthalamic nucleus).

When looking at the strength of connectivity of the motor loops, we found lower connectivity strength especially in the right hemisphere in both patient groups, i.e. patients with Huntington's disease and Parkinson's disease, when compared with their matched healthy control groups. This effect was not significant in the left hemisphere, but the connectivity pattern was the same but weaker, with lower connectivity in both patient groups. This finding indicates that the GPi was less connected to the motor cortices in patients with HD/PD, which probably reflects an early and subtle degradation or degeneration of the white matter tracts between the motor cortex and GPi. This finding is similar to what has been previously revealed using TBSS (see chapter 5), where we found similar alterations in both mean diffusivity (significant) and fractional anisotropy (trend) in both patient groups in

the posterior limb of the internal capsule. Indeed, the tracts with lower connectivity, that connect the motor cortex with the GPi pass through the posterior limb of the internal capsule as the cortico-striatal or cortico-pallidal tracts. We also found that the strength of connectivity was associated with latent variables from exploratory factor analysis in both the Huntington's and Parkinson's disease groups that showed high loadings on various motor symptoms of the diseases, and in the Huntington's disease group also high loadings on cognitive tasks, including the Stroop tasks, and various tests measuring verbal intelligence.

In the left hemisphere both the motor connectivity and the overall connectivity was higher than in the right hemisphere in both the patients and control groups. This effect might be related to hemispheric lateralization of the basal ganglia pathways. Indeed, previous MRI studies in healthy subjects showed a leftward bias in putaminal and globus pallidus volumes (Guadalupe *et al.*, 2017), or in caudate and putaminal volumes (Okada *et al.*, 2016) respectively. Another reason why the connectivity was higher in the left hemisphere might be that the GPi seed volumes were already higher in the left hemisphere (average over groups: 773.47 mm3), when compared with the right hemisphere (average over groups: 653.69 mm3). These differences are due to a known leftward asymmetry of the globus pallidus (Guadalupe *et al.*, 2017), and might have resulted in higher connectivity, because the number of streamlines

seeded is the product of the number of particles (specified in the algorithm), and the number of seed voxels.

It should be noted that the effect seen for the motor connectivity were not significant anymore after normalization by individual differences in the GPi volume. Since the Huntington's disease and the control group differed significant in their GPi volume, this might have been propagated during tractography by seeding less streamlines in the Huntington's disease group. Lower GPi volumes and lowered connectivity seem to be confounding factors both associated with Huntington's disease, thereby making it difficult to disentangle the effects without reducing the construct validity of the research methods, i.e. using the same GPi seed for all subjects might have introduced even more bias as it might have resulted in seeding from the white matter in patients with volume loss in the GPi.

Patients with Huntington's and Parkinson's disease differed significantly relative to their matched controls in the relative motor volume in the left hemisphere, whereby patients with Parkinson's disease had a significantly lower relative motor volume (in both the left and right hemisphere), and patients with Huntington's disease had a slightly higher relative motor volume (not significant) compared with their matched controls. This finding was specific to the motor volume, and associative/limbic volumes did not show any significant effect. Such a volume loss in the motor territory

of patients with Parkinson's disease most likely corresponds to specific atrophy of this part of the GPi that is reflected in lowered connectivity of this functional region of the GPi to the motor cortex.

The relative motor volume seems to capture the overall increased influence of the motor GPi on the basal ganglia pathways in Huntington's disease that leads to hyperkinetic symptoms, and the decreased influence of motor GPi in PD on the basal ganglia circuits that leads to hypokinetic symptoms. Indeed, in the Huntington's disease group the higher motor volumes in the left hemisphere were positively associated with components 2 (high loadings on dystonia and chorea, i.e. hyperkinetic symptoms) and component 10 (high loadings on proximal dystonia, Luria, and cognitive symptoms), as well as negatively associated with components 4 (**low** loadings on motor symptoms of rigidity, balance, and ocular pursuit, well as irritability as a psychiatric symptom, hence the negative correlation) and component 7 (low loadings on motor symptoms of the fingers and hand). This clearly shows that the higher volume of the motor territory is deleterious in Huntington's disease. By contrast, in Parkinson's disease the relative motor volume in the left hemisphere was negatively correlated with component 8 (low loadings on rigidity neck) that mean that this might be an adaptive or compensatory process in patients with early Parkinson's disease.

This effect of a difference between HD and PD seems to be much more pronounced in the left hemisphere, which might be driven by an hemispheric lateralization of the GPi toward the left. This is similar to what we had found when testing for difference in diffusion metrics in both diseases relative to their age-matched control groups using voxel-wise analyses of diffusion metrics (chapter 4), where the effects were mainly lateralized to the left hemisphere.

Based on both clinical research and animal models, it is well known that the GPi shows less inhibitory outflow to the thalamus in Huntington's disease, leading to hyperkinetic symptoms, whereas in Parkinson's disease the GPi exerts more inhibitory outflow to the thalamus, leading to hypokinetic symptoms (Obeso *et al.*, 2000, 2002). This effect might be captured by opposite changes in the volumes of the motor territories of the GPi in these diseases, when looking at the effect of primarily inhibitory corticopetal/efferent connections to the GPi that might result in reduced modulation of the GPi motor territories. The reason why the motor volume was lower in Parkinson's disease might be that due to the degeneration of nigrostriatal dopaminergic connections, both the GABA-ergic medium-size spiny neurons that use substance-P as co-transmitter and express the D_1-receptor, and the GABA-ergic medium-size spiny neurons that use enkephalin as co-transmitter and express D_2-receptors degenerate, thereby reducing the detected connections going through the

striatum as both the direct and indirect basal ganglia pathways, and resulting in lower motor connections and lower volume of the motor territory. By contrast, in the early stages of Huntington's disease HD only the enkephalin-containing, D_2-receptor-type medium size spiny neurons degenerate, whereas the Substance-P-containing, D_1-receptor-type nigrostriatal connections are relatively spared, which leads to less degeneration of striatal axons. This effectively perseveres the inhibitory connections of the direct pathway that are relatively spared, and now can be easier tracked as they remain the primary fiber direction in within the basal ganglia, thereby resulting in an increase in the motor volume in Huntington's disease compared with controls.

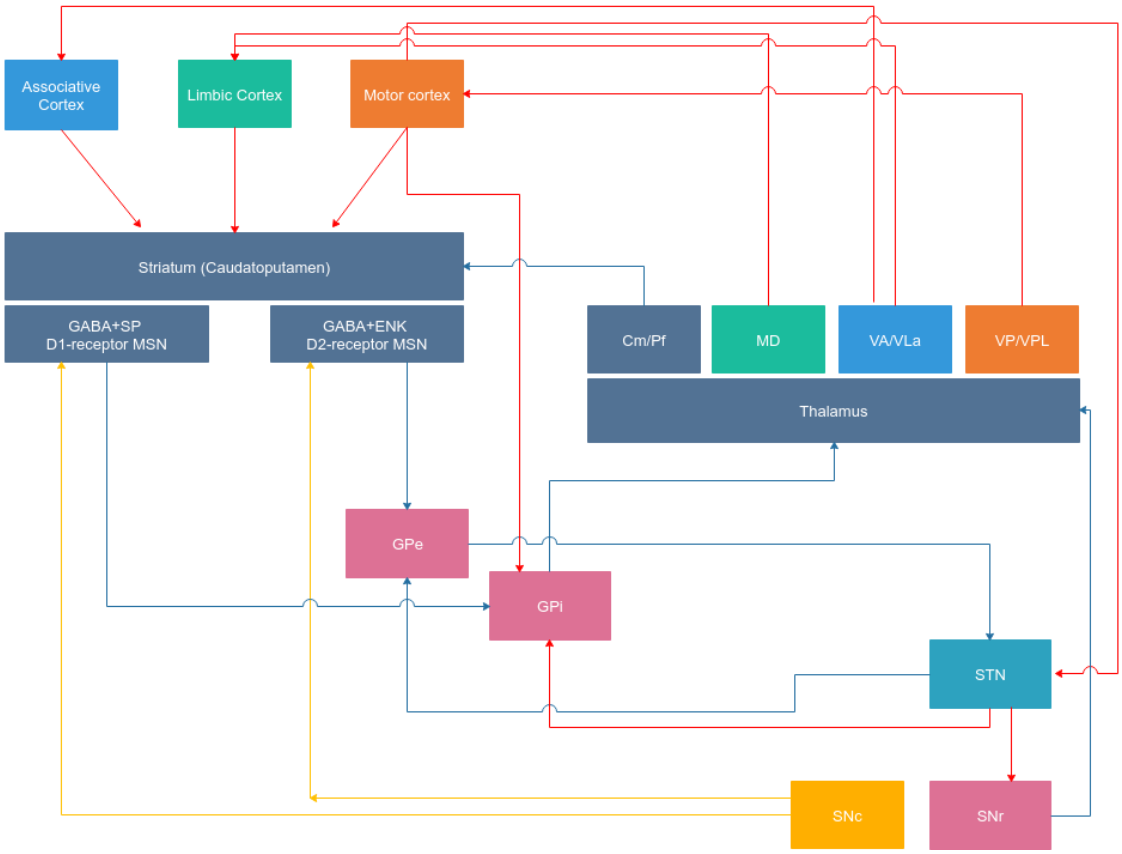

Figure 7.31. A simplified, schematic drawing of the basal ganglia loops in the healthy state providing a conceptual framework for interpreting the findings of the present study. Red arrows: excitatory glutamatergic connections, Blue arrows: inhibitory GABAergic connections, Yellow arrows: modulatory dopaminergic connections (D1 receptor binding results in excitatory effects, D2 receptor binding result in inhibitory effects). Abbreviations: SP: Substance P, ENK: enkephaline, MSN: medium-size spiny neuron, GPe: globus pallidus, pars externa, GPi: globus pallidus, pars interna, STN: nucleus subthalamicus, SNc: substantia nigra, pars compacta, SNr: substantia nigra, pars reticulata, CM/Pf:

centromedian/parafascicular, MD: mediodorsal, VA: ventral anterior, VLa: ventral lateral, VP: ventral posterior, VPL: ventral posterior lateral).

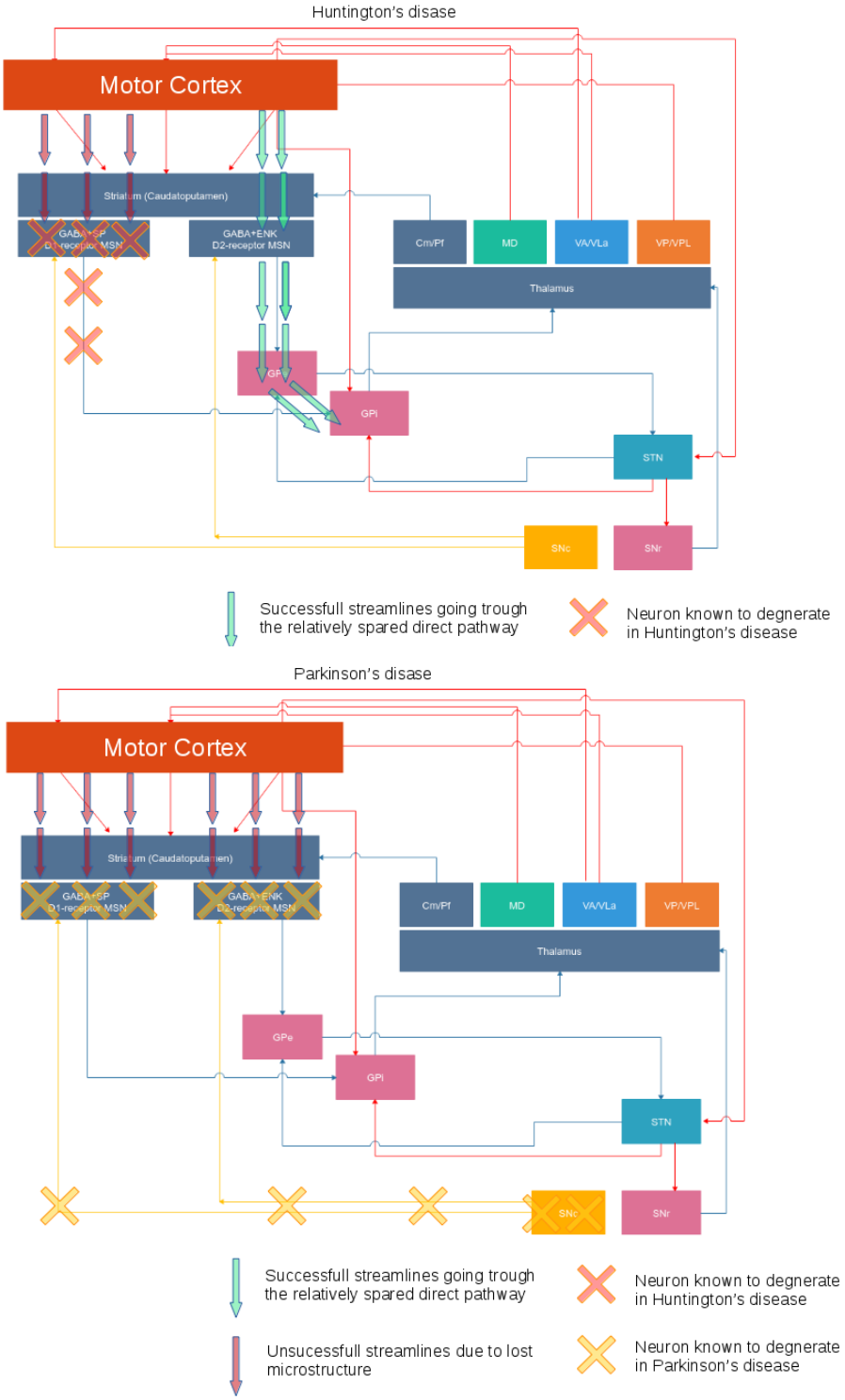
Huntington's disase
Motor Cortex
Striatum (Caudatoputamen)
GABA+SP
D1-receptor MSN
GABA+ENK
D2-receptor MSN
Cm/Pf
MD
VA/VLa
VP/VPL
Thalamus
GPe
GPi
STN
SNc
SNr
Successfull streamlines going trough the relatively spared direct pathway
Neuron known to degrenerate in Huntington's disease
Parkinson's disase
Motor Cortex
Striatum (Caudatoputamen)
GABA+SP
D1-receptor MSN
GABA+ENK
D2-receptor MSN
Cm/Pf
MD
VA/VLa
VP/VPL
Thalamus
GPe
GPi
STN
SNc
SNr
Successfull streamlines going trough the relatively spared direct pathway
Neuron known to degrenerate in Huntington's disease
Unsucessfull streamlines due to lost microstructure
Neuron known to degrenerate in Parkinson's disease

Figure 7.32. Schematic drawing illustrating the alterations seen in the basal ganglia system in Huntington's and Parkinson's disease, and how they can be used for interpreting differential changes in the volume of the motor GPi in these diseases.

Interestingly, we found an opposite pattern in disease-specific alterations in the relative motor volume in the internal segment of the globus pallidus, when compared with the alterations seen in the relative associative volume of the subthalamic nucleus as seen in chapter 6, i.e. lower volume in the motor GPi in Parkinson's disease, and higher volume in the associative STN in Parkinson's disease compared with matched controls, and vice versa in Huntington's disease. This might be due to the known antagonistic functioning of the hyperdirect cortico-subthalamic pathway that inhibits motor programs from their release, and direct basal ganglia pathway that ultimately dis-inhibits the motor progmmes (Nambu, Tokuno and Takada, 2002; Nambu, 2008b; Nambu, Tachibana and Chiken, 2015). Thus, lower volumes in the GPi, and higher volumes in the STN in Parkinson's disease taken together would result in less disinhibition, and more inhibition of motor programs resulting in hypo-kinetic symptoms in Parkinson's disease. By contrast, higher volumes in the GPi, and lower volumes in the STN in Huntington's disease taken together would result in more disinhibition, and less inhibition of motor programs resulting in hyper-kinetic symptoms in Huntington's disease. Further research is needed to confirm that the

cumulative effects on the GPi seen in probabilistic tractography correspond to the direct pathway, and how the opposing effects of the indirect pathway would fit in this model.

A previous study used a similar approach to our study to compare volumes of these tripartite functional regions of the striatum in patients with HD, and found a decrease in limbic territories, and an increase in associative territories, but failed to detect any effect in the motor volumes (Marrakchi-Kacem *et al.*, 2014). By contrast, we only found a trend towards an increase in the associative volume of the GPi (z= 1.723, 0.0849) in Huntington's disease. This might be due to differences in the seed selection, i.e. GPi in our study vs. caudate and putamen in (Marrakchi-Kacem *et al.*, 2014). Another study found a decrease in volume in the HD group that was specific to sub-territories of the caudate and putamen that were connected to M1 and S1 respectively (Bohanna *et al.*, 2011).

Using post-hoc correlations with UHDRS/UPDRS components we found associations between motor volume and symptoms. A previous study that was based on connectivity-based parcellation also showed that the volume of tissue activated within the motor territory of the GPi correlated with improvement of UPDRS symptoms, but not in other GPi territories (see **Table 7.1** for details) (Middlebrooks *et al.*, 2018).

The relative overlap and the Jaccard index between the left motor and associative GPi was significantly higher in the Huntington's disease group when compared with their matched controls. This effect might be driven by the increase of the motor volume in Huntington's disease that then results in an increased overlap with the associative territory. The effect seen in the relative motor and associative overlap in Huntington's disease was correlated with sparse component 7 (motor symptoms of the fingers and hands), as well as latent variable 3 (mainly psychiatric and cognitive symptoms) from exploratory factor analysis, thereby indicating that this increase in the overlap in Huntington's disease is clearly maladaptive.

In both patient groups, i.e. patients with Parkinson's disease, and Huntington's disease the x-coordinate of the motor GPi of the right hemisphere was lower when compared with their matched control groups, which is indicative of either a shift of the motor territory from medial to more lateral, or a gradient of connectivity loss running from medial (less connectivity) to lateral (more connectivity). In the HD group the x-coordinate of the right motor COG was correlated with the latent variable 4 from factor analysis that showed high loadings on psychiatric, cognitive, and to a lesser extent motor scores of the UHDRS.

In both patient groups, i.e. patients with Parkinson's disease and Huntington's disease the z-coordinate of the left motor GPi was higher when compared with their

matched controls, which is indicative of either a dorsal shift of the motor territory, or a gradient of connectivity loss running from ventral (less connectivity) to dorsal (more connectivity). This shift in the z-coordinate was correlated with various components from sparse PCA and exploratory factor analysis of UHDRS/UPDRS data, thereby showing that this imaging result was strongly associate with the clinical data.

As mentioned in the section on the alteration seen in the motor COG, they can reflect either a shift in the motor territory, or a gradient of connectivity loss in the opposite direction, however it is not possible to distinguish between these two options. For convenience, we will refer only to the shift in territories in the following when discussing associative and limbic COGs.

The left associative GPi was shifted dorsally in both patients with HD and PD, as well as rostrally in the patient group with HD when compared with their matched control groups. Since we have also seen an increase of overlap between motor and associative territories in Huntington's disease compared with controls, the dorsal shift most likely corresponds to a shift in the associative volume within the entire GPi, that then results in a higher overlap with the dorsal motor territory of the GPi. The right associative GPi was shifted laterally and dorsally in both patient groups when

compared with healthy control groups. The right limbic GPi was shifted laterally in the Huntington's disease group when compared with their matched control groups. These shifts in the COG of the tripartite GPi territories are inherently hard to interpret, and there was also a large variability in patient groups that probably reflects individual idiosyncrasies. However, since the patient groups differed significantly from the matched control groups in their motor COG coordinates, the motor territory might undergo neurodegenerative changes due to disease. This information might be relevant in the clinical setting as an additional guidance for deep brain stimulation in PD/HD; the present gold standard for neurosurgery is to base the insertion of the electrode on altlas-based stereotactic coordinates of the motor GPi, but these coordinates themselves as we have seen are affected by the disease state. Indeed, patients with Parkinson's disease treated with DBS have a high revision rate of the electrode placement of up to 34.0%, that is due to a lack of a therapeutic effect, or not hitting the right DBS target, i.e. the motor GPi on the first attempt (Rolston *et al.*, 2016). Since a previous study found a clear association between improved clinical outcomes, and DBS activation of the motor territories of the GPi (Middlebrooks *et al.*, 2018), probabilistic tractography might be a valuable tool providing additional information for DBS patients that provides individual information and be used alongside stereotactic information. Further research is

needed to replicate these changes in the centre of gravity of the tripartite GPi territories, and to investigate if such information can be translated into the clinical context, and improve the outcomes of DBS surgery.

Nevertheless, the present study has certain limitations that merit discussion. Even though ultra-high-field diffusion MRI was used to boost the spatial resolution of the diffusion images, this increase in resolution comes at the price of a decrease in signal-to-noise ratio (SNR) when compared with 3T diffusion MRI data. The increase in field strength inevitably leads to an increase in radio-frequency inhomogeneities that then result in a larger bias field in the diffusion images. This increase in the bias field results in SNR that varies across the image. Furthermore, the signal from brain regions relatively close to the receiving coils (e.g. the cortex, white matter blades) are less affected by the bias field than brain regions farther away from the receiving coils (e.g. deep white matter and basal ganglia), which could have led to spurious fiber counts during the probabilistic tracking. Even though it has been suggested that these effects would cancel out during the statistical analyses, further research is needed to investigate if 7T diffusion data are substantially affected in this way.

Another limitation was that the sample size is relatively small, and we therefore did not apply a correction for multiple comparisons, when analyzing multiple tractography outcomes, or correlating them with the dimensionality-reduced

questionnaire data, because such a multiple comparison correction would have been too conservative to detect any effect. This was done because this is a preliminary analysis of a study currently still running at the Wellcome Centre for Integrative Neuroimaging in Oxford.

A further limitation was that the data acquisition protocol was based on a single b-value of 1000 s/mm², however the associative and motor fibers pass through various regions of crossing fibers, including the centrum semiovale, and all three tracts go through the internal capsule that contains multiple fiber directions as well. Single-shell diffusion imaging, however, cannot easily distinguish between various configurations of crossing fibers, kissing fibers and fanning fibers (Jbabdi and Johansen-Berg, 2011b), and multi-shell diffusion spectrum imaging could be used to improve the reconstruction of the exact trajectories of these fibers. The precise fiber orientation of the striato-pallidal connections might only be reconstructable using multi-shell diffusion data (Beukema, Yeh and Verstynen, 2015)

A further limitation was that the meaning of the COG statics are inherently hard to interpret, and a shift in a given direction can have several meanings: (1) a real shift of the territory within the GPi in that given direction without any change in volume, (2) a connectivity atrophy gradient running in the opposite direction and causing an change in the centre of gravity without any change in volume, (3) the volume getting

bigger by extending in the given direction of the COG shift, (4) a decrease in volume in the directions perpendicular to the direction of the COG shift, (5) a combination of the aforementioned effects. Since we have investigated volumetric changes as well, we have partially ruled out some of these cases, but the precise effect seen still remains elusive.

In conclusion, probabilistic tractography was able to detect disease-specific alterations in the strength of connectivity of functionally segregated basal ganglia loops in patients with Huntington's and Parkinson's disease. Our findings indicate a selective vulnerability of the motor pathway in Huntington's disease. Volumetric changes in the motor territory of the globus pallidus, pars interna, in Huntington's and Parkinson's disease were consistent with its role within the framework of the basal ganglia loops. Motor and associative territories within the globus pallidus, pars interna, undergo shifts due to disease, that might be of clinical importance, and require further investigation.

8. Future work and perspectives on diffusion MRI in Huntington's and Parkinson's disease

Science is an open-ended system where answering a specific research hypothesis inevitably raises new research questions. In chapters 1 and 2, I have presented one of the few investigations on the longitudinal utility of diffusion MRI in presymptomatic Huntington's disease as a surrogate marker for the evaluation of various presymptomatic stages. Whereas a plethora of promising cross-sectional diffusion MRI research has been carried out, I believe that further longitudinal research in larger cohorts will be highly desirable, since the relatively high longitudinal sensitivity of diffusion MRI clearly seems to be one of its advantages over structural MRI.

In chapters 2 and 5, voxel-wise, mass univariate, cross-subject comparisons were carried out to falsify scientific hypotheses about the white matter in presymptomatic/early Huntington's disease, and early Parkinson's disease. Indeed, science advances through the falsification of research hypotheses thereby creating genuinely new knowledge. However, of equally importance is a scientists ability to predict and control future events. Future neuroimaging research in larger samples will shift the focus from these cross-subject comparisons towards the aim of making predictions at the individual level, and classify new cases. Indeed, one interesting

research topic would be to use machine learning techniques on diffusion MRI data to train a multivariate classifier that is then able to make new predictions about new scans, for example, classifying a scan as belonging to a patient with Huntington's or Parkinson's disease, or classifying a scan as being far from onset vs. near the onset of symptoms. This would be a very good milestone to further establish the predictive validity of diffusion MRI in these diseases.

In chapters 4-7, we saw that imaging outcomes were associated with dimensionality-reduced clinical data that were composites of motor, psychiatric, and cognitive symptoms. An interesting research question in a larger sample will be to investigate disease-specific imaging phenotypes, for example comparing early Huntington's disease patients with predominant early motor symptoms vs. patients with predominant cognitive symptoms vs. patients with predominant psychiatric symptoms. Similarly, it would be interesting to contrast Parkinson's disease patients with tremor-dominant motor symptoms and bradykinetic-rigid symptoms, or patients with unilateral and bilateral symptoms.

In chapters 6 and 7, I have reconstructed the hyperdirect basal ganglia pathway, as well as the cumulative cortico-pallidal connections. With rapidly increasing technical advances in ultra-highfield diffusion MRI, as well as pulse sequencing, tractographic fibre reconstructions are getting more and more accurate. As previously suggested

the advances in multi-shell imaging and its combination with ultra-highfield MRI might boost the level of detail at which white matter tracts can be reconstructed (Jbabdi and Johansen-Berg, 2011b; Beukema, Yeh and Verstynen, 2015). This opens formidable research questions in basal ganglia research. For example, whereas I have only looked at the cumulative effect of the direct, indirect, hyperdirect, and cortico-pallidal pathways in chapter 6, using multi-shell diffusion spectrum imaging it might be possible to reconstruct these fiber pathways individually and compare and contrast their alterations in movement disorders. This will be of outstanding interest, because opposing functions and dysfunctioning due to disease have been suggested in these pathways based on animal research (Nambu, 2008b).

Given our current knowledge and understanding of the basal ganglia functioning and their alterations in movement disorders, an interesting research question will be to investigate alterations in the lenticulothalamic fasciculus, and ansa lenticularis, the tracts that send the final output of the basal ganglia integrative function to the thalamus. On the basis of animal research the lenticular fasciculus mainly contains axons from the motor territories of the putamen and pallidum projecting the thalamus, whereas the ansa lenticularis contains fibres from the associative and limbic territories. In an initial analysis attempt, I tried to reconstructed theses tracts using the 7T diffusion MRI data (chapter 4-7), however I found that the

reconstructions were not neuroanatomically meaningful, which was due to an unreliable estimation of the secondary fiber direction. Indeed, the lenticular fasciculus needs to pass through the posterior limb of the internal capsule, a region of crossing fibers, where it represents a minor and third fiber population (alongside the thalamostriatal fibres). Data of higher resolution and reliable secondary/teritiary fibers would have been necessary to derive reconstructions that have enough trustworthiness for reliable group inferences.

In conclusion, diffusion MRI in movement disorders has a bright future and provides valuable surrogate markers for clinical and pharmacological research that might also translate into improvements in clinical practice.

9. Appendix : Results tables of chapter 3

Test	Control				all preHD				FAR				MID			
	Mean	SD	t(18)	P	Mean	SD	t(34)	P	Mean	SD	t(10)	P	Mean	SD	t(10)	P
UHDRS motor score	NA	NA	NA	NA	2.914	6.046	2.852	0.007	1.000	3.162	1.049	0.319	0.091	1.921	0.157	0.878
UHDRS modified motor score	NA	NA	NA	NA	2.514	4.217	3.527	**0.001**	1.364	1.748	2.588	0.027	0.182	1.537	0.392	0.703
UHDRS confidence score	NA	NA	NA	NA	0.600	1.063	3.340	0.002	0.273	0.905	1.000	0.341	-0.091	0.539	-0.559	0.588
MOCA	0.368	1.770	0.907	0.376	-0.171	2.561	-0.396	0.695	0.364	2.730	0.442	0.668	0.182	1.401	0.430	0.676
MMSE	-0.421	1.644	-1.117	0.279	-0.771	1.610	-2.834	0.008	-0.545	1.753	-1.032	0.326	-1.000	1.265	-2.622	0.026
Stroop color	-0.053	9.101	-0.025	0.980	0.457	7.010	0.386	0.702	4.091	8.142	1.666	0.127	-0.818	4.423	-0.614	0.553
Stroop word	1.263	10.066	0.547	0.591	-0.657	7.530	-0.516	0.609	0.273	8.247	0.110	0.915	-0.545	7.090	-0.255	0.804
Stroop interference	1.579	5.368	1.282	0.216	-1.114	6.466	-1.020	0.315	2.455	4.390	1.854	0.093	-2.909	8.384	-1.151	0.277
Verbal Fluency FAStotal	2.895	7.187	1.756	0.096	1.114	6.253	1.054	0.299	0.364	4.985	0.242	0.814	1.182	7.468	0.525	0.611
Symbol digit	-0.105	4.433	-0.103	0.919	0.229	4.815	0.281	0.781	0.636	4.822	0.438	0.671	-0.364	5.005	-0.241	0.814
Digit span forward	-0.579	1.805	-1.398	0.179	-0.286	1.601	-1.056	0.298	-0.273	1.737	-0.521	0.614	0.273	1.794	0.504	0.625
Digit span backward	0.947	1.870	2.208	0.040	-0.143	2.046	-0.413	0.682	0.091	1.973	0.153	0.882	0.091	2.166	0.139	0.892
Digit span total	0.368	2.650	0.606	0.552	-0.429	2.524	-1.005	0.322	-0.182	1.940	-0.311	0.762	0.364	3.202	0.377	0.714
WASI matrix	2.053	4.836	1.850	0.081	-0.314	3.225	-0.577	0.568	-0.182	3.995	-0.151	0.883	-0.182	2.676	-0.225	0.826
SCL90 somatization	-3.053	8.657	-1.537	0.142	-1.882	9.660	-1.136	0.264	-1.273	9.477	-0.445	0.666	-3.800	9.331	-1.288	0.230
SCL90 obsessive compulsive	-5.632	9.376	-2.618	0.017	-12.088	10.958	-6.432	**2.719E-07**	-9.455	12.380	-2.533	0.030	-11.400	9.252	-3.896	0.004
SCL90 interpersonal sensitivity	-2.895	9.291	-1.358	0.191	5.529	11.010	2.928	0.006	3.182	11.695	0.902	0.388	7.200	12.541	1.815	0.103
SCL90 depression	-0.947	9.664	-0.427	0.674	-1.912	10.229	-1.090	0.284	-6.273	9.307	-2.235	0.049	1.500	8.580	0.553	0.594
SCL90 anxiety	-2.000	11.518	-0.757	0.459	2.000	10.123	1.152	0.258	-0.273	7.185	-0.126	0.902	4.500	12.140	1.172	0.271
SCL90 hostility	-2.000	7.141	-1.221	0.238	0.500	9.053	0.322	0.749	-3.455	8.251	-1.389	0.195	6.500	10.596	1.940	0.084
SCL90 phobia	0.000	5.207	0.000	1.000	4.088	9.861	2.417	0.021	4.545	9.943	1.516	0.160	3.800	11.516	1.043	0.324
SCL90 paranoia	1.211	6.179	0.854	0.404	1.853	11.468	0.942	0.353	-1.000	8.809	-0.377	0.714	2.600	11.007	0.747	0.474
SCL90 psychoticism	-3.158	10.227	-1.346	0.195	-5.353	9.921	-3.146	0.003	-6.364	8.755	-2.411	0.037	-4.900	10.170	-1.524	0.162
SCL90 global severity index	0.684	9.678	0.308	0.762	-2.353	6.910	-1.985	0.055	-1.818	6.705	-0.899	0.390	-2.300	7.646	-0.951	0.366
SCL90 positive symptoms distress	-4.526	10.890	-1.812	0.087	0.294	11.112	0.154	0.878	1.091	8.055	0.449	0.663	4.600	9.395	1.548	0.156
SCL90 positive symptoms total	-2.211	10.310	-0.935	0.362	-3.118	8.434	-2.155	0.039	-4.273	9.177	-1.544	0.154	-2.700	7.875	-1.084	0.306
Barratt attentional	-1.684	2.496	-2.942	0.009	-0.118	3.073	-0.223	0.825	-0.545	3.446	-0.525	0.611	0.000	2.749	0.000	1.000
Barratt motor	-0.632	2.753	-1.000	0.331	0.000	2.730	0.000	1.000	-0.091	2.071	-0.146	0.887	-0.900	3.542	-0.804	0.442
Barratt nonplanning	0.053	4.262	0.054	0.958	1.353	3.724	2.118	0.042	0.909	4.230	0.713	0.492	1.400	2.989	1.481	0.173
Barratt total	-2.263	6.017	-1.639	0.118	-0.600	12.871	-0.276	0.784	0.273	6.544	0.138	0.893	-5.273	20.015	-0.874	0.403

Test	NEAR				all preHD vs CON				ANOVA			Post-hoc
	Mean	SD	t(12)	P	Statistic		Z	P	Statistic		P	
UHDRS motor score	6.923	8.005	3.118	0.009	NA	NA	NA	NA	Chi2(2) =	10.801	**.005**	§
UHDRS modified motor score	5.462	5.502	3.579	0.004	NA	NA	NA	NA	Chi2(2) =	15.511	**###**	§
UHDRS confidence score	1.462	0.967	5.447	**###**	NA	NA	NA	NA	Chi2(2) =	11.356	**.003**	§
MOCA	-0.923	3.121	-1.066	0.307	U(52) =	276.500	-1.035	0.301	Chi2(3) =	2.479	0.479	
MMSE	-0.769	1.833	-1.513	0.156	U(52) =	279.500	-0.978	0.328	F(3,50) =	0.229	0.876	
Stroop color	-1.538	7.055	-0.786	0.447	t(52) =	-0.229		0.819	F(3,50) =	1.228	0.310	
Stroop word	-1.538	7.774	-0.714	0.489	t(52) =	0.793		0.431	F(3,50) =	0.299	0.826	
Stroop interference	-2.615	5.173	-1.823	0.093	U(52) =	248.500	-1.526	0.127	F(3,50) =	3.103	0.035	
Verbal Fluency FAStotal	1.692	6.537	0.933	0.369	t(52) =	0.948		0.348	F(3,50) =	0.388	0.762	
Symbol digit	0.385	4.992	0.278	0.786	t(52) =	-0.250		0.804	F(3,50) =	0.083	0.969	
Digit span forward	-0.769	1.235	-2.245	0.044	U(52) =	328.500	-0.074	0.941	F(3,50) =	0.875	0.461	
Digit span backward	-0.538	2.106	-0.922	0.375	U(52) =	239.500	-1.727	0.084	F(3,50) =	1.478	0.232	
Digit span total	-1.308	2.213	-2.131	0.055	t(52) =	1.089		0.281	F(3,50) =	1.234	0.307	
WASI matrix	-0.538	3.178	-0.611	0.553	U(52) =	220.500	-2.045	0.041	Chi2(3) =	4.369	0.224	
SCL90 somatization	-0.923	10.587	-0.314	0.759	U(51) =	287.000	-0.670	0.503	Chi2(3) =	0.961	0.811	
SCL90 obsessive compulsive	-14.846	11.104	-4.820	**0.000**	t(51) =	2.162		0.035	F(3,50) =	2.095	0.113	
SCL90 interpersonal sensitivity	6.231	9.671	2.323	0.039	t(51) =	-2.818		0.007	F(3,50) =	2.872	0.046	
SCL90 depression	-0.846	11.488	-0.266	0.795	t(51) =	0.336		0.739	Chi2(3) =	3.548	0.315	
SCL90 anxiety	2.000	10.878	0.663	0.520	U(51) =	263.000	-1.116	0.265	Chi2(3) =	3.250	0.355	
SCL90 hostility	-0.769	6.193	-0.448	0.662	t(51) =	-1.036		0.305	F(3,50) =	3.348	0.026	
SCL90 phobia	3.923	9.233	1.532	0.151	U(51) =	264.000	-1.104	0.270	Chi2(3) =	1.335	0.721	
SCL90 paranoia	3.692	13.949	0.954	0.359	t(51) =	-0.265		0.792	F(3,50) =	0.482	0.697	
SCL90 psychoticism	-4.846	11.305	-1.546	0.148	t(51) =	0.764		0.448	F(3,50) =	0.241	0.868	
SCL90 global severity index	-2.846	7.034	-1.459	0.170	t(51) =	1.326		0.191	F(3,50) =	0.596	0.621	
SCL90 positive symptoms distress	-3.692	13.641	-0.976	0.348	U(51) =	241.500	-1.513	0.130	F(3,50) =	1.918	0.139	
SCL90 positive symptoms total	-2.462	8.781	-1.011	0.332	t(51) =	0.346		0.730	F(3,50) =	0.123	0.946	
Barratt attentional	0.154	3.184	0.174	0.865	t(51) =	-1.898		0.063	F(3,50) =	1.283	0.291	
Barratt motor	0.769	2.488	1.115	0.287	t(51) =	-0.805		0.424	F(3,50) =	0.924	0.436	
Barratt nonplanning	1.692	4.029	1.515	0.156	U(51) =	251.000	-1.342	0.180	Chi2(3) =	2.035	0.565	
Barratt total	2.615	8.242	1.144	0.275	t(51) =	-0.531		0.598	F(3,50) =	1.385	0.258	

Table 10.1. Longitudinal changes in clinical and behavioural measures. P-values are uncorrected, P-values in bold are significant after Bonferroni-correction for multiple ROIs. (§: significant difference between MID and NEAR).

Stroop interference	48.316	8.049	45.514	10.667	46.091	8.994	47.636	11.604	43.231	11.519
Verbal Fluency FAStotal	43.211	10.223	43.314	13.319	44.818	7.400	45.909	15.359	39.846	15.464
Symbol digit	54.895	10.071	47.771	7.612	50.364	5.537	50.909	7.700	42.923	6.970
Digit span forward	12.684	1.974	11.571	2.033	11.727	2.453	12.000	2.000	11.077	1.706
Digit span backward	7.579	2.775	8.171	2.431	8.545	2.583	8.545	2.770	7.538	2.025
Digit span total	20.263	4.012	19.743	4.017	20.273	4.496	20.545	4.435	18.615	3.203
WASI matrix	25.684	5.687	27.429	3.346	28.182	2.892	27.455	4.435	26.769	2.713
SCL90 somatization	49.947	7.814	52.057	8.728	52.727	8.638	53.182	7.679	50.538	10.022
SCL90 obsessive compulsive	52.526	8.903	62.743	8.593	61.818	10.419	61.636	5.870	64.462	9.216
SCL90 interpresonal sensitivity	51.789	9.813	56.114	11.122	57.273	12.001	55.909	7.476	55.308	13.487
SCL90 depression	49.000	9.866	57.343	9.305	59.364	10.930	58.091	6.188	55.000	10.182
SCL90 anxiety	47.316	9.793	55.486	9.537	57.273	6.724	56.636	8.857	53.000	11.993
SCL90 hostility	47.895	6.716	53.886	10.148	58.455	9.202	50.636	9.113	52.769	11.039
SCL90 phobia	48.000	5.925	50.229	8.353	50.909	8.479	51.364	9.341	48.692	7.804
SCL90 paranoia	46.474	7.633	50.829	10.004	52.727	9.707	51.091	8.043	49.000	12.007
SCL90 psychoticism	48.895	8.640	56.600	9.293	57.636	10.072	57.091	6.610	55.308	10.988
SCL90 global severity index	48.421	10.292	57.857	9.447	59.091	11.649	57.818	5.671	56.846	10.511
SCL90 positive symptoms distress	49.000	9.928	55.657	8.405	54.273	9.446	53.182	8.875	58.923	6.422
SCL90 positive symptoms total	48.368	9.793	56.457	8.315	58.455	9.730	57.455	4.435	53.923	9.438
Barratt attentional	16.579	3.656	18.086	4.355	18.636	4.342	17.909	3.910	17.769	4.986
Barratt motor	19.368	3.435	20.600	4.265	21.091	5.186	20.364	4.273	20.385	3.686
Barratt nonplanning	23.632	4.705	23.829	4.860	24.909	3.081	23.545	6.121	23.154	5.113
Barratt total	59.579	9.901	62.514	10.899	64.636	9.973	61.818	13.014	61.308	10.315

Questionaire - Baseline	**all preHD vs CON**				**ANOVA**		
	Statistic		**Z**	**P**	**Statistic**		**P**
UHDRS motor score	NA	NA	NA	NA	$\chi^2(2) =$	1.370	0.504
UHDRS modified motor score	NA	NA	NA	NA	$\chi^2(2) =$	2.484	0.289
UHDRS confidence score	NA	NA	NA	NA	$\chi^2(2) =$	0.317	0.853
MOCA	U(52) =	322.000	-0.192	0.847	$\chi^2(3) =$	1.535	0.674
MMSE	U(52) =	314.500	-0.347	0.728	$\chi^2(3) =$	4.253	0.235
Stroop color	U(52) =	300.500	-0.580	0.562	$\chi^2(3) =$	1.102	0.777
Stroop word	U(52) =	261.500	-1.287	0.198	$\chi^2(3) =$	4.213	0.239
Stroop interference	U(52) =	292.000	-0.735	0.463	$\chi^2(3) =$	1.549	0.671
Verbal Fluency FAStotal	U(52) =	321.000	-0.209	0.835	$\chi^2(3) =$	1.490	0.685
Symbol digit	U(52) =	204.000	-2.332	**0.020**	$\chi^2(3) =$	11.980	**0.007**
Digit span forward	U(52) =	220.500	-2.055	0.040	$\chi^2(3) =$	5.997	0.112
Digit span backward	U(52) =	300.500	-0.584	0.559	$\chi^2(3) =$	1.792	0.617
Digit span total	U(52) =	299.000	-0.609	0.543	$\chi^2(3) =$	2.155	0.541
WASI matrix	U(52) =	280.500	-0.948	0.343	$\chi^2(3) =$	2.131	0.546
SCL90 somatization	U(52) =	283.500	-0.893	0.372	$\chi^2(3) =$	1.709	0.635
SCL90 obsessive compulsive	U(52) =	140.500	-3.482	**0.00050**	$\chi^2(3) =$	12.712	**0.005**
SCL90 interpresonal sensitivity	U(52) =	247.000	-1.555	0.120	$\chi^2(3) =$	2.970	0.396
SCL90 depression	U(52) =	174.500	-2.867	0.004	$\chi^2(3) =$	9.620	0.022
SCL90 anxiety	U(52) =	183.000	-2.716	0.007	$\chi^2(3) =$	9.027	0.029
SCL90 hostility	U(52) =	217.500	-2.100	0.036	$\chi^2(3) =$	7.809	0.050
SCL90 phobia	U(52) =	284.000	-0.929	0.353	$\chi^2(3) =$	2.802	0.423
SCL90 paranoia	U(52) =	252.000	-1.542	0.123	$\chi^2(3) =$	4.232	0.237
SCL90 psychoticism	U(52) =	167.500	-3.100	**0.002**	$\chi^2(3) =$	10.465	**0.015**
SCL90 global severity index	U(52) =	158.000	-3.166	**0.002**	$\chi^2(3) =$	10.665	**0.014**
SCL90 positive symptoms distress	U(52) =	171.000	-2.929	**0.003**	$\chi^2(3) =$	11.680	**0.009**
SCL90 positive symptoms total	U(52) =	172.500	-2.902	**0.004**	$\chi^2(3) =$	10.890	**0.012**
Barratt attentional	U(52) =	264.500	-1.236	0.216	$\chi^2(3) =$	2.296	0.513
Barratt motor	U(52) =	276.500	-1.019	0.308	$\chi^2(3) =$	1.387	0.709
Barratt nonplanning	U(52) =	331.000	-0.027	0.978	$\chi^2(3) =$	1.202	0.752
Barratt total	U(52) =	282.000	-0.916	0.360	$\chi^2(3) =$	1.581	0.664

Table 10.2. Cross-sectional alterations in clinical and behavioural measures at baseline. P-values are uncorrected, P-values in bold are significant after Bonferroni-correction for multiple ROIs. (§: significant difference between MID and NEAR).

Questionaire - Follow-up	CON		all preHD		FAR		MID		NEAR	
	Mean	SD	Mean	SD	Mean	SD	Mean	SD	Mean	SD
UHDRS motor score	NA	NA	NA	6.404	2.455	2.505	1.545	2.018	9.077	8.549
UHDRS modified motor score	NA	NA	NA	4.546	1.909	1.578	1.364	1.629	6.692	6.061
UHDRS confidence score	NA	NA	NA	1.138	0.636	0.809	0.273	0.467	1.923	1.188
MOCA	27.526	2.195	26.914	2.454	27.818	2.040	27.364	1.690	25.769	2.976
MMSE	28.474	1.744	28.343	1.413	28.727	1.555	28.545	1.036	27.846	1.519
Stroop color	74.632	12.742	72.286	15.616	79.273	13.850	68.364	11.227	69.692	18.971
Stroop word	103.158	11.495	94.171	23.348	101.455	20.815	90.091	13.390	91.462	31.020
Stroop interference	49.895	7.688	44.400	12.386	48.545	8.525	44.727	13.792	40.615	13.574
Verbal Fluency FAStotal	46.105	8.768	44.429	12.298	45.182	9.642	47.091	11.995	41.538	14.666
Symbol digit	54.789	8.155	48.000	9.668	51.000	9.370	50.545	9.363	43.308	8.976
Digit span forward	12.105	2.447	11.286	2.217	11.455	1.695	12.273	2.649	10.308	1.932
Digit span backward	8.526	2.170	8.029	2.281	8.636	2.730	8.636	1.859	7.000	1.958
Digit span total	20.632	4.323	19.314	4.020	20.091	3.885	20.909	4.036	17.308	3.521
WASI matrix	27.737	4.370	27.114	3.332	28.000	2.898	27.273	3.663	26.231	3.419
SCL90 somatization	46.895	8.875	50.265	10.955	51.455	14.038	49.800	10.261	49.615	9.215
SCL90 obsessive compulsive	46.895	8.875	50.559	11.484	52.364	15.273	49.800	10.261	49.615	9.215
SCL90 interpresonal sensitivity	48.895	8.931	61.529	12.091	60.455	13.988	62.700	11.935	61.538	11.399
SCL90 depression	48.053	7.043	55.324	11.069	53.091	11.970	59.300	9.381	54.154	11.503
SCL90 anxiety	45.316	9.730	57.500	11.874	57.000	11.933	61.300	9.534	55.000	13.485
SCL90 hostility	45.895	7.978	54.382	10.810	55.000	12.394	56.800	10.591	52.000	9.891
SCL90 phobia	48.000	5.099	54.206	9.859	55.455	11.031	54.900	9.826	52.615	9.430
SCL90 paranoia	47.684	6.138	52.588	9.538	51.727	11.270	53.400	9.070	52.692	9.022
SCL90 psychoticism	45.737	7.950	51.059	10.857	51.273	11.429	51.600	9.913	50.462	11.872
SCL90 global severity index	49.105	6.091	55.441	10.500	57.273	10.817	55.300	8.394	54.000	12.145
SCL90 positive symptoms distress	44.474	10.145	56.176	12.626	55.364	13.844	58.300	10.730	55.231	13.676
SCL90 positive symptoms total	46.158	9.963	53.147	10.532	54.182	11.923	54.200	9.355	51.462	10.767
Barratt attentional	14.895	3.398	18.000	4.592	18.091	5.856	18.000	4.643	17.923	3.639
Barratt motor	18.737	3.263	20.588	4.918	21.000	5.814	19.400	5.275	21.154	3.976
Barratt nonplanning	23.684	4.028	25.147	6.204	25.818	5.400	24.800	6.443	24.846	7.057
Barratt total	57.316	7.623	61.914	17.037	64.909	14.741	56.545	23.123	63.923	12.520

Questionaire - Follow-up	all preHD vs CON				ANOVA		
	Statistic		Z	P	Statistic		P
UHDRS motor score	NA	NA	NA	NA	$\chi^2(2) =$	10.426	**0.005**
UHDRS modified motor score	NA	NA	NA	NA	$\chi^2(2) =$	9.651	**0.008**
UHDRS confidence score	NA	NA	NA	NA	$\chi^2(2) =$	14.743	**0.001**
MOCA	U(52) =	285.500	-0.860	0.390	$\chi^2(3) =$	4.187	0.242
MMSE	U(52) =	296.000	-0.681	0.496	$\chi^2(3) =$	3.362	0.339
Stroop color	U(52) =	303.500	-0.526	0.599	$\chi^2(3) =$	3.642	0.303
Stroop word	U(52) =	247.500	-1.541	0.123	$\chi^2(3) =$	5.064	0.167
Stroop interference	U(52) =	265.000	-1.224	0.221	$\chi^2(3) =$	3.746	0.290
Verbal Fluency FAStotal	U(52) =	288.000	-0.807	0.420	$\chi^2(3) =$	1.668	0.644
Symbol digit	U(52) =	203.000	-2.348	**0.019**	$\chi^2(3) =$	9.015	**0.029**
Digit span forward	U(52) =	259.000	-1.348	0.178	$\chi^2(3) =$	8.345	0.039
Digit span backward	U(52) =	283.000	-0.908	0.364	$\chi^2(3) =$	4.939	0.176
Digit span total	U(52) =	263.000	-1.263	0.207	$\chi^2(3) =$	7.190	0.066
WASI matrix	U(52) =	258.500	-1.348	0.178	$\chi^2(3) =$	3.021	0.388
SCL90 somatization	U(51) =	266.500	-1.052	0.293	$\chi^2(3) =$	1.113	0.774
SCL90 obsessive compulsive	U(51) =	265.500	-1.070	0.284	$\chi^2(3) =$	1.160	0.763
SCL90 interpresonal sensitivity	U(51) =	131.500	-3.556	**3.76E-04**	$\chi^2(3) =$	12.910	0.005
SCL90 depression	U(51) =	197.000	-2.356	0.018	$\chi^2(3) =$	8.037	0.045
SCL90 anxiety	U(51) =	135.500	-3.489	**4.86E-04**	$\chi^2(3) =$	13.704	0.003
SCL90 hostility	U(51) =	171.000	-2.836	0.005	$\chi^2(3) =$	8.771	0.032
SCL90 phobia	U(51) =	186.500	-2.552	**0.011**	$\chi^2(3) =$	6.936	0.074
SCL90 paranoia	U(51) =	219.500	-2.000	0.046	$\chi^2(3) =$	4.412	0.220
SCL90 psychoticism	U(51) =	233.000	-1.809	0.070	$\chi^2(3) =$	3.563	0.313
SCL90 global severity index	U(51) =	205.500	-2.276	**0.023**	$\chi^2(3) =$	6.377	0.095
SCL90 positive symptoms distress	U(51) =	145.500	-3.296	**0.001**	$\chi^2(3) =$	11.417	**0.010**
SCL90 positive symptoms total	U(51) =	197.500	-2.343	**0.019**	$\chi^2(3) =$	5.976	0.113
Barratt attentional	U(51) =	197.000	-2.350	**0.019**	$\chi^2(3) =$	5.749	0.124
Barratt motor	U(51) =	246.500	-1.425	0.154	$\chi^2(3) =$	4.348	0.226
Barratt nonplanning	U(51) =	278.500	-0.827	0.408	$\chi^2(3) =$	1.363	0.714
Barratt total	U(51) =	244.500	-1.596	0.110	$\chi^2(3) =$	3.310	0.346

Table 10.3. Cross-sectional alterations in clinical and behavioural measures at follow-up. P-values are uncorrected, P-values in bold are significant after Bonferroni-correction for multiple ROIs.

Aboitiz, F. *et al.* (1992) ‘Fiber composition of the human corpus callosum’, *Brain Research*, 598(1–2), pp. 143–153. doi: 10.1016/0006-8993(92)90178-C.

Aboitiz, F. and Montiel, J. (2003) ‘One hundred million years of interhemispheric communication: the history of the corpus callosum’, *Brazilian Journal of Medical and Biological Research*. Brazilian Journal of Medical and Biological Research, 36(4), pp. 409–420. doi: 10.1590/S0100-879X2003000400002.

Abosch, A. *et al.* (2010) ‘An assessment of current brain targets for deep brain stimulation surgery with susceptibility-weighted imaging at 7 tesla.’, *Neurosurgery*. United States, 67(6), p. 1745–56; discussion 1756. doi: 10.1227/NEU.0b013e3181f74105.

Albin, R. L. *et al.* (1990) ‘Abnormalities of striatal projection neurons and N-methyl-D-aspartate receptors in presymptomatic Huntington’s disease.’, *The New England journal of medicine*. UNITED STATES, 322(18), pp. 1293–1298. doi: 10.1056/NEJM199005033221807.

Alexander, A. L. *et al.* (2007) ‘Diffusion tensor imaging of the brain.’, *Neurotherapeutics : the journal of the American Society for Experimental NeuroTherapeutics*. United States, 4(3), pp. 316–329. doi: 10.1016/j.nurt.2007.05.011.

Andersson, J. L. R., Skare, S. and Ashburner, J. (2003) ‘How to correct susceptibility distortions in spin-echo echo-planar images: application to diffusion tensor imaging.’, *NeuroImage*. United States, 20(2), pp. 870–888. doi: 10.1016/S1053-8119(03)00336-7.

Andersson, J. L. R. and Sotiropoulos, S. N. (2016) ‘An integrated approach to correction for off-resonance effects and subject movement in diffusion MR imaging’, *NeuroImage*. Academic Press, 125, pp. 1063–1078. doi: 10.1016/J.NEUROIMAGE.2015.10.019.

Atkinson-Clement, C. *et al.* (2017) ‘Diffusion tensor imaging in Parkinson’s disease: Review and meta-analysis’, *NeuroImage: Clinical*. Netherlands, 16, pp. 98–110. doi: 10.1016/j.nicl.2017.07.011.

Aylward, E. H. *et al.* (1996) ‘Basal ganglia volume and proximity to onset in presymptomatic Huntington disease.’, *Archives of neurology*. UNITED STATES, 53(12), pp. 1293–1296.

Aylward, E. H. *et al.* (1998) ‘Frontal lobe volume in patients with Huntington’s disease.’, *Neurology*. United States, 50(1), pp. 252–258.

Aylward, E. H. *et al.* (2011) ‘Longitudinal change in regional brain volumes in prodromal Huntington disease.’, *Journal of neurology, neurosurgery, and psychiatry*, 82(4), pp. 405–10. doi: 10.1136/jnnp.2010.208264.

Aylward, E. H. (2014) ‘Magnetic resonance imaging striatal volumes: a biomarker for clinical trials in Huntington’s disease.’, *Movement disorders : official journal of the Movement Disorder Society*, 29(11), pp. 1429–33. doi: 10.1002/mds.26013.

Bartzokis, G. *et al.* (2007) ‘Myelin Breakdown and Iron Changes in Huntington’s Disease: Pathogenesis and Treatment Implications’, *Neurochemical Research*, 32(10), pp. 1655–1664. doi: 10.1007/s11064-007-9352-7.

Basser, P. J. (1995) ‘Inferring microstructural features and the physiological state of tissues from diffusion-weighted images.’, *NMR in biomedicine*. England, 8(7–8), pp. 333–344.

Basser, P. J., Mattiello, J. and LeBihan, D. (1994a) ‘Estimation of the effective self-diffusion tensor from the NMR spin echo.’, *Journal of magnetic resonance. Series B*. United States, 103(3), pp. 247–254.

Basser, P. J., Mattiello, J. and LeBihan, D. (1994b) ‘MR diffusion tensor spectroscopy and imaging.’, *Biophysical Journal*, 66(1), pp. 259–267. Available at: http://www.ncbi.nlm.nih.gov/pmc/articles/PMC1275686/.

Beaulieu, C. (2002) ‘The basis of anisotropic water diffusion in the nervous system - a technical review’, *NMR in Biomedicine*, (15), pp. 435–455. doi: 10.1002/nbm.782.

Beaulieu, C. (2010) ‘What Makes Diffusion Anisotropic in the Nervous System?’, in *Diffusion MRI: Theory, Methods, and Applications*. Oxford University Press, pp. 92–109. doi: 10.1093/med/9780195369779.003.0007.

Beaulieu, C. (2014) ‘Chapter 8 - The Biological Basis of Diffusion Anisotropy’, in Johansen-Berg, H. and Behrens, T. E. J. B. T.-D. M. R. I. (Second E. (eds). San Diego: Academic Press, pp. 155–183. doi: https://doi.org/10.1016/B978-0-12-396460-1.00008-1.

Beglinger, L. J. *et al.* (2010) ‘Cognitive change in patients with Huntington disease on the Repeatable Battery for the Assessment of Neuropsychological Status’, *Journal of clinical and experimental neuropsychology*, 32(6), pp. 573–578. doi: 10.1080/13803390903313564.

Behrens, T. E. J., Woolrich, M. W., *et al.* (2003) ‘Characterization and propagation of uncertainty in diffusion-weighted MR imaging.’, *Magnetic resonance in medicine*. United States, 50(5), pp. 1077–1088. doi: 10.1002/mrm.10609.

Behrens, T. E. J., Johansen-Berg, H., *et al.* (2003) ‘Non-invasive mapping of connections between human thalamus and cortex using diffusion imaging.’, *Nature neuroscience*, 6, pp. 750–757. doi: 10.1038/nn1075.

Behrens, T. E. J., Berg, H. J., *et al.* (2007) ‘Probabilistic diffusion tractography with multiple fibre orientations: What can we gain?’, *NeuroImage*. United States, 34(1), pp. 144–155. doi: 10.1016/j.neuroimage.2006.09.018.

Behrens, T. E. J., Berg, H. J., *et al.* (2007) ‘Probabilistic diffusion tractography with multiple fibre orientations: What can we gain?’, *NeuroImage*. United States, 34(1), pp. 144–155. doi: 10.1016/j.neuroimage.2006.09.018.

Benabid, A. L. *et al.* (2009) ‘Deep brain stimulation of the subthalamic nucleus for the treatment of Parkinson’s disease.’, *The Lancet. Neurology*. England, 8(1), pp. 67–81. doi: 10.1016/S1474-4422(08)70291-6.

Benarroch, E. E. (2008) ‘Subthalamic nucleus and its connections’, *Neurology*, 70(21), p. 1991 LP-1995. Available at: http://n.neurology.org/content/70/21/1991.abstract.

Beukema, P., Yeh, F.-C. and Verstynen, T. (2015) ‘In vivo characterization of the connectivity and subcomponents of the human globus pallidus’, *NeuroImage*, 120, pp. 382–393. doi: 10.1016/j.neuroimage.2015.07.031.

Biomarkers Definitions Working Group (2001) ‘Biomarkers and surrogate endpoints: Preferred definitions and conceptual framework’, *Clinical Pharmacology & Therapeutics*, 69(3), pp. 89–95. doi: 10.1067/mcp.2001.113989.

Bohanna, I. *et al.* (2008) ‘Magnetic resonance imaging as an approach towards identifying neuropathological biomarkers for Huntington’s disease.’, *Brain research reviews*, 58, pp. 209–225. doi: 10.1016/j.brainresrev.2008.04.001.

Bohanna, I. *et al.* (2011) ‘Diffusion tensor imaging in Huntington’s disease reveals distinct patterns of white matter degeneration associated with motor and cognitive deficits.’, *Brain imaging and behavior*, 5(3), pp. 171–80. doi: 10.1007/s11682-011-9121-8.

Bohanna, I., Georgiou-Karistianis, N. and Egan, G. F. (2011) ‘Connectivity-based segmentation of the striatum in Huntington’s disease: vulnerability of motor pathways.’, *Neurobiology of disease*, 42(3), pp. 475–81. doi: 10.1016/j.nbd.2011.02.010.

Bot, M. *et al.* (2018) ‘Deep brain stimulation for Parkinson’s disease: defining the optimal location within the subthalamic nucleus.’, *Journal of neurology, neurosurgery, and psychiatry*. England, 89(5), pp. 493–498. doi: 10.1136/jnnp-2017-316907.

Bourbon-Teles, J. *et al.* (2017) ‘Myelin breakdown in human Huntington’s disease: Multi-modal evidence from diffusion MRI and quantitative magnetization transfer’, *Neuroscience*. doi: https://doi.org/10.1016/j.neuroscience.2017.05.042.

Bronshtein, I. N. *et al.* (eds) (2007) ‘Linear Algebra BT - Handbook of Mathematics’, in. Berlin, Heidelberg: Springer Berlin Heidelberg, pp. 251–285. doi: 10.1007/978-3-540-72122-2_4.

Burgel, U. *et al.* (2006) ‘White matter fiber tracts of the human brain: three-dimensional mapping at microscopic resolution, topography and intersubject variability.’, *NeuroImage*. United States, 29(4), pp. 1092–1105. doi: 10.1016/j.neuroimage.2005.08.040.

Burke, R. E. and O’Malley, K. (2013) ‘Axon degeneration in Parkinson’s disease.’, *Experimental neurology*. United States, 246, pp. 72–83. doi: 10.1016/j.expneurol.2012.01.011.

Button, K. S. *et al.* (2013) ‘Power failure: why small sample size undermines the reliability of neuroscience.’, *Nature reviews. Neuroscience*. England, pp. 365–376. doi: 10.1038/nrn3475.

Carpenter, M. B., Fraser, R. A. R. and Shriver, J. E. (1968) ‘The organization of pallidosubthalamic fibers in the monkey’, *Brain Research*, 11(3), pp. 522–559. doi: https://doi.org/10.1016/0006-8993(68)90145-5.

Carpenter, M. B., Whittier, J. R. and Mettler, F. A. (1950) ‘Analysis of choreoid hyperkinesia in the Rhesus monkey; surgical and pharmacological analysis of hyperkinesia resulting from lesions in the subthalamic nucleus of Luys.’, *The Journal of comparative neurology*. United States, 92(3), pp. 293–331.

Cavanagh, J. F. *et al.* (2011) ‘Subthalamic nucleus stimulation reverses mediofrontal influence over decision threshold.’, *Nature neuroscience*, 14(11), pp. 1462–7. doi: 10.1038/nn.2925.

Chan, L.-L. *et al.* (2007a) ‘Case control study of diffusion tensor imaging in Parkinson’s disease.’, *Journal of neurology, neurosurgery, and psychiatry*, 78, pp. 1383–1386. doi: 10.1136/jnnp.2007.121525.

Chan, L.-L. *et al.* (2007b) ‘Case control study of diffusion tensor imaging in Parkinson’s disease.’, *Journal of neurology, neurosurgery, and psychiatry*, 78(12), pp. 1383–6. doi: 10.1136/jnnp.2007.121525.

Chandra, A., Johri, A. and Beal, M. F. (2014) ‘Prospects for neuroprotective therapies in prodromal Huntington’s disease’, *Movement Disorders*. United States, 29(3), pp. 285–293. doi: 10.1002/mds.25835.

Chen, J. J. and Swope, D. M. (2007) ‘Pharmacotherapy for Parkinson’s disease.’, *Pharmacotherapy*. United States, 27(12 Pt 2), p. 161S–173S. doi: 10.1592/phco.27.12part2.161S.

Chen, Y. *et al.* (2018) ‘Role of the Cortico-Subthalamic Hyperdirect Pathway in Deep Brain Stimulation for the Treatment of Parkinson Disease: A Diffusion Tensor Imaging Study’, *World Neurosurgery*, 114, pp. e1079–e1085. doi: https://doi.org/10.1016/j.wneu.2018.03.149.

Chiang, P.-L. *et al.* (2017) ‘White matter damage and systemic inflammation in Parkinson’s disease’, *BMC Neuroscience*, 18(1), p. 48. doi: 10.1186/s12868-017-0367-y.

Ciccarelli, O. *et al.* (2001) ‘Investigation of MS normal-appearing brain using diffusion tensor MRI with clinical correlations’, *Neurology*, 56(7), pp. 926–933. Available at: http://www.scopus.com/inward/record.url?eid=2-s2.0-0035836716&partnerID=tZOtx3y1.

Cieslik, E. C. *et al.* (2013) ‘Is There “One” DLPFC in Cognitive Action Control? Evidence for Heterogeneity From Co-Activation-Based Parcellation’, *Cerebral Cortex*, 23(11), pp. 2677–2689. Available at: http://dx.doi.org/10.1093/cercor/bhs256.

Curran, K. M., Emsell, L. and Leemans, A. (2016) ‘Quantitative DTI Measures BT - Diffusion Tensor Imaging: A Practical Handbook’, in Van Hecke, W., Emsell, L., and Sunaert, S. (eds). New York, NY: Springer New York, pp. 65–87. doi: 10.1007/978-1-4939-3118-7_5.

Demetrio, M. *et al.* (2014) ‘Basal ganglia network by constrained spherical deconvolution: A possible cortico-pallidal pathway?’, *Movement Disorders*. Wiley-Blackwell, 30(3), pp. 342–349. doi: 10.1002/mds.25995.

Deng, Y. P. *et al.* (2004a) ‘Differential loss of striatal projection systems in Huntington’s disease: a quantitative immunohistochemical study.’, *Journal of chemical neuroanatomy*, 27, pp. 143–164. doi: 10.1016/j.jchemneu.2004.02.005.

Deng, Y. P. *et al.* (2004b) ‘Differential loss of striatal projection systems in Huntington’s disease: a quantitative immunohistochemical study.’, *Journal of chemical neuroanatomy*, 27(3), pp. 143–64. doi: 10.1016/j.jchemneu.2004.02.005.

Desikan, R. S. *et al.* (2006) ‘An automated labeling system for subdividing the human cerebral cortex on MRI scans into gyral based regions of interest.’, *NeuroImage*. United States, 31(3), pp. 968–980. doi: 10.1016/j.neuroimage.2006.01.021.

Dhollander, T. (2016) ‘From Diffusion to the Diffusion Tensor BT - Diffusion Tensor Imaging: A Practical Handbook’, in Van Hecke, W., Emsell, L., and Sunaert, S. (eds). New York, NY: Springer New York, pp. 37–63. doi: 10.1007/978-1-4939-3118-7_4.

Domínguez, D. J. F. *et al.* (2013) ‘Multi-modal neuroimaging in premanifest and early Huntington’s disease: 18 month longitudinal data from the IMAGE-HD study.’, *PloS one*, 8(9), p. e74131. doi: 10.1371/journal.pone.0074131.

Douaud, G., Behrens, T. E., *et al.* (2009) ‘In vivo evidence for the selective subcortical degeneration in Huntington’s disease’, *NeuroImage*, 46(4), pp. 958–966. doi: 10.1016/j.neuroimage.2009.03.044.

Douaud, G., Mackay, C., *et al.* (2009) ‘Schizophrenia delays and alters maturation of the brain in adolescence’, *Brain*, 132(9), pp. 2437–2448. Available at: http://dx.doi.org/10.1093/brain/awp126.

Douaud, G. *et al.* (2011) ‘DTI measures in crossing-fibre areas: increased diffusion anisotropy reveals early white matter alteration in MCI and mild Alzheimer’s disease.’, *NeuroImage*. United States, 55(3), pp. 880–890. doi: 10.1016/j.neuroimage.2010.12.008.

Dowie, M. J. *et al.* (2014) ‘Cannabinoid receptor CB2 is expressed on vascular cells, but not astroglial cells in the post-mortem human Huntington’s disease brain.’, *Journal of chemical neuroanatomy*. Netherlands, 59–60, pp. 62–71. doi: 10.1016/j.jchemneu.2014.06.004.

Draganski, B. *et al.* (2008) ‘Evidence for segregated and integrative connectivity patterns in the human Basal Ganglia.’, *The Journal of neuroscience : the official journal of the Society for Neuroscience*. United States, 28(28), pp. 7143–7152. doi: 10.1523/JNEUROSCI.1486-08.2008.

Duff, K. *et al.* (2010) ‘Mild cognitive impairment in prediagnosed Huntington disease.’, *Neurology*. United States, 75(6), pp. 500–507. doi: 10.1212/WNL.0b013e3181eccfa2.

Eickhoff, S. B. *et al.* (2007) ‘Assignment of functional activations to probabilistic cytoarchitectonic areas revisited.’, *NeuroImage*. United States, 36(3), pp. 511–521. doi: 10.1016/j.neuroimage.2007.03.060.

Eickhoff, S. B. *et al.* (2010) ‘Anatomical and functional connectivity of cytoarchitectonic areas within the human parietal operculum.’, *The Journal of neuroscience : the official journal of the Society for Neuroscience*. United States, 30(18), pp. 6409–6421. doi: 10.1523/JNEUROSCI.5664-09.2010.

Ennis, D. B. and Kindlmann, G. (2006) ‘Orthogonal tensor invariants and the analysis of diffusion tensor magnetic resonance images.’, *Magnetic resonance in medicine*. United States, 55(1), pp. 136–146. doi: 10.1002/mrm.20741.

Epping, E. A. *et al.* (2016) ‘Longitudinal Psychiatric Symptoms in Prodromal Huntington’s Disease: A Decade of Data.’, *The American journal of psychiatry*. United States, 173(2), pp. 184–192. doi: 10.1176/appi.ajp.2015.14121551.

Evans, J. R. *et al.* (2011) ‘The factor structure of the UPDRS as an index of disease progression in Parkinson’s disease.’, *Journal of Parkinson’s disease*. Netherlands, 1(1), pp. 75–82. doi: 10.3233/JPD-2011-0002.

Folstein, M. F., Folstein, S. E. and McHugh, P. R. (2015) '"Mini-mental state"', *Journal of Psychiatric Research*. Elsevier, 12(3), pp. 189–198. doi: 10.1016/0022-3956(75)90026-6.

Forstmann, B. U. *et al.* (2010) 'Cortico-striatal connections predict control over speed and accuracy in perceptual decision making.', *Proceedings of the National Academy of Sciences of the United States of America*. National Academy of Sciences, 107(36), pp. 15916–20. doi: 10.1073/pnas.1004932107.

Friston, K. (2012) 'Ten ironic rules for non-statistical reviewers', *NeuroImage*, 61(4), pp. 1300–1310. doi: https://doi.org/10.1016/j.neuroimage.2012.04.018.

Friston, K. J. (2009) 'Modalities, modes, and models in functional neuroimaging.', *Science (New York, N.Y.)*, 326(5951), pp. 399–403. doi: 10.1126/science.1174521.

Froeling, M., Pullens, P. and Leemans, A. (2016) 'DTI Analysis Methods: Region of Interest Analysis BT - Diffusion Tensor Imaging: A Practical Handbook', in Van Hecke, W., Emsell, L., and Sunaert, S. (eds). New York, NY: Springer New York, pp. 175–182. doi: 10.1007/978-1-4939-3118-7_9.

Furtado, S. *et al.* (1996) 'Relationship between trinucleotide repeats and neuropathological changes in Huntington's disease.', *Annals of neurology*, 39(1), pp. 132–6. doi: 10.1002/ana.410390120.

Galvez, V. *et al.* (2018) 'Extrastriatal degeneration correlates with deficits in the motor domain subscales of the UHDRS', *Journal of the Neurological Sciences*. Elsevier, 385, pp. 22–29. doi: 10.1016/j.jns.2017.11.040.

Gattellaro, G. *et al.* (2009) 'White Matter Involvement in Idiopathic Parkinson Disease: A Diffusion Tensor Imaging Study', *American Journal of Neuroradiology*, 30(6), p. 1222 LP-1226. Available at: http://www.ajnr.org/content/30/6/1222.abstract.

Gonzalez, V. *et al.* (2014) 'Deep brain stimulation for Huntington's disease: long-term results of a prospective open-label study.', *Journal of neurosurgery*. United States, 121(1), pp. 114–122. doi: 10.3171/2014.2.JNS131722.

Graveland, G. A., Williams, R. S. and DiFiglia, M. (1985) 'Evidence for degenerative and regenerative changes in neostriatal spiny neurons in Huntington's disease', *Science*, 227(4688), pp. 770–773. Available at: http://www.scopus.com/inward/record.url?eid=2-s2.0-0021982117&partnerID=tZOtx3y1.

Gregory, S. *et al.* (2015) 'Neuropsychiatry and White Matter Microstructure in Huntington's Disease.', *Journal of Huntington's disease*. IOS Press, 4(3), pp. 239–49. doi: 10.3233/JHD-150160.

Guadalupe, T. *et al.* (2017) ‘Human subcortical brain asymmetries in 15,847 people worldwide reveal effects of age and sex’, *Brain Imaging and Behavior*. New York: Springer US, 11(5), pp. 1497–1514. doi: 10.1007/s11682-016-9629-z.

Guo, Z. *et al.* (2012) ‘Striatal neuronal loss correlates with clinical motor impairment in Huntington’s disease.’, *Movement disorders : official journal of the Movement Disorder Society*. Division of Neuropathology, Department of Pathology, Johns Hopkins University School of Medicine, Baltimore, Maryland 21205, USA., 27(11), pp. 1379–86. doi: 10.1002/mds.25159.

Hagmann, P. *et al.* (2006) ‘Understanding diffusion MR imaging techniques: from scalar diffusion-weighted imaging to diffusion tensor imaging and beyond.’, *Radiographics : a review publication of the Radiological Society of North America, Inc*. United States, 26 Suppl 1, pp. S205-23. doi: 10.1148/rg.26si065510.

Hague, S. M., Klaffke, S. and Bandmann, O. (2005) ‘Neurodegenerative disorders: Parkinson{\textquoteright}s disease and Huntington{\textquoteright}s disease’, *Journal of Neurology, Neurosurgery & Psychiatry*. BMJ Publishing Group Ltd, 76(8), pp. 1058–1063. doi: 10.1136/jnnp.2004.060186.

Hare, D. J. and Double, K. L. (2016) ‘Iron and dopamine: a toxic couple.’, *Brain : a journal of neurology*. England, 139(Pt 4), pp. 1026–1035. doi: 10.1093/brain/aww022.

Harrington, D. L. *et al.* (2012) ‘Cognitive domains that predict time to diagnosis in prodromal Huntington disease.’, *Journal of neurology, neurosurgery, and psychiatry*. England, 83(6), pp. 612–619. doi: 10.1136/jnnp-2011-301732.

Haynes, W. I. A. and Haber, S. N. (2013) ‘The organization of prefrontal-subthalamic inputs in primates provides an anatomical substrate for both functional specificity and integration: implications for Basal Ganglia models and deep brain stimulation.’, *The Journal of neuroscience : the official journal of the Society for Neuroscience*, 33(11), pp. 4804–14. doi: 10.1523/JNEUROSCI.4674-12.2013.

He, N. *et al.* (2017) ‘Dentate nucleus iron deposition is a potential biomarker for tremor-dominant Parkinson’s disease.’, *NMR in biomedicine*. England, 30(4). doi: 10.1002/nbm.3554.

Van Hecke, W., Emsell, L. and Sunaert, S. (2015) *Diffusion Tensor Imaging: A Practical Handbook*. Springer New York.

Hernandez-Fernandez, M. *et al.* (2016) ‘A fast and flexible toolbox for tracking brain connections in diffusion MRI datasets using GPUs’, in *Proceedings of the 22nd Annual Meeting of the Organization for Human Brain Mapping (OHBM)*.

Herz, D. M. *et al.* (2016) ‘Neural Correlates of Decision Thresholds in the Human Subthalamic Nucleus’, *Current Biology*, 26(7), pp. 916–920. doi: https://doi.org/10.1016/j.cub.2016.01.051.

Ho, A. K. *et al.* (2003) ‘Profile of cognitive progression in early Huntington’s disease.’, *Neurology*. United States, 61(12), pp. 1702–1706.

Hoehn, M. M. and Yahr, M. D. (1967) ‘Parkinsonism’, *Neurology*, 17(5), p. 427 LP-427. Available at: http://n.neurology.org/content/17/5/427.abstract.

Hoshi, E. (2006) ‘Functional specialization within the dorsolateral prefrontal cortex: A review of anatomical and physiological studies of non-human primates’, *Neuroscience Research*, 54(2), pp. 73–84. doi: https://doi.org/10.1016/j.neures.2005.10.013.

Jaccard, P. (1901) *Etude de la distribution florale dans une portion des Alpes et du Jura*, *Bulletin de la Societe Vaudoise des Sciences Naturelles*. doi: 10.5169/seals-266450.

Jahanshahi, M. *et al.* (2015) ‘A fronto-striato-subthalamic-pallidal network for goal-directed and habitual inhibition.’, *Nature reviews. Neuroscience*. England, 16(12), pp. 719–732. doi: 10.1038/nrn4038.

Jbabdi, S. and Johansen-Berg, H. (2011a) ‘Tractography: where do we go from here?’, *Brain connectivity*, 1, pp. 169–183. doi: 10.1089/brain.2011.0033.

Jbabdi, S. and Johansen-Berg, H. (2011b) ‘Tractography: where do we go from here?’, *Brain connectivity*. United States, 1(3), pp. 169–183. doi: 10.1089/brain.2011.0033.

Jellison, B. J. *et al.* (2004) ‘Diffusion tensor imaging of cerebral white matter: a pictorial review of physics, fiber tract anatomy, and tumor imaging patterns.’, *AJNR. American journal of neuroradiology*. United States, 25(3), pp. 356–369.

Jenkinson, M. *et al.* (2012) ‘FSL.’, *NeuroImage*. United States, 62(2), pp. 782–790. doi: 10.1016/j.neuroimage.2011.09.015.

Jones, D. K. (2010) ‘Challenges and limitations of quantifying brain connectivity in vivo with diffusion MRI’, *Imaging in Medicine*, 2(3), pp. 341–355. doi: 10.2217/iim.10.21.

Jones, D. K. (2010) *Diffusion MRI*. Oxford University Press.

Jones, E. *et al.* (no date) ‘SciPy: Open source scientific tools for Python’. Available at: http://www.scipy.org/.

Kalia, L. V (2018) ‘Biomarkers for cognitive dysfunction in Parkinson’s disease.’, *Parkinsonism & related disorders*. England, 46 Suppl 1, pp. S19–S23. doi: 10.1016/j.parkreldis.2017.07.023.

Kassubek, J. *et al.* (2005) ‘Thalamic atrophy in Huntington’s disease co-varies with cognitive performance: a morphometric MRI analysis.’, *Cerebral cortex (New York, N.Y. : 1991)*. United States, 15(6), pp. 846–853. doi: 10.1093/cercor/bhh185.

Kingsley, P. B. (2006) ‘Introduction to diffusion tensor imaging mathematics: Part I. Tensors, rotations, and eigenvectors’, *Concepts in Magnetic Resonance Part A*. Wiley-Blackwell, 28A(2), pp. 101–122. doi: 10.1002/cmr.a.20048.

Kirkwood, S. C. *et al.* (2000) ‘Subtle changes among presymptomatic carriers of the Huntington{\textquoteright}s disease gene’, *Journal of Neurology, Neurosurgery & Psychiatry*. BMJ Publishing Group Ltd, 69(6), pp. 773–779. doi: 10.1136/jnnp.69.6.773.

Kita, H., Chang, H. T. and Kitai, S. T. (1983) ‘Pallidal inputs to subthalamus: Intracellular analysis’, *Brain Research*, 264(2), pp. 255–265. doi: https://doi.org/10.1016/0006-8993(83)90823-5.

Kitai, S. T. and Deniau, J. M. (1981) ‘Cortical inputs to the subthalamus: intracellular analysis.’, *Brain research*. Netherlands, 214(2), pp. 411–415.

Kljajevic, V. (2014) ‘White matter architecture of the language network’, *Translational Neuroscience*, 5(4), pp. 239–252. doi: 10.2478/s13380-014-0232-8.

Krack, P. *et al.* (2010) ‘Deep brain stimulation: from neurology to psychiatry?’, *Trends in neurosciences*. England, 33(10), pp. 474–484. doi: 10.1016/j.tins.2010.07.002.

Kreutzberg, G. W. (1996) ‘Microglia: a sensor for pathological events in the CNS.’, *Trends in neurosciences*. ENGLAND, 19(8), pp. 312–318.

Kunzle, H. (1978) ‘An autoradiographic analysis of the efferent connections from premotor and adjacent prefrontal regions (areas 6 and 9) in macaca fascicularis.’, *Brain, behavior and evolution*. Switzerland, 15(3), pp. 185–234. doi: 10.1159/000123779.

Kunzle, H. and Akert, K. (1977) ‘Efferent connections of cortical, area 8 (frontal eye field) in Macaca fascicularis. A reinvestigation using the autoradiographic technique.’, *The Journal of comparative neurology*. United States, 173(1), pp. 147–164. doi: 10.1002/cne.901730108.

de la Monte, S. M., Vonsattel, J. P. and Richardson, E. P. J. (1988) ‘Morphometric demonstration of atrophic changes in the cerebral cortex, white matter, and neostriatum in Huntington’s disease.’, *Journal of neuropathology and experimental neurology*. England, 47(5), pp. 516–525.

Lambert, C. *et al.* (2012) ‘Confirmation of functional zones within the human subthalamic nucleus: patterns of connectivity and sub-parcellation using diffusion weighted imaging.’, *NeuroImage*. United States, 60(1), pp. 83–94. doi: 10.1016/j.neuroimage.2011.11.082.

Langbehn, D. R. *et al.* (2010) ‘CAG-repeat length and the age of onset in Huntington disease (HD): A review and validation study of statistical approaches’, *American Journal of Medical*

Genetics Part B: Neuropsychiatric Genetics. Wiley Subscription Services, Inc., A Wiley Company, 153B(2), pp. 397–408. doi: 10.1002/ajmg.b.30992.

Lange, H. *et al.* (1976) 'Morphometric studies of the neuropathological changes in choreatic diseases.', *Journal of the neurological sciences*. Netherlands, 28(4), pp. 401–425.

Lehericy, S. *et al.* (2004) 'Diffusion tensor fiber tracking shows distinct corticostriatal circuits in humans.', *Annals of neurology*. United States, 55(4), pp. 522–529. doi: 10.1002/ana.20030.

Lenglet, C. *et al.* (2012) 'Comprehensive in vivo Mapping of the Human Basal Ganglia and Thalamic Connectome in Individuals Using 7T MRI', *PLoS ONE*. Edited by K. Bankiewicz. San Francisco, USA: Public Library of Science, 7(1), p. e29153. doi: 10.1371/journal.pone.0029153.

Liu, H. *et al.* (2013) 'Altered resting-state functional connectivity of the dentate nucleus in Parkinson's disease.', *Psychiatry research*. Ireland, 211(1), pp. 64–71. doi: 10.1016/j.pscychresns.2012.10.007.

Lotfipour, A. K. *et al.* (2012) 'High resolution magnetic susceptibility mapping of the substantia nigra in Parkinson's disease.', *Journal of magnetic resonance imaging : JMRI*. United States, 35(1), pp. 48–55. doi: 10.1002/jmri.22752.

Lotharius, J. and Brundin, P. (2002) 'Pathogenesis of parkinson's disease: dopamine, vesicles and [alpha]-synuclein', *Nat Rev Neurosci*, 3(12), pp. 932–942. Available at: http://dx.doi.org/10.1038/nrn983.

Luys, J. (1865) *Recherches sur le système nerveux cérébro-spinal: sa structure, ses fonctions et ses maladies*. J.-B. Bailliére et fils (Recherches sur le système nerveux cérébro-spinal: sa structure, ses fonctions et ses maladies).

Magaudda, L. *et al.* (2013) *The cortico-pallidal projection in the human: a tracking study with DT I technique*. doi: 10.13128/IJAE-12189.

Mairal, J. *et al.* (2009) 'Online Dictionary Learning for Sparse Coding', in *Proceedings of the 26th Annual International Conference on Machine Learning*. New York, NY, USA: ACM (ICML '09), pp. 689–696. doi: 10.1145/1553374.1553463.

Majid, D. S. A., Stoffers, D., *et al.* (2011) 'Automated structural imaging analysis detects premanifest Huntington's disease neurodegeneration within 1 year.', *Movement disorders : official journal of the Movement Disorder Society*. United States, 26(8), pp. 1481–1488. doi: 10.1002/mds.23656.

Majid, D. S. A., Aron, A. R., *et al.* (2011) 'Basal ganglia atrophy in prodromal Huntington's disease is detectable over one year using automated segmentation.', *Movement disorders :*

official journal of the Movement Disorder Society. United States, 26(14), pp. 2544–2551. doi: 10.1002/mds.23912.

Marrakchi-Kacem, L. *et al.* (2014) ‘Using tractography to infer Basal ganglia’s functional subterritories distribution change in Huntington disease’, in *2014 1st International Conference on Advanced Technologies for Signal and Image Processing (ATSIP)*, pp. 167–171. doi: 10.1109/ATSIP.2014.6834599.

Mars, R. B. *et al.* (2016) ‘The extreme capsule fiber complex in humans and macaque monkeys: a comparative diffusion MRI tractography study’, *Brain Structure & Function*. Berlin/Heidelberg: Springer Berlin Heidelberg, 221(8), pp. 4059–4071. doi: 10.1007/s00429-015-1146-0.

Martin, J. P. (1927) ‘Hemichorea resulting from a local lesion of the brain.(the syndrome of the body of luys’, *Brain*. Oxford University Press, 50(3–4), pp. 637–649.

Maschke, M. *et al.* (2004) ‘Age-related changes of the dentate nuclei in normal adults as revealed by 3D fast low angle shot (FLASH) echo sequence magnetic resonance imaging.’, *Journal of neurology*. Germany, 251(6), pp. 740–746. doi: 10.1007/s00415-004-0420-5.

McFarland, N. R. and Haber, S. N. (2002) ‘Thalamic relay nuclei of the basal ganglia form both reciprocal and nonreciprocal cortical connections, linking multiple frontal cortical areas.’, *The Journal of neuroscience : the official journal of the Society for Neuroscience*, 22, pp. 8117–8132. doi: 22/18/8117 [pii].

McKinney, W. (2010) ‘Data Structures for Statistical Computing in Python’, in van der Walt, S. and Millman, J. (eds) *Proceedings of the 9th Python in Science Conference*, pp. 51–56.

Melzer, T. R. *et al.* (2013) ‘White matter microstructure deteriorates across cognitive stages in Parkinson disease’, *Neurology*, 80(20), pp. 1841–1849. doi: 10.1212/WNL.0b013e3182929f62.

Middlebrooks, E. H. *et al.* (2018) ‘Segmentation of the Globus Pallidus Internus Using Probabilistic Diffusion Tractography for Deep Brain Stimulation Targeting in Parkinson Disease’, *American Journal of Neuroradiology*. Available at: http://www.ajnr.org/content/early/2018/04/26/ajnr.A5641.abstract.

Milardi, D. *et al.* (2015) ‘Basal ganglia network by constrained spherical deconvolution: a possible cortico-pallidal pathway?’, *Movement disorders : official journal of the Movement Disorder Society*. United States, 30(3), pp. 342–349. doi: 10.1002/mds.25995.

Miller, E. K. and Cohen, J. D. (2001) ‘An integrative theory of prefrontal cortex function.’, *Annual review of neuroscience*. United States, 24, pp. 167–202. doi: 10.1146/annurev.neuro.24.1.167.

Monakow, K. H., Akert, K. and Kunzle, H. (1978) ‘Projections of the precentral motor cortex and other cortical areas of the frontal lobe to the subthalamic nucleus in the monkey.’, *Experimental brain research*. Germany, 33(3–4), pp. 395–403.

Mori, S. *et al.* (2008) ‘Stereotaxic white matter atlas based on diffusion tensor imaging in an ICBM template.’, *NeuroImage*. United States, 40(2), pp. 570–582. doi: 10.1016/j.neuroimage.2007.12.035.

Myers, R. H. (2004) ‘Huntington’s disease genetics.’, *NeuroRx : the journal of the American Society for Experimental NeuroTherapeutics*. United States, 1(2), pp. 255–262. doi: 10.1602/neurorx.1.2.255.

Nakanishi, H., Kita, H. and Kitai, S. T. (1988) ‘An N-methyl-d-aspartate receptor mediated excitatory postsynaptic potential evoked in subthalamic neurons in an in vitro slice preparation of the rat’, *Neuroscience Letters*, 95(1), pp. 130–136. doi: https://doi.org/10.1016/0304-3940(88)90645-3.

Nambu, A. *et al.* (2000) ‘Excitatory cortical inputs to pallidal neurons via the subthalamic nucleus in the monkey.’, *Journal of neurophysiology*. United States, 84(1), pp. 289–300. doi: 10.1152/jn.2000.84.1.289.

Nambu, A. (2008a) ‘Seven problems on the basal ganglia.’, *Current opinion in neurobiology*. England, 18(6), pp. 595–604. doi: 10.1016/j.conb.2008.11.001.

Nambu, A. (2008b) ‘Seven problems on the basal ganglia.’, *Current opinion in neurobiology*, 18, pp. 595–604. doi: 10.1016/j.conb.2008.11.001.

Nambu, A., Tachibana, Y. and Chiken, S. (2015) ‘Cause of parkinsonian symptoms: Firing rate, firing pattern or dynamic activity changes?’, *Basal Ganglia*, 5(1), pp. 1–6. doi: https://doi.org/10.1016/j.baga.2014.11.001.

Nambu, A., Tokuno, H. and Takada, M. (2002) ‘Functional significance of the cortico-subthalamo-pallidal “hyperdirect” pathway.’, *Neuroscience research*. Ireland, 43(2), pp. 111–117.

Nauta, H. J. and Cole, M. (1978) ‘Efferent projections of the subthalamic nucleus: an autoradiographic study in monkey and cat.’, *The Journal of comparative neurology*. United States, 180(1), pp. 1–16. doi: 10.1002/cne.901800102.

Della Nave, R. *et al.* (2010a) ‘Regional distribution and clinical correlates of white matter structural damage in Huntington disease: a tract-based spatial statistics study.’, *AJNR. American journal of neuroradiology*. United States, 31(9), pp. 1675–1681. doi: 10.3174/ajnr.A2128.

Della Nave, R. *et al.* (2010b) ‘Regional distribution and clinical correlates of white matter structural damage in Huntington disease: a tract-based spatial statistics study.’, *AJNR. American journal of neuroradiology*, 31, pp. 1675–1681. doi: 10.3174/ajnr.A2128.

Nelson, A. B. and Kreitzer, A. C. (2014) ‘Reassessing models of Basal Ganglia function and dysfunction.’, *Annual review of neuroscience*, 37, pp. 117–35. doi: 10.1146/annurev-neuro-071013-013916.

Nichols, T. *et al.* (2005) ‘Valid conjunction inference with the minimum statistic.’, *NeuroImage*. United States, 25(3), pp. 653–660. doi: 10.1016/j.neuroimage.2004.12.005.

Novak, M. J. U. *et al.* (2015) ‘Basal ganglia-cortical structural connectivity in Huntington’s disease’, *Human Brain Mapping*. John Wiley and Sons Inc., 36(5), pp. 1728–1740. doi: 10.1002/hbm.22733.

Obeso, I. *et al.* (2014) ‘The subthalamic nucleus and inhibitory control: impact of subthalamotomy in Parkinson’s disease.’, *Brain : a journal of neurology*, 137(Pt 5), pp. 1470–80. doi: 10.1093/brain/awu058.

Obeso, J. A. *et al.* (2000) ‘Pathophysiology of the basal ganglia in Parkinson’s disease.’, *Trends in neurosciences*. England, 23(10 Suppl), pp. S8-19.

Obeso, J. A. *et al.* (2002) ‘The Basal Ganglia and Disorders of Movement: Pathophysiological Mechanisms’, *Physiology*, 17(2), pp. 51–55. Available at: http://physiologyonline.physiology.org/content/17/2/51.abstract.

Obeso, J. A. *et al.* (2008) ‘Functional organization of the basal ganglia: therapeutic implications for Parkinson’s disease.’, *Movement disorders : official journal of the Movement Disorder Society*. United States, 23 Suppl 3, pp. S548-59. doi: 10.1002/mds.22062.

Odish, O. F. F., Caeyenberghs, K., *et al.* (2015) ‘Dynamics of the connectome in Huntington’s disease: A longitudinal diffusion MRI study.’, *NeuroImage. Clinical*. Elsevier Inc., 9, pp. 32–43. doi: 10.1016/j.nicl.2015.07.003.

Odish, O. F. F., Leemans, A., *et al.* (2015) ‘Microstructural brain abnormalities in Huntington’s disease: A two-year follow-up.’, *Human brain mapping*. John Wiley and Sons Inc., 36(6), pp. 2061–74. doi: 10.1002/hbm.22756.

Oishi, K. *et al.* (2008) ‘Human brain white matter atlas: identification and assignment of common anatomical structures in superficial white matter.’, *NeuroImage*. United States, 43(3), pp. 447–457. doi: 10.1016/j.neuroimage.2008.07.009.

Oishi, K. *et al.* (2010) *MRI Atlas of Human White Matter*. Elsevier Science.

Okada, N. *et al.* (2016) ‘Abnormal asymmetries in subcortical brain volume in schizophrenia’, *Molecular Psychiatry*. The Author(s), 21, p. 1460. Available at: http://dx.doi.org/10.1038/mp.2015.209.

Okun, M. S. (2012) ‘Deep-brain stimulation for Parkinson’s disease.’, *The New England journal of medicine*. United States, 367(16), pp. 1529–1538. doi: 10.1056/NEJMct1208070.

Oliphant, T. E. (2007) ‘Python for Scientific Computing’, *Computing in Science & Engineering*, 9(3), pp. 10–20. doi: 10.1109/MCSE.2007.58.

Paek, S. H. *et al.* (2013) ‘The clinical impact of precise electrode positioning in STN DBS on three-year outcomes.’, *Journal of the neurological sciences*. Netherlands, 327(1–2), pp. 25–31. doi: 10.1016/j.jns.2013.01.037.

Di Paola, M. *et al.* (2012) ‘Multimodal MRI analysis of the corpus callosum reveals white matter differences in presymptomatic and early Huntington’s disease’, *Cerebral Cortex*, 22(12), pp. 2858–2866. doi: 10.1093/cercor/bhr360.

Parent, A. (2002) ‘Jules Bernard Luys and the subthalamic nucleus.’, *Movement disorders : official journal of the Movement Disorder Society*. United States, 17(1), pp. 181–185.

Parent, A. and Hazrati, L. N. (1995) ‘Functional anatomy of the basal ganglia. II. The place of subthalamic nucleus and external pallidum in basal ganglia circuitry.’, *Brain research. Brain research reviews*. Netherlands, 20(1), pp. 128–154.

Parkinson, J. (2002) ‘An Essay on the Shaking Palsy’, *The Journal of Neuropsychiatry and Clinical Neurosciences*. American Psychiatric Publishing, 14(2), pp. 223–236. doi: 10.1176/jnp.14.2.223.

Patriat, R. *et al.* (2018) ‘Individualized tractography-based parcellation of the globus pallidus pars interna using 7T MRI in movement disorder patients prior to DBS surgery.’, *NeuroImage*. United States, 178, pp. 198–209. doi: 10.1016/j.neuroimage.2018.05.048.

Patton, J. H., Stanford, M. S. and Barratt, E. S. (1995) ‘Factor structure of the Barratt impulsiveness scale.’, *Journal of clinical psychology*. UNITED STATES, 51(6), pp. 768–774.

Paulsen, J. S. *et al.* (2001) ‘Neuropsychiatric aspects of Huntington’s disease.’, *Journal of neurology, neurosurgery, and psychiatry*. England, 71(3), pp. 310–314.

Paulsen, J. S. *et al.* (2006) ‘Brain structure in preclinical Huntington’s disease.’, *Biological psychiatry*, 59(1), pp. 57–63. doi: 10.1016/j.biopsych.2005.06.003.

Paulsen, J. S. (2011) ‘Cognitive impairment in Huntington disease: diagnosis and treatment.’, *Current neurology and neuroscience reports*. United States, 11(5), pp. 474–483. doi: 10.1007/s11910-011-0215-x.

Pedregosa, F. *et al.* (2012) ‘Scikit-learn: Machine Learning in Python’, *Journal of Machine Learning Research*, 12.

Phillips, O. *et al.* (2014) ‘Deep White Matter in Huntington’s Disease’, *PLOS ONE*. Public Library of Science, 9(10), pp. 1–11. doi: 10.1371/journal.pone.0109676.

Pierpaoli, C. and Basser, P. J. (1996) ‘Toward a quantitative assessment of diffusion anisotropy’, *Magnetic Resonance in Medicine*, 36(6), pp. 893–906. Available at: http://www.scopus.com/inward/record.url?eid=2-s2.0-0029908076&partnerID=tZOtx3y1.

Plantinga, B. R. *et al.* (2018) ‘Individualized parcellation of the subthalamic nucleus in patients with Parkinson’s disease with 7T MRI’, *NeuroImage*, 168, pp. 403–411. doi: 10.1016/j.neuroimage.2016.09.023.

Poewe, W. *et al.* (2017) ‘Parkinson disease’, *Nature Reviews Disease Primers*. Macmillan Publishers Limited, 3, p. 17013. Available at: http://dx.doi.org/10.1038/nrdp.2017.13.

Polders, D. L. *et al.* (2011) ‘Signal to noise ratio and uncertainty in diffusion tensor imaging at 1.5, 3.0, and 7.0 Tesla.’, *Journal of magnetic resonance imaging : JMRI*. United States, 33(6), pp. 1456–1463. doi: 10.1002/jmri.22554.

Poudel, G. R. *et al.* (2015) ‘Longitudinal change in white matter microstructure in Huntington’s disease: The IMAGE-HD study.’, *Neurobiology of disease*. Academic Press Inc., 74(1), pp. 406–12. doi: 10.1016/j.nbd.2014.12.009.

Qiu, M. *et al.* (2012) ‘Diffusion Tensor Imaging-Based Research on Human White Matter Anatomy’, *The Scientific World Journal*. The Scientific World Journal, 2012, p. 530432. doi: 10.1100/2012/530432.

Reading, S. A. J. *et al.* (2005) ‘Regional white matter change in pre-symptomatic Huntington’s disease: a diffusion tensor imaging study.’, *Psychiatry research*, 140(1), pp. 55–62. doi: 10.1016/j.pscychresns.2005.05.011.

Rees, E. M., Scahill, R. I. and Hobbs, N. Z. (2013) ‘Longitudinal neuroimaging biomarkers in Huntington’s Disease.’, *Journal of Huntington’s disease*. Netherlands, 2(1), pp. 21–39. doi: 10.3233/JHD-120030.

Rektor, I. *et al.* (2018) ‘White matter alterations in Parkinson’s disease with normal cognition precede grey matter atrophy’, *PLoS ONE*. Edited by J. Najbauer. San Francisco, CA USA: Public Library of Science, 13(1), p. e0187939. doi: 10.1371/journal.pone.0187939.

Rolston, J. D. *et al.* (2016) ‘An unexpectedly high rate of revisions and removals in deep brain stimulation surgery: Analysis of multiple databases’, *Parkinsonism & related disorders*, 33, pp. 72–77. doi: 10.1016/j.parkreldis.2016.09.014.

Rosas, H. D. *et al.* (2001) ‘Striatal volume loss in HD as measured by MRI and the influence of CAG repeat.’, *Neurology*, 57(6), pp. 1025–8. doi: 10.1212/WNL.57.6.1025.

Rosas, H. D. *et al.* (2006a) ‘Diffusion tensor imaging in presymptomatic and early Huntington’s disease: Selective white matter pathology and its relationship to clinical measures.’, *Movement disorders : official journal of the Movement Disorder Society*, 21(9), pp. 1317–25. doi: 10.1002/mds.20979.

Rosas, H. D. *et al.* (2006b) ‘Diffusion tensor imaging in presymptomatic and early Huntington’s disease: Selective white matter pathology and its relationship to clinical measures.’, *Movement disorders : official journal of the Movement Disorder Society*, 21(9), pp. 1317–25. doi: 10.1002/mds.20979.

Rosas, H. D. *et al.* (2010) ‘Altered white matter microstructure in the corpus callosum in Huntington’s disease: implications for cortical “disconnection”.’, *NeuroImage*. United States, 49(4), pp. 2995–3004. doi: 10.1016/j.neuroimage.2009.10.015.

Rosenblatt, A. *et al.* (2012) ‘Age, CAG repeat length, and clinical progression in Huntington’s disease.’, *Movement disorders : official journal of the Movement Disorder Society*. United States, 27(2), pp. 272–276. doi: 10.1002/mds.24024.

Ross, C. A. and Tabrizi, S. J. (2011) ‘Huntington’s disease: from molecular pathogenesis to clinical treatment.’, *The Lancet. Neurology*, 10(1), pp. 83–98. doi: 10.1016/S1474-4422(10)70245-3.

Ryan, N. S. *et al.* (2013) ‘Magnetic resonance imaging evidence for presymptomatic change in thalamus and caudate in familial Alzheimer’s disease.’, *Brain : a journal of neurology*. England, 136(Pt 5), pp. 1399–1414. doi: 10.1093/brain/awt065.

Saga, Y., Hoshi, E. and Tremblay, L. (2017) ‘Roles of Multiple Globus Pallidus Territories of Monkeys and Humans in Motivation, Cognition and Action: An Anatomical, Physiological and Pathophysiological Review’, *Frontiers in Neuroanatomy*, 11, p. 30. doi: 10.3389/fnana.2017.00030.

Sallet, J. *et al.* (2013) ‘The Organization of Dorsal Frontal Cortex in Humans and Macaques’, *The Journal of Neuroscience*. Society for Neuroscience, 33(30), pp. 12255–12274. doi: 10.1523/JNEUROSCI.5108-12.2013.

Samii, A., Nutt, J. G. and Ransom, B. R. (2004) ‘Parkinson’s disease.’, *Lancet (London, England)*. England, 363(9423), pp. 1783–1793. doi: 10.1016/S0140-6736(04)16305-8.

Schmahmann, J. D. *et al.* (2008) ‘Cerebral White Matter: Neuroanatomy, Clinical Neurology, and Neurobehavioral Correlates’, *Annals of the New York Academy of Sciences*, 1142, pp. 266–309. doi: 10.1196/annals.1444.017.

Schmahmann, J. and Pandya, D. (2009) *Fiber Pathways of the Brain*. Oxford University Press, USA.

Schneider, S. A. and Obeso, J. A. (2015a) ‘Clinical and pathological features of Parkinson’s disease.’, *Current topics in behavioral neurosciences*. Germany, 22, pp. 205–220. doi: 10.1007/7854_2014_317.

Schneider, S. A. and Obeso, J. A. (2015b) ‘Clinical and Pathological Features of Parkinson’s Disease BT - Behavioral Neurobiology of Huntington’s Disease and Parkinson’s Disease’, in Nguyen, H. H. P. and Cenci, M. A. (eds). Berlin, Heidelberg: Springer Berlin Heidelberg, pp. 205–220. doi: 10.1007/7854_2014_317.

Seabold, S. and Perktold, J. (2010) ‘Statsmodels: Econometric and statistical modeling with python’, in *9th Python in Science Conference*.

Smith, S. M. (2002) ‘Fast robust automated brain extraction.’, *Human brain mapping*. United States, 17(3), pp. 143–155. doi: 10.1002/hbm.10062.

Smith, S. M. *et al.* (2004) ‘Advances in functional and structural MR image analysis and implementation as FSL.’, *NeuroImage*. United States, 23 Suppl 1, pp. S208-19. doi: 10.1016/j.neuroimage.2004.07.051.

Smith, S. M. *et al.* (2006) ‘Tract-based spatial statistics: voxelwise analysis of multi-subject diffusion data.’, *NeuroImage*. United States, 31(4), pp. 1487–1505. doi: 10.1016/j.neuroimage.2006.02.024.

Smith, Y. *et al.* (2014) ‘A putative vGluT1-positive glutamatergic cortico-pallidal projection: differential organization between the internal and external globus pallidus’, in *Soc Neurosci Abstr*.

Smith, Y., Hazrati, L. N. and Parent, A. (1990) ‘Efferent projections of the subthalamic nucleus in the squirrel monkey as studied by the PHA-L anterograde tracing method.’, *The Journal of comparative neurology*. United States, 294(2), pp. 306–323. doi: 10.1002/cne.902940213.

Smith, Y. and Wichmann, T. (2015) ‘The cortico-pallidal projection: an additional route for cortical regulation of the basal ganglia circuitry.’, *Movement disorders : official journal of the Movement Disorder Society*. John Wiley and Sons Inc., 30(3), pp. 293–5. doi: 10.1002/mds.26095.

Sritharan, A. *et al.* (2010) ‘A longitudinal diffusion tensor imaging study in symptomatic Huntington’s disease.’, *Journal of neurology, neurosurgery, and psychiatry*, 81(3), pp. 257–62. doi: 10.1136/jnnp.2007.142786.

Stoffers, D. *et al.* (2010) ‘Contrasting gray and white matter changes in preclinical Huntington disease: an MRI study.’, *Neurology*, 74(15), pp. 1208–16. doi: 10.1212/WNL.0b013e3181d8c20a.

Tabrizi, S. J. *et al.* (2013) ‘Predictors of phenotypic progression and disease onset in premanifest and early-stage Huntington’s disease in the TRACK-HD study: analysis of 36-month observational data.’, *The Lancet. Neurology*, 12(7), pp. 637–49. doi: 10.1016/S1474-4422(13)70088-7.

Tagliaferro, P. and Burke, R. E. (2016) ‘Retrograde Axonal Degeneration in Parkinson Disease.’, *Journal of Parkinson’s disease*. Netherlands, 6(1), pp. 1–15. doi: 10.3233/JPD-150769.

Tai, Y. F. *et al.* (2007a) ‘Imaging microglial activation in Huntington’s disease.’, *Brain research bulletin*. United States, 72(2–3), pp. 148–151. doi: 10.1016/j.brainresbull.2006.10.029.

Tai, Y. F. *et al.* (2007b) ‘Microglial activation in presymptomatic Huntington’s disease gene carriers.’, *Brain : a journal of neurology*. England, 130(Pt 7), pp. 1759–1766. doi: 10.1093/brain/awm044.

Thiebaut de Schotten, M. *et al.* (2011) ‘A lateralized brain network for visuospatial attention.’, *Nature neuroscience*. United States, 14(10), pp. 1245–1246. doi: 10.1038/nn.2905.

Thomas, A. G. *et al.* (2009) ‘Functional but not structural changes associated with learning: An exploration of longitudinal Voxel-Based Morphometry (VBM)’, *NeuroImage*, 48(1), pp. 117–125. doi: 10.1016/j.neuroimage.2009.05.097.

Thorner, G., Lange, H. and Hopf, A. (1975) ‘[Morphometrical-statistical structure analysis of human striatum, pallidus and subthalamic nucleus. II. Globus pallidus].’, *Journal fur Hirnforschung*. Germany, 16(5), pp. 401–413.

Tournier, J.-D. *et al.* (2004) *Direct estimation of the fiber orientation density function from diffusion-weighted MRI data using spherical deconvolution*, *NeuroImage*. doi: 10.1016/j.neuroimage.2004.07.037.

Tsukamoto, K. *et al.* (2012) ‘Significance of apparent diffusion coefficient measurement for the differential diagnosis of multiple system atrophy, progressive supranuclear palsy, and Parkinson’s disease: evaluation by 3.0-T MR imaging’, *Neuroradiology*, 54(9), pp. 947–955. doi: 10.1007/s00234-012-1009-9.

Vaillancourt, D. E. *et al.* (2009a) ‘High-resolution diffusion tensor imaging in the substantia nigra of de novo Parkinson disease.’, *Neurology*, 72, pp. 1378–1384. doi: 10.1212/01.wnl.0000340982.01727.6e.

Vaillancourt, D. E. *et al.* (2009b) ‘High-resolution diffusion tensor imaging in the substantia nigra of de novo Parkinson disease.’, *Neurology*, 72(16), pp. 1378–84. doi: 10.1212/01.wnl.0000340982.01727.6e.

Vandenberghe, W. *et al.* (2009) ‘Diffusion-weighted versus volumetric imaging of the striatum in early symptomatic Huntington disease.’, *Journal of neurology*, 256(1), pp. 109–14. doi: 10.1007/s00415-009-0086-0.

Vassar, S. D. *et al.* (2012) ‘Confirmatory Factor Analysis of the Motor Unified Parkinson’s Disease Rating Scale’, *Parkinson’s Disease*. Hindawi Publishing Corporation, 2012, p. 719167. doi: 10.1155/2012/719167.

Veraart, J. and Sijbers, J. (2016) ‘Diffusion Kurtosis Imaging BT - Diffusion Tensor Imaging: A Practical Handbook’, in Van Hecke, W., Emsell, L., and Sunaert, S. (eds). New York, NY: Springer New York, pp. 407–418. doi: 10.1007/978-1-4939-3118-7_21.

Visser, E. *et al.* (2016) ‘Automatic segmentation of the striatum and globus pallidus using MIST: Multimodal Image Segmentation Tool.’, *NeuroImage*. United States, 125, pp. 479–497. doi: 10.1016/j.neuroimage.2015.10.013.

Vonsattel, J. P. *et al.* (1985) ‘Neuropathological classification of huntington’s disease’, *Journal of Neuropathology and Experimental Neurology*, 44(6), pp. 559–577. Available at: http://www.scopus.com/inward/record.url?eid=2-s2.0-0022395922&partnerID=tZOtx3y1.

Vonsattel, J. P., Keller, C. and Cortes Ramirez, E. P. (2011) ‘Huntington’s disease - neuropathology.’, *Handbook of clinical neurology*, 100, pp. 83–100. doi: 10.1016/B978-0-444-52014-2.00004-5.

Vu, A. T. *et al.* (2015) ‘High resolution whole brain diffusion imaging at 7T for the Human Connectome Project.’, *NeuroImage*. United States, 122, pp. 318–331. doi: 10.1016/j.neuroimage.2015.08.004.

Walker, F. O. (2007) ‘Huntington’s disease.’, *Lancet (London, England)*, 369(9557), pp. 218–28. doi: 10.1016/S0140-6736(07)60111-1.

Wang, J.-W. *et al.* (2016) ‘Cognitive and Psychiatric Effects of STN versus GPi Deep Brain Stimulation in Parkinson’s Disease: A Meta-Analysis of Randomized Controlled Trials’, *PLOS ONE*. Public Library of Science, 11(6), p. e0156721. Available at: https://doi.org/10.1371/journal.pone.0156721.

Wang, Q., Wang, Y., *et al.* (2015) ‘Diffusion tensor imaging detected neurodegeneration in preclinical Alzheimer disease’, *Alzheimer’s & Dementia*. Elsevier, 11(7), pp. P77–P78. doi: 10.1016/j.jalz.2015.06.134.

Wang, Q., Wang, Y., *et al.* (2015) ‘Diffusion Tensor Imaging Detects White Matter Changes in Preclinical Stages of Alzheimer Disease’, *ISMRM 23rd Annual Meeting*. Toronto, Ontario, Canada.

Weir, D. W. *et al.* (2011) ‘Development of biomarkers for Huntington’s disease.’, *The Lancet. Neurology*. England: Elsevier, 10(6), pp. 573–590. doi: 10.1016/S1474-4422(11)70070-9.

Whittier, J. R. (1949) ‘Byperkinesia and other physiologic effects of subthalamic lesions, with special reference to the subthalamic nucleus of Luys’, *J Comp Neurol*, 90, pp. 319–372.

Williams, J. K. *et al.* (2015) ‘Everyday cognition in prodromal Huntington disease.’, *Neuropsychology*. United States, 29(2), pp. 255–267. doi: 10.1037/neu0000102.

Wojtecki, L. *et al.* (2016) ‘Deep Brain Stimulation in Huntington’s Disease-Preliminary Evidence on Pathophysiology, Efficacy and Safety.’, *Brain sciences*. Switzerland, 6(3). doi: 10.3390/brainsci6030038.

Yeterian, E. H. and Pandya, D. N. (1989) ‘Thalamic connections of the cortex of the superior temporal sulcus in the rhesus monkey.’, *The Journal of comparative neurology*. United States, 282(1), pp. 80–97. doi: 10.1002/cne.902820107.

Yeterian, E. H. and Pandya, D. N. (1991) ‘Corticothalamic connections of the superior temporal sulcus in rhesus monkeys.’, *Experimental brain research*. Germany, 83(2), pp. 268–284.

Yokoyama, T. *et al.* (1998) ‘Neural activity of the subthalamic nucleus in Parkinson’s disease patients.’, *Acta neurochirurgica*. Austria, 140(12), p. 1287–90; discussion 1291.

Yoshikawa, K. (2004) ‘Early pathological changes in the parkinsonian brain demonstrated by diffusion tensor MRI’, *Journal of Neurology, Neurosurgery & Psychiatry*, 75(3), pp. 481–484. doi: 10.1136/jnnp.2003.021873.